THE OPTICAL PROPERTIES OF CAESIUM PENTACHLOROMANGANATE (II)

by

R.J. Tacon MA

Submitted to the Faculty of Physical Sciences

for the Degree of Doctor of Philosophy

October 1977

Magdalen College, Oxford

THE OPTICAL PROPERTIES OF CAESIUM PENTACHLOROMANGANATE (II)
R.J. TACON, MAGDALEN COLLEGE, OXFORD.
D. Phil, Thesis.
Michaelmas Term, 1977

S H O R T A B S T R A C T

Absorption spectra of tetragonal single crystals of Cs_3MnCl_5 have been measured at 4.2K over the wavelength range 5200-2600Å. Spin forbidden bands of low oscillator strengths were observed for the $^4\Gamma \longleftarrow {}^6A_1$ transitions of the $MnCl_4^{2-}$ chromophore. All the intensity arose from the electric dipole mechanism, but for small magnetic dipole contributions to the intensities of $^4E(G)$ and $^4T_2(F)$. Magnetic circular dichroism spectra measured at 4.2K in a field of 4.75 Teslas were dominated by C-term signals.

The band intensities were assumed to arise via the spin orbit interaction, allowing "intensity borrowing" from higher energy charge transfer transitions. A model based on tetrahedral symmetry for the chromophore ion allowed the calculation of MCD:absorption intensity ratios for the quartet states. Good agreement was found with the experimental values for most quartets.

Crystal Field calculations were performed in support of the MCD-based band assignments. Covalency was introduced into Stout's electrostatic matrices via the Koide and Pryce parameter ϵ. The following parameter values were found: $B = 600cm^{-1}$, $C = 2940cm^{-1}$, $Dq = 350cm^{-1}$, and $\epsilon = 0.03$, giving the correct ordering of the states and an rms. deviation from the observed energies of $520cm^{-1}$. $^4A_2(F)$ was placed above $^4T_1(F)$ in energy, a departure from the "conventional" ^4F term assignment.

A simplified model for the perturbation of the cubic states by the tetragonal component of the crystal field was developed to account for the observed linear polarisations. The spectra were examined in detail to identify the electronic origins and assign them using a tetrahedral or tetragonal scheme. The latter appeared to be the more realistic model for most states. Assisted by data from the Raman spectrum, the vibrational sidebands were also assigned. When very sharp origin lines were present, some of the sidebands showed small splittings attributable to the presence of the two chlorine isotopes.

A B S T R A C T

Absorption spectra of the tetragonal single crystals of caesium pentachloromanganate(II) have been measured at 293 and 4.2K over the wavelength range 5200 to 2600Å. Bands of low oscillator strengths, between $3x10^{-6}$ and $3x10^{-8}$, were observed corresponding to the spin forbidden $^4\Gamma \leftarrow {}^6A_1$ transitions of the Mn^{2+} ion. Magnetic circular dichroism (MCD) spectra have been measured at 4.2K in a field of 4.75 Teslas parallel to the unique axis of the crystal. Under these conditions, the dominant contribution to the MCD signal arises from the Zeeman splitting of the $^6A_1$ ground state, whose g-value was known to be very close to 2.

The intensities of the spin and Laporte forbidden transitions were assumed to arise via the spin orbit interaction, allowing "intensity borrowing" from the $^6T_2 \leftarrow {}^6A_1$ charge transfer transitions occuring at high energies. A model based on tetrahedral symmetry for the $MnCl_4^{2\ominus}$ chromophore ion was used to calculate the ratio of MCD:absorption intensity for each quartet state. Good agreement was found with the experimentally determined intensity ratios for most of the ten quartet states.

Crystal Field calculations have been performed in order to fit the observed band positions. Covalency was incorporated into the electrostatic matrices by means of the Koide and Pryce parameter ϵ, and the following parameter values were found: $B = 600\ cm^{-1}$, $C = 2940\ cm^{-1}$, $Dq = 350\ cm^{-1}$, and $\epsilon = 0.03$. This placed the quartet states in the correct order of decreasing energies:

$^4T_2(F)$ $^4A_2(F)$ $^4T_1(F)$ $^4T_1(P)$ $^4E(D)$ $^4T_2(D)$ $^4A_1(G)$ $^4E(G)$ $^4T_2(G)$ $^4T_1(G)$

and minimised the standard deviation between calculated and observed band maxima at 521 cm^{-1}. The trees correction was included in the energy matrices, with α = 76 cm^{-1}.

A simplified model for the perturbation of the cubic quartet states by the low symmetry component of the crystal field was developed. This is present as a result of a z-elongation of the $MnCl_4$ tetrahedra, reducing the point symmetry from T_d to D_{2d} at the manganese site, and gives rise to the linear polarisations. The low temperature spectra of each quartet state were examined in detail in order to identify the electronic origins and to assign them as spin orbit components of either the unperturbed cubic state or the tetragonal components arising from the cubic state in D_{2d} symmetry. With the assistance of vibrational data from the Raman and infra red spectra of Cs_3MnCl_5, the lines in each band were assigned as sidebands of the electronic origins. In this way, the majority of the spectral features were analysed.

The lowest energy band, $^4T_1(G)$, was found to be broad with no vibrational structure resolved. It was clearly split into tetragonal components, ^4E and $^4A_2$, separated by about 600 cm^{-1}. $^4T_2(G)$ contained sharp lines with vibrational structure resolved, and was again split into tetragonal components ^4E and $^4B_2$ separated by about 280 cm^{-1}. Further, small spin orbit splittings of ^4E were observed over a 30 cm^{-1} range. The $^4E(G)$ band consisted of sharp lines built upon two intense and very sharp origins, the $^4B_1$ tetragonal component lying 36 cm^{-1} below the $^4A_1$ component. Each origin showed a further small splitting into spin orbit components. Some of the vibrational sidebands,

particularly involving ν_1, showed structure attributable to the presence of the two chlorine isotopes. Weak features about 220 cm^{-1} above the $^4E(G)$ origins were tentatively assigned to $^4A_1(G)$. The $^4T_2(D)$ band showed a wealth of sharp line structure based on the ^4E tetragonal component, and broad features from $^4B_2$. $^4E(D)$ hardly resembled $^4E(G)$ at all, and suffered from overlap with stronger bands to either side so that no assignments could be made, while the intense $^4T_1(P)$ band failed to exhibit any clear structure. At high energy, $^4T_1(F)$ was split into $^4A_2$ and ^4E components separated by about 60 cm^{-1}, with $^4A_2$ showing clear spin orbit splitting. The $^4A_2(F)$ band was the narrowest and weakest of the quartets, $^4A_1(G)$ excepted, and the two D_{2d}^* origin lines were 58 cm^{-1} apart. $^4T_2(F)$ failed to fit the pattern predicted by either the tetragonal perturbation or the cubic model, but showed strong linear and circular polarisations and large origin separations. Magnetic dipole contributions to the intensity of this state were present, and also to $^4E(G)$, but otherwise only electric dipole transitions were present.

A C K N O W L E D G E M E N T S

The author wishes to thank the following people :

His supervisor, Dr R.G.Denning, for his advice, encouragement, and patience throughout a prolonged period of study.

Professor A.Davies for making Stoneman's thesis available for reference.

Professor M.T.Vala for his BESTFIT calculations on Cs_3MnCl_5, and, with Drs J.C.Rivoual and J.Badoz, for copies of MCD results prior to their publication.

Drs S.Thomas and D.R.Drury for recording Raman and infra red spectra of Cs_3MnCl_5 crystals.

All his friends and colleagues in Oxford, especially Drs E.R.Krausz, P.N.Quested, T.R.Snellgrove, and D.R.Woodwark, for help in ways too numerous to mention ... I wouldn't have missed it for the world.

His parents whose support and encouragement has been invaluable.

His wife Deborah for devotion beyond the call of duty.

Dale for coping patiently with a difficult manuscript, and B.R.Smedley Esq. for the kind loan of a typewriter.

The financial support of the Science Research Council and Magdalen College is also gratefully acknowledged.

C O N T E N T S

L I S T O F T A B L E S

L I S T O F F I G U R E S

CHAPTER 1

INTRODUCTION

1.1 GENERAL

Continuing progress in chemistry is strongly dependent on the use of physical methods to investigate the structure and properties of chemical compounds. Of the various techniques available, spectroscopy in general is probably the most widely used as electromagnetic radiation is an extremely versatile and sensitive probe. Optical spectroscopy involves the study of electronic transitions occurring at wavelengths in the near infra red, visible, and near ultraviolet regions of the spectrum. It gives information about the electronic structures and properties of excited energy states involving bonding, non-bonding, and anti-bonding orbitals. The current "state of the art" is such that data can be easily obtained. Spectra of ions and molecules in solution can be recorded in a matter of minutes, while high resolution spectra of crystals cooled to the temperature of liquid helium can be obtained using polarised light and magnetic fields as a matter of routine. Therefore it is necessary to exercise some care in choosing chemical systems for study. Cs_3MnCl_5 might be described as a "model" compound, exhibiting a high degree of symmetry, in which to examine in some detail the spin forbidden transitions of the Mn^{2+} ion, modified by the environment of the crystal lattice.

1.2 SYMMETRY

All objects, including molecules, exhibit a degree of symmetry. Depending on the observed symmetry properties, they

can be classified as belonging to space and point groups. The branch of mathematics known as Group Theory can then be applied, and its results are very powerful - see [1] for examples. In particular, we are interested in the forms of the electronic wavefunctions of molecules. Group Theory tells us that the wavefunctions must have the correct transformation properties under the symmetry operations of the point group to which the molecule belongs, and must form a proper basis for the irreducible representations of the point group. Crystals of Cs_3MnCl_5 are known [2] to belong to the tetragonal class (space group D_{4h}^{18}) with D_{2d} point symmetry at the manganese site. However, the deviation of the $MnCl_4^{2\ominus}$ ion from strict tetrahedral symmetry is very slight, and it is treated initially as belonging to the higher T_d symmetry. Both T_d and D_{2d} are contained in the cubic group O. The use of the cubic representations in analysing the optical spectrum of the tetragonal crystal Cs_3MnCl_5 illustrates a general point, namely the use of high symmetry for as long as possible to simplify the calculations. Eventually the lower symmetry can be produced by the addition of a suitable perturbation term once the overall picture is established.

All the optical transitions of Cs_3MnCl_5 reported here violate two important selection rules which derive from atomic spectroscopy:

(i) They are "ligand field" d$\longleftrightarrow$d transitions and are Laporte forbidden.

(ii) They occur between states of different spin multiplicity and are spin forbidden. As a consequence, the transitions are weak. That they occur at all is due to the partial relaxation of both selection rules, the first as a result of d-p mixing,

the second as a result of spin orbit coupling. To treat spin orbit coupling, the theory of double groups must be used [1, 3] so that the tetrahedral group becomes T_d^*. In APPENDIX I are given the character tables for T_d and T_d^*, the multiplication table, and the correlation table 4 . Their derivation and use are given in [3]. There are five irreducible representations A_1, A_2, E, T_1, and T_2 in T_d, to which are added E', E'', and U' in T_d^*. The latter three represenations are used to describe states whose total angular momentum $\underset{\sim}{J}$ is an odd number of units of $\hbar/2$, and may have the quantum number m_J added as a subscript to define them uniquely.

The half-filled 3d shell of the Mn^{2+} ion gives rise to a $^6A_1$ ground state with L = 0, S = 5/2 (J = 5/2). In cubic symmetry, the electric vector $\underset{\sim}{E}$ of the electromagnetic wave transforms as T_2, so that the only electric dipole allowed transition is $^6T_2 \longleftarrow {}^6A_1$ as the direct product $(T_2 \times T_2 \times A_1)$ is the only one of the type $(\Gamma_j \times \Gamma_{\underset{\sim}{\hat{m}}} \times \Gamma_a)$ which contains A_1. $|j\rangle$ and $|a\rangle$ are the excited and ground state wavefunctions respectively, and $\underset{\sim}{\hat{m}}$ is the electric dipole operator. The transition occurs via $\hat{m}_x$, $\hat{m}_y$, and $\hat{m}_z$. In the lower D_{2d} symmetry, $\Gamma_{\underset{\sim}{\hat{m}}} = B_2(\hat{m}_z) + E(\hat{m}_x, \hat{m}_y)$, and the single cubic transition becomes split and polarised:

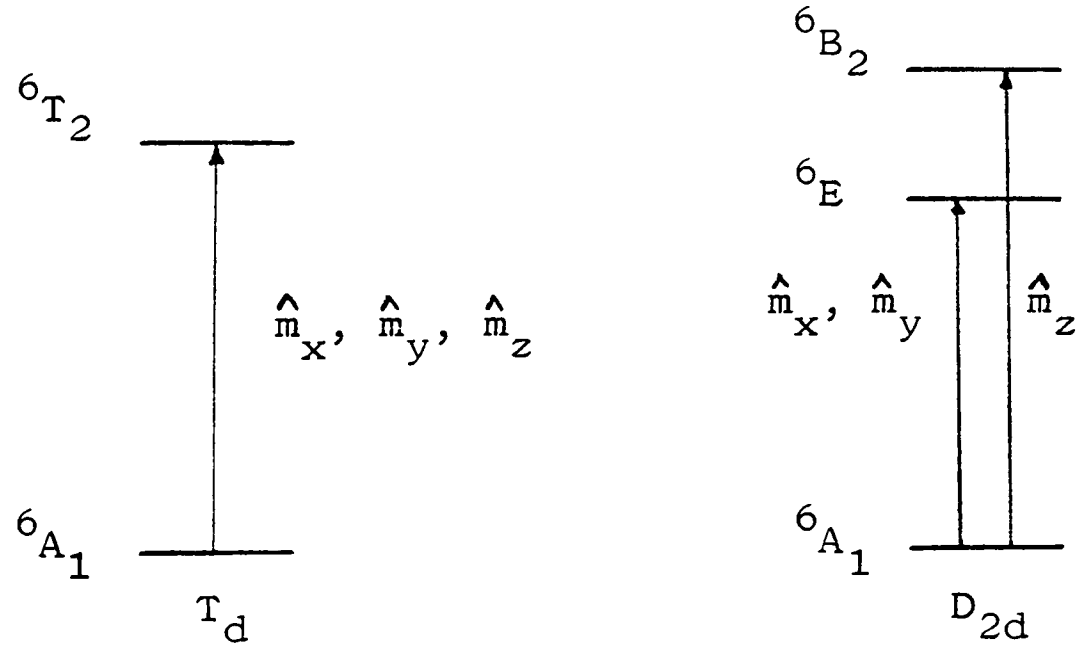

In addition, the ^6E component coming from $^6T_1$ will become apparent in the xy-spectuum because it will be able to mix with ^6E from $^6T_2$. This is a simple example of the application of molecular symmetry in the form of group theoretic arguments. It allows powerful predictions about which electric dipole transitions are allowed, and their polarisations, but does not make any statements about the energies of the transitions or the ordering of the split components of $^6T_2$. Such properties can only be determined by detailed calculations using actual wavefunctions of the full Hamiltonian operator $\hat{\mathcal{H}}$. Also, there has been no introduction of spin into the calculations performed so far; it has been implicitly ignored except in the sense that all the states have had sextet spin labels. This in no way affects the calculation in this case, but must be added when the operation of spin orbit coupling is considered (see CHAPTER 3).

1.3 ABSORPTION AND MCD SPECTROSCOPY

Both these techniques are contained within the general term "optical spectroscopy", and relate to the absorption of light by the sample. Absorption spectra have been measured for over 40 years, at first using photographic methods - for example the study of Gielessen in 1935 [5] of the sharp line spectra of manganous salts cooled to 77K - but now most commonly by photometric means using commerically built instruments. The use of polarised light, magnetic (and electric) fields, and low sample temperatures, together with improvements in the efficiency and stability of light sources and detectors has made absorption spectroscopy a very powerful technique. MCD spectroscopy owes its origin to Faraday's discovery of magnetically induced optical

activity, and its use by chemists was prompted by the theoretical work of Buckingham and Stephens [6] in 1966. MCD is a differential technique measuring directly the difference between the absorption indices of left and right circularly polarised light, which obey different selection rules from linearly polarised light.

In this thesis, we shall be primarily concerned with optical transitions occurring via the electric dipole moment operator $\hat{\underset{\sim}{m}}$, that is, transitions induced by the electric field vector $\underset{\sim}{E}$ of the electromagnetic wave. These should be of the order of 10^4 - 10^6 times as strong as magnetic dipole transitions [3] induced by the magnetic vector $\underset{\sim}{M}$ via the magnetic dipole operator $\hat{\underset{\sim}{\mu}}$:

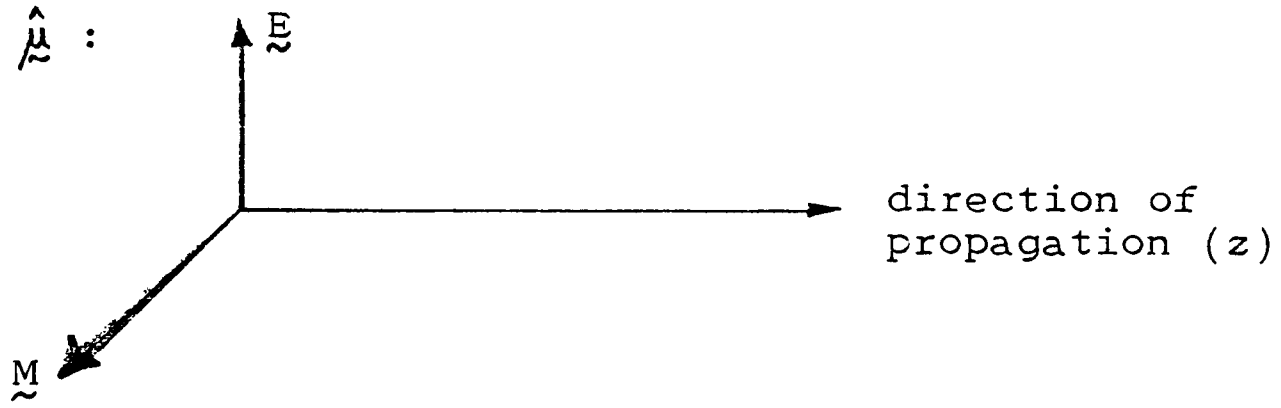

We examine the optical properties of single crystals of Cs_3MnCl_5, which are tetragonal. The unique optic axis is the crystallographic c-axis, which coincides with the molecular z-direction. When light propagates along the unique axis, both $\underset{\sim}{E}$ and $\underset{\sim}{M}$ lie in the ab-plane in which the directions x and y are not distinguished. There is no difference in the refractive indices n_x and n_y, so that an MCD spectrum can be recorded provided the external magnetic field H lies along the c-axis. With zero field, this orientation gives the axial (α) absorption spectrum for unpolarised light, with transitions induced by the x- and y-components of $\underset{\sim}{E}$ and $\underset{\sim}{M}$:

$\alpha = E_{xy} + M_{xy}$ for $\underset{\sim}{E}$ and $\underset{\sim}{M}$ perpendicular to $\underset{\sim}{c}$. EQUATION (1.1)

When the light is propagated perpendicular to the c- axis, two linear polarisations are distinguished:

$\sigma = E_{xy} + M_z$ for $\underset{\sim}{E} \perp \underset{\sim}{c}$, $\underset{\sim}{M} \parallel \underset{\sim}{c}$ EQUATION (1.2)

$\pi = E_z + M_{xy}$ for $\underset{\sim}{E} \parallel \underset{\sim}{c}$, $\underset{\sim}{M} \perp \underset{\sim}{c}$. EQUATION (1.3)

If the electric dipole mechanism alone is responsible for the absorption intensity, then α- and σ-spectra should be identical in all respects, while the π-spectrum remains distinct.

(Electric quadrupole transitions are in theory possible, and one has recently been observed in $Cs_2UO_2Cl_4$ crystals [7] , but they will not be considered here as they are weaker than magnetic dipole transitions [3] .) Also, electric dipole transitions are expected to have a very simple temperature dependence: the overall intensity, as measured by the oscillator strength, should remain constant [8] . Thus cooling the crystal from room temperature to 4K should merely cause the bands to sharpen by reducing the half-widths, but not to change in total intensity. This will not be the case, however, if there is magnetic coupling between individual ions, if a phase change occurs, or if there are low-lying levels above the ground state. Fortunately such complications are not present in Cs_3MnCl_5.

1.4 LIGAND FIELD THEORY [8, 9, 10, 11, 12]

One of the most obvious features of chemical compounds is their colour, and in particular colour is associated with transition metal ions in compounds and complexes. As early as 1926, it had been observed that the number and type of ligands attached to a particular transition metal ion played a part in determining the colour, and there were speculations as to a possible relationship between colour and electronic structure [13] . In 1929,

Bethe [14] applied group theoretic arguments to show that the electronic terms of transition metal ions are affected by purely electrostatic fields such as might be found in ionic crystals. This work provided the key link between the spectra of free atoms and ions in the gas phase, and the colours of compounds in solution or the solid state.

(i) Free Ion Spectra

These consist of sharp lines, and were easy to record photographically. Theories for their interpretation were developed as relativistic quantum mechanical methods were applied. Very briefly, the wavefunctions ψ of the atom or ion are written as products of radial and angular parts:

$$\psi_{n,l,m_l} = R_{n,l}(r) \times Y_l^{m_l}(\Theta,\phi) \qquad \text{EQUATION (1.4)}$$

The Hamiltonian operator is:

$$\hat{\mathcal{H}} = \sum_i \hat{f}_i + \sum_{i \neq j} \hat{g}_{ij} \qquad \text{EQUATION (1.5)}$$

where $\hat{f}_i$ relates to the kinetic and potential energies of electron i in the field of the nucleus, and $\hat{g}_{ij}$ deals with the repulsion forces between electrons i and j. In order to calculate the energies $E = \langle \psi | \hat{\mathcal{H}} | \psi \rangle$, the integrals $\langle i | \hat{f} | i \rangle$ and $\langle ij | \hat{g} | ij \rangle$ must be evaluated. The first type, the one-electron integrals, are straightforward, while the two-electron integrals are more difficult. It is these electron-electron repulsion energies $\langle ij | \hat{g} | ij \rangle$ which are important in optical spectroscopy in splitting the various terms of a given electronic configuration. They produce two types of integral, the classical Coulomb term $\langle ij | \hat{g} | ij \rangle$, and the quantum mechanical exchange term $\langle ij | \hat{g} | ji \rangle$, both of which will be expressed as sums of products of radial and angular parts. These

can be simplified in terms of the Slater-Condon parameters F_o, F_2, and F_4, so that compilations of the term energies can be made, e.g. [15].

In 1942, Racah [16] found that many free ion spectra of the transition metals could be described in terms of two parameters, B and C, derived from the Slater-Condon parameters as follows:

$$A = F_o - 49F_4, \quad B = F_2 - 5F_4, \quad C = 35F_4. \qquad \text{EQUATION (1.6)}$$

A, B, and C are the Racah parameters. For assumed hydrogenic wavefunctions, $A = 17937\ Z_e$, $B = 129\ Z_e$, and $C = 516\ Z_e$ in cm^{-1}, where Z_e is the effective nuclear charge experienced by a 3d-electron. Then the ratio C/B = 4 exactly.

The ion Mn^{2+}, or MnIII in the notation of atomic spectroscopy, has a $3d^5$ electronic configuration. The 3d sub-shell is half-filled (just as in the neutral atom, MnI, $3d^5 4s^2$) and the ground state is ^6S with an energy (10A - 35B). Electronic rearrangements within $3d^5$ produce four quartet terms with the following energies relative to the ground state:

$$^4F = 22B + 7C \quad (= 50B \text{ for } C/B = 4)$$
$$^4D = 17B + 5C \quad (= 37B)$$
$$^4P = 7B + 7C \quad (= 35B) \qquad \text{EQUATION (1.7)}$$
$$^4G = 10B + 4C \quad (= 26B)$$

as well as eleven doublets. Despite the violation of the $\Delta S = 0$ selection rule, transitions from ^6S to all four quartets are observed. They are seen to have fine structure associated with spin orbit coupling $\zeta_{3d} \sim 320\ cm^{-1}$. An exact fit of the quartet energies cannot be obtained using just two parameters, and there is quite a large range of C/B values which will

give a reasonable fit, e.g.:

Tanabe and Sugano [17] B = 860 cm^{-1}, C = 3853 cm^{-1}, C/B = 4.48

Griffith [3] and Orgel [18] B = 960 cm^{-1}, C = 3325 cm^{-1}, C/B = 3.46

These results are shown diagramatically in FIGURE 1.

A further theoretical development due to Trees and Racah [19, 20] introduced two further parameters, and hence a better fit to the observed energies. The Trees correction α appears as $\alpha L(L + 1)$ in the term energies, while the seniority correction β appears as βQ - see APPENDIX VI for further details. There are now four observed energies [21] and four parameters, and the solutions are exact [22] :

^4F: 43617 = 22B + 7C + 12α + 2β

^4D: 32355 = 17B + 5C + 6α

^4P: 29199 = 7B + 7C + 2α + 2β giving B = 918 cm^{-1}, C = 3273 cm^{-1}, (C/B = 3.565), α = 65 cm^{-1}

^4G: 26845 = 10B + 5C + 20α β = -131 cm^{-1}

These values place the ^2I level 163 cm^{-1} below its observed energy of 39175 cm^{-1}, compared with errors of +1109 cm^{-1} [17] and -2015 cm^{-1} [18] .

(ii) Crystal Field Theory

This is the simplest approach to the description of the influence of the ligands upon the central ion in a complex. The ligands are regarded as point charges (ions) or point dipoles (neutral molecules) which interact with the 3d-electrons on the transition metal ion electrostatically. In cubic symmetry, the d-orbitals fall into two sets on the basis of their angular distributions:

Regular Octahedron (6 ligands) Tetrahedron (4) or Cube (8 ligands)

The e-orbital set comprises the $d_{x^2-y^2}$ and d_{z^2} orbitals with effectively zero angular momentum, while the t_2-orbitals are d_{xy}, d_{yz}, and d_{zx} with one unit of angular momentum. Mathematically, these results may be derived by expressing the electrostatic potential $\hat{V}$ in terms of spherical harmonics, and calculating the perturbation energies $\langle \psi | \hat{V} | \psi \rangle$. Using the product forms of the wavefunctions given in EQUATION (1.4), the energies are obtained in terms of a parameter Dq, which in turn is a product of radial and angular parts. The angular integrals D may be performed explicitly, while the radial integrals q remain in a generalised form involving the mean fourth power radius of the d-orbitals $\langle r^4 \rangle$. For equal ligand-metal separations and the same charges, we find:

$$Dq(T_d) = -4/9Dq(O_h) \qquad \text{EQUATION (1.8)}$$

Dq is a one-electron orbital energy. Similar results may be obtained for other coordination geometries, but in cases of lower symmetry, the orbital energies cannot be determined by a single parameter. However, they allow predictions to be made about the electronic ground state of the complex, from which the magnetic properties are derived, about the likely electronic configurations of excited states which give rise to optical absorption, and about certain thermodynamic properties in which the crystal field stabilisation energy plays a part, such as heats of hydration.

(iii) Molecular Orbital Theory

When applied to transition metal complexes, MO theory considers the possibilities for covalent bond formation. These are governed by the symmetry of the metal orbitals and the ligand orbital combinations. Ionic forces are also considered. The same energy level pattern emerges for cubic complexes as in (ii) above [23], but the e-t_2 energy difference is signified by Δ which is a sum of ionic, σ-, and π-bonding contributions. The orbitals which may be identified as being made up mostly of metal 3d-orbitals are non-bonding or antibonding in nature, and are partially filled, see FIGURE 2. In order to obtain realistic numerical results, it is necessary to use a many-centre MO approach of considerable mathematical complexity. However, the simpler non-mathematical results are still of great value in the interpretation of data such as identifying the trends along a series of metals or ligands.

1.5 WEAK AND STRONG CRYSTAL FIELDS

Although the Crystal Field model is somewhat unrealistic, it is simple to apply and the results have been very widely used. Two schemes, known as the Weak Field and the Strong Field, have been developed. In the Weak Field treatment, it is recognised that the crystal field acts as a minor perturbation of the free ion wavefunctions, so that Dq $<<$ B. The five basis functions are those which diagonalise $\hat{\underset{\sim}{L}}$ and $\hat{\underset{\sim}{S}}$, i.e. the d_o, $d_{\pm1}$, and $d_{\pm2}$ orbitals. The Strong Field treatment, brought to prominence by the work of Tanabe and Sugano [17], uses the e- and t_2-wavefunctions which diagonalise the potential

field of the ligands as its basis set. The electron-electron repulsions are then added as a perturbation term, i.e. Dq >> B. Strong Field states $t_2^n e^{(N-n)}$ in octahedral symmetry have energies (6N-10n)Dq. For example, for the Mn^{2+} ion in a tetrahedral ligand field, we have possible configurations:

ENERGY	CONFIGURATION	CUBIC TERMS ARISING
+20Dq	t_2^5	$^2T_2$ only
+10Dq	et_2^4	$^4T_1$, $^4T_2$, and doublets.
0	$e^2t_2^3$	$^6A_1$, $^4A_1$, $^4A_2$, $^4E(1)$, $^4E(2)$, $^4T_1$, $^4T_2$, and various doublets.
-10Dq	$e^3t_2^2$	$^4T_1$, $^4T_2$, and doublets.
-20Dq	e^4t_2	$^2T_2$ only

Because d^5 is its own hole-equivalent, there is symmetry about the zero of energy so that if Dq changes sign (T_d to O_h), the energy level and the cubic term patterns remain unchanged.

The electrostatic matrices of Tanabe and Sugano [17] contain B, C, and Dq as parameters, and the cubic term energies depend on them. If a value of C/B is chosen, then it is possible to plot an energy level diagram whose ordinate E/B and abscissa Dq/B increase from zero. Two reasonable choices of C/B are the hydrogenic value (4), or that observed for the free ion, the latter being the most common. Such plots are known as Tanabe-Sugano diagrams, and that for $3d^5$ is shown in FIGURE 3. The zero of energy is the ground term, which may change as Dq/B increases. At the changeover point, all the lines suffer a discontinuous change of slope.

The relationship between the Weak and Strong Field schemes may be expressed in terms of transformation matrices. The basic difference lies in the order in which the perturbations are applied to the 3d-wavefunctions, and depends on whether Dq is considered to be greater than or less than B. Very often it is the case that a real compound falls between the two extremes of behaviour. This may be represented in terms of a correlation diagram, and FIGURE 4 shows the case for the quartet states of Mn^{2+}. The diagram is constructed by determining what cubic terms arise from the free ion terms on the left and from the strong field configurations on the right. The correlation is between terms bearing the same spin and symmetry labels, and is governed by the non-crossing rule.

The Strong Field scheme has been successfully used to analyse the spectra of many transition metal complexes. The values of B and C are generally found to be smaller than in the free ion, corresponding to an increase in the average radial extension of the d-orbitals in the complex. The order of Dq values gives rise to the well known Spectrochemical Series. However, the exact way in which spectra are analysed can change the parameter values, and the validity of using a single set of (reduced) Racah parameters to calculate the energies of terms arising from different free ion states or strong field configurations has been questioned [24, 25, 26]. It is probably best to regard B,C, and Dq as parameters to be used to fit the observed spectra, and to exercise great care when comparing values between different compounds.

1.6 ESR OF S-STATE IONS

Electron spin resonance experiments yield much very precise data on the ground states of complex ions. The $3d^5$ ions Mn^{2+} and Fe^{3+} have, in weak and intermediate fields, $^6A_1$ ground states coming from free ion ^6S terms:

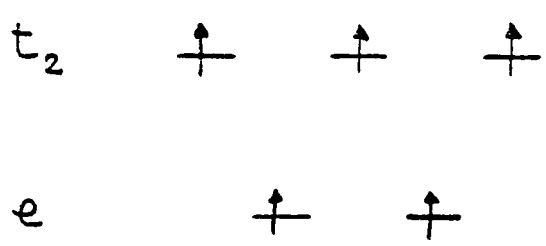

These are orbitally non-degenerate, and give (E" + U') in the double group representation O^*. The degeneracy of these two levels is only lifted in high order perturbation theory by the simultaneous action of spin orbit coupling, allowing partial mixing between $^6A_1$ and $^4T_1$ excited states, and the crystal field operator [27]. The result is a small zero field splitting (zfs) for cubic symmetry. The theory of Wanatabe [28] allows the calculation of the zfs parameter a:

$$a = \alpha Dq^2 - \beta Dq^4 \qquad \text{EQUATION (1.9)}$$

where α and β are functions of ζ_{3d}, and $\alpha >> \beta$. Therefore a is predicted to be positive in both cubal, octahedral, and tetrahedral coordination as only even powers of Dq are involved. Many experimental studies have been performed with Mn^{2+} doped into cubic and axial host lattices, and have confirmed that a is positive, e.g.:

HOST LATTICE	SITE SYMMETRY	VALUE OF a(cm^{-1})	REFERENCE
CaF_2	O_h	$+0.6 \times 10^{-4}$	[29]
CdF_2	O_h		[30]
$KMgF_3$	O_h	$+6.5 \times 10^{-4}$	[30]
$MgCl_2$	O_h		[30]
$CdCl_2$	O_h		[30]
MgO	O_h	$+18.6 \times 10^{-4}$	[31]
CdTe	T_d		[30]
ZnO	T_d		[30]
ZnS	T_d	$+8 \times 10^{-4}$	[32]
Cs_3ZnCl_5	D_{2d}	$+10.7 \times 10^{-4}$	[33]

The results on Cs_3ZnCl_5 are especially significant. It is isomorphous with Cs_3MnCl_5 (and with Cs_3CoCl_5) [34], and the lattice dimensions are very similar:

Cs_3ZnCl_5 [34] $\quad a = 9.25$ Å, $\quad c = 14.50$ Å

Cs_3MnCl_5 [2] $\quad a = 9.21$ Å, $\quad c = 14.91$ Å,

so that the parameter values for Mn^{2+} in each lattice should be almost identical. Henning and Bongers found that the effect of the low symmetry component of the crystal field is roughly an order of magnitude larger than the cubic zfs, giving the pattern as follows:

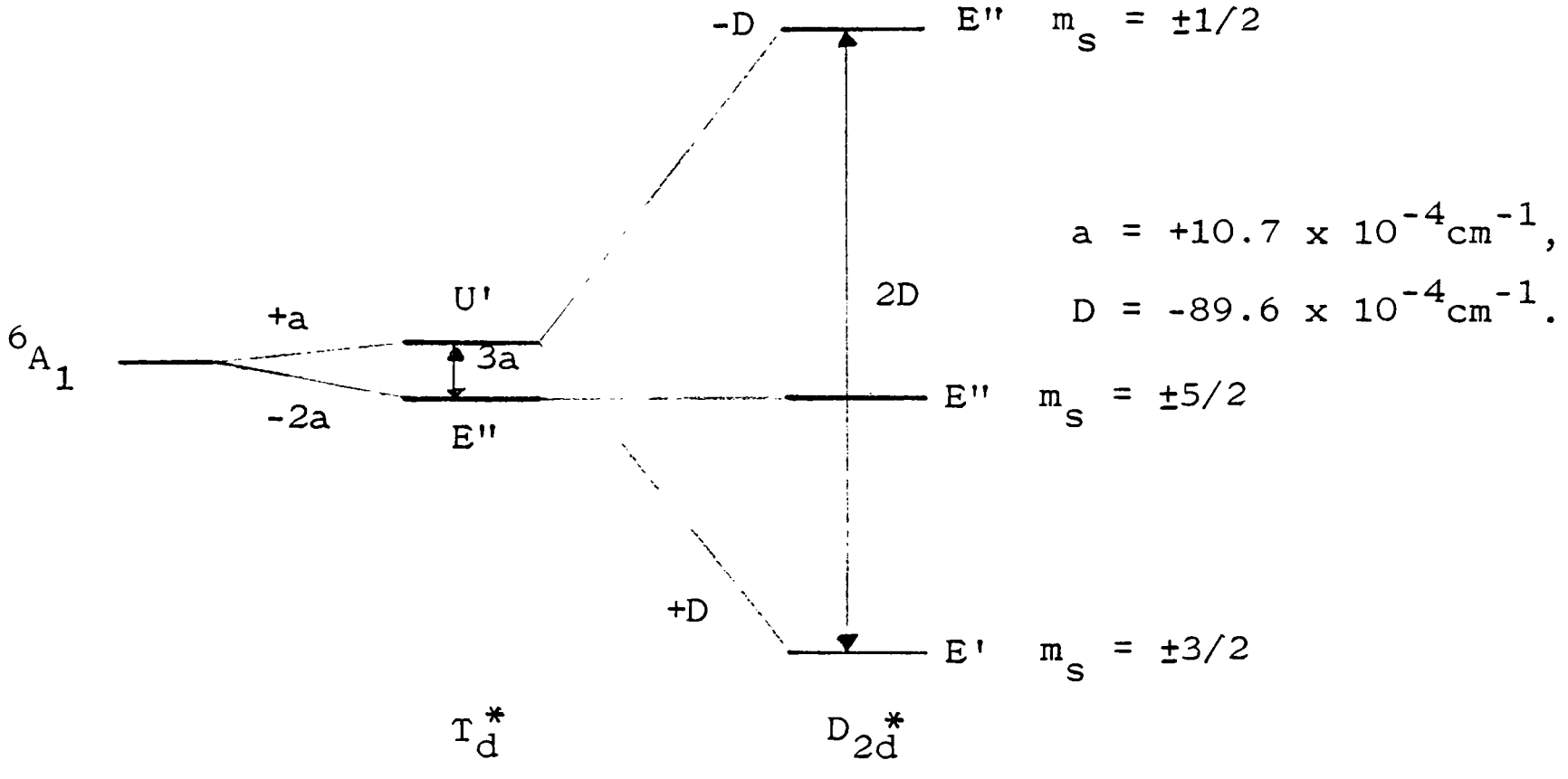

Tiny splittings such as these are, however, not significant under the conditions we have employed with Cs_3MnCl_5, and so for the purposes of optical spectroscopy we shall consider the components of $^6A_1$ to be degenerate in absence of a magnetic field. Further, the g-values for Mn^{2+} doped into Cs_3ZnCl_5 measured parallel and perpendicular to the unique axis are respectively 2.011_o and 1.992_6 [33] , both very close to the free ion spin-only value of 2.0023. We shall use these values for Cs_3MnCl_5.

1.7 SPECTROSCOPIC STUDIES OF MANGANESE (II) COMPLEXES

This section is in no way intended to be an exhaustive review of the topic, but will briefly augment and update the data on Mn^{2+} presented by Hush and Hobbs [35] in their general article on the spectra of transition metal compounds published in 1968. Our particular interest will be in tetrahedral chloro complexes, in the use of MCD as an aid to interpretation, and in the source of intensity of the doubly forbidden $^4\Gamma \longleftarrow {}^6A_1$ transitions.

Many of the earliest studies were performed photographically, and were restricted to the identification of the terms arising from free ion ^4G, ^4D, and ^4P, as seen in aqueous solutions of Mn^{2+} salts and in simple cubic crystals. Interpretation of the energy levels was much influenced by the work of Tanabe and Sugano [17], and Orgel [36] . He produced the energy level diagrams of term energies plotted against Dq - see FIGURE 3 for the Orgel diagram for Mn^{2+}. Kiode and Pryce [37] showed that the accidental degeneracy of $^4A_1$ and ^4E from ^4G - AE(G)- was lifted by the effect of covalency through σ-bonding.

It was also shown that the observed intensities of the $^4\Gamma \longleftarrow {}^6A_{1g}$ transitions in octahedral complexes could be accounted for on the assumption of spin orbit mixing of $^4T_{1g}$ character into the $^6A_{1g}$ ground state wavefunction, in conjunction with coupling to odd-parity vibrations. Englman [38] later showed that spin orbit mixing of charge transfer states $^6T_{1g}$, lying outside the $3d^5$ configuration, into the $^4\Gamma$ wavefunctions could also give rise to the observed intensities, again assuming vibronic coupling.

The simple halide crystals were among the first systems to be examined at low temperature using polarised light: MnF_2 [39, 40] , $MnCl_2$ and $MnBr_2$ [41, 42] , and $MnX_2 . 4H_2O$ (X = Cl or Br) [43] , and immediately showed many interesting details. There were band shifts, and intensity and polarisation changes associated with the onset of magnetic ordering, particularly for the sharp lines of the AE(G) region. An absorption study of $Mn(H_2O)_6SiF_6$ was made at 1.7K, and use of the Zeeman effect later established $^4A_{1g}$ to be about 130 cm^{-1} above ^4E_g [44, 45] . A classic early work by McClure [46] used ZnS doped with Mn^{2+} at varying concentrations. At very low $[Mn^{2+}]$, the single ion spectrum was seen, and Beer's Law was obeyed, while as $[Mn^{2+}]$ increased the intensity was dominated by pair absorptions of higher extinction coefficient which do not violate the $\Delta S = 0$ selection rule. The possibility of investigating the details of magnetic coupling between ions in the lattice, of the coupling between aligned spins and lattice vibrations, and of perturbation effects such as stress, crystal contraction, structure change, etc. led to a large number of spectroscopic studies. Many of these

were on MnF_2, and on perovskite fluorides such as $RbMnF_3$ and $KZnF_3$ doped with Mn^{2+}. A long-standing controversy arose over the $^4A_1$ - ^4E ordering in $RbMnF_3$, with Ferguson et al [47, 48] supporting the earlier result of Tsujikawa for $Mn(H_2O)_6SiF_6$, while Stevenson [49] proposed a reversed scheme with ^4E above $^4A_1$. This was not resolved until MCD measurements were made on $KMgF_3$ and $KZnF_3$ doped with Mn^{2+}, in which ^4E was found to be 90-100 cm^{-1} below $^4A_1$ [50] .

The first systematic study to involve tetrahedral complexes was by Cotton, Goodgame, and Goodgame [51] , who reported the spectra of the halides $R_2Mn\ X_4$ in solution, mulls, and crystal form. (R is a large organic cation, X = Cl, Br, or I.) Intensities were up to 100 times larger than in octahedral complexes, and the order of intensities I $\gg$ Br $\gtrsim$ Cl suggested involvement of halogen orbitals in the transition mechanism. The system studied by McClure, Mn^{2+} doped into ZnS crystals, involves tetrahedral coordination of the manganese atom, and further experiments were performed on this and similar compounds doped with Mn^{2+}, e.g.: ZnS [52, 53] ; ZnSe and CdS [54] ; ZnSe [55] ; and also MnS itself [56] . In these, the number of bands available for study is limited by the presence of host lattice charge transfer bands. However, Parrot and Blanchard made a detailed investigation into the AE(G) region aided by the application of a uniaxial stress to the ZnS crystal and could find no evidence for a $^4A_1 \longleftarrow {}^6A_1$ transition [57] . They calculated that the $^4A_1$ level should lie above the observed ^4E, but that the transition to it should be roughly 1000 times weaker. In 1967, Lawson [58] reported low temperature polarised spectra of the tetraalkylammonium

chlorides $(R_4N)MnCl_3$-octahedral, and $(R_4N)_2MnCl_4$-tetrahedral, while at the same time Stoneman and Dunn were investigating Cs_2MnCl_4 and Cs_3MnCl_5. This work was not widely published, with illustrations of some Cs_2MnCl_4 spectra appearing in the books of Figgis [9] and Dunn [11] , while the full results are to be found in the thesis of Stoneman [59] . Only the ^4G and ^4D terms were observed, the spectra of Cs_3MnCl_5 being very similar to those reported later (CHAPTER 6) but of lower resolution and slightly poorer quality. High resolution spectra of $(R_4N)_2MnCl_4$ and $(R_4N)_2MnBr_4$ have recently been reported by Vala et al [60] , together with crystal field and spin orbit calculations. These results are discussed in some detail later (CHAPTERS 5 and 6).

Manganese salts in aqueous solution were first studied using MCD by McCaffery et al [61] , who found the high $\Delta\varepsilon/\varepsilon$ ratio predicted for an MCD spectrum dominated by C-terms (see CHAPTER 2 for explanation). Kato [62] has reported the MCD spectra of $(Et_4N)_2MnCl_4$ and $(Et_4N)_2MnBr_4$ in CH_3CN solution, but only at low resolution. However, the overall signs of the MCD bands agree with those reported later (CHAPTER 6) for Cs_3MnCl_5. High resolution MCD and MLD spectra have been recorded for $(Et_4N)_2MnX_4$ single crystals, X = Cl, Br, or I, by Vala et al [63] , and again these results will be discussed in detail later (CHAPTER 6).

Further references to spectroscopic studies of manganese(II) complexes can be found by means of annual literature reviews, e.g. [64, 65] , review articles, e.g. [8, 35], and from the series of papers by Lohr [66, 67, 68] . These include types of

compounds outside our present scope: oxides and salts of oxy-acids, minerals, phosphors, organometallics, etc.

1.8 AIMS OF THE CURRENT STUDY

Cs_3MnCl_5 contains $MnCl_4^{2\ominus}$ ions which are very close to tetrahedral symmetry, and from work done on the similar Cs_3CoCl_5 and Cs_3CoBr_5 crystals [69, 70] the lattice is known to be suitable for high resolution spectroscopy. The tetragonal symmetry of the crystal allows the use of MCD, and the compound remains magnetically dilute down to very low temperatures: the transition to an antiferromagnetic state occurs at 0.6K, with a small amount of short range ordering present up to 1K [71] . Charge transfer bands are only found at very high energies, above $45{,}000cm^{-1}$ for $MnCl_4^{2\ominus}$ in solution [72] . These factors mean that a detailed study can be made of all ten quartet states of the $MnCl_4^{2\ominus}$ ion, given crystals of good optical quality. There is particular interest in several areas:

(i) The mechanism by which the doubly forbidden transitions gain intensity. In tetrahedral coordination, the complication of coupling with odd parity vibrations is removed as there is no centre of inversion. This simplifies the calculation of band intensities.

(ii) The use of MCD spectroscopy to clarify band assignments, and to assist in the location and identification of band origins.

(iii) The extension of Stoneman's earlier results on Cs_3MnCl_5 [59] to the higher energy terms ^4P and ^4F. The latter occurs at lower energy than in octahedral Mn(II) complexes, so that details of the three cubic terms are clearer, with less interference from scattering of light (which increases as λ^{-4}).

(iv) The interpretation of the fine detail seen under high resolution. With the aid of Raman data on Cs_3MnCl_5, the coupling of vibrational modes to the electronic origins can be analysed.

(v) The AE(G) degeneracy. Particularly sharp origin lines are found here, exhibiting strong linear and circular polarisations.

(vi) The degree of deviation from purely tetrahedral behaviour. The manganese site symmetry is actually D_{2d}, but the distortion of the $MnCl_4^{2\ominus}$ ion from strict tetrahedral symmetry is slight.

Details of the preparation and properties of single crystals of Cs_3MnCl_5 are given in APPENDIX II, while experimental details of the methods used for measuring the spectra are contained in APPENDIX III (MCD) and APPENDIX IV (absorption and Zeeman). The experimental results are presented in CHAPTERS 3, 4, 5, and 6.

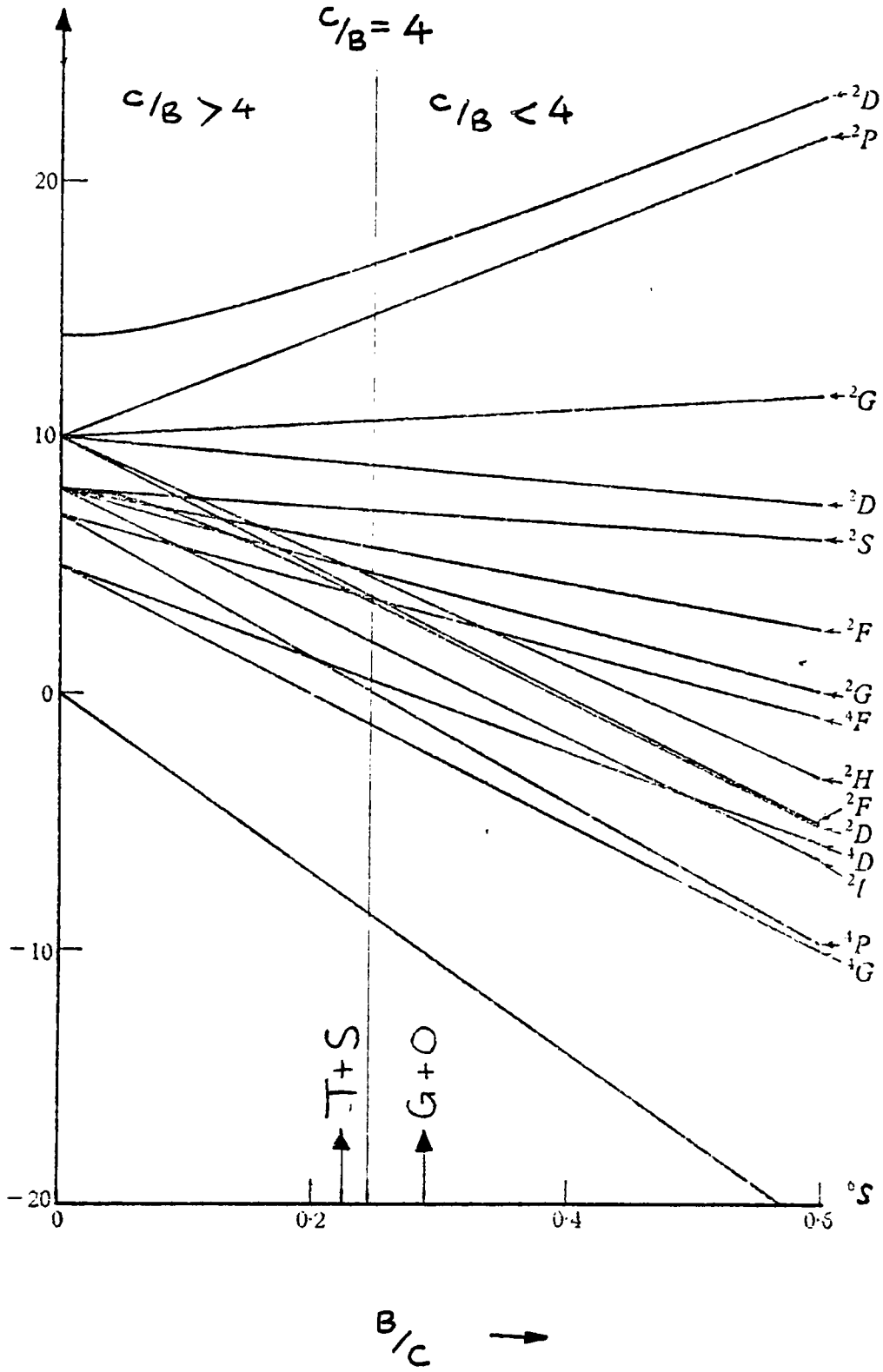

FIGURE 1 .

ENERGY LEVELS OF THE $3d^5$ FREE ION', Mn^{2+} , PLOTTED AS A FUNCTION OF THE RATIO B/C . THE VERTICAL LINE CORRESPONDS TO THE HYDROGENIC RATIO C/B = 4 . TO THE LEFT IS THE PARAMETER CHOICE OF TANABE AND SUGANO , C/B = 4.477 , AND TO THE RIGHT THAT OF GRIFFITH AND ORGEL , C/B = 3.464 .

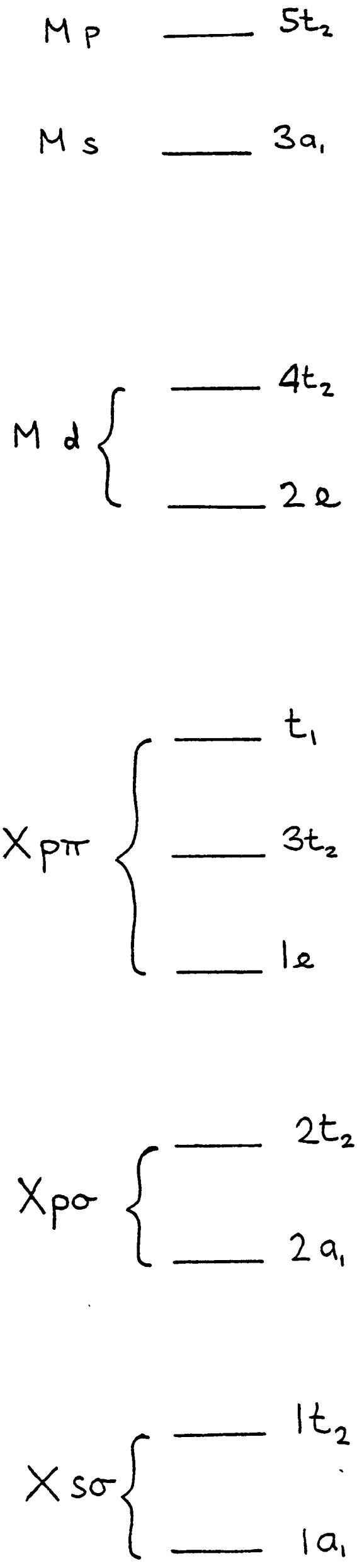

FIGURE 2.

APPROXIMATE MOLECULAR ORBITAL ENERGY LEVEL ORDERING IN TETRAHEDRAL MX_4 HALIDE COMPLEXES .

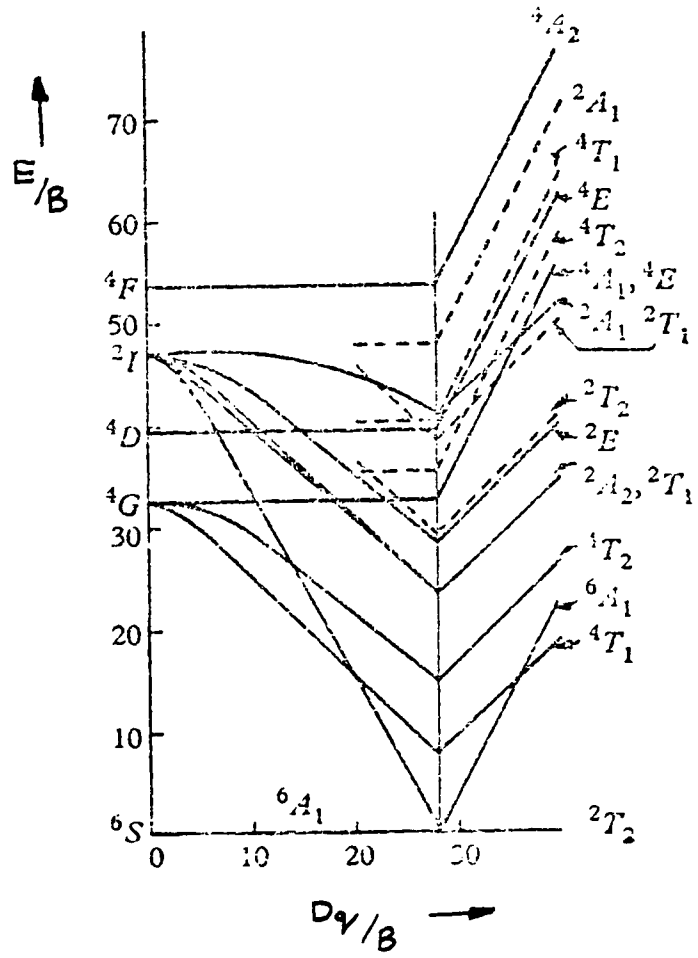

C/B = 4.477

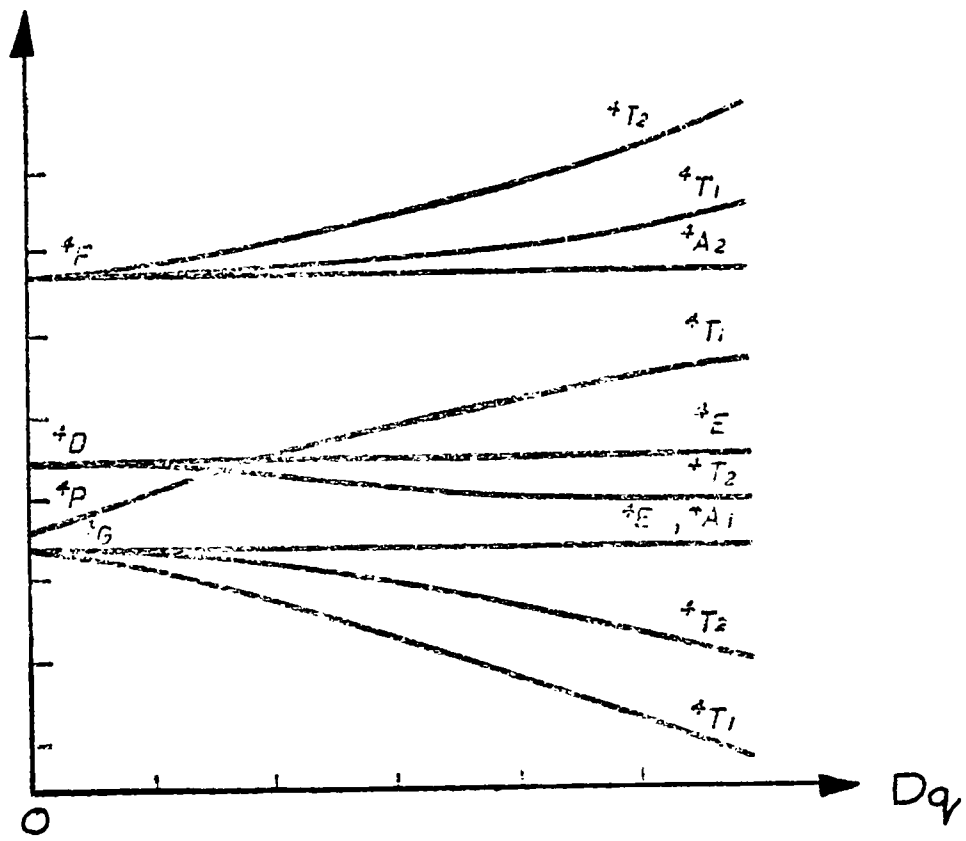

FIGURE 3 .

[TOP] TANABE - SUGANO AND [BOTTOM] ORGEL DIAGRAMS FOR $3d^5$, Mn^{2+} .

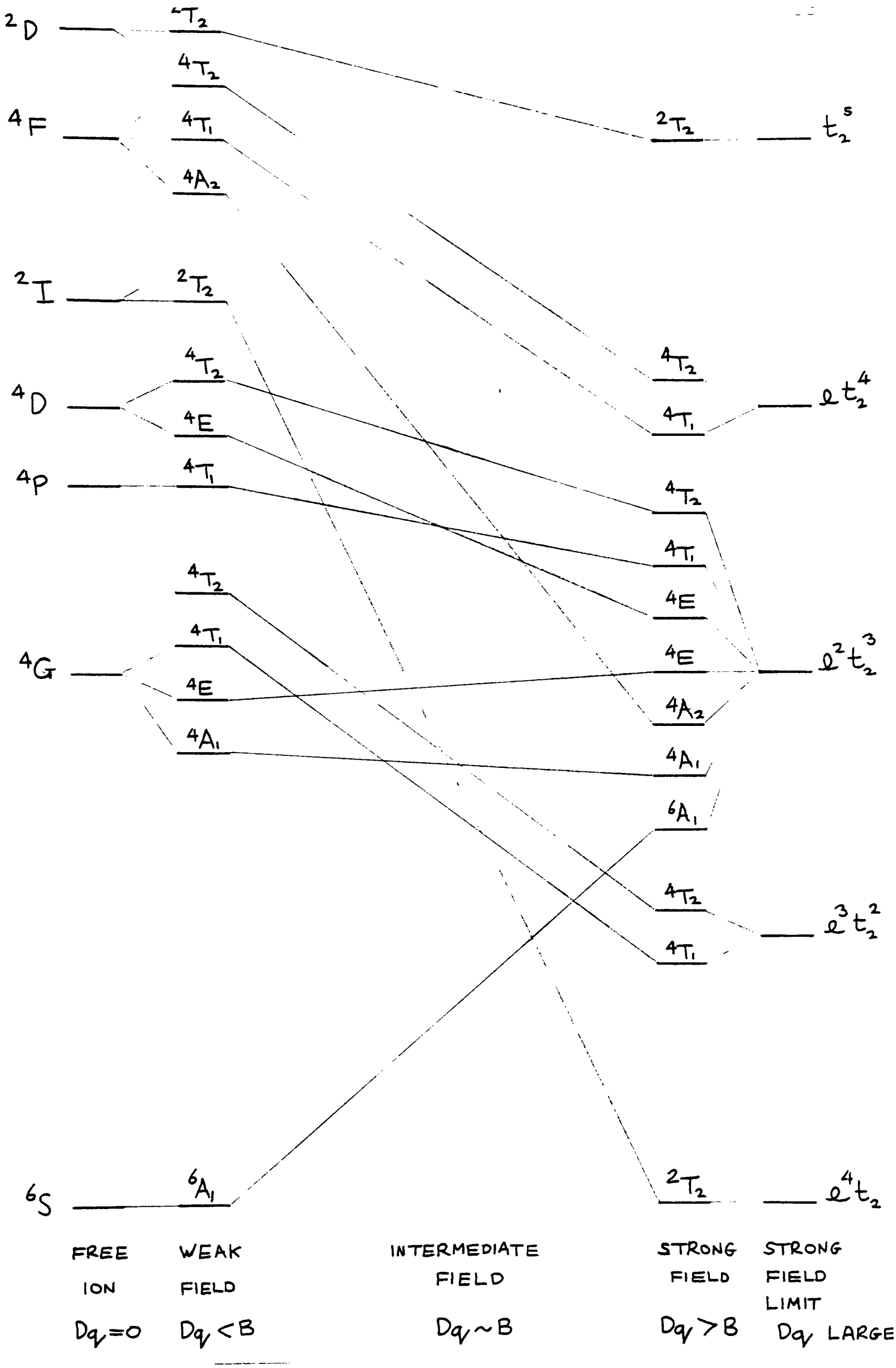

FIGURE 4 .

SCHEMATIC CORRELATION DIAGRAM FOR $3d^5$ Mn^{2+} IN TETRAHEDRAL SYMMETRY .

C H A P T E R 2

THE THEORY OF MAGNETIC CIRCULAR DICHROISM

2.1 INTRODUCTION

In 1845, Michael Faraday discovered that the application of a magnetic field upon any medium altered its optical properties so that it became optically active. This became known as the Faraday Effect. For a magnetic field with a component H along the direction of propagation of a linearly polarised beam of light, the induced rotation ϕ' is given by:

$$\phi' = VHd \qquad \text{EQUATION (2.1)}$$

The Verdet Constant V is a characteristic of the medium at a given temperature, concentration, and radiation frequency; d is the path length. Plane polarised light may be considered to consist of equal amounts of left and right circularly polarised light (LCP and RCP respectively). Rotation of the plane of polarisation by an optically active medium arises because the refractive indices for LCP and RCP light (n_- and n_+ respectively) are not equal, producing a phase difference between the two components. This phenomenon can be measured as a function of frequency, and is the optical rotatory dispersion (ORD):

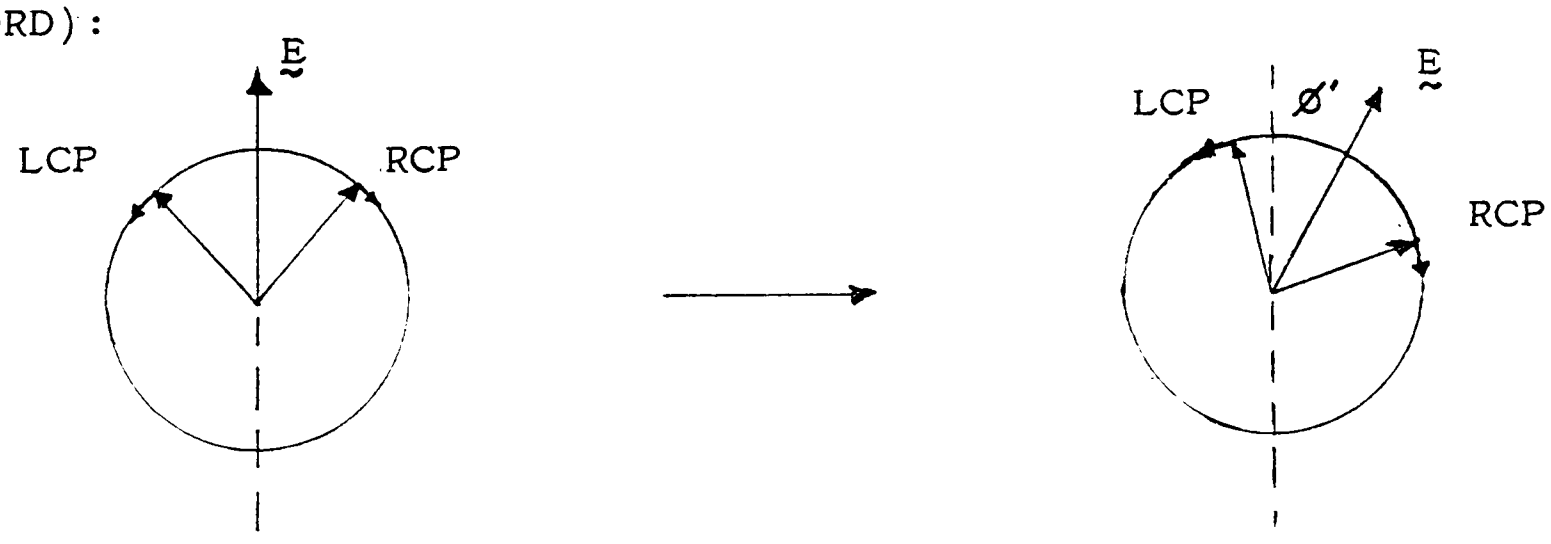

The labels in this diagram are correct for light travelling out of the plane of the paper, and the sign convention is the same as for natural optical activity [73].

In regions of the spectrum where the medium absorbs light, the ORD changes rapidly as n_- and n_+ vary under the band. Also, the extinction coefficients for LCP and RCP light are in general no longer equal. This causes the emergent light to be elliptically polarised:

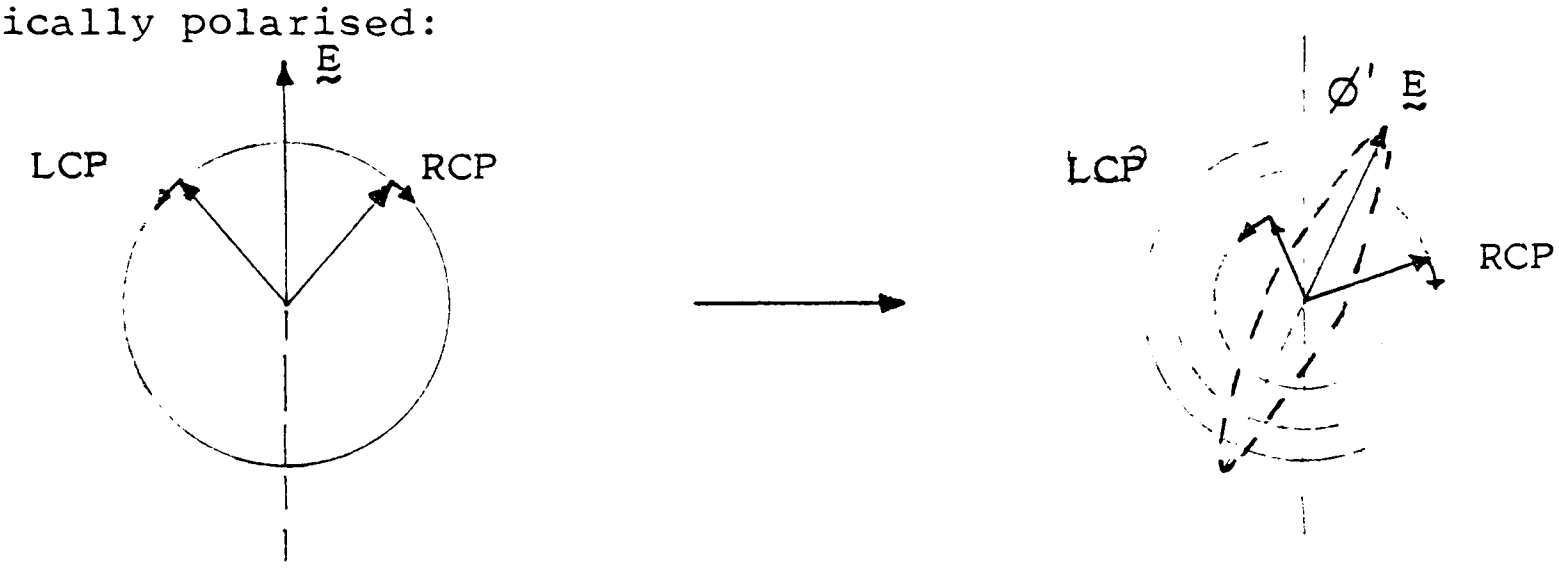

The ellipticity Θ' is related simply to the ratio of the major and minor axes of the ellipse. The phenomenon is known as circular dichroism (CD), and is non-zero only in regions of the spectrum where the medium absorbs light. FIGURE 5 shows typical dispersion curves for ORD and CD. They can be observed for all naturally optically active materials, or can arise from the Faraday Effect. In this latter case, they are referred to as magnetic optical rotatory dispersion (MORD) and magnetic circular dichroism (MCD). The MCD is of particular interest as it is restricted to regions of absorption and obeys different selection rules from the linearly polarised absorption spectrum.

2.2 THE THEORY OF MCD

The treatment given here follows that of Schatz and McCaffery [74], but is given in full to avoid certain errors

in that article. Also, we wish to draw attention to the different ways in which MCD data may be described as a result of the use of differing experimental conditions.

The above EQUATION (2.1) can be generalised into:

$$\hat{\phi} = \phi - i\theta = \frac{\pi}{\lambda}(\hat{n}_- - \hat{n}_+) \qquad \text{EQUATION (2.2)}$$

in which $\hat{\phi}$ is the complex magnetic rotation per unit length whose real part ϕ is the rotation and whose imaginary part θ is the ellipticity. These two quantities are related to each other by Kramers-Kronig transforms [75]. $\hat{n}_\pm$ is the complex refractive index defined by:

$$\hat{n}_\pm = n_\pm - i\chi_\pm \qquad \text{EQUATION (2.3)}$$

where $n_\pm$ is the real refractive index and $\chi_\pm$ the index of extinction. Subscripts - and + refer to LCP and RCP light respectively. To obtain chemically useful information from the observed rotation or ellipticity, the bulk property must be related to properties of the individual molecules. For θ, this can be done as follows. The light emerging from a dichroic medium has an ellipticity θ' given by:

$$\tan\theta' = \frac{\text{minor axis}}{\text{major axis}} \qquad \text{EQUATION (2.4)}$$

$$= \frac{(a_- - a_+)}{(a_- + a_+)}$$

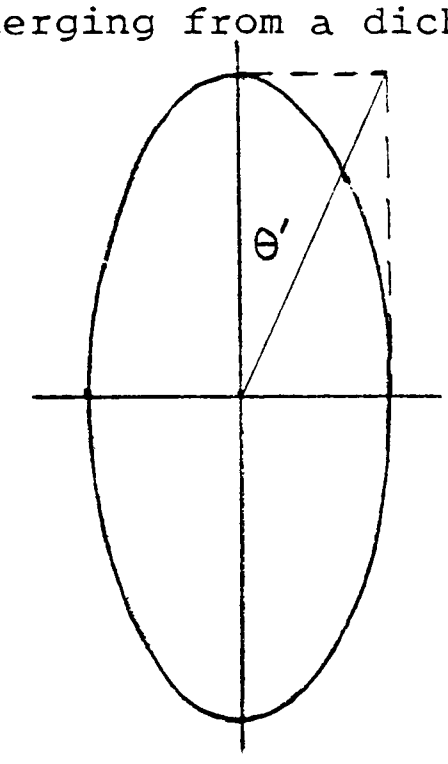

in which $a_\pm$ stands for the amplitude of a circularly polarised component of the light. The Beer-Lambert Law can be written in the form:

$$I = I_o e^{-4\pi\chi d/\lambda} \qquad \text{EQUATION (2.5)}$$

Since intensity equals amplitude squared we have:

$$a = a_o e^{-2\pi\chi d/\lambda} \qquad \text{EQUATION (2.6)}$$

Substitution into (2.4) gives the result:

$$\tan\theta' = \tanh\left[\frac{\pi d}{\lambda}(\chi_- - \chi_+)\right] \qquad \text{EQUATION (2.7)}$$

An alternative statement of the Beer-Lambert Law is in terms of the molecular absorption coefficient $\alpha_\pm$, $I = I_o e^{-\alpha d}$, giving:

$$\tan\theta' = \tanh\left[\frac{d}{4}(\alpha_- - \alpha_+)\right] \qquad \text{EQUATION (2.8)}$$

MCD instruments record the differential absorbance ΔOD as a function of wavelength:

$$\Delta OD = A_{LCP} - A_{RCP} \qquad \text{EQUATION (2.9)}$$

and operate in decadic units. Then:

$$\tan\theta' = \tanh\left[\Delta OD \ \frac{\ln 10}{4}\right] \qquad \text{EQUATION (2.10)}$$

If small values of θ' and ΔOD are assumed, the trigonometric functions may be discarded:

$$\theta' \simeq \Delta OD \ \frac{\ln 10}{4} \simeq \frac{d}{4}(\alpha_- - \alpha_+) \qquad \text{EQUATION (2.11)}$$

The ellipticity per unit length θ is then:

$$\theta = \frac{1}{4}(\alpha_- - \alpha_+) \qquad \text{EQUATION (2.12)}$$

The molecular absorption coefficients $\alpha_\pm$ can be calculated by applying time-dependent perturbation techniques (see, for example, reference [4], Section 7-9):

$$\alpha_\pm = \frac{8\pi^3}{hc}(N_a - N_j)\, f(\nu, \nu_o)\, |\langle a | \hat{m}_\pm | j \rangle|^2 \qquad \text{EQUATION (2.13)}$$

Remembering that:

$$|\langle a|\hat{m}_\pm|j\rangle|^2 = |\langle j|\hat{m}_\mp|a\rangle|^2 \qquad \text{EQUATION (2.14)},$$

reference [76], p. 175, we then have:

$$(\alpha_- - \alpha_+) = \frac{8\pi^3}{hc}(N_a - N_j) f(\nu,\nu_o)\left\{|\langle j|\hat{m}_+|a\rangle|^2 - |\langle j|\hat{m}_-|a\rangle|^2\right\}$$

EQUATION (2.15).

N_a and N_j are respectively the numbers of molecules per unit volume in states $|a\rangle$ and $|j\rangle$ (for electronic transitions, $N_j \simeq 0$), $\nu_o = (E_j - E_a)/h$, and $f(\nu,\nu_o)$ is a line-shape function. The absorption coefficient α is related to the more familiar extinction coefficient ε by:

$$\alpha = \varepsilon\, c \ln 10$$ EQUATION (2.16),

so that (2.15) becomes:

$$(\varepsilon_- - \varepsilon_+) = \frac{1}{c \ln 10}\,\frac{8\pi^3}{hc}\,N_a\, f(\nu,\nu_o)\left\{|\langle j|\hat{m}_+|a\rangle|^2 - |\langle j|\hat{m}_-|a\rangle|^2\right\}$$

EQUATION (2.17)

$(\varepsilon_- - \varepsilon_+)$ is equivalent to $(\varepsilon_L - \varepsilon_R) = \Delta\varepsilon$; at unit concentration, $N_a = L/1000$ where L is the Avogadro Number. Therefore:

$$\Delta\varepsilon = \frac{8\pi^3}{hc}\,\frac{L}{10^3 \ln 10}\, f(\nu,\nu_o)\left\{|\langle j|\hat{m}_+|a\rangle|^2 - |\langle j|\hat{m}_-|a\rangle|^2\right\}$$

EQUATION (2.18)

This equation does not rely on any approximation for small ellipticity, whereas this assumption is implicit in Schatz and McCaffery's treatment [74], which gives the result:

$$\theta = \frac{2\pi^3}{hc}\, N_a\, f(\nu,\nu_o) \sum_{j \leftarrow a}\left\{|\langle j|\hat{m}_+|a\rangle|^2 - |\langle j|\hat{m}_-|a\rangle|^2\right\}$$

EQUATION (2.19)

The summation is over all the degenerate components of the transition.

2.3 THE FARADAY PARAMETERS

The optical activity induced when a magnetic field is applied to a medium arises from three first-order effects which are illustrated with the simplest example, atomic ^1S and ^1P levels.

(i) Zeeman splitting of the Excited State: Faraday A-term

When this occurs, the separate circularly polarised transitions occur at different energies. If the Zeeman splitting is smaller than the linewidth, a "derivative-shaped" curve is obtained.

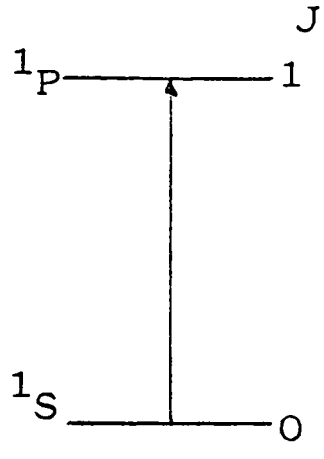

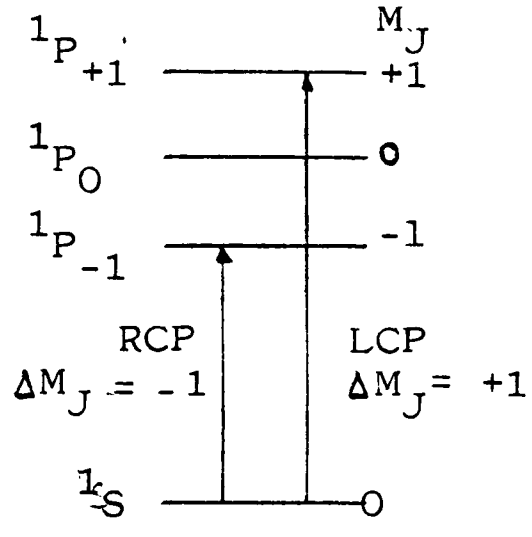

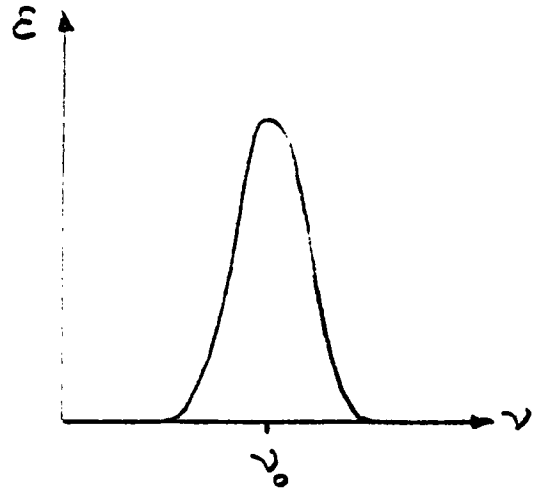

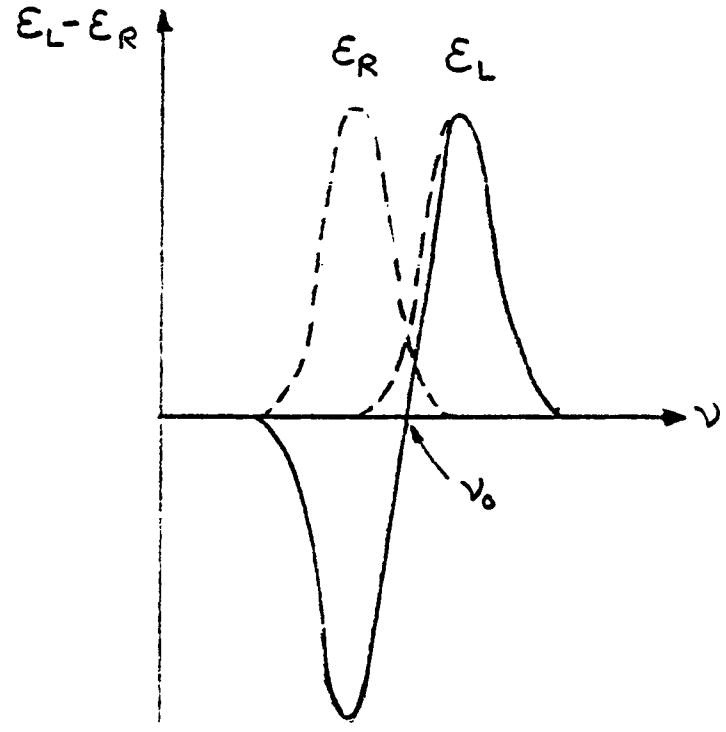

As the linewidth increases relative to the Zeeman splitting, the A-term becomes smaller.

(ii) Field-induced mixing of states: Faraday B-term

Under the influence of the magnetic field, the wavefunctions $|a\rangle$ and $|j\rangle$ can be modified by field-induced mixing with other excited states $|k\rangle$, provided the states are linked by the z-component of the magnetic dipole operator, $\hat{\mu}_z$. Then the MCD of the $j \longleftarrow a$ transition will contain contributions from these

other states.

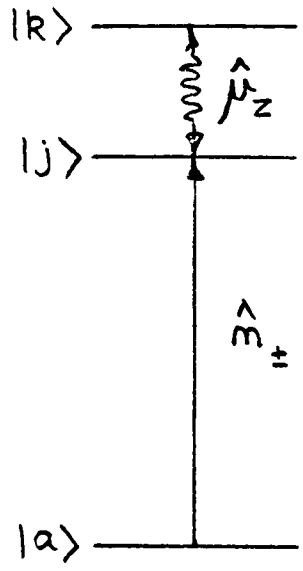

The resulting line-shape is the same as for the C-term explained below. The effect increases linearly with magnetic field, but is not temperature dependent.

(iii) Zeeman splitting of the Ground State: Faraday C-term

When the ground state is split up into separate Zeeman components, we have a situation comparable to (i) above, but with the additional factor of the distribution of population over the Zeeman levels to be considered.

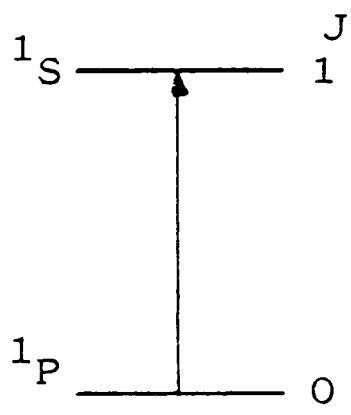

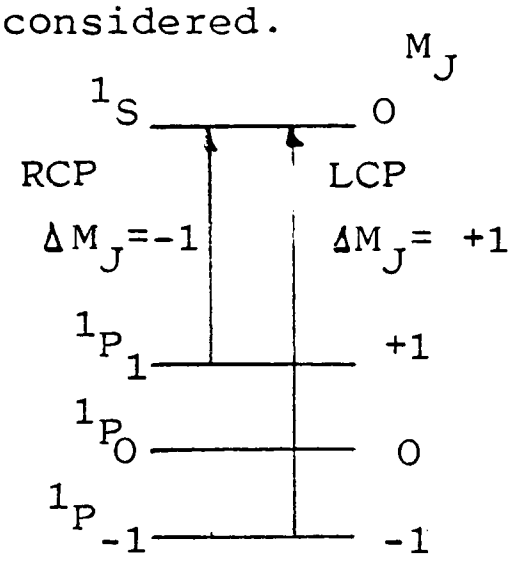

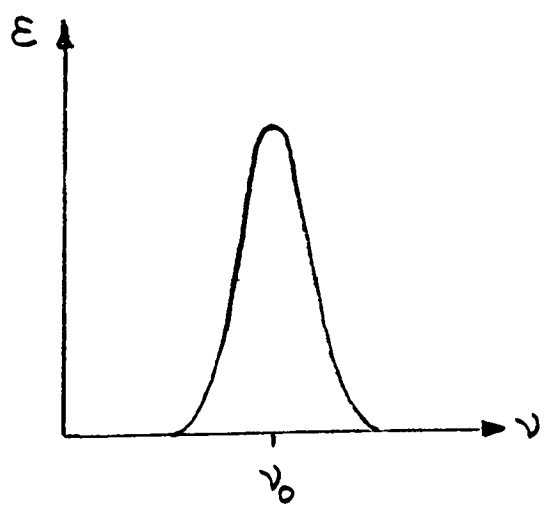

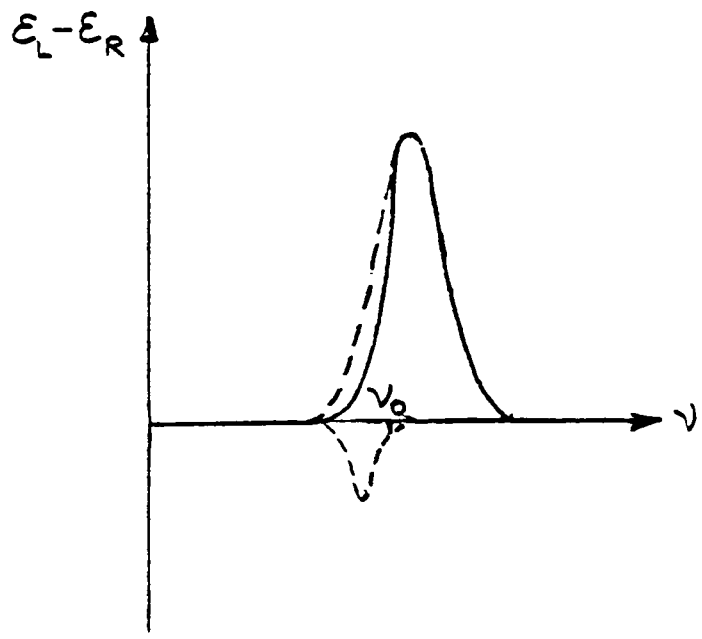

The size of the MCD signal will depend on the intrinsic intensities of the circularly polarised transitions, and the populations of the ground state components, controlled by the magnetic moment, the field strength, and the temperature. C-term contributions are most important in MCD spectra recorded at low temperatures with high magnetic fields.

Schatz and McCaffery outline how these three first order effects can be treated in quantum mechanical terms. The complete calculations are rather complicated, and are given in full in a paper by Stephens [77]. The final result for the ellipticity is:

$$\theta = - \frac{8\pi^2 N}{3hc} \left\{ f_1 A + f_2 (B + C/kT) \right\} H_z \qquad \text{EQUATION (2.20)}$$

where N is the total number of molecules per unit volume, f_1 and f_2 are lineshape functions, and:

$$A = \frac{3}{d_a} \sum_{j \leftarrow a} \left[\langle j|\hat{\mu}_z|j\rangle - \langle a|\hat{\mu}_z|a\rangle \right] \mathcal{I}m \langle a|\hat{m}_x|j\rangle \langle j|\hat{m}_y|a\rangle$$

EQUATION (2.21)

$$B = \frac{3}{d_a} \sum_{j \leftarrow a} \mathcal{I}m \left\{ \sum_{k \neq a} \left[\frac{\langle k|\hat{\mu}_z|a\rangle}{(E_k - E_a)} \right] \left[\langle a|\hat{m}_x|j\rangle\langle j|\hat{m}_y|k\rangle - \langle a|\hat{m}_y|j\rangle\langle j|\hat{m}_x|k\rangle \right] \right.$$
$$\left. + \sum_{k \neq j} \left[\frac{\langle j|\hat{\mu}_z|k\rangle}{(E_k - E_j)} \right] \left[\langle a|\hat{m}_x|j\rangle\langle k|\hat{m}_y|a\rangle - \langle a|\hat{m}_y|j\rangle\langle k|\hat{m}_x|a\rangle \right] \right\}$$

EQUATION (2.22)

$$C = \frac{3}{d_a} \sum_{j \leftarrow a} \langle a|\hat{\mu}_z|a\rangle \mathcal{I}m \left\{ \langle a|\hat{m}_x|j\rangle \langle j|\hat{m}_y|a\rangle \right\}$$

EQUATION (2.23)

The matrix elements of $\hat{m}_x$ and $\hat{m}_y$ appearing above can be re-written in terms of the raising and lowering operators $\hat{m}_+$ and $\hat{m}_-$. In APPENDIX V, we calculate C for the transition $^1S \leftarrow {}^1P$ to show that the result agrees with the definitions

contained in the labelling of the diagram given above, i.e. $\hat{m}_+$ corresponds to LCP, $\hat{m}_-$ to RCP.

2.4 DISCUSSION

Modern MCD machines measure the differential optical density ΔOD directly rather than ellipticity Θ . In the treatment above, it was necessary to assume a small ellipticity in order to arrive at EQUATION (2.20), and this assumption must be repeated to obtain a relationship between ΔOD and the Faraday Parameters:

$$\Delta OD = \Delta\varepsilon \, cd \quad \text{and} \quad \Delta\varepsilon = -6.472 \times 10^{-3} \left\{ f_1 A + f_2 (B + C/kT) \right\} H_z$$

EQUATION (2.24)

From EQUATION (2.16) it can be seen that $\Delta\varepsilon$ is linearly related to $(\alpha_- - \alpha_+)$, so that the expression for $\Delta\varepsilon$ (2.18) holds true under all conditions. The corresponding relationship for ellipticity is a functional one (2.8) which rapidly departs from linearity as the quantities involved increase.

We shall now go on to consider the conditions under which it is valid to use the Faraday Parameters to describe MCD spectra.

(i) Small Zeeman splitting relative to kT

This limitation refers to the splitting of the ground state by the magnetic field, which gives rise to the C-term. The Boltzmann distribution of population over the ground state Zeeman levels is:

$$N_a = N_a^{\,o} \, e^{-(E_a - E_a^{\,o})/kT}$$

$$= N_a^{\,o} \, (1 + \langle a | \hat{\mu}_z | a \rangle H_z/kT + \text{higher terms})$$

EQUATION (2.25)

In the expansion, only the term linear in H_z is retained, a procedure valid only if $\langle a | \hat{\mu}_z | a \rangle H_z/kT$ is small compared to

unity. This condition is liable to be violated at low temperatures and high magnetic fields, when the effect known as "saturation" is observed - see 2.6.

(ii) Small Zeeman splitting relative to linewidth

If the field-induced splitting of either the ground or excited state is large compared to the width of the absorption lines, then it will no longer be correct to consider the components of the transition to be degenerate. Under extreme conditions, separate circularly polarised component to component transitions will be seen. To talk of A-, B-, or C-terms becomes impossible, and the separate LCP and RCP intensities for each transition should be calculated. A, B, and C form the basis for a valid description if the difference between the ground and excited state Zeeman splittings is less than half the linewidth.

In spite of these limitations, the Faraday Parameters have some very useful qualitative properties which assist in the assignment of spectra:

(i) A-terms change sign at the absorption maximum whereas B- and C-terms peak at this wavelength.

(ii) C-terms are inversely proportional to absolute temperature.

(iii) A-terms are only possible if either the ground or excited state of the transition is degenerate.

(iv) C-terms are only possible if the ground state is degenerate.

(v) B-terms are a general feature of all molecular electronic transitions.

(vi) Faraday Parameters, unlike absorption coefficients, have a sign as well as a magnitude, a most important feature aiding the interpretation of spectra.

2.5 FARADAY PARAMETERS FROM EXPERIMENTAL DATA

The most direct method is by least squares curve fitting of the experimental MCD spectra. This fails to make use of the properties of the Faraday Parameters listed above, and the results will vary with the type of band shape functions assumed (e.g. Gaussian, Lorentzian, damped oscillator, etc.). A much more powerful technique making use of the above properties is the method of moments, first applied to the Faraday Effect by Henry et al [78]. Moments are computed by numerically integrating the MCD and absorption data. The n-th moments of the MCD and absorption are respectively:

$$\langle\theta\rangle_n = \int_{\text{band}} \frac{[\theta]_m}{\nu} \nu^n \, d\nu \qquad \text{and} \qquad \langle\varepsilon\rangle_n = \int_{\text{band}} \frac{\underline{\underline{\varepsilon}}}{\nu} \nu^n \, d\nu$$

EQUATION (2.26)

In the zeroth moment $\langle\theta\rangle_0$, the A-term contribution integrates out to zero, allowing (B + C/kT) to be extracted. The value does not depend on any assumption of a band shape, and is also valid where the band represents the total vibronic envelope of a single electronic transition. Further information may be obtained from higher order moments of the MCD, see [78]. The zeroth moment of the absorption, $\langle\varepsilon\rangle_0$, is closely related to the dipole strength D, which is defined as:

$$D = \frac{1}{d_a} \sum_{j \leftarrow a} |\langle a| \hat{\underline{\underline{m}}} |j\rangle|^2$$

$$= \frac{9.1834 \times 10^{-3}}{\nu_0} \int_{\text{band}} \varepsilon(\nu) \, d\nu \qquad \text{EQUATION (2.27)}$$

$$\simeq 9.1834 \times 10^{-3} \langle\varepsilon\rangle_0 \quad \text{for a reasonably narrow band.}$$

(The derivation of (2.27) is given in [76], Appendix 10.2.)

2.6 TEMPERATURE DEPENDENCE AND SATURATION BEHAVIOUR

The temperature dependence of the MCD spectrum is important as it indicates the extent to which C-terms contribute. The MCD due to C-terms varies as 1/T, so that if a plot of MCD band intensity against 1/T at constant field goes through the origin, then it is safe to assign the low temperature MCD entirely to C-terms. For example, the MCD of the spin forbidden and the allowed bands of Co^{2+} doped into $(Et_4N)_2ZnI_4$ arises entirely from C-terms [79]. The sign of the C-term is determined by the symmetry of the transition, and the magnitude of C/D depends on the ground-state magnetic moment. This will be sensitive to Jahn-Teller distortions and low symmetry crystal field components.

Saturation behaviour is most valuable when working at high fields and low temperatures. Under such conditions, almost the entire ground state population will be concentrated in the lowest energy Zeeman level, transitions from which may be completely circularly polarised. It then becomes relatively easy to identify the symmetries of excited states from the sign of the MCD, as was done for Cs_3CoBr_5 [70]. Such experiments cannot be described directly in terms of Faraday Parameters; later in CHAPTER 3 we develop a means of treating such data numerically. If the field dependence of the bands is recorded at constant temperature, the initial slope of the plot of ΔOD against H_z can be related to the Faraday Parameters for that particular band. Care must be taken with sharp lines as there will in general be a wavelength shift as H_z increases from zero. A saturation plot

typically has the form:

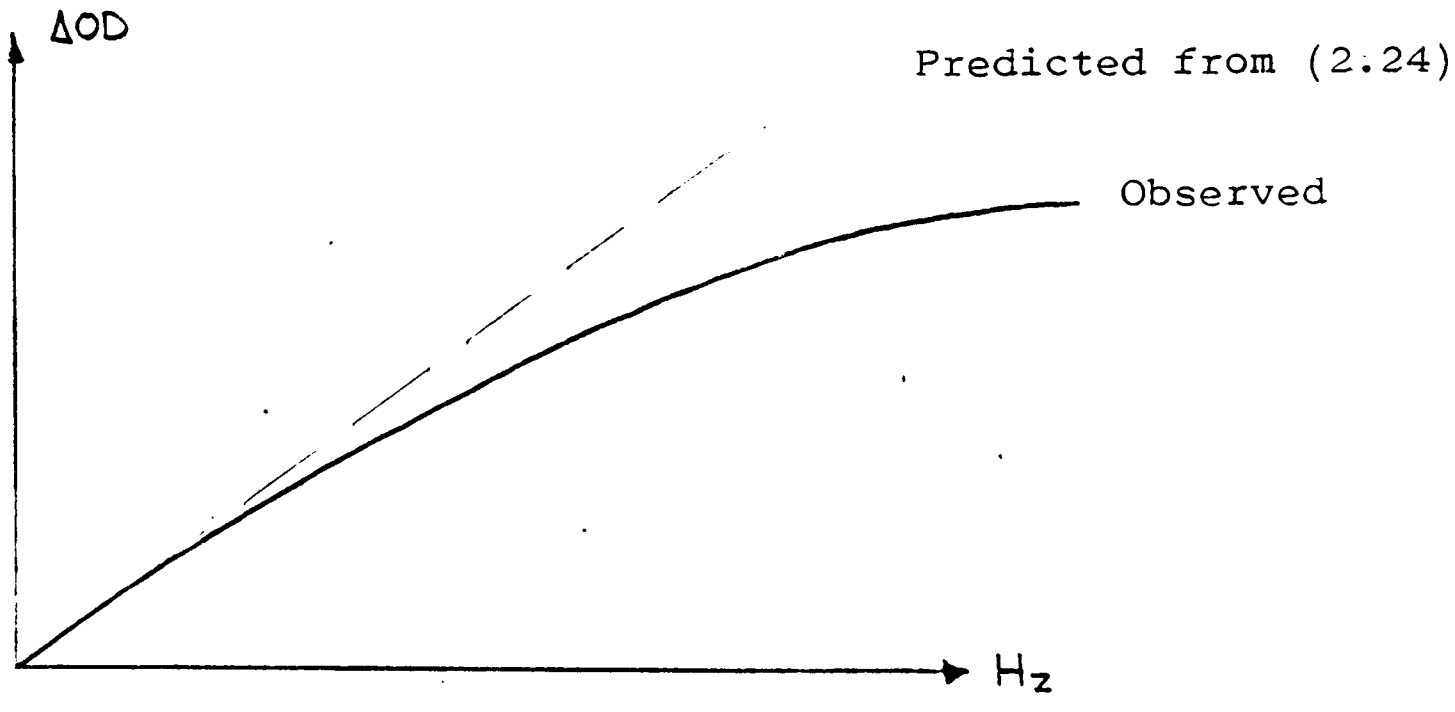

2.7 GENERAL REQUIREMENTS FOR MCD

MCD experiments can be performed on materials which are either isotropic, e.g. gases and vapours, solutions, polymer films, glasses, or cubic crystals, or are uniaxial, e.g. hexagonal or tetragonal crystals. All these materials give complete extinction of light when viewed through crossed polarisers. The refractive indices for LCP and RCP light are equal, and the MCD baseline at zero field is flat. The mounting arrangements within the instrument must be such that the light beam and magnetic field are coaxial, and parallel to the unique axis of the sample crystal (if it has one). The sample must be maintained at a constant temperature, and a zero field baseline should be recorded to ensure that there is no stray birefringence in the optics of the instrument.

The sample thickness and concentration should be controlled to give a reasonable absorbance, a value of 0.86 being optimum from signal to noise considerations [80]. It may be necessary to exceed this value for pure crystals with very intense bands,

or if the ratio ΔOD to absorbance is very small. On the other hand, since ΔOD can be up to twice the normal isotropic absorbance, it may be necessary to work at lower values in order to retain the validity of the formulae relating ellipticity to the Faraday Parameters.

A further requirement for low temperature crystal work is that the material should be magnetically dilute. There are good practical reasons for saying this, aside from the theoretical problems involved. Firstly, magnetic forces in an ordered material can be of such a magnitude as to physically move the sample out of the light beam as the applied field is increased. Secondly, hysteresis effects can be detected in the way that the MCD signal responds to changes in the magnetic field, especially in the region of a spin-flip transition. Thirdly, the presence of domains in the magnetically ordered material can give rise to interference effects, which are apparent as large variable sinusoidal changes in ΔOD when the wavelength is scanned; these mask the expected MCD signal. All these effects have been observed in this laboratory in experiments with pure crystals of $FeCl_2$ and $FeBr_2$, materials which behave in a normal way when doped into the corresponding cadmium halide at low concentration. If it were possible to record an MCD spectrum of such magnetically coupled compounds, then it would be necessary to take into account the internal magnetic field generated at each ion by the aligned spins of neighbouring ions. Such internal fields can be very intense, for example, in MnF_2 the spin-flip field is about 9.3T [81].

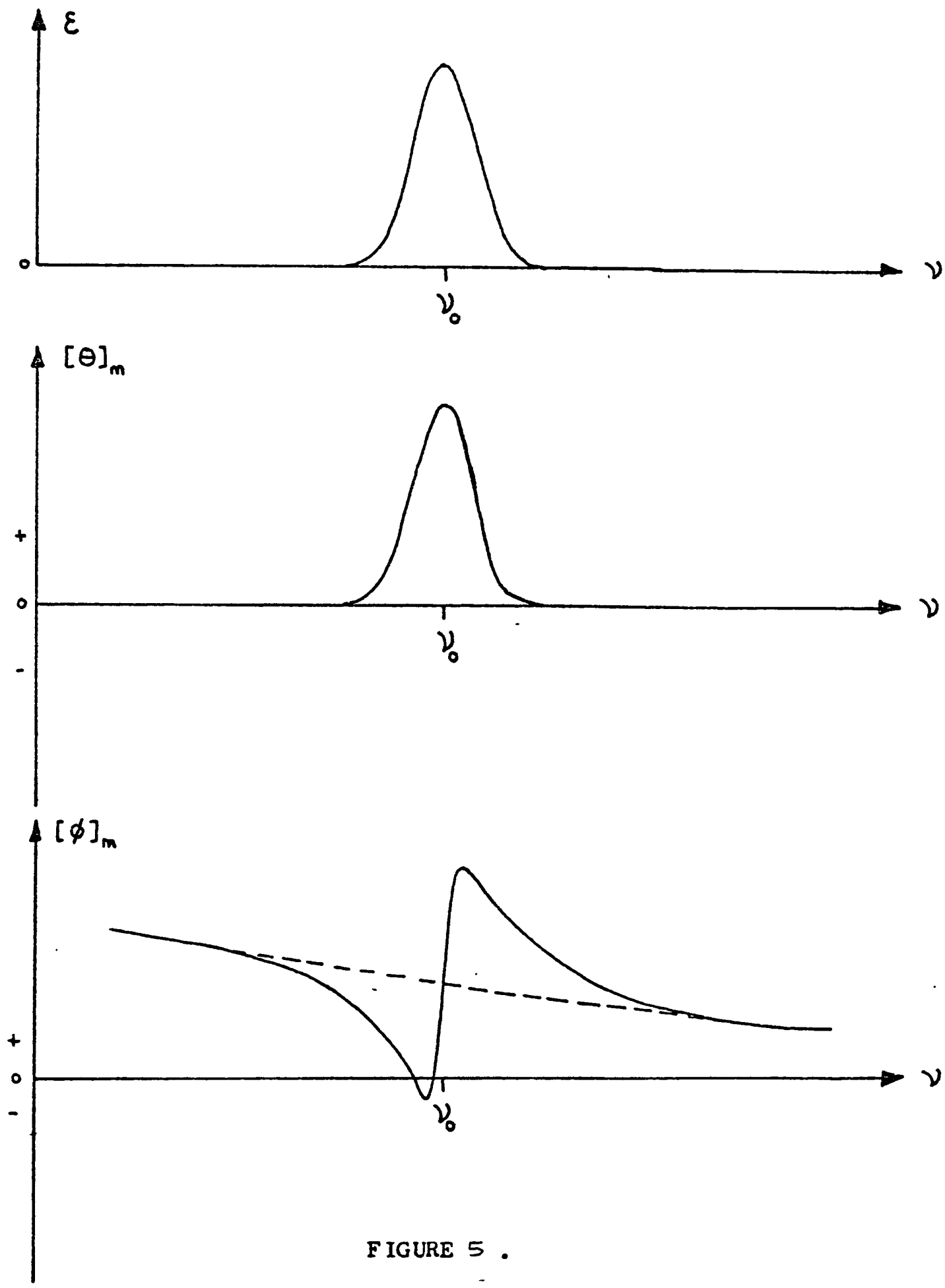

FIGURE 5 .

TYPICAL DISPERSION CURVES FOR (TOP) ABSORPTION , (MIDDLE) CIRCULAR DICHROISM , (BOTTOM) OPTICAL ROTATION .

Note that the ORD curve for the transition extends over a wider frequency range than the absorption or CD , and is superimposed on a sloping background which contains contributions from all the other transitions of the molecule .

C H A P T E R 3

THE OPTICAL TRANSITIONS OF TETRAHEDRAL Mn(II)

3.1 INTRODUCTION

In order for the spin forbidden transitions $^4\Gamma \longleftarrow {}^6A_1$ to gain intensity, the $\Delta S = 0$ selection rule must be partially relaxed. For the tetrahedral ion $MnCl_4^{2\ominus}$, we believe that the mechanism first proposed by Englman [38] is dominant. This involves "intensity borrowing" from the fully allowed charge transfer transition $^6T_2 \longleftarrow {}^6A_1$, and occurs by means of spin orbit mixing of slight $^6T_2$ character into the $^4\Gamma$ wavefunctions. A very similar mechanism of intensity borrowing successfully accounted for the intensities of the spin forbidden bands of Cs_3CoBr_5 crystals [70].

The calculations proceed as follows. The wavefunctions which diagonalise the spin orbit interaction are taken as the basis set. The properties of the charge transfer transition are determined first, then the spin orbit coupling matrix elements between $^6T_2$ and $^4\Gamma$ are calculated by the method of Griffith [82]. It is then possible to predict the intensity ratio MCD: absorption for each spin orbit component of each quartet state, and the results are compared with the experimental results. As the MCD was measured at 4.2 K with an axial field of 4.75T, the Faraday Parameters do not give an accurate description, but the C-terms are calculated to allow comparison with other MCD studies on $MnCl_4^{2\ominus}$ [62, 63]. Instead, we calculate a parameter which describes the MCD arising

as a result of the Zeeman splitting of the ground state of Cs_3MnCl_5 under these specific conditions, ΔD for $^6T_2$ and Δd for quartets. Tetrahedral symmetry is assumed to simplify the calculations, which may be represented schematically as follows:

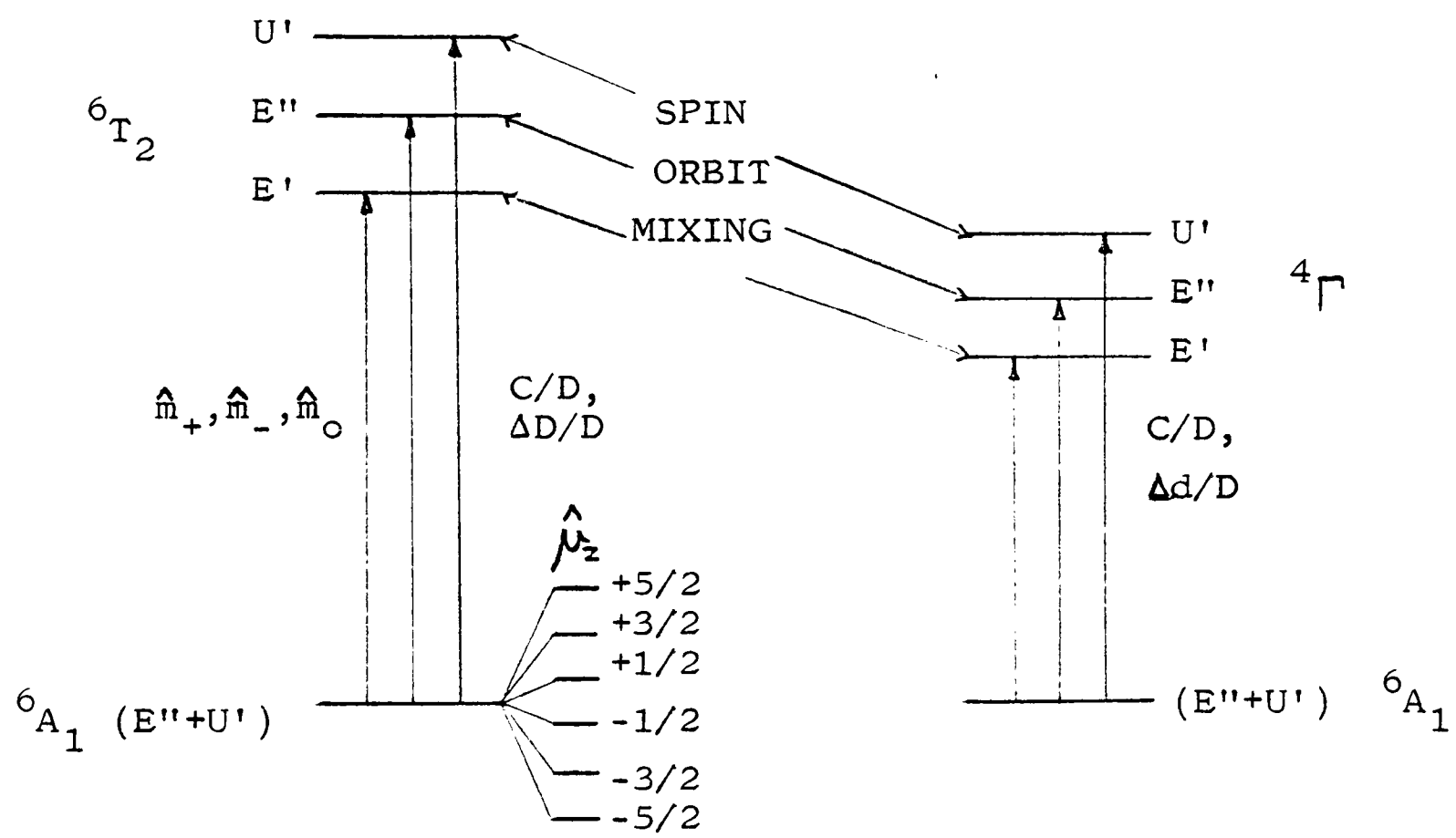

T_d^*

3.2 THE GROUND STATE

For $^6A_1$, L = 0 and S = 5/2, and the spinor wavefunctions are generated from the product: (E'' + U') x A_1 = E'' + U'. These are given in [3], Table A19, and we shall consider the six components to be degenerate (see 1.6). The degeneracy is lifted by a magnetic field; in the case of the MCD and Zeeman experiments on Cs_3MnCl_5 single crystals, the field was parallel to the unique crystal axis, which corresponds to the molecular z-direction. The component energies are given by:

$$E_a = -\langle a|\hat{\mu}_z|a\rangle H_z \qquad \text{EQUATION (3.1)}$$

where $$\hat{\mu}_z = -\beta(\hat{l}_z + 2\hat{s}_z) \qquad \text{EQUATION (3.2)}$$

The factor 2 above will generally be replaced by the Landé g-factor. For Cs_3MnCl_5, we take this to be 2.011 (see 1.6); $^6A_1(S)$ behaves as an almost pure spin-only state. The result is that the energies of the individual Zeeman components are determined by their m_s values:

	Energy E_a	Wavefunction	% Population for 4.2K, 4.75T.
+5/2	$+5g\beta H_z$	$\sqrt{5/6}\|U'\nu\rangle\|a_1\rangle + \sqrt{1/6}\|E'\alpha\rangle\|a_1\rangle$	0.04
+3/2	$+4g\beta H_z$	$\sqrt{1/6}\|U'\kappa\rangle\|a_1\rangle - \sqrt{5/6}\|E''\beta\rangle\|a_1\rangle$	0.17
+1/2	$+3g\beta H_z$	$\|U'\lambda\rangle\|a_1\rangle$	0.80
-1/2	$+2g\beta H_z$	$-\|U'\mu\rangle\|a_1\rangle$	3.69
-3/2	$+g\beta H_z$	$\sqrt{1/6}\|U'\nu\rangle\|a_1\rangle - \sqrt{5/6}\|E''\alpha\rangle\|a_1\rangle$	17.00
-5/2	zero	$\sqrt{5/6}\|U'\kappa\rangle\|a_1\rangle + \sqrt{1/6}\|E''\beta\rangle\|a_1\rangle$	78.30

The population figures are obtained by applying the Boltzmann Law:

$$N_a = N_o\, e^{-E_a/kT} \qquad \text{EQUATION (3.3)}$$

and refer to the MCD experiments. The functional dependence of the Zeeman component populations on the magnetic field is shown in FIGURE 6 for a temperature of 4.2K. At the maximum available field of 4.75T, 99% of the ground state population will lie in the lowest three Zeeman levels, and upward transitions from these levels will be dominant in determining the sign and magnitude of the MCD.

3.3 ALLOWED EXCITED STATES

The electric dipole allowed transitions from $^6A_1$ will be to $^6T_2$ excited states. These cannot arise from any electron rearrangement within the $3d^5$ configuration, but must involve halogen as well as metal orbitals. In the MO diagram, FIGURE 2, the filled halogen pπ-orbitals lie below the partially filled non-bonding 3d-orbitals 2e and $4t_2$. Transfer of an electron from either t_1 or $3t_2$ to either of the 3d-orbitals will produce a $^6T_2$ excited state, the transition being a fully allowed charge transfer transition. As such, it should be very intense, $\varepsilon \simeq 10^4$ as compared with $\sim$0.1 - 1.0 for the $^4\Gamma \leftarrow {}^6A_1$ transitions.

The charge transfer bands of $MnCl_4^{2\ominus}$ are at energies above 45,000 cm^{-1} [72], and will be slightly split by the effects of spin orbit coupling and the tetragonal crystal field component. The ligand field bands lie closer to the ground state, at energies from 18,000 to 38,000 cm^{-1}. Schematically, we may consider the situation to be as follows:

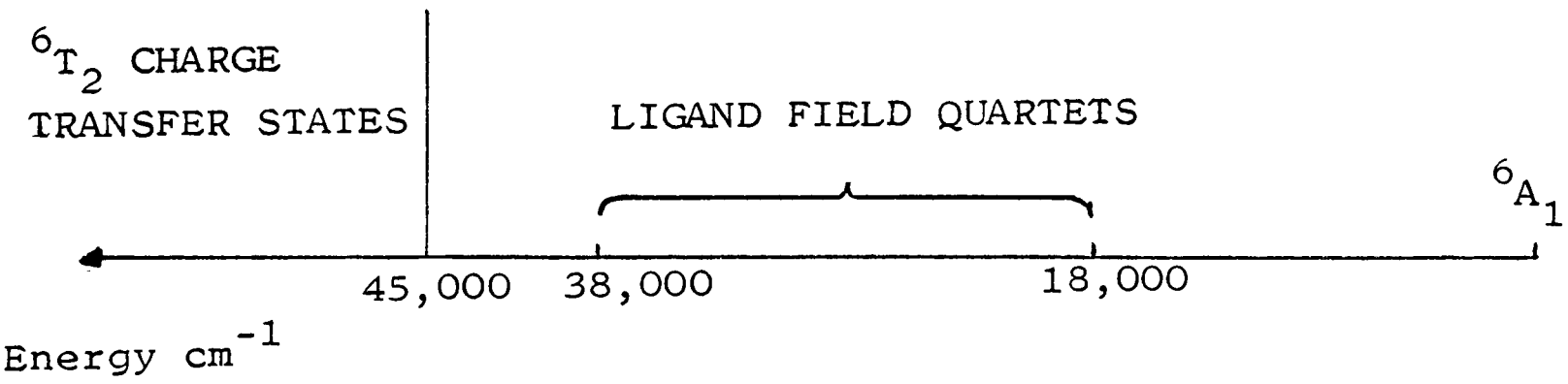

If the splitting of a $^6T_2$ state is small compared with its separation from a quartet state, then the mixing between them can be simply expressed in terms of a single energy separation ΔE. Otherwise, separate values of ΔE will have to be used for each component of $^6T_2$, and the calculations become more complex and less general. Below we will justify the use of the simpler of the two possibilities by showing that the

splitting of the lowest energy $^6T_2$ state is likely to be small.

In the double group T_d^*, the wavefunctions $^6T_2$ arise from the direct product: $(E''+U') \times T_2 = E'_{5/2} + E'_{7/2} + E'' + U'_{3/2} + U'_{5/2} + U'_{7/2}$. These six spin orbit components can be written as sums of products of spin and space parts, with the appropriate coupling coefficients, and are given in TABLE I. The coupling coefficients were originally calculated by Bird [83], while the phases of $E'_{5/2}$ and $U'_{5/2}$ have been corrected following recalculation by Vala, Rivoual, and Badoz [63]. These extent the tabulations given by Griffith [3]. The effect of first order spin orbit coupling is to remove the degeneracy of components with different angular momentum $\underset{\sim}{J}$ as follows [84, 85]:

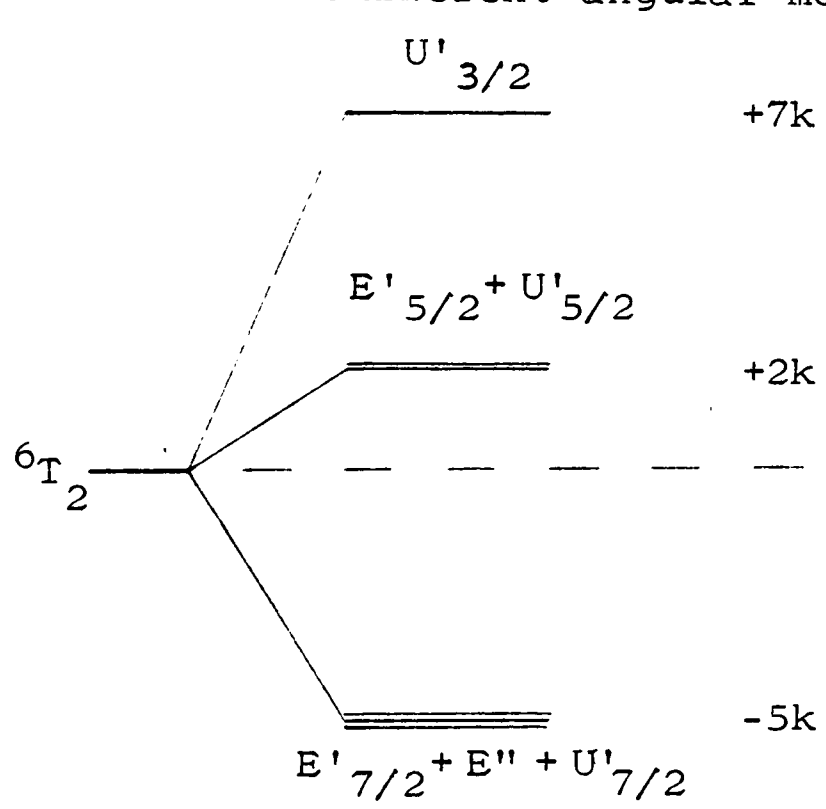

where $k = \frac{1}{6\sqrt{35}} \langle T_2 \| \Sigma su \| T_2 \rangle$

EQUATION (3.4)

The sign and magnitude of k depend on the value of the reduced matrix element of spin orbit coupling. This multi-electron element can be expressed in single-electron terms by the method of Griffith [82], and will depend on the electronic configuration from which $^6T_2$ arises. For the $^6T_2$ state of lowest energy, the electronic configuration is $t_1^5 2e^3 4t_2^3$, and:

$$\langle t_1^5 2e^3 4t_2^3 \| \sum su \| t_1^5 2e^3 4t_2^3 \rangle = \frac{1}{2}\sqrt{\frac{7}{5}} \langle \tfrac{1}{2}t_1 \| \sum su \| \tfrac{1}{2}t_1 \rangle$$

EQUATION (3.5)

so that $$k = \frac{1}{60} \langle \tfrac{1}{2}t_1 \| \sum su \| \tfrac{1}{2}t_1 \rangle$$ EQUATION (3.6)

Only the halogen t_1-orbitals appear in EQUATION (3.6), and for the tetrahedral ion $MnCl_4^{2\Theta}$ the molecular orbital coefficients are known [84, 85], so that k can be calculated explicitly:

$$k = -\frac{1}{40} \zeta_{Cl_{p\pi}}$$ EQUATION (3.7)

Taking the chlorine $p\pi$ spin orbit coupling constant to be 600 cm^{-1}, the total spread of the spin orbit components of this $^6T_2$ state will be about 180 cm^{-1}. This is small compared with its separation from the quartet states.

In addition to first order spin orbit coupling, the $^6T_2$ state will be perturbed by the presence of the tetragonal component of the crystal field, causing further splitting. It is beyond the scope of this work to calculate the resultant energy level diagram for $^6T_2$, and therefore we shall continue with the assumption that the overall splitting is small. Any breakdown of this will only be important for the quartets closest to $^6T_2$, that is, for $^4A_2$, $^4T_1$, and $^4T_2$ from ^4F. In any case, the error will be minimised by considering the MCD:absorption intensity ratio.

3.4 THE $^6T_2 \leftarrow {}^6A_1$ TRANSITION PARAMETERS

Measurements on $MnCl_4^{2\Theta}$ in solution [62] show that the dominant contribution to the MCD comes from C-terms, i.e. from the Zeeman splitting of the ground state. In order to account for the high field (4.75T) and low temperature (4.2K) conditions

under which the MCD of Cs_3MnCl_5 was recorded, we calculate the LCP and RCP intensities arising from each Zeeman component of $^6A_1$, and weight them with the appropriate population factor. This gives us a parameter ΔD analogous to C but taking into account the effect of saturation - see 2.6. For absorption, only the conventional dipole strength D is required.

The transitions all occur by the electric dipole mechanism, and are induced by the electric dipole operator $\hat{\underset{\sim}{m}}$. Circular polarisation depends on the use of the raising and lowering operators $\hat{m}_+$ and $\hat{m}_-$, which can be written in the form given by Griffith [3], Table A16:

$\hat{m}_+ = \frac{-i}{\sqrt{2}} (\hat{m}_x + i\,\hat{m}_y)$, transforming as T_2+1 in cubic symmetry

$\hat{m}_o = i\,\hat{m}_z$, transforming as T_2O

$\hat{m}_- = \frac{+i}{\sqrt{2}} (\hat{m}_x - i\,\hat{m}_y)$, transforming as T_2-1 EQUATION (3.8)

Using these definitions and the relevant formulae for C and D, we have:

$$C = \frac{3}{d_a} \sum_{j \leftarrow a} \langle a|\hat{\mu}_z|a\rangle \, \mathcal{I}m \left\{ \langle a|\hat{m}_x|j\rangle \langle j|m_y|a\rangle \right\} \qquad \text{EQUATION (2.23)}$$

$$= \frac{3}{2d_a} \sum_{j \leftarrow a} \langle a|\hat{\mu}_z|a\rangle \left\{ |\langle j|\hat{m}_-|a\rangle|^2 - |\langle j|\hat{m}_+|a\rangle|^2 \right\} \qquad \text{EQUATION (3.9).}$$

(Note that positive C corresponds to negative MCD.)

$$D = \frac{1}{d_a} \sum_{j \leftarrow a} |\langle a|\hat{\underset{\sim}{m}}|j\rangle|^2 \qquad \text{EQUATION (2.27)}$$

$$= \frac{3}{d_a} \sum_{j \leftarrow a} |\langle j|\hat{m}_i|a\rangle|^2 \qquad \text{EQUATION (3.10)}$$

Also we define:

$$\Delta D = \sum_{j \leftarrow a} \frac{N_a}{N} \left\{ |\langle j|\hat{m}_+|a\rangle|^2 - |\langle j|\hat{m}_-|a\rangle|^2 \right\} \quad \text{EQUATION (3.11)}$$

(Note that positive ΔD corresponds to positive MCD.)

The summations will be over the six Zeeman components of $^6A_1$, $d_a = 6$, and a single spin orbit component of $^6T_2$.

Evaluation of the matrix elements of $\hat{\underset{\sim}{m}}$ between $^6T_2$ and $^6A_1$ is straightforward using the spinor wavefunctions. Operator $\hat{\underset{\sim}{m}}$ only acts on the orbital part of the wavefunction, so $\langle j|\hat{m}|a\rangle$ will be zero unless the spin functions are the same. The only non-zero orbital integrals are:

$$\langle T_2{+1}|\hat{m}_+|A_1\rangle, \quad \langle T_2 0|\hat{m}_o|A_1\rangle, \quad \text{and} \quad \langle T_2{-1}|\hat{m}_-|A_1\rangle \ .$$

The results are shown in TABLE II, in which only the three lowest Zeeman components of $^6A_1$ appear. The pattern of entries is such that for $+m_s$ and $\hat{m}_+$ there is an identical entry for $-m_s$ and $\hat{m}_-$, and vice versa. Also, these three components contain 99% of the population under the conditions for which ΔD is calculated. When all the levels are equally populated, at "infinite temperature" or zero field, both C and ΔD disappear. It is interesting to note that the components of $^6T_2$ with equal J also have equal values of C/D:

J = 3/2	$U'_{3/2}$	C/D = $\frac{-7}{2}\beta$	Spin orbit energy +7k
J = 5/2	$E'_{5/2}$, $U'_{5/2}$	C/D = $-\beta$	+2k
J = 7/2	$E'_{7/2}$, E", $U'_{7/2}$	C/D = $\frac{+5}{2}\beta$	-5k

These results complete the first stage of the calculation of quartet intensities.

$S = 5/2$		$m_s = +5/2$			$m_s = +3/2$			$m_s = +1/2$			$m_s = -1/2$			$m_s = -3/2$			$m_s = -5/2$		
	T_2	+1	0	−1	+1	0	−1	+1	0	−1	+1	0	−1	+1	0	−1	+1	0	−1
$E'_{5/2}$	α		$\sqrt{\frac{5}{42}}$		$-\sqrt{\frac{1}{21}}$								$-\sqrt{\frac{8}{21}}$		$\sqrt{\frac{3}{14}}$		$\sqrt{\frac{5}{21}}$		
	β			$-\sqrt{\frac{5}{21}}$		$-\sqrt{\frac{3}{14}}$		$\sqrt{\frac{8}{21}}$								$\sqrt{\frac{1}{21}}$		$-\sqrt{\frac{5}{42}}$	
$E'_{7/2}$	α		$\sqrt{\frac{3}{14}}$		$\sqrt{\frac{15}{28}}$								$-\sqrt{\frac{5}{42}}$		$-\sqrt{\frac{5}{42}}$		$-\sqrt{\frac{1}{84}}$		
	β			$\sqrt{\frac{1}{84}}$		$\sqrt{\frac{5}{42}}$		$\sqrt{\frac{5}{42}}$								$-\sqrt{\frac{15}{28}}$		$-\sqrt{\frac{3}{14}}$	
E''	α						$\sqrt{\frac{1}{12}}$		$\sqrt{\frac{1}{3}}$		$\sqrt{\frac{1}{6}}$								$\sqrt{\frac{5}{12}}$
	β	$-\sqrt{\frac{5}{12}}$								$-\sqrt{\frac{1}{6}}$		$-\sqrt{\frac{1}{3}}$		$-\sqrt{\frac{1}{12}}$					
$U'_{3/2}$	κ									$-\sqrt{\frac{1}{5}}$		$\sqrt{\frac{2}{5}}$		$-\sqrt{\frac{2}{5}}$					
	λ												$\sqrt{\frac{1}{15}}$		$-\sqrt{\frac{4}{15}}$		$\sqrt{\frac{2}{3}}$		
	μ			$\sqrt{\frac{2}{3}}$		$-\sqrt{\frac{4}{15}}$		$\sqrt{\frac{1}{15}}$											
	ν						$-\sqrt{\frac{2}{5}}$		$\sqrt{\frac{2}{5}}$		$-\sqrt{\frac{1}{5}}$								
$U'_{5/2}$	κ									$\sqrt{\frac{18}{35}}$		$-\sqrt{\frac{1}{35}}$		$-\sqrt{\frac{16}{35}}$					
	λ		$\sqrt{\frac{25}{42}}$		$-\sqrt{\frac{5}{21}}$								$\sqrt{\frac{8}{105}}$		$-\sqrt{\frac{3}{70}}$		$-\sqrt{\frac{1}{21}}$		
	μ			$-\sqrt{\frac{1}{21}}$		$-\sqrt{\frac{3}{70}}$		$\sqrt{\frac{8}{105}}$								$-\sqrt{\frac{5}{21}}$		$\sqrt{\frac{25}{42}}$	
	ν						$-\sqrt{\frac{16}{35}}$		$-\sqrt{\frac{1}{35}}$		$\sqrt{\frac{18}{35}}$								
$U'_{7/2}$	κ	$-\sqrt{\frac{7}{12}}$								$\sqrt{\frac{5}{42}}$		$\sqrt{\frac{5}{21}}$		$\sqrt{\frac{5}{84}}$					
	λ		$\sqrt{\frac{1}{14}}$		$\sqrt{\frac{5}{28}}$								$\sqrt{\frac{5}{14}}$		$\sqrt{\frac{5}{14}}$		$\sqrt{\frac{1}{28}}$		
	μ			$\sqrt{\frac{1}{28}}$		$\sqrt{\frac{5}{14}}$		$\sqrt{\frac{5}{14}}$								$\sqrt{\frac{5}{28}}$		$\sqrt{\frac{1}{14}}$	
	ν						$\sqrt{\frac{5}{84}}$		$\sqrt{\frac{5}{21}}$		$\sqrt{\frac{5}{42}}$								$-\sqrt{\frac{7}{12}}$

TABLE I.

COUPLING COEFFICIENTS FOR $^6T_2$ CUBIC SPINOR FUNCTIONS.

These were originally calculated by Bird [83], and the phases are as corrected by Vala et. al. [63].

j a $({}^6T_2\, t)({}^6A_1, m_s)$	$\lvert\langle j\rvert\hat{m}_-\rvert a\rangle\rvert^2$	$\lvert\langle j\rvert\hat{m}_+\rvert a\rangle\rvert^2$	$\lvert\langle j\rvert\hat{m}_0\rvert a\rangle\rvert^2$	$\langle - \rangle^2 - \langle + \rangle^2$	C	D	C/D	ΔD
$E'_{5/2}$ $-1/2$	$8/21$	0	0	$+8/21$	$-\frac{1}{3}\beta$	$\frac{1}{3}$	$-\beta$	$+0.164$
$-3/2$	$1/21$	0	$3/14$	$+1/21$				
$-5/2$	0	$5/21$	$5/42$	$-5/21$				
$E'_{7/2}$ $-1/2$	$5/42$	0	0	$+5/42$	$+\frac{5}{6}\beta$	$\frac{1}{3}$	$+\frac{5}{2}\beta$	-0.091
$-3/2$	$15/28$	0	$5/42$	$+15/28$				
$-5/2$	0	$1/84$	$3/14$	$-1/84$				
E'' $-1/2$	0	$1/6$	$1/3$	$-1/6$	$+\frac{5}{6}\beta$	$\frac{1}{3}$	$+\frac{5}{2}\beta$	-0.306
$-3/2$	0	$1/12$	0	$-1/12$				
$-5/2$	$5/12$	0	0	$+5/12$				
$U'_{3/2}$ $-1/2$	$1/15$	$1/5$	$2/5$	$-2/15$	$-\frac{7}{3}\beta$	$\frac{2}{3}$	$-\frac{7\beta}{2}$	$+0.595$
$-3/2$	0	$2/5$	$4/15$	$-2/5$				
$-5/2$	0	$2/3$	0	$-2/3$				
$U'_{5/2}$ $-1/2$	$8/105$	$18/35$	$1/35$	$-40/105$	$-\frac{2}{3}\beta$	$\frac{2}{3}$	$-\beta$	$+0.091$
$-3/2$	$5/21$	$16/35$	$3/70$	$-23/105$				
$-5/2$	0	$1/21$	$25/42$	$-1/21$				
$U'_{7/2}$ $-1/2$	$6/14$	$5/42$	$5/21$	$+5/21$	$+\frac{5}{3}\beta$	$\frac{2}{3}$	$+\frac{5}{2}\beta$	-0.458
$-3/2$	$5/28$	$5/84$	$5/14$	$+5/42$				
$-5/2$	$7/12$	$1/28$	$1/14$	$+23/42$				

TABLE II .

ABSORPTION AND MCD PARAMETERS FOR THE ELECTRIC DIPOLE ALLOWED TRANSITION ${}^6T_2 \leftarrow {}^6A_1$ FOR Mn (II) IN TETRAHEDRAL SYMMETRY . ALL ENTRIES EXCEPT C/D ARE IN UNITS OF $\frac{I}{3}\langle T_2 \| \underset{\sim}{\hat{m}} \| A_1 \rangle^2$.

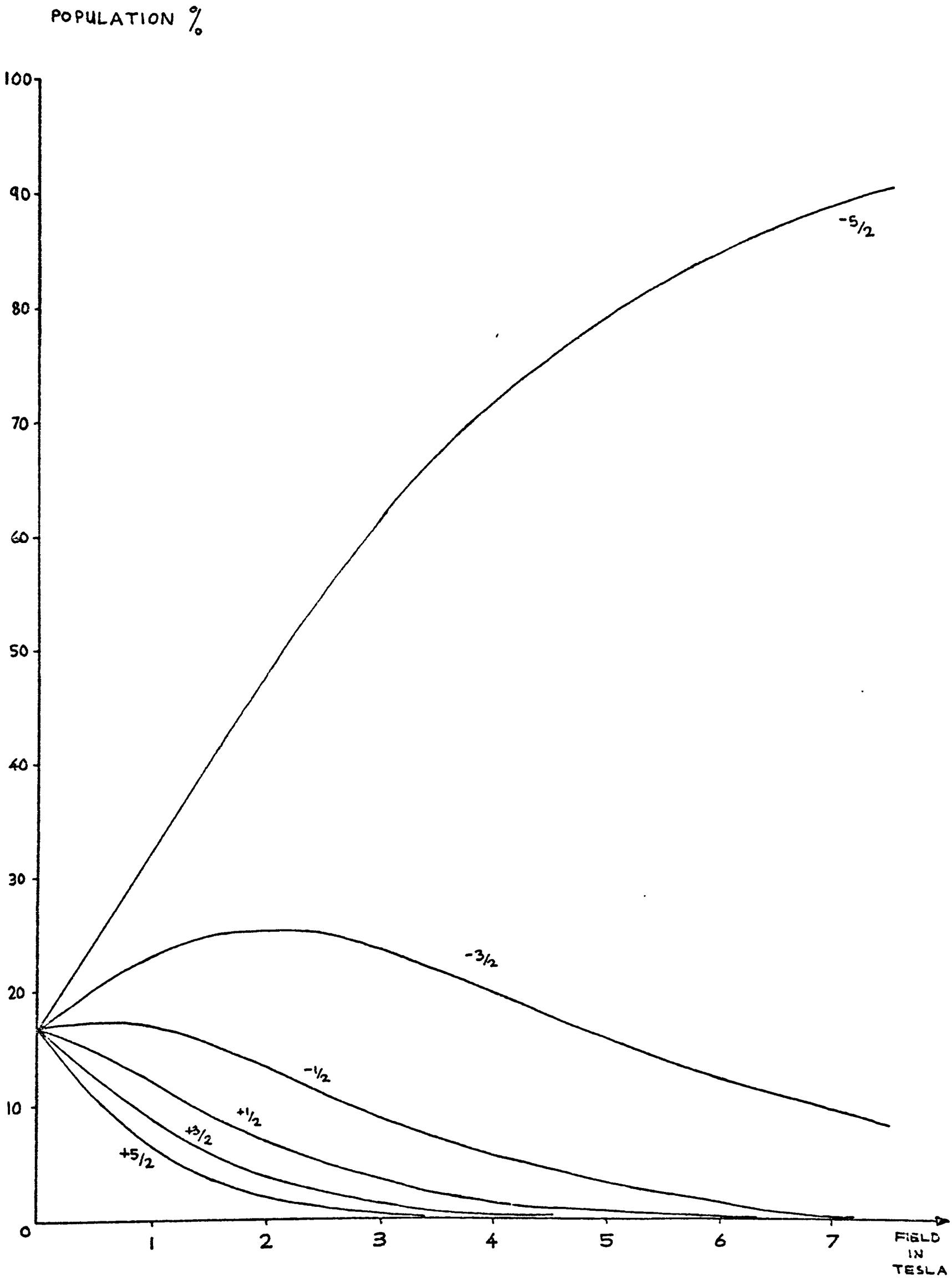

FIGURE 6 .

POPULATIONS OF ZEEMAN COMPONENTS OF $^6A_1$ IN AN AXIAL MAGNETIC FIELD AT 4.2K.

3.5 SPIN ORBIT MIXING OF STATES

Because the spin orbit interaction couples together spin and orbital angular momenta, it allows states of different spin multiplicity to interact with one another, subject to certain restrictions. The operator $\hat{\mathcal{H}}_{soc}$ is a part of the total Hamiltonian for the system, and the integrals $\langle \psi_1 | \hat{\mathcal{H}} | \psi_2 \rangle$ must transform with A_1 symmetry. Also, $\Delta S = 0, \pm 1$. Using spinor functions in the double group T_d^*, the spin orbit coupling matrix elements can be expressed as products of spin and orbital parts:

$$\langle \text{spin (1)} | \hat{\underset{\sim}{S}} | \text{spin (2)} \rangle \cdot \langle \Gamma_{(1)} | \hat{\underset{\sim}{L}} | \Gamma_{(2)} \rangle \quad ; \quad \Gamma_{\underset{\sim}{L}} = T_1 .$$

If the matrix element $\langle \psi_1 | \hat{\mathcal{H}}_{soc} | \psi_2 \rangle$ is not to vanish, both of these parts must be non-zero simultaneously. The correct expansion of the dot product is:

$$\hat{\underset{\sim}{S}} . \hat{\underset{\sim}{L}} = \hat{L}_o \hat{S}_o + \tfrac{1}{2}(\hat{L}_+ \hat{S}_- + \hat{L}_- \hat{S}_+) \qquad \text{EQUATION (3.12)}$$

When the above criteria are satisfied and spin orbit mixing does occur between ψ_1 and ψ_2, the zero order wavefunctions will be perturbed,

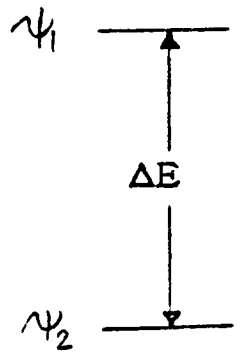

$$|\psi_2\rangle' = |\psi_2\rangle + \lambda |\psi_1\rangle \quad \text{where} \quad \lambda = \frac{\langle \psi_1 | \hat{\mathcal{H}}_{soc} | \psi_2 \rangle}{\Delta E}$$

EQUATION (3.13).

λ is the first order mixing coefficient. When first order spin orbit coupling is the mechanism by which ψ_2 borrows intensity from an optical transition involving ψ_1, the borrowed intensity is proportional to λ^2.

For cubic Mn(II) complexes, there are two possibilities to be considered whereby spin orbit coupling can partially relieve the restrictions forbidding the $^4\Gamma \longleftarrow {}^6A_1$ transitions:

(i) Mixing of $^4T_1$ character into the $^6A_1$ ground state wavefunction.

(ii) Mixing of $^6T_2$ character into the $^4\Gamma$ wavefunctions.

In the firxt case, proposed by Koide and Pryce [37] as the source of intensity, the $^6A_1$ wavefunctions is modified and acquires partial $^4T_1$ character λ_1. Then the spin forbidden $^4\Gamma \longleftarrow {}^6A_1$ transition will become a spin allowed quartet-quartet transition with intensity proportional to λ_1^2. The transition does, however, remain Laporte forbidden. There are three $^4T_1$ states available to mix into $^6A_1$, but according to Low and Rosengarten [86] only the lower energy pair contribute significantly, giving the ground state 0.09% $^4T_1$ character. This mechanism will give intensity to transitions to $^4A_2$, ^4E, $^4T_1$, and $^4T_2$.

In the second case, proposed by Englman [38] as the source of intensity, the $^4\Gamma$ wavefunctions are modified and each acquires partial $^6T_2$ character λ_2. Then the spin forbidden $^4\Gamma \longleftarrow {}^6A_1$ transition will become a spin allowed sextet-sextet transition with intensity proportional to λ_2^2. In addition, since $^6T_2$ is a charge transfer state lying outside the $3d^5$ configuration, the Laporte forbidden nature of the transition is removed. It is this factor which we believe will make this second mechanism dominant, together with the presence of several $^6T_2$ states. Again, transitions to $^4A_2$, ^4E, $^4T_1$, and

$^4T_2$ can gain intensity by this mechanism.

There is experimental evidence in support of this conclusion, Lohr and McClure [67], in their survey of the intensities of $^4\Gamma \longleftarrow {}^6A_1$ transitions of Mn(II) complexes, found a correlation between the intensity of the AE band and the inverse square of its separation from the charge transfer edge. The case (ii) mechanism would predict approximately this behaviour:

$$\text{Intensity of AE} \propto \lambda_2{}^2 = \frac{\langle {}^6T_2 | \hat{\mathcal{H}}_{soc} | {}^4AE \rangle^2}{\Delta E^2} \quad \text{from EQUATION (3.13)}$$

3.6 MATRIX ELEMENTS OF $\hat{\mathcal{H}}_{soc}$

The spin orbit coupling matrix elements required for the calculation of quartet intensities by the mechanism (ii) above are $\langle {}^6T_2 | \hat{\mathcal{H}}_{soc} | {}^4\Gamma \rangle$. These are numerically the same as $\langle {}^4\Gamma | \hat{\mathcal{H}}_{soc} | {}^6T_2 \rangle$ except for a phase factor of ± 1, and this will disappear when the elements are squared to calculate the intensities. The method of calculation and notation are those of Griffith [82]. The $^6T_2$ wavefunctions are taken from TABLE I, and the $^4\Gamma$ wavefunctions [3] are given in TABLE III. Written this way, they are the functions which form the bases for irreducible representations of the double group $T_d{}^*$, and the matrix of $\hat{\mathcal{H}}_{soc}$ is diagonal, e.g. an $|E'\alpha'\rangle$ function has non-zero matrix elements only with other $|E'\alpha'\rangle$ functions. In generalised form, the wavefunctions are $|S\ h\ t_J\ \tau\rangle$, where:

S = spin; 5/2 for sextets, 3/2 for quartets.

h = orbital symmetry label; T_2 or Γ .

t_J = spinor basis function with angular momentum J; this will

be E', E", or U'.

τ = component of t_J; α or β for E'and E"; κ, λ, μ, or ν for U'.

Each function $|S\ h\ t_J\ \tau\rangle$ can be expanded as sums of coupling coefficients $\langle S\ h\ t_J\ \tau | S\ h\ M\ \Theta\rangle$ times uncoupled functions $|S\ h\ M\ \Theta\rangle$ [3], where S and h are as given above, and:

M = orbital component of h: a_1 for A_1; a_2 for A_2; Θ or ϵ for E; 0, +1, or -1 for T_1 and T_2.

Θ = spin component m_s: ±1/2, ±3/2, ±5/2 for S = 5/2; ±1/2, ±3/2 for S = 3/2.

Each diagonal element $\langle S\ h\ t_J\ \tau | \hat{\mathcal{H}}_{soc} | S'\ h'\ t_{J'}\ \tau\rangle$ in the spin orbit coupling matrix is then expanded as a sum [82, page 82] involving products of coupling coefficients and matrix elements $\langle S\ h\ M\ \Theta | \hat{\mathcal{H}}_{soc} | S'\ h'\ M'\ \Theta'\rangle$ which can be evaluated as follows:

$$\langle S\ h\ t_J\tau|\hat{\mathcal{H}}_{soc}|S'\ h'\ t_{J'},\tau\rangle = \sum_{MM'\Theta\Theta'}\langle S\ h\ t_J\tau|S\ h\ M\ \Theta\rangle\langle S\ h\ M\Theta|\hat{\mathcal{H}}_{soc}|S'\ h'\ M'\ \Theta'\rangle\langle S'\ h'\ M'\Theta'|S'\ h'\ t_{J'},\tau\rangle$$

EQUATION (3.14)

where: $\langle S\ h\ M\Theta|\hat{\mathcal{H}}_{soc}|S'\ h'\ M'\ \Theta'\rangle =$

$$\langle Sh\ \|\sum su\|S'\ h'\rangle \sum_i (-1)^{1+i+S-M'}[-1]^{h+\Theta}\bar{V}\begin{pmatrix} S & S' & 1\\ -M & M' & i\end{pmatrix}V\begin{pmatrix} h & h' & T_1\\ -\Theta & \Theta' & -i\end{pmatrix}$$

EQUATION (3.15)

The $\bar{V}$ coefficient is a 6-j symbol, taken from the tables of Rotenberg et al [87]. It is zero unless i-M+M' = 0, and this property "selects" the part of the operator $\hat{\underset{\sim}{S}}.\hat{\underset{\sim}{L}}$ which connects $|S\ h\ M\ \Theta\rangle$ with $|S'\ h'\ M'\ \Theta'\rangle$. The V coefficients are listed by Griffith [82, page 111]. In EQUATION (3.15), h = T_2, and the factor:

$$[-1]^{h+\Theta} = -1 \quad \text{for } \Theta = \pm 1$$
$$= +1 \quad \text{for } \Theta = 0.$$

EQUATION (3.16)

The above formulae are derived from the application of the Wigner-Eckhart theorem to the coupling of angular momenta. A simple explanation of this is given by Atkins [76], while rigorous proof is given by Griffith[3].

The complete set of results for $\langle {}^6T_2 | \hat{\mathcal{H}}_{soc} | {}^4\Gamma \rangle$ is given in TABLE IV. These are in terms of the appropriate reduced matrix elements $\langle T_2 \| \sum su \| \Gamma \rangle$. Vala et al [63] have independently calculated $\langle {}^4\Gamma | \hat{\mathcal{H}}_{soc} | {}^6T_2 \rangle$, and their results agree exactly with the present work if the following phase factors are assumed:

$$\langle T_2 \| \textstyle\sum su \| A_2 \rangle = +\langle A_2 \| \sum su \| T_2 \rangle$$

$$\langle T_2 \| \textstyle\sum su \| E \rangle = -\langle E \| \sum su \| T_2 \rangle$$

$$\langle T_2 \| \textstyle\sum su \| T_1 \rangle = -\langle T_1 \| \sum su \| T_2 \rangle$$

$$\langle T_2 \| \textstyle\sum su \| T_2 \rangle = +\langle T_2 \| \sum su \| T_2 \rangle .$$

This completes the second stage of the calculation of quartet intensities.

$A_1 \times U' = U'$

$A_2 \times U'$		U'			
		κ	λ	μ	ν
a_2	κ	.	.	1	.
a_2	λ	.	.	.	-1
a_2	μ	-1	.	.	.
a_2	ν	.	1	.	.

$E \times U'$		E'		E''		U'			
		α'	β'	α''	β''	κ	λ	μ	ν
θ	κ	.	.	.	$\frac{1}{\sqrt{2}}$	$\frac{1}{\sqrt{2}}$	.	.	.
θ	λ	$\frac{1}{\sqrt{2}}$	.	.	.	.	$-\frac{1}{\sqrt{2}}$	.	.
θ	μ	.	$-\frac{1}{\sqrt{2}}$	.	.	.	.	$-\frac{1}{\sqrt{2}}$	.
θ	ν	.	.	$-\frac{1}{\sqrt{2}}$	.	.	.	.	$\frac{1}{\sqrt{2}}$
ϵ	κ	.	$-\frac{1}{\sqrt{2}}$	.	.	.	.	$\frac{1}{\sqrt{2}}$	.
ϵ	λ	.	.	$\frac{1}{\sqrt{2}}$	.	.	.	.	$\frac{1}{\sqrt{2}}$
ϵ	μ	.	.	.	$-\frac{1}{\sqrt{2}}$	$\frac{1}{\sqrt{2}}$	.	.	.
ϵ	ν	$\frac{1}{\sqrt{2}}$	.	.	.	.	$\frac{1}{\sqrt{2}}$	.	.

TABLE III.

Coupling coefficients for Quartet wavefunctions.

$S = 3/2$ transforms as U' with components κ, λ, μ, and ν. Each component has a different M_S value:

$$|U'\kappa\rangle = |^{3/2}\ ^{+3/2}\rangle$$

$$|U'\lambda\rangle = |^{3/2}\ ^{+1/2}\rangle$$

$$|U'\mu\rangle = |^{3/2}\ ^{-1/2}\rangle$$

$$|U'\nu\rangle = |^{3/2}\ ^{-3/2}\rangle$$

$T_1 \times U'$	E'		E''		$\frac{3}{2}U'$				$\frac{5}{2}U'$			
	α'	β'	α''	β''	κ	λ	μ	ν	κ	λ	μ	ν
1 κ	.	.	$\frac{1}{\sqrt{6}}$	.	.	.	.	.	.	.	.	$\frac{\sqrt{5}}{\sqrt{6}}$
0 κ	.	.	. .	$-\frac{1}{\sqrt{3}}$	$\frac{\sqrt{3}}{\sqrt{5}}$	.	.	.	$-\frac{1}{\sqrt{15}}$	.	.	.
−1 κ	$\frac{1}{\sqrt{2}}$	.	.	.	.	$\frac{\sqrt{2}}{\sqrt{5}}$	.	.	.	$\frac{1}{\sqrt{10}}$	.	.
1 λ	.	.	.	$-\frac{1}{\sqrt{2}}$	$-\frac{\sqrt{2}}{\sqrt{5}}$	.	.	.	$-\frac{1}{\sqrt{10}}$	.	.	.
0 λ	$-\frac{1}{\sqrt{3}}$	.	.	.	.	$\frac{1}{\sqrt{15}}$	.	.	.	$\frac{\sqrt{3}}{\sqrt{5}}$	.	.
−1 λ	.	$\frac{1}{\sqrt{6}}$	.	.	.	.	$\frac{2\sqrt{2}}{\sqrt{15}}$	.	.	.	$-\frac{\sqrt{3}}{\sqrt{10}}$	.
1 μ	$\frac{1}{\sqrt{6}}$	.	.	.	.	$-\frac{2\sqrt{2}}{\sqrt{15}}$	.	.	.	$\frac{\sqrt{3}}{\sqrt{10}}$	.	.
0 μ	.	$-\frac{1}{\sqrt{3}}$	.	.	.	.	$-\frac{1}{\sqrt{15}}$	.	.	.	$-\frac{\sqrt{3}}{\sqrt{5}}$	.
−1 μ	.	.	$-\frac{1}{\sqrt{2}}$	.	.	.	.	$\frac{\sqrt{2}}{\sqrt{5}}$	.	.	.	$\frac{1}{\sqrt{10}}$
1 ν	.	$\frac{1}{\sqrt{2}}$	.	.	.	.	$-\frac{\sqrt{2}}{\sqrt{5}}$	.	.	.	$-\frac{1}{\sqrt{10}}$	.
0 ν	.	.	$-\frac{1}{\sqrt{3}}$	.	.	.	.	$-\frac{\sqrt{3}}{\sqrt{5}}$	.	.	.	$\frac{1}{\sqrt{15}}$
−1 ν	.	.	.	$\frac{1}{\sqrt{6}}$	.	.	.	.	$-\frac{\sqrt{5}}{\sqrt{6}}$	.	.	.

$T_2 \times U'$	E'		E''		$\frac{3}{2}U'$				$\frac{5}{2}U'$			
	α'	β'	α''	β''	κ	λ	μ	ν	κ	λ	μ	ν
1 κ	$\frac{1}{\sqrt{6}}$	.	.	.	.	.	.	.	.	$\frac{\sqrt{5}}{\sqrt{6}}$	.	.
0 κ	.	$-\frac{1}{\sqrt{3}}$	.	.	.	.	$\frac{\sqrt{3}}{\sqrt{5}}$	.	.	.	$-\frac{1}{\sqrt{15}}$	.
−1 κ	.	.	$\frac{1}{\sqrt{2}}$	.	.	.	.	$-\frac{\sqrt{2}}{\sqrt{5}}$	.	.	.	$-\frac{1}{\sqrt{10}}$
1 λ	.	$-\frac{1}{\sqrt{2}}$	.	.	.	.	$-\frac{\sqrt{2}}{\sqrt{5}}$	.	.	.	$-\frac{1}{\sqrt{10}}$	.
0 λ	.	.	$-\frac{1}{\sqrt{3}}$	.	.	.	.	$-\frac{1}{\sqrt{15}}$	.	.	.	$-\frac{\sqrt{3}}{\sqrt{5}}$
−1 λ	.	.	.	$\frac{1}{\sqrt{6}}$	$-\frac{2\sqrt{2}}{\sqrt{15}}$	.	.	.	$\frac{\sqrt{3}}{\sqrt{10}}$	.	.	.
1 μ	.	.	$\frac{1}{\sqrt{6}}$	.	.	.	.	$\frac{2\sqrt{2}}{\sqrt{15}}$	.	.	.	$-\frac{\sqrt{3}}{\sqrt{10}}$
0 μ	.	.	.	$-\frac{1}{\sqrt{3}}$	$\frac{1}{\sqrt{15}}$	.	.	.	$\frac{\sqrt{3}}{\sqrt{5}}$	.	.	.
−1 μ	$-\frac{1}{\sqrt{2}}$	.	.	.	.	$\frac{\sqrt{2}}{\sqrt{5}}$	.	.	.	$\frac{1}{\sqrt{10}}$	.	.
1 ν	.	.	.	$\frac{1}{\sqrt{2}}$	$\frac{\sqrt{2}}{\sqrt{5}}$	.	.	.	$\frac{1}{\sqrt{10}}$	.	.	.
0 ν	$-\frac{1}{\sqrt{3}}$	.	.	.	.	$-\frac{\sqrt{3}}{\sqrt{5}}$	.	.	.	$\frac{1}{\sqrt{15}}$	.	.
−1 ν	.	$\frac{1}{\sqrt{6}}$	.	.	.	.	.	.	.	.	$-\frac{\sqrt{5}}{\sqrt{6}}$	.

Coupling coefficients for Quartet wavefunctions (continued).

$^4A_2$

t \ t′	U′
$U'_{3/2}$	$\frac{+1}{2\sqrt{3}}$

^4E

t \ t′	E′	E″	U′
$E'_{5/2}$	$\frac{-3}{2\sqrt{105}}$		
$E'_{7/2}$	$\frac{+1}{2\sqrt{21}}$		
E''		$\frac{-1}{2\sqrt{5}}$	
$U'_{3/2}$			$\frac{-1}{10\sqrt{6}}$
$U'_{5/2}$			$\frac{+3}{10\sqrt{21}}$
$U'_{7/2}$			$\frac{-1}{2\sqrt{7}}$

$^4T_1$

t \ t′	E′	E″	$U'_{3/2}$	$U'_{5/2}$
$E'_{5/2}$	$\frac{-1}{2\sqrt{105}}$			
$E'_{7/2}$	$\frac{-1}{\sqrt{21}}$			
E''		$\frac{+1}{3\sqrt{5}}$		
$U'_{3/2}$			$\frac{+1}{10\sqrt{30}}$	$\frac{-1}{5\sqrt{30}}$
$U'_{5/2}$			$\frac{-4}{5\sqrt{105}}$	$\frac{-9}{10\sqrt{105}}$
$U'_{7/2}$			$\frac{-1}{\sqrt{35}}$	$\frac{+1}{3\sqrt{35}}$

$^4T_2$

t \ t′	E′	$U'_{3/2}$	$U'_{5/2}$
$E'_{5/2}$	$\frac{+7}{6\sqrt{35}}$		
$U'_{3/2}$		$\frac{+1}{2\sqrt{10}}$	
$U'_{5/2}$			$\frac{+7}{6\sqrt{35}}$

TABLE IV .

SPIN – ORBIT COUPLING MATRIX ELEMENTS BETWEEN COMPONENTS t OF $^6T_2$ AND t′ OF $^4\Gamma$ IN UNITS OF $\langle T_2 \| \sum s.u \| \Gamma \rangle$.

3.7 CALCULATION OF TRANSITION PARAMETERS FOR QUARTETS

Using the results of 3.4 and 3.6, summarised in TABLES II and IV, we are now able to complete the calculation of the $^4\Gamma \leftarrow {}^6A_1$ transition parameters. Both sets of results are in terms of arbitrary factors $\langle T_2 \| \hat{\underset{\sim}{m}} \| A_1 \rangle$, and $\langle T_2 \| \sum su \| \Gamma \rangle / \Delta E$, which vary from quartet to quartet. By taking the ratio MCD:absorption, these factors cancel, and comparisons can be made between different quartet states.

The method of calculation is best illustrated by an example, and we chose E' from ^4E. The spin orbit interaction mixes $E'_{5/2}$ and $E'_{7/2}$ from $^6T_2$ into the wavefunction, so that the spin forbidden transition

$$E'(^4E) \leftarrow (E'' + U')\ {}^6A_1$$

has properties derived from the properties of the fully allowed charge transfer transitions:

$$E'_{5/2}(^6T_2) \leftarrow (E'' + U')\ {}^6A_1 \text{ and } E'_{7/2}(^6T_2) \leftarrow (E'' + U')\ {}^6A_1$$

weighted by the squares of the mixing coefficients:

	C	D	ΔD	$\langle {}^6T_2 E' \| \hat{\mathcal{H}}_{soc} \| {}^4E\ E' \rangle$
$E'_{5/2}$	$-1/3\beta$	1/3	+0.164	$-3/2\sqrt{105}$
$E'_{7/2}$	$+5/6\beta$	1/3	-0.091	$+1/2\sqrt{21}$

C, D, and ΔD are in units of $1/3\langle T_2 \| \hat{\underset{\sim}{m}} \| A_1 \rangle^2$, and the spin orbit coupling matrix elements are in units of $\langle T_2 \| \sum su \| E \rangle / \Delta E$. Then for E' of ^4E, we have:

$$C = -1/3\beta \times \left(\frac{-3}{2\sqrt{105}}\right)^2 + 5/6\beta \times \left(\frac{1}{2\sqrt{21}}\right)^2 = \frac{+\beta}{360}$$

$$D = 1/3 \times \left(\frac{-3}{2\sqrt{105}}\right)^2 + 1/3 \times \left(\frac{1}{2\sqrt{21}}\right)^2 = 1/90$$

$$\Delta d = +0.164 \times \left(\frac{-3}{2\sqrt{105}}\right)^2 - 0.091 \times \left(\frac{1}{2\sqrt{21}}\right)^2 = +0.00243,$$

where Δd refers to the quartet state and is defined in the same way as ΔD in EQUATION (3.11)

$C/D = +\beta/4, \quad \Delta d/D = +0.219.$

The complete set of results for the spin orbit components of all the quartet states is given in TABLE V. In general, the ratios C/D and $\Delta d/D$ have opposite signs for any given component, and this arises from the defining equations. The example shown above is an exception under the given conditions of field and temperature; if these are changed, the relative contributions from each ground state Zeeman component will be altered, and a different Δd results. For example, for ^4E:

	Δd		C
	4.2K, 4.75T	6.6K, 0.7T	
E'	+0.00243	-0.00008	$+\beta/360$
E''	-0.0153	-0.00205	$+\beta/24$
U'	-0.0150	-0.00250	$+19\beta/360$

This illustrates that the Faraday Parameter C cannot be used to describe high field-low temperature situations.

The $^4A_1(G)$ state is unique among the quartets in that neither of the mechanisms discussed in 3.5 can give the $^4A_1 \longleftarrow {}^6A_1$ transition any electric dipole intensity. Some intensity may be acquired in higher order perturbation theory, such as by mixing with other $^4\Gamma$ states under the influence of the magnetic field, by spin orbit mixing with $^4T_1$, by vibronic coupling, or by the action of the tetragonal component of the crystal field. For example, for Mn^{2+} doped into $KZnF_3$ and

$KMgF_3$, the vibronically induced $^4A_{1g}$ and ^4E_g single ion transitions are of comparable intensity[50]. In addition, by mechanisms analogous to (i) and (ii) above, the $^4A_1 \leftarrow {}^6A_1$ transition may gain magnetic dipole intensity. Generally, such transitions are of low intensity, but they are well characterised in a number of compounds, e.g. MnF_2, where the $^4T_{1g}$ (G) origin is a pure magnetic dipole line [88]. The test to detect the presence of magnetic dipole contributions to the intensity in uniaxial crystals is to look for differences between the α- and σ-spectra [89]. When this is applied to Cs_3MnCl_5, the only positive results occur for the AE(G) band and $^4T_2(F)$.

This concludes the theoretical discussion of the intensities of the spin forbidden transitions of Cs_3MnCl_5. By assuming tetrahedral symmetry, the calculations have been greatly facilitated, but the results need to be applied with care as the manganese site symmetry is D_{2d}. The spectra show a fair degree of linear polarisation, whereas the tetrahedral model gives no linear polarisation. However, the correct wavefunctions of any $^4\Gamma$ state in symmetry $D_{2d}{}^*$ can be expressed as linear combinations of the wavefunctions used in $T_d{}^*$. Therefore the properties summed over the whole $^4\Gamma$ state will remain constant, e.g. the total $\Delta d/D$ ratio should not be affected by the lowering of symmetry.

		C	D	C/D	Δd	Δd/D
$^4A_1$	U'	0	0	-	0	-
$^4A_2$	U'	$\frac{-7\beta}{36}$	$\frac{1}{18}$	$\frac{-7\beta}{2}$	+0.0496	+0.896
^4E	E'	$\frac{+\beta}{360}$	$\frac{1}{90}$	$\frac{+\beta}{4}$	+0.00243	+0.219
	E''	$\frac{+\beta}{24}$	$\frac{1}{60}$	$\frac{+5\beta}{2}$	-0.0153	-0.916
	U'	$\frac{+19\beta}{360}$	$\frac{5}{180}$	$\frac{+19\beta}{10}$	-0.0150	-0.540
	TOTAL	$\frac{+7\beta}{72}$	$\frac{1}{18}$	$\frac{+7\beta}{4}$	-0.0278	-0.500
$^4T_1$	E'	$\frac{+7\beta}{180}$	$\frac{1}{60}$	$\frac{+7\beta}{3}$	-0.00394	-0.237
	E''	$\frac{+\beta}{54}$	$\frac{1}{135}$	$\frac{+5\beta}{2}$	-0.00680	-0.918
	$U'_{3/2}$	$\frac{+77\beta}{1800}$	$\frac{7}{300}$	$\frac{+11\beta}{6}$	-0.0123	-0.528
	$U'_{5/2}$	$\frac{-2\beta}{675}$	$\frac{11}{1350}$	$\frac{-4\beta}{11}$	+0.0000414	+0.00508
	TOTAL	$\frac{+7\beta}{72}$	$\frac{1}{18}$	$\frac{+7\beta}{4}$	-0.0230	-0.414
$^4T_2$	E'	$\frac{-7\beta}{540}$	$\frac{7}{540}$	$-\beta$	+0.00638	+0.492
	E''	0	0	-	0	-
	$U'_{3/2}$	$\frac{-7\beta}{120}$	$\frac{1}{60}$	$\frac{-7\beta}{2}$	+0.0149	+0.893
	$U'_{5/2}$	$\frac{-7\beta}{270}$	$\frac{7}{270}$	$-\beta$	+0.00354	+0.137
	TOTAL	$\frac{-7\beta}{72}$	$\frac{1}{18}$	$\frac{-7\beta}{4}$	+0.0248	+0.447

TABLE V .

DIPOLE STRENGTHS AND MCD PARAMETERS FOR SPIN - FORBIDDEN TRANSITIONS $^4\Gamma \leftarrow {}^6A_1$ OF Mn^{2+} , CALCULATED FROM SPIN - ORBIT MIXING OF $^6T_2$ WITH $^4\Gamma$ WAVEFUNCTIONS IN SYMMETRY T_d *.

3.8 EXPERIMENTAL BAND AREA MEASUREMENTS

The spectra of Cs_3MnCl_5 were recorded as plots of (differential) decadic absorbance against wavelength in Ångstroms. The absorbances were converted into extinction coefficients using the formula:

$$\text{Absorbance} = \varepsilon\, c\, d \qquad \text{EQUATION (3.17)}$$

where c is the chromophore concentration (moles per litre) and d the crystal thickness (cms). The former was calculated from the unit cell dimensions given by Ijdo [2], while the latter was measured using a precision micrometer as the crystals ranged from about 1 to 2.5 mm. thick. The spectra of the individual quartets were drawn out with absorption and MCD on the same wavelength scale. The laborious point by point conversion from Å to cm^{-1} was not performed because the deviation of the abscissa scale from linearity over the relatively narrow wavelength range of each quartet is not very important. It was from these drawings that the band areas were measured simply by counting squares on the graph paper. In the sharp line AE(G) region, where accurate small scale reproduction was difficult, the original spectra were traced, and the bands cut out and weighed, with conversion to areas from the weight of a known area of tracing paper. The absorption band areas are probably accurate to 5%, but the MCD band areas may be subject to larger errors. This arises because the MCD signal goes through several stages of electronic processing, as compared to one stage for absorption, and because of the correction necessary when the differential absorbance exceeds 0.3. This correction is very sensitive to the calibration factor determined in a separate

experiment (see APPENDIX III); in contrast, the absorption spectrophotometer had a built in electronic calibration.

The experimental band areas are designated $\int_{band} \varepsilon(\nu)d\nu$ for absorption and $\int_{band} \Delta\varepsilon(\nu)d\nu$ for MCD, and we wish to relate them to the theoretical parameters D and Δd respectively. This is done as follows:

For an absorption band, it can be shown (e.g. [76], Appendix 10.2) that the oscillator strength f is given by:

$$f = 4.33 \times 10^{-9} \int_{band} \varepsilon(\nu)d\nu \qquad \text{EQUATION (3.18)}$$

provided that the half-width $\Delta\nu$ is small compared with the energy of maximum absorption ν_o. In terms of the dipole strength

$$f = \frac{8\pi^2 m \nu_o D}{3 h e^2} \qquad \text{EQUATION (3.19)}$$

so that:

$$D = \frac{9.1834 \times 10^{-3}}{\nu_o} \int_{band} \varepsilon(\nu)d\nu \qquad \text{EQUATION (3.20)}$$

Here, D is in $Debye^2$, and ν in cm^{-1}.

For the MCD, we have previously shown that:

$$\Delta\varepsilon = \frac{8\pi^3 L}{hc\ 10^3\ ln\ 10} f(\nu,\nu_o)\left\{|\langle j|\hat{m}_+|a\rangle|^2 - |\langle j|\hat{m}_-|a\rangle|^2\right\}$$

EQUATION (2.18)

and:

$$\Delta d = \sum_{j \leftarrow a} \frac{N_a}{N}\left\{|\langle j|\hat{m}_+|a\rangle|^2 - |\langle j|\hat{m}_-|a\rangle|^2\right\} \qquad \text{EQUATION (3.11)}$$

If $\Delta\varepsilon$ is integrated over the whole quartet band, this has the effect of taking the sum over all the components of the transition, and the normalised lineshape function $f(\nu,\nu_o) = 1$, so that:

$$\frac{1}{\nu_o} \int_{band} \Delta\varepsilon(\nu)d\nu = \frac{8\ ^3L\ \Delta d}{hc\ 10^3\ \ln\ 10} \qquad \text{EQUATION (3.21)}$$

giving:

$$\Delta d = \frac{3.0650 \times 10^{-3}}{\nu_o} \int_{band} \Delta\varepsilon(\nu)d\nu \qquad \text{EQUATION (3.22)}$$

Here Δd is in $Debye^2$. Taking the MCD:absorption ratio, from EQUATIONS (3.22) and (3.20), we obtain:

$$\Delta d/D = 0.33375 \frac{\int_{band} \Delta\varepsilon(\nu)d\nu}{\int_{band} \varepsilon(\nu)d\nu} \qquad \text{EQUATION (3.23)}$$

3.9 COMPARISON BETWEEN THEORY AND EXPERIMENT

Using the relationships developed in 3.8 above, and the band areas measured from the spectra, the oscillator and dipole strengths of the individual quartet absorption bands may be found, and their experimental $\Delta d/D$ ratios. This data is collected in TABLE VI. As expected for spin forbidden bands, the oscillator strengths are very low, varying between about 3×10^{-6} and 3×10^{-8}, as compared with unity for a fully allowed transition. More interesting is the comparison between the theoretical and experimental $\Delta d/D$ parameter ratios. (Note that in the experimental ratio, the axial band area corresponding to D_{α} has been used.) The overall agreement is good, which justifies the choice of the intensity mechanism made in 3.5 above, and the use of a simplified model based on tetrahedral symmetry. Also, it confirms that the assignment of the transitions implicit in the analysis of the data is correct, so that the crystal field calculations of CHAPTER 5 may be tackled with confidence. The limitations of the tetrahedral model will become apparent when the finer details of the individual quartet states, particularly origin assignments, are examined - see CHAPTER 6. The states

for which agreement between experiment and theory is not particularly close are discussed briefly below:

(i) REGION III, AE(G).

This band consists of many sharp intense lines, so that area measurements are more difficult to make accurately, and there are magnetic dipole contributions to the observed intensity. Nevertheless, the agreement is quite good.

(ii) REGION IV, the $^4E(D)$ band.

This contains three bands which overlap slightly with one another. The two intense outer bands, $^4T_2(D)$ and $^4T_1(P)$, show reasonable agreement between experiment and theory, while the weaker $^4E(D)$ band sandwiched between them shows very poor agreement, although the overall sign of its MCD (-ve) is correctly predicted.

(iii) REGION VI, the $^4A_2(F)$ band.

This is the least intense of the quartets, and overlaps with $^4T_2(F)$. Accurate area measurements are difficult as sharp lines are again involved, and the signal:noise ratio is lower than for other bands. This is due to increased scattering of light at shorter wavelengths, together with a reduction in the efficiency of the monochromator (blaze wavelength 5000 Å) and the light source. The sign of the MCD signal (+ve) is correctly predicted.

BAND		$\int_{band} \varepsilon \, d\nu$	OSCILLATOR STRENGTH	DIPOLE STRENGTH	$\int_{band} \Delta\varepsilon \, d\nu$	$\Delta d / D$ OBS.	$\Delta d / D$ CALC.	AREA RATIO α/π
$^4T_1(G)$	α	130	5.7×10^{-7}	5.7×10^{-5}	−158	−0.406	−0.414	0.331
	π	393	1.7×10^{-6}	1.8×10^{-4}				
$^4T_2(G)$	α	437	1.9×10^{-6}	1.8×10^{-4}	+599	+0.457	+0.447	0.963
	π	454	2.0×10^{-6}	1.9×10^{-4}				
$^4A_1$ + $^4E(G)$	α	116	5.0×10^{-7}	4.7×10^{-5}	−141	−0.406	−0.500	1.568
	σ	99	4.3×10^{-7}	4.1×10^{-5}				
	π	74	3.2×10^{-7}	3.0×10^{-5}				
$^4T_2(D)$	α	187	8.1×10^{-7}	6.6×10^{-5}	+189	+0.337	+0.447	0.639
	π	293	12.7×10^{-7}	10.3×10^{-5}				
$^4E(D)$	α	256	1.1×10^{-6}	8.7×10^{-5}	~ −51	−0.066	−0.500	1.094
	π	234	1.0×10^{-6}	7.6×10^{-5}				
$^4T_1(P)$	α	612	2.7×10^{-6}	2.0×10^{-4}	~ −1102	−0.601	−0.414	0.984
	π	622	2.7×10^{-6}	2.1×10^{-4}				
$^4T_1(F)$	α	181	7.8×10^{-7}	4.8×10^{-5}	−273	−0.503	−0.414	1.740
	π	104	4.6×10^{-7}	2.8×10^{-5}				
$^4A_2(F)$	α	7.62	3.3×10^{-8}	1.95×10^{-6}	+7.27	+0.318	+0.896	~2.5
	π	~3	$\sim1.3\times10^{-8}$	$\sim1\times10^{-6}$				
$^4T_2(F)$	α	176	7.6×10^{-7}	4.4×10^{-5}	+256	+0.485	+0.447	0.338
	σ	225	9.7×10^{-7}	5.6×10^{-5}				
	π	520	2.3×10^{-6}	1.3×10^{-4}				

TABLE VI.

OBSERVED DATA FOR THE QUARTET ABSORPTION BANDS OF Cs_3MnCl_5 AT 4.2K.

UNITS OF :

BAND AREA - litres per mole per cm times cm^{-1}.

DIPOLE STRENGTH - $Debye^2$.

ALL OTHERS - dimensionless.

MCD DATA REFER TO AN AXIAL MAGNETIC FIELD OF 4.75T.

CHAPTER 4

THE SPECTRA OF Cs_3MnCl_5 SINGLE CRYSTALS

4.1 INTRODUCTION

The general features of the spectra of Cs_3MnCl_5 single crystals will be discussed here: temperature dependence, linear and circular polarisation, the assignment of the bands, and comparison with other studies. In addition, Crystal Field calculations will be presented later to support the assignment of the higher energy bands as this is not in agreement with the general pattern found in cubic Mn(II) complexes. The high resolution spectra reported here were recorded at liquid helium temperatures using the apparatus and methods of APPENDIX III for MCD and APPENDIX IV for absorption. These results extend the previous work of Stoneman [59] who was unable to observe the bands above 27,700 cm^{-1}. They parallel the studies made by Vala and co-workers on the tetra-alkylammonium manganese halide salts $(R_4N)_2MnX_4$, to which frequent reference will be made for purposes of comparison. For the sake of brevity, these results will be given the label "Vala's". Vala's absorption data, along with Crystal Field and spin orbit calculations, were for the orthorhombic crystals $(Me_4N)_2MnCl_4$ and $(Me_4N)_2MnBr_4$ at low temperatures [60]. MCD spectra were recorded for the tetragonal crystals $(Et_4N)_2MnX_4$, X = Cl, Br, and I at 6.6K in a field of 0.7T [63]. Under these conditions, the description in terms of Faraday parameters is valid. High resolution was employed in both these studies, but owing to the different natures of the lattices,

neither of the chloride salts gave lines as sharp as the ones observed in Cs_3MnCl_5.

4.2 OVERALL APPEARANCE AND TEMPERATURE DEPENDENCE

FIGURE 7 shows the axial (α) absorption spectrum of single crystal Cs_3MnCl_5 at room temperature and 4.2K over the wavelength range 2600Å to 5200Å. The pattern of the bands is such that the spectrum can conveniently be discussed in terms of six separate parts, REGIONS I to VI. The linearly polarised (σ and π) spectra are shown in FIGURE 8, together with the band assignments. In both FIGURES, the flat baselines are indicative of the good optical quality of the crystals and the stability of the McPherson spectrophotometer. These survey spectra have been photoreduced from tracings of the original chart recordings obtained from 100Å per minute scans with the minimum slit width (5μm). The crystals were about 2 mm. thick, so that on a O-2A absorbance scale the extinction coefficients are low as the calculated concentration of chromophore units is 5.25M.

A brief reference has already been made in 3.9 to the low oscillator strengths of the $^4\Gamma \leftarrow {}^6A_1$ transitions in Cs_3MnCl_5. They are, however, roughly one order of magnitude larger than the values given by Stout for MnF_2 [39], or for the hydrated Mn^{2+} ion in solution [92], in line with the general trend for the ratio of tetrahedral:octahedral intensities to be roughly 10 to 100 for comparable compounds. There is no trend in the oscillator strengths towards higher values at higher energies, in spite of the intensity mechanism being "borrowing" from charge transfer via spin orbit mixing with $^6T_2$. The reason for the lack of a trend is that other factors

beside the energy separation ΔE are involved in determining the $^4\Gamma$ intensities, principally the multi-element reduced matrix elements of spin orbit coupling $\langle {}^6T_2 \| \sum su \| {}^4\Gamma \rangle$, which have not been explicitly evaluated. The arguments presented in CHAPTER 3 remain valid. In the $\Delta d/D$ ratio, these unknown factors and the energy separation terms cancel out.

It can be seen from FIGURE 7 that there is a remarkably small change in the intensities of the bands on cooling the crystal from 294 to 4.2K. There is, however, a considerable reduction in the half-widths $\Delta\nu$ of the bands, so that there is less overlapping and clearly defined vibrational structure emerges. The extinction coefficients also increase so that the product $\varepsilon_{max}\Delta\nu$ remains roughly constant to maintain a constant oscillator strength. In addition to the sharpening of lines and bands, there are small shifts in the intensity maxima. Further, the spectra of the most intense sharp origin lines, P and Q of REGION III, were examined over the range 2.6 to 21.0K under the highest available resolution. No "hot" bands appeared, changes in intensity were very slight, and the lines merely became a little broader (cf Cs_3CoBr_5 [70] where the ground state shows an appreciable zero field splitting). From these observations it is concluded that the electric dipole mechanism is dominant, co-operative effects between adjacent $MnCl_4^{2\ominus}$ ions are not apparent at these temperatures, and the ground state is not split in the absence of a magnetic field. This latter pair of conclusions support our earlier pair of assumptions, based respectively on magnetic susceptibility [71] and ESR data [33], about the nature of the $^6A_1$ ground state.

4.3 LINEAR AND CIRCULAR POLARISATIONS

The upper trace in FIGURE 8 was recorded with $\underset{\sim}{E}$ perpendicular to the unique axis, i.e. it is the σ-spectrum. This is identical in every detail with the α-spectrum: band areas and the positions and intensities of individual lines, again demonstrating that the electric dipole mechanism is responsible for the transitions [89]. Only in the case of AE(G) is there any large discrepancy, while $^4T_2(F)$ shows a small difference in α- and σ-intensities.

The lower trace was recorded with $\underset{\sim}{E}$ parallel to the unique axis, and is broadly similar to the σ-spectrum. In particular, sharp lines common to both spectra are found at the same wavelengths, within the experimental error ($\pm$0.1Å). This shows that Davydov effects are not important, in contrast to Cs_3CoBr_5 where line shifts of up to $10cm^{-1}$ are seen between σ- and π-spectra [90]. (The Davydov effect arises from coupling of the transition dipoles of individual chromophores in the unit cell. In Cs_3MnCl_5, each unit cell contains four $MnCl_4^{2\ominus}$ ions reasonably close together, so that the opportunity for coupling exists. McClure [91] gives further details and examples of the effect.)

The origin of the magnetically induced circular polarisation has been fully discussed in CHAPTER 3. The signs of the MCD signals have been used together with comparison with Vala's results [60, 63] in the assignment of the bands. MCD spectra of Cs_3MnCl_5 quartet states are presented individually in CHAPTER 6.

Hereafter, all discussions of the optical properties of Cs_3MnCl_5 single crystals will relate to spectra recorded at low temperatures, 4.2K unless otherwise stated. Resolution is 0.15Å in absorption, about 1Å for MCD except for the ^4F terms. We refer to absorption spectra for the most part, so that other data will be specified as such where it occurs.

4.4 DOUBLETS AND MYSTERY BANDS

In his review article [8] and in several papers, Ferguson mentions broad absorption features seen in thick Mn(II) crystals which he assigns to doublet excited states. No such features were found in Cs_3MnCl_5 single crystals up to 2.4 mm thick, nor was there any evidence of "mystery bands" similar to those reported by Vala for $(Me_4N)_2MnCl_4$ [60]. The bands we report arise solely from $^4\Gamma \leftarrow {}^6A_1$ electronic transitions of the ion $MnCl_4^{2\ominus}$ coupled with vibrations characteristic of the Cs_3MnCl_5 crystal lattice.

4.5 ASSIGNMENT OF THE BANDS

Crystal field calculations on the ordering of energy levels of the Mn^{2+} ion in a cubic environment of O_h or T_d point symmetry generally give rise to the following scheme:
$^4T_2(F)$, $^4T_1(F)$, $^4A_2(F)$, $^4T_1(P)$, $^4E(D)$, $^4T_2(D)$, $^4A_1+{}^4E(G)$, $^4T_2(G)$, $^4T_1(G)$.
Here the states are written in order of decreasing energy. Experimental results have been in accord with this scheme, including the earlier work on Cs_3MnCl_5 [59] and Vala's study of $(Me_4N)_2MnCl_4$ [60]. This is supported by the MCD results obtained here, the sign of the signal and the $\Delta d/D$ ratio, for all but the highest energy terms arising from ^4F, REGION VI of FIGURE 7. In Cs_3MnCl_5, $^4A_2(F)$ is identified as two origin lines

with accompanying vibrational sidebands lying between the two main ^4F absorption bands. In absorption, the lines are sharp and rather weak, and are associated with a +ve MCD. Vala's later work [63] supports this assignment. In addition to these MCD results, there is some indirect evidence to support this "novel" assignment. First, Lohr [66] has predicted that for tetrahedral symmetry, $^4A_2(F)$ should be the narrowest of the $^4\Gamma \leftarrow {}^6A_1$ absorption bands. In Cs_3MnCl_5, the "crystal field independent" bands $^4A_2(F)$ and AE(G) are of equal width, being restricted to two ν_1 quanta, all the other bands being broader. Secondly, Ferguson [8] has found that in many octahedral Mn(II) complexes, the ratios of the energies of all three crystal field independent states to the corresponding free ion energies are equal. Applying this test, we have:

STATE	ENERGY in cm^{-1}		RATIO %
AE(^4G)	22,920	26,850	85.4
$^4E(^4D)$	27,030	32,360	83.5
$^4A_2(^4F)$	35,860	43,620	82.2
	Cs_3MnCl_5	Free Mn^{2+} ion	

From this constancy of the ratio, it is inferred that $^4A_2(F)$ is at the "correct" energy; assignment to a position below $^4T_1(F)$ would place it out of step with these other states. The relationship between the energies can be expressed as [93] :

$$^4A_2(F) = \frac{9}{35}\,{}^4E(G) + \frac{8}{7}\,{}^4E(D) \qquad \text{EQUATION (4.1)}$$

which is strictly correct only for zero covalency. For Cs_3MnCl_5, this predicts the $^4A_2(F)$ state to lie at 36,790 cm^{-1}, in quite good agreement with the observed position.

The only other plausible explanation for the presence of these lines we assign as $^4A_2(F)$ would be as a spin orbit component of $^4T_2(F)$. However, the total spread of the components of $^4T_2(F)$ would then become rather large, about 590 cm^{-1} as against 190 cm^{-1} predicted by Vala [60] , but more important, the sharp $^4A_2(F)$ band would then be missing. This explains the presence of REGION V in the spectrum of Cs_3MnCl_5, the area where $^4A_2(F)$ was initially expected to be. Careful examination showed no absorption bands present, nor was there any sign of an MCD signal even at high gain. Again, this is supporting evidence for the assignment of the high energy bands we have made:

$$^4T_2(F),\ ^4A_2(F),\ ^4T_1(F),$$

in order of decreasing energy.

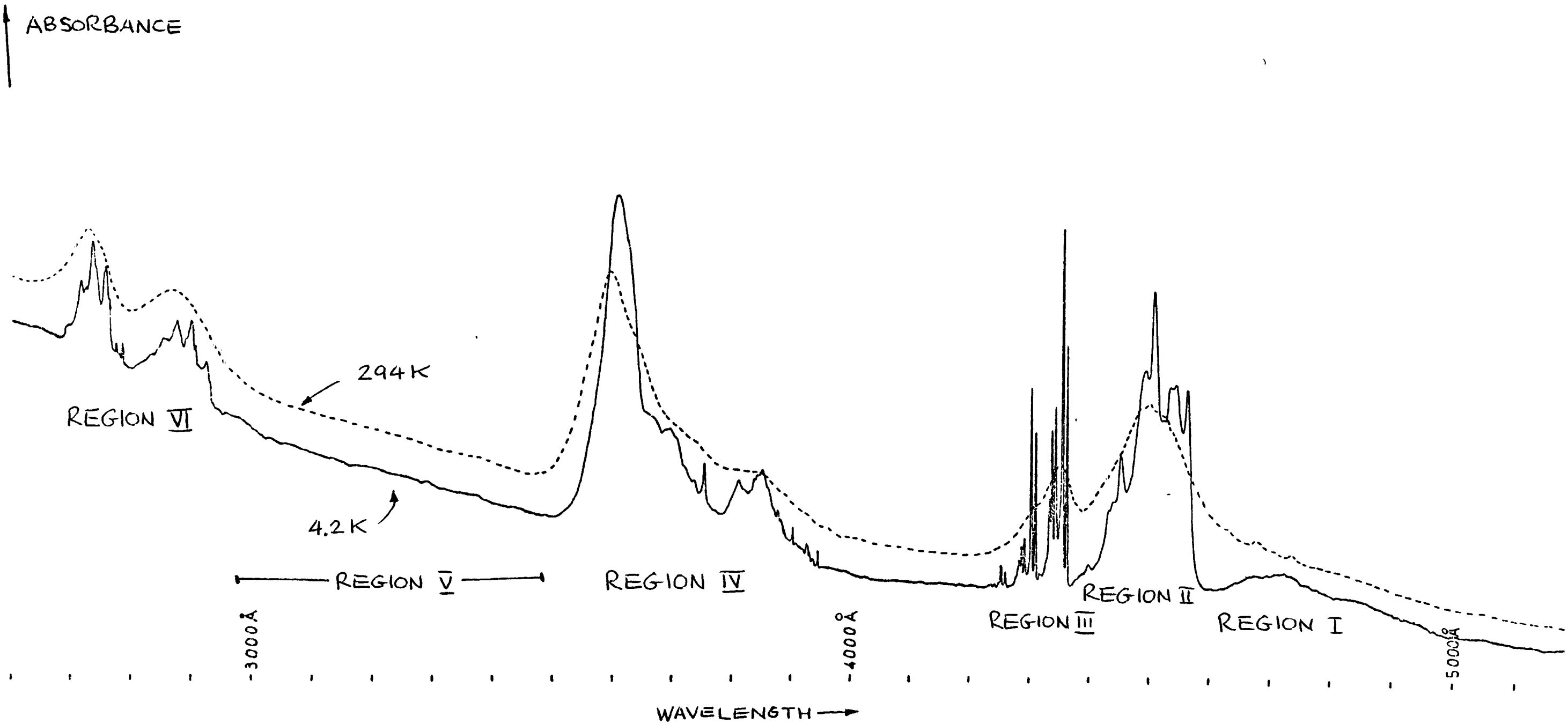

FIGURE 7.

AXIAL (α) SPECTRUM OF Cs_3MnCl_5 AT ROOM AND LIQUID HELIUM TEMPERATURES.

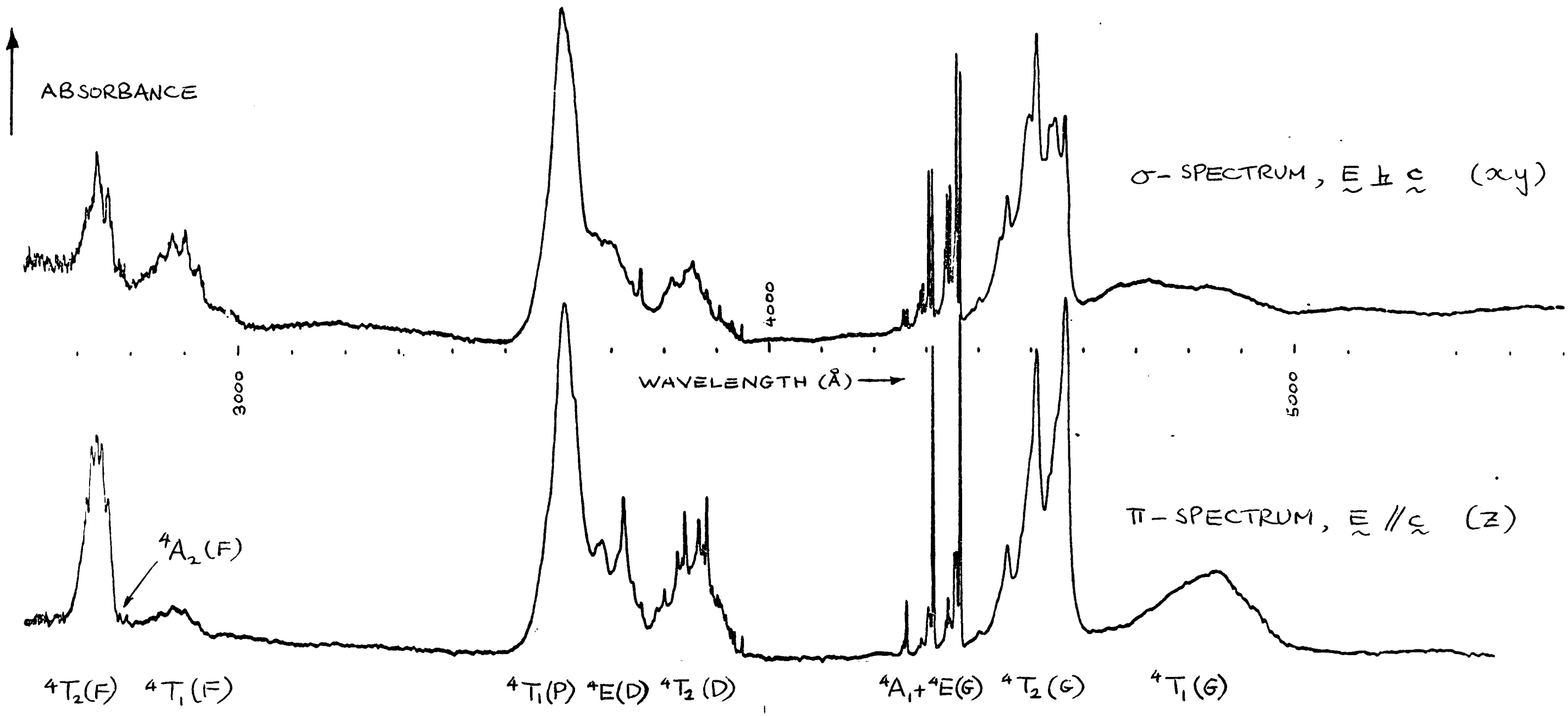

FIGURE 8 .

LINEARLY POLARISED SPECTRA OF Cs_3MnCl_5 AT 4.2K .

C H A P T E R 5

CRYSTAL FIELD CALCULATIONS

5.1 INTRODUCTION

The principal aim of the calculations is to obtain a fit to the observed energy levels of Cs_3MnCl_5. In particular, we wish to support the "novel" assignment of the ^4F bands which has placed $^4A_2(F)$ above $^4T_1(F)$ in energy, while retaining the conventional ordering of the other levels. To do this, the electrostatic model is modified to include the effect of covalency on the energy levels using the method of Koide and Pryce [37]. Most of the calculations were performed using the energy matrices given by Stout [39] which are given in full in APPENDIX VI, together with explanatory notes on the Trees correction and the use of negative values of parameters D_q and ϵ . Diagonalisation was undertaken numerically using a standard FORTRAN library routine for real symmetric matrices, FO2ABF.

5.2 COMPARISON WITH $(Me_4N)_2MnCl_4$

The optical spectra of $(Me_4N)_2MnCl_4$ are very similar in overall appearance to those of Cs_3MnCl_5. Vala [60] has performed a series of Crystal Field calculations upon the former compound using the Strong Field representation, and these provide a starting point for our own analysis of Cs_3MnCl_5. Below in TABLE VII the positions of the band maxima of the two compounds are given, together with Vala's calculated

energies. In all cases, the observed energy represents the position of maximum absorption intensity of the Franck-Condon envelope of the band. This was derived by taking the wavelength in Ångstroms and dividing into 10^8, i.e. without vacuum correction. The figures refer to 4.2K, and are rounded to the nearest ten wavenumbers.

		ENERGY cm^{-1} OF BAND MAXIMUM				
		Cs_3MnCl_5			$(Me_4N)_2MnCl_4$ [60]	
BAND	REGION	α	π	Weighted Mean	Calculated	Observed
$^4T_1(G)$	I	21160	20580	20800	20960	21250
$^4T_2(G)$	II	22180	21890	22120	22180	22230
AE(G)	III	22940	22900	22920	22970	23020
$^4T_2(D)$	IV	25930	25900	25930	26240	26080
$^4E(D)$	IV	27030	26860	27030	26460	26930
$^4T_1(P)$	IV	27700	27700	27700	27470	27770
$^4T_1(F)$	VI	34430	34820	34430	36320	34530
$^4A_2(F)$	VI	35860	35860	35860	36140	Not clearly distinguished
$^4T_2(F)$	VI	36490	36520	36510	37140	36620

TABLE VII

COMPARISON OF THE LOW TEMPERATURE SPECTRA OF Cs_3MnCl_5 AND $(Me_4N)_2MnCl_4$.

The table clearly shows the close similarity between the band maxima of the two compounds. For this reason, the calculated energies give quite a close fit to the levels observed

for Cs_3MnCl_5. The parameter values were as follows:

$B = 650\ cm^{-1}$, $C = 2990\ cm^{-1}$, $D_q = 330\ cm^{-1}$ for $\alpha = 76\ cm^{-1}$ and ϵ = zero,

and were found from a least squares BEST FIT analysis of the bands of $(Me_4N)_2MnCl_4$ below 30,000 cm^{-1}. A similar analysis of the eight E, T_1, and T_2 bands of Cs_3MnCl_5 gave very similar parameter values [95]:

$B = 625\ cm^{-1}$, $C = 3000\ cm^{-1}$, $D_q = 325\ cm^{-1}$ for $\alpha = 76\ cm^{-1}$ and ϵ = zero.

In either case, however, the calculations place $^4A_2(F)$ below $^4T_1(F)$, whereas we have made the opposite assignment. Also, neither set of values approaches either the Weak or Strong Field limit, $Dq \ll B$ or $Dq \gg B$ respectively, so that an intermediate regime applies. The grouping of the bands is suggestive of the Weak Field modification of the free ion term pattern, however, and the appropriate notation is used throughout the current study.

5.3 METHOD OF CALCULATION

The present calculations differ from those of Vala [60] in several ways. The effects of the spin orbit interaction and the tetragonal distortion are not considered, as both are regarded as small perturbations which will merely split each $^4\Gamma$ state by a few tens to hundreds of wavenumbers but will not affect the baricentres. The Koide and Pryce covalency parameter ϵ is included in the electrostatic matrices of Stout [39], and its effect on the energy levels will be investigated. No energy level fitting routine comparable with

Vala's BEST FIT program was available, so that the computer was simply used to diagonalise the matrices for a series of values of the four adjustable parameters B, C, Dq, and ϵ, the value of α being fixed at 76 cm^{-1}. The relative merits of such sets of parameter values depend on their ability to give the correct ordering of the $^4\Gamma$ excited states, and on the closeness of the fit to the observed energies. The first criterion is the more important, while the second was assessed by calculating a "figure of merit", abbreviated fom., as follows:

$$\text{fom.} = 10^8 \Big/ \sum_{^4\Gamma} (\text{Observed energy minus Calculated energy})^2 \qquad \text{EQUATION (5.1)}$$

Thus, smaller deviations between observed and calculated energies give rise to larger fom. values. 10^8 is an arbitrarily chosen large number to give fom.'s in the range 1 - 100. All energies were rounded to the nearest 10 cm^{-1}, and $^4A_1(G)$ was not included in the calculation owing to uncertainty of its observed position (see CHAPTER 6).

Vala's calculations were based on the Strong Field electrostatic matrices of Tanabe and Sugano [17], but were not explicitly given in his paper [60]. We have found it convenient to use the Weak Field matrices for $3d^5$ given by Stout [39], obtained from those of Tanabe and Sugano by performing the appropriate unitany transformation. According to Curie et al [22], Stout's phase factors are correct. When a full diagonalisation is carried out in either scheme, a given set of parameter values should give the same calculated energy levels.

Thus the first target was to reproduce Vala's calculated energy levels using the matrices of APPENDIX VI, with B = 650, C = 2990, Dq = -330, and ϵ = 0. The results were as follows (units of cm^{-1} are to be taken throughout except for ϵ and fom.):

	Vala [60]	Present study
$^4T_1(G)$	20961	20961
$^4T_2(G)$	22182	22580
$^4E(G)$	22969	22969
$^4T_2(D)$	26244	25928
$^4E(D)$	26456	26456
$^4T_1(P)$	27467	27467
$^4A_2(F)$	36142	36142
$^4T_1(F)$	36316	36316
$^4T_2(F)$	37142	37060
	fom 21.78	fom 21.72

Only the $^4T_2$ energies differ, but in both cases the trace (the sum of the diagonal elements, equal to the sum of the energies) is the same, 95569 cm^{-1}. This indicates a discrepancy in one or more of the off-diagonal matrix elements for $^4T_2$, as it is these which give rise to the interactions between the states.

In an attempt to eliminate this discrepancy, a unitary transformation was performed upon Tanabe and Sugano's Strong Field matrix for $^4T_2$ states of $3d^5$, as follows:

(i) The electrostatic part of the Strong Field matrix (Dq = 0, ϵ = 0), which is off-diagonal, was diagonalised on the computer, and the eigenvalues compared with the diagonal entries in the Weak Field matrix. They were identical for corresponding states, lowest $^4T_2$ and $^4T_2(G)$, etc.

(ii) The eigenvectors so produced were used to transform the crystal field Dq terms of the Strong Field matrix (which appear only as diagonal entries), according to the equation [95]:

$$\mathbf{T} = \mathbf{R}^{-1}\mathbf{U}\mathbf{R} \qquad \text{EQUATION (5.2)}$$

As only two Dq terms appear in the Strong Field matrix **U**, the calculation was performed longhand. **R** is the eigenvector array which diagonalises the Strong Field electrostatic matrix, and and $\mathbf{R}^{-1}$ is its inverse. Because the original Strong Field electrostatic matrix is real and symmetric, $\mathbf{R}^{-1}$ can be replaced by the transpose $\mathbf{R}^{T}$, simplifying the calculation. **T** is the resultant matrix of the crystal field interaction in the Weak Field basis, and was added to the electrostatic part from (i). The resulting matrix was identical with Stout's, which we take to be correct.

(iii) The Trees correction terms, diagonal in Weak Field, were added, and the diagonalisation repeated using Vala's parameter values B = 650, C = 2990, Dq = 330. The figures were the same as those tabulated above for $^4T_2$, and we therefore believe that our calculated energies for the $^4T_2$ states are the correct ones, and that the matrix Vala used for $^4T_2$ contained an error. Possibly the error was related to the off-diagonal nature of

the Trees correction in the Strong Field formalism. The discrepancies in the calculated energy levels for $^4T_2$ states only amount to a few hundreds of wavenumbers, and a negligible effect upon the BESTFIT parameter values would be produced; the two fom. values are very close.

5.4 THE EFFECT OF COVALENCY PARAMETER ϵ

It is apparent from the structures of the matrices of APPENDIX VI that when negative values of ϵ are introduced, corresponding to covalency in tetrahedral coordination, the energies of all the quartet states will be raised. Also, the interactions between states of the same symmetry will be altered, and FIGURE 9 shows that these interactions are increased. It can clearly be seen that $^4A_2(F)$ is the state most sensitive to changes in ϵ , and is found between $^4T_1$ and $^4T_2$ for a narrow range of ϵ values. Within this range, the ordering of the other states is unchanged from the "conventional" cubic pattern except that the $^4A_1$ - $^4E(G)$ degeneracy is removed. This result is most encouraging as it indicates that covalency may be the factor involved in determining the ordering of the terms arising from ^4F where we have made a "novel" band assignment.

Further calculations were performed over a narrow range of ϵ values using the same B and C, and varying Dq over a narrow range to try to improve the overall fit. Again it was found that ϵ had the larger influence as the tabulated fom. values show:

	Dq = -360	Dq = -330	Dq = -300
ϵ = zero	20.83	21.72	21.33
ϵ =-0.02	10.48	10.64	10.44
ϵ =-0.04	5.06	5.07	5.01
B = 650	C = 2990		α = 76

In order to match the observed ordering of the ^4F terms, a 2% covalency is required, see FIGURE 10. The best Dq value would then be -330 cm^{-1} as indicated by the fom. values.

5.5 CRYSTAL FIELD PARAMETERS OF Cs_3MnCl_5

The above calculations used B and C values given by Vala for $(Me_4N)_2MnCl_4$. Considering the trends observed, several sets of calculations were performed on a trial and error basis in order to try to find parameter values more appropriate to Cs_3MnCl_5 itself. The best set so obtained was as follows: B = 690, C = 2750, Dq = -340, ϵ = -0.02, and the fom. = 23.06. This gave the correct ordering of the levels, and an fom. only marginally worse than Vala's BESTFIT result for Cs_3MnCl_5, 25.93 [94]. It became apparent, however, that comparable fits with correct ordering could be achieved within a large parameter space, and a different approach to the problem was required. This would be by the use of a simplifying assumption, e.g. fixing C/B at the free ion value, finding some helpful mathematical feature of the model, or engaging in extended systematic computations. In the event, a combination of the last two methods was used as these proved to be complimentary to one another, the mathematical simplification reducing the amount of calculation necessary.

The "method of traces", introduced by Curie, Barthou, and Canny [22] as a means of comparing spectroscopic results for various Mn(II) compounds, highlighted an important feature of the d^5 matrices: none of the traces depends on crystal field parameter Dq. Thus any analytical approach to the behaviour of the energy levels is simplified, the three remaining parameter values B, C, and ϵ may be more readily determined, and relationships between structurally similar Mn(II) compounds may

be clarified. Curie et al restricted themselves to using the E, T_1, and T_2 matrix traces, and C/B = 3.565 as found in the free ion [21]. Using the Koide and Pryce model, they obtained satisfactory results for octahedral coordination but experienced difficulties with tetrahedral Mn(II) halide salts. Possibly this was due to the use of the free ion C/B (γ) ratio, as Vala's analysis of $(Me_4N)_2MnCl_4$ indicated a much higher value, γ = 4.6. By taking the method of traces one step further, adding together the energies of all ten $^4\Gamma$ states, the problem is reduced to a single equation:

$$\sum 10\Gamma = 147B + 58C + 130\alpha - \epsilon(134B + 51C) \qquad \text{EQUATION (5.3)}$$

Assuming $^4A_1$ and $^4E(G)$ to be degenerate, $\sum 10\Gamma$ = 276,220 cm^{-1} for Cs_3MnCl_5. Putting α = 76 cm^{-1}, and C = γB, we have:

$$B(147 + 58\gamma) - \epsilon B(134 + 51\gamma) = 266{,}340 \qquad \text{EQUATION (5.4)}$$

Rearranging:

$$\epsilon = -\left\{\frac{266340/B - (147 + 58\gamma)}{(134 + 51\gamma)}\right\} \qquad \text{EQUATION (5.5)}$$

This defines a relationship between B, C and ϵ such that values satisfying the equation will give the correct total energy of all ten $^4\Gamma$ excited states. For any given value of γ, the solutions to EQUATION (5.5) can be plotted as a graph of ϵ against B. This is done in FIGURE 11, for the range of γ = 4.0 to 5.0 with B between 600 and 660 cm^{-1}.

The information contained in FIGURE 11 was used as follows. For a chosen value of γ, the B value is given by the point where the line crosses the ϵ = 0 axis. Using the values of B and C so derived, the energy matrices were diagonalised for a range of values of Dq and ϵ. By choosing ϵ to be about -0.02, the correct ^4F ordering can be maintained, and fom.'s then indicate the closeness of the fit. Note that Vala's BESTFIT analysis

of Cs_3MnCl_5, which did not include covalency, gave B = 625, C = 3000 (γ = 4.8), while the "total trace" plot for γ = 4.8 intercepts the axis at B = 626 cm^{-1}. This demonstrates a very close agreement between two different approaches to the problem of fitting the energy levels.

Using a simple computer program, the following parameter space was investigated:

C/B values from 4.60 to 4.90 by intervals of 0.05;

B values from 600 to 640 by intervals of 10;

Dq values from -380 to -300 by intervals of 20;

ϵ values from -0.060 to zero by intervals of 0.004.

The highest fom. with correct ordering was 40.91 for B = 600, C/B = 4.90, Dq = -360, and ϵ = - 0.032. Further refinement was obtained with a finer parameter mesh in the region around these values, and gave as the result:

B = 600 cm^{-1}, C = 2940 cm^{-1}, Dq = -350 cm^{-1}, ϵ = -0.030, α = 76 cm^{-1}, the figure of merit being 41.30.

5.6 DISCUSSION

The crystal field parameter values resulting from our calculations on Cs_3MnCl_5 are similar to those obtained by Vala's BESTFIT analysis [94]. However, they give a closer numerical fit to the observed energies, and more important, produce the correct ordering of the energy levels including the high energy terms from ^4F. Hence our two original criteria are satisfied. Below are tabulated the observed and calculated quartet energy levels of Cs_3MnCl_5:

ENERGY LEVELS	CALCULATED cm^{-1} PRESENT STUDY	OBSERVED cm^{-1} FOR Cs_3MnCl_5	CALCULATED cm^{-1} BY VALA 94
$^4T_1(G)$	20840	20800	20830
$^4T_2(G)$	22250	22120	21980
$^4E(G)$	22690	22920	22770
$^4A_1(G)$	22840	-	22770
$^4T_2(D)$	25300	25930	25880
$^4E(D)$	26140	27030	26080
$^4T_1(P)$	27260	27700	27300
$^4T_1(F)$	35290	34430	35830
$^4A_2(F)$	36350	35860	35660
$^4T_2(F)$	36550	36510	36650
fom.	41.30	-	25.93
RMS DEVIATION	521 cm^{-1}	-	592 cm^{-1}
PARAMETER VALUES	B=600 cm^{-1} C=2940 cm^{-1} γ=4.9 α=76 cm^{-1} Dq=-350 cm^{-1} ϵ=-0.03		B=625 cm^{-1} C=3000 cm^{-1} γ=4.8 α=76 cm^{-1} Dq=-325 cm^{-1} ϵ not used

TABLE VIII

ANALYSIS OF THE QUARTET ENERGY LEVELS OF Cs_3MnCl_5

It is to be expected that our calculations employing four adjustable parameters should yield a closer fit than Vala's, which only had three parameters. The differences between the two sets of B, C, and Dq values are not significant; our B and C must be lower to counteract the raising of the diagonal energies when ϵ is present. The use of this simple Koide and Pryce

covalency parameter is open to criticism, but it does give an improvement in the results without greatly increasing the amount of calculation necessary. Also, a 3% covalency figure does not seem unreasonable; Curie et al [22] calculated a value of 5.1% for Mn^{2+} doped into NaCl.

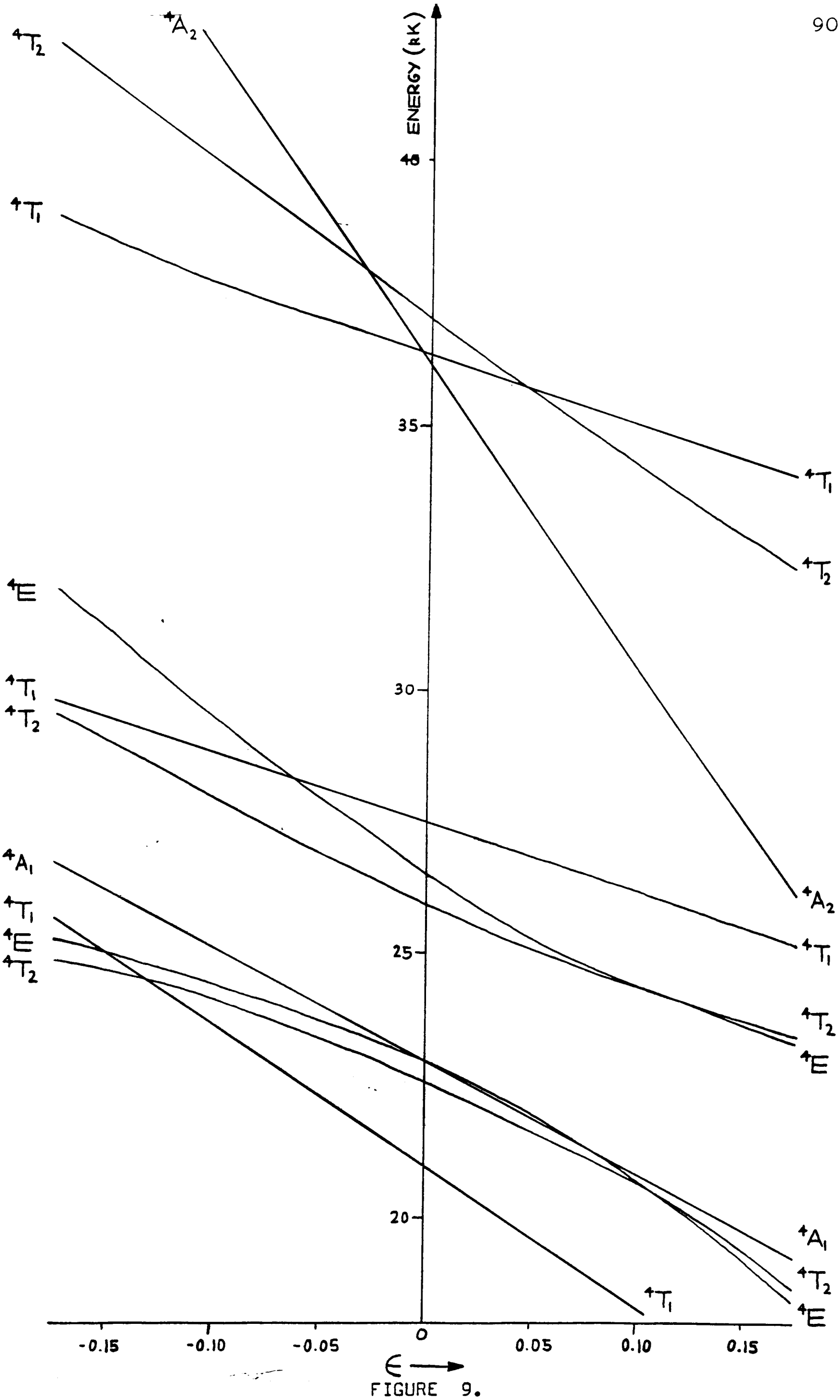

FIGURE 9.

ENERGY LEVELS OF Cs_3MnCl_5 PLOTTED AS A FUNCTION OF THE COVALENCY PARAMETER ϵ .

$B = 650cm^{-1}$, $C = 2990cm^{-1}$, $Dq = -330cm^{-1}$, $\alpha = 76cm^{-1}$.

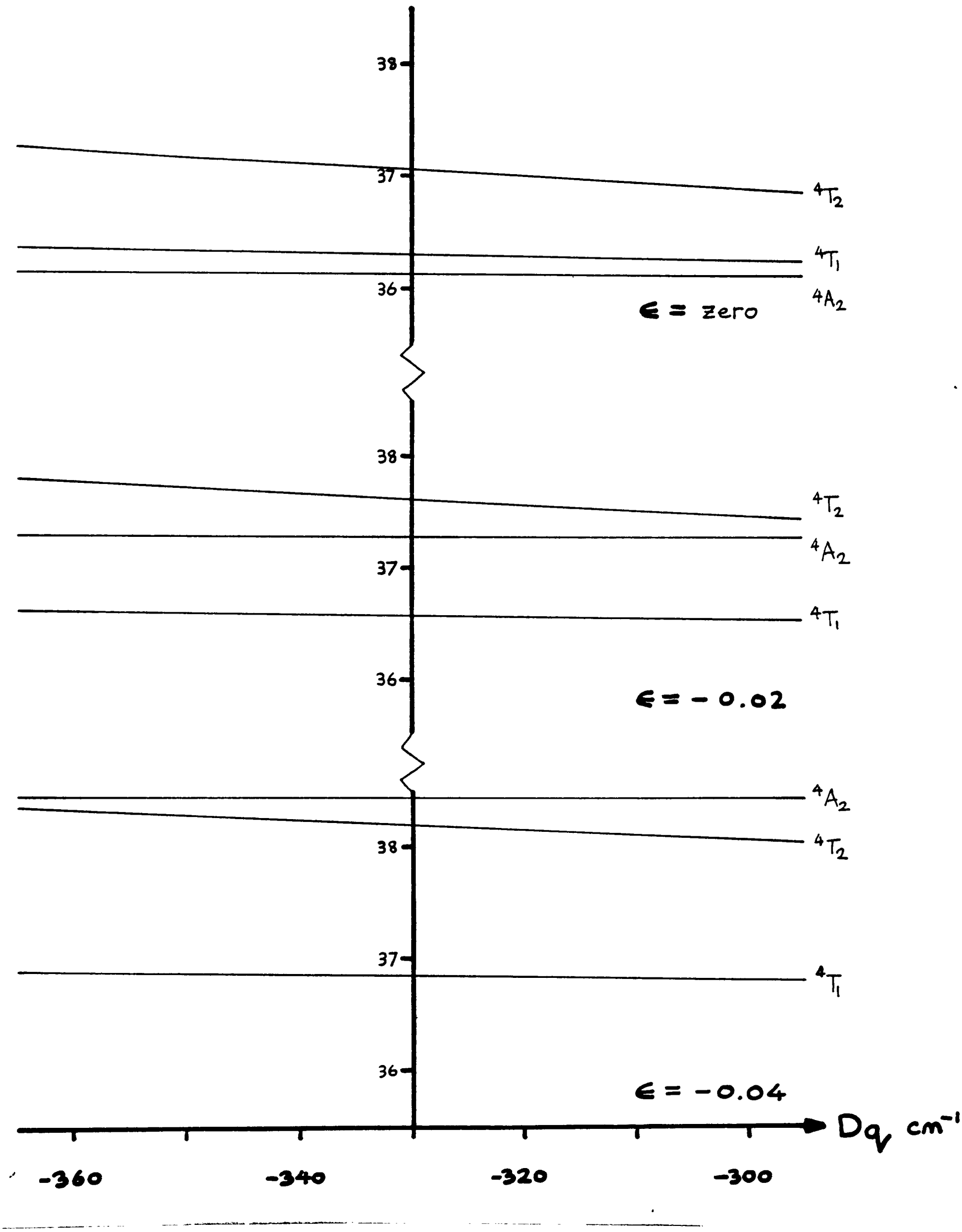

FIGURE 10.

Cs_3MnCl_5 BAND ENERGIES IN REGION VI , ^4F , PLOTTED AS A FUNCTION OF Dq .

B = 650cm^{-1}, C = 2990cm^{-1}, α = 76cm^{-1}.

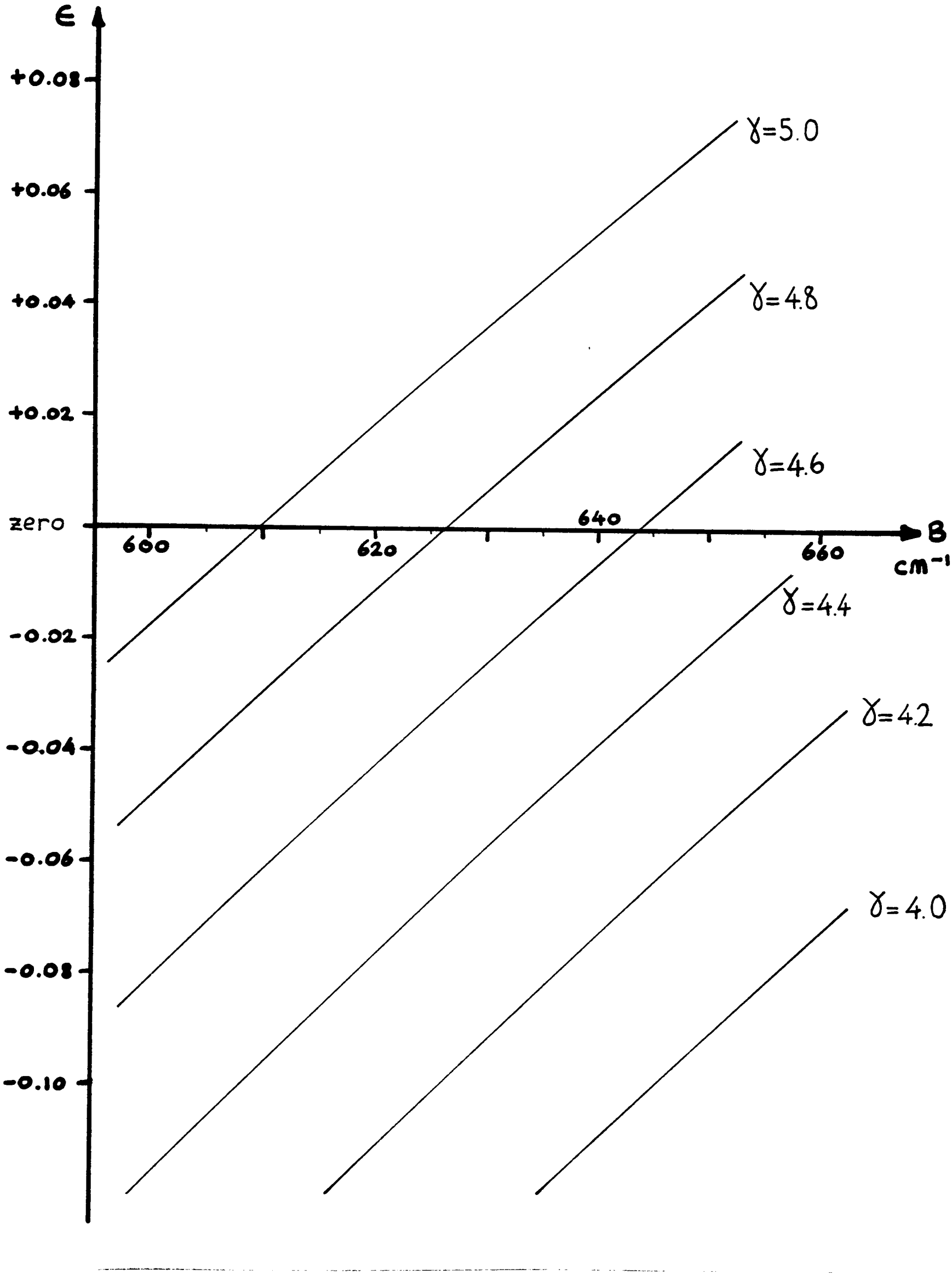

FIGURE 11.

GRAPHICAL SOLUTIONS TO EQUATION (42), GIVING THE CORRECT TOTAL ENERGY FOR ALL TEN $^4\Gamma$ EXCITED STATES OF Cs_3MnCl_5 (for $\alpha = 76cm^{-1}$).

C H A P T E R 6

DETAILED ASSIGNMENT OF THE SPECTRA

6.1 INTRODUCTION

In previous chapters, the intensity mechanism of the spin forbidden $^4\Gamma \leftarrow {}^6A_1$ transitions has been investigated, and the general features and positions of the observed bands have been described. Our aim is now to give a detailed assignment to as many of the individual lines and bands as possible. From FIGURES 7 and 8, it can be seen that the linearly polarised low temperature spectra contain a wealth of detail, in addition to which we have data obtained in the presence of an axial magnetic field and with circularly polarised radiation. The method of assignment was as follows: the electronic origins were located by means of MCD and linear polarisation measurements, after which the majority of the remaining features could be assigned as vibrational sidebands built upon these origins. Finally, the natures of the origins themselves were determined where possible. In the event that spin orbit coupling is the dominant cause of the splitting of a given state into components, the $\Delta d/D$ values calculated in CHAPTER 3 will assist in the origin line assignments. Unfortunately an additional perturbation is present in Cs_3MnCl_5, the low symmetry component of the crystal field, which also has the effect of splitting each state into components and giving rise to linear polarisation. This may dominate over the spin orbit interaction, or the two may be present together giving rise to a more complex behaviour.

6.2 VIBRATIONAL DATA

A study similar to the present one on the isomorphous Cs_3CoBr_5 [70] had shown the value of vibrational data, especially Raman, on the compound itself rather than just the chromophore ion, as lattice modes of the unit cell and acoustic modes of the crystal itself were present. Data relevant to Cs_3MnCl_5 was limited to the internal modes of the $MnCl_4^{2\Theta}$ ion in the crystal $(Et_4N)_2MnCl_4$ [96]:

Raman active ν_1 258 cm^{-1} ν_4 116 cm^{-1}

Infrared active ν_2 78 cm^{-1} ν_3 284 cm^{-1} ν_4 118 cm^{-1}

Accordingly the Raman [97] and Infrared [98] spectra of Cs_3MnCl_5 were recorded, using respectively polarised single crystals on a Cary 81 spectrometer and nujol mulls on a Beckman IR 11. Both sets of spectra were analysed in terms of the known factor group splitting pattern [99]:

$MnCl_4^{2\Theta}$ MODE	T_d ION	D_{2d} SITE	D_{4h} UNIT CELL	ACTIVITY
ν_1	a_1	a_1	a_{1g}	Raman
			b_{1u}	-
ν_2	e	a_1	a_{1g}	Raman
			b_{1u}	-
		b_1	a_{1u}	-
			b_{1g}	Raman
$\nu_3 + \nu_4$	$2t_2$	$2b_2$	$2b_{2g}$	Raman
			$2a_{2u}$	Infrared
		2e	$2e_g$	Raman
			$2e_u$	Infrared

TABLE IX

FACTOR GROUP SPLITTING PATTERN FOR Cs_3MnCl_5

This shows how vibrations of the four $MnCl_4^{2\ominus}$ ions in the unit cell are derived from the four modes of the individual ions. Lattice modes, which involve coupled motions of not only the four $MnCl_4^{2\ominus}$ ions but also the twelve $Cs^{\oplus}$ and four free $Cl^{\ominus}$ ions are not included in the above table. These modes will occur at lower frequencies than those of the chromophore, say below 100 cm^{-1}.

The infrared spectrum of a nujol mull of Cs_3MnCl_5 showed several bands which were assigned by comparison with known data on the isomorphous series Cs_3MCl_5, where M = Fe, Co, Ni, and Cu [100]:

Lattice modes 44, 82, and 92 cm^{-1};

ν_3 270 cm^{-1} (e_u) and 298 cm^{-1} (a_{2u});

ν_4 108 and 120 cm^{-1} (a_{2u} and e_u);

Combinations with ν_1 376, 384, and 392 cm^{-1}.

The Raman spectra were assigned by Thomas [97] on the basis of polarisation behaviour and by comparison with Cs_3CoCl_5 as follows:

MODE	ENERGY cm^{-1}	SYMMETRY
ν_{L1}	18	
ν_{L2}	33	Lattice
ν_{L3}	52	Modes
ν_{L4}	61	
ν_1	277	a_{1g}
ν_2	125	a_{1g}
	148	b_{1g}
ν_3	305	$b_{2g} + e_g$
ν_4	94	b_{2g}
	135	e_g

TABLE X
LINES IN THE RAMAN SPECTRUM OF Cs_3MnCl_5 AT 293K

It is these Raman active modes which couple with the electronic transitions to produce vibrational sidebands, so that the modes and energies tabulated above are important in the full assignment of the spectra.

The above vibrational spectra were recorded at room temperature, while the crystal electronic spectra were measured at 4.2K. Two opposing effects are present which may alter the energy of a given vibrational mode:

(i) Thermal contraction effectively shortens all the bonds and increases vibrational frequencies.

(ii) Change in the force constant brought about as a result of the electronic excitation. Generally, the electronic excited state configuration will contain a larger contribution from non-bonding or anti-bonding orbitals than that of the ground state, and the vibrational frequency in the excited state will be reduced. In addition, the frequency of a mode seen in one electronic band may not be the same as that seen in a different band.

In the observed spectra of Cs_3MnCl_5, the vibrational energies are found to be close to the values given in TABLE X.

6.3 SPECTRA OF INDIVIDUAL $^4\Gamma$ STATES - POLARISATION PROPERTIES

The model used to describe the intensity mechanism and general features of the spectra assumed tetrahedral symmetry for the $MnCl_4^{2\ominus}$ ion, and hence excluded the presence of linear polarisation. However, z-elongation of the ion [2] lowers the point symmetry to D_{2d}, and results in linear polarisation of nearly all the quartet absorption bands. This could have been taken into account by the use of D_{2d} symmetry throughout, but

this complicates the arguments and lengthens the calculations. Alternatively, perturbation theory could be used to add a tetragonal field component together with spin orbit coupling, but again the calculations are lengthened and lose generality.

Several observations can be made about the qualitative effect of the tetragonal field component. If we consider all the components of a particular $^4\Gamma$ state, then the sum of their properties should remain constant (see 3.9). However, individual components may be quite dramatically affected, so that the $\Delta d/D$ values calculated in TABLE V may only be of limited use in making origin assignments. Assuming that the situation can only be described in D_{2d} terms, a linear polarisation scheme can be quite simply produced. The T_d allowed transition to $^6T_2$ becomes split and polarised into $^6B_2(z)$ and $^6E(xy)$ components as shown in 1.2. There are now two separate spin orbit couplings, with matrix elements $\langle {}^6B_2 | \hat{\mathcal{H}}_{soc} | {}^4\Gamma \rangle$ and $\langle {}^6E | \hat{\mathcal{H}}_{soc} | {}^4\Gamma \rangle$ to be evaluated. To a certain degree, it is possible to treat orbital and spin separately; symmetry defines which pairs of orbital functions may be involved in spin orbit coupling, and this will occur between the two states if $\Delta S = 0, \pm 1$, and if the necessary combinations of orbital and spin parts occur in the spinor wavefunctions of the two states. Applying the first test to $^6T_2$ and $^4\Gamma$ in tetrahedral symmetry, we predict that spin orbit mixing may be allowed when $\Gamma = A_2$, E, T_1, or T_2 only. The full calculations of CHAPTER 3 show that this is indeed the case. Extending this argument to D_{2d}, we have:

$\hat{\underset{\sim}{L}}$ transforms as $A_2 + E$, so that $\langle B_2 | \hat{\underset{\sim}{L}} | \Gamma \rangle$ contains A_1 for $\Gamma = B_1$ and E with the A_2 - component of $\hat{\underset{\sim}{L}}$,

and $\langle E | \hat{\underset{\sim}{L}} | \Gamma \rangle$ contains A_1 for $\Gamma = A_1$, A_2, B_1, B_2, and E with the E - component of $\hat{\underset{\sim}{L}}$.

The ΔS condition is also satisfied, so in principle we expect spin orbit mixing of states to confer intensity as follows:

TETRAHEDRAL STATE	D_{2d}	ALLOWED POLARISATIONS
$^4A_1$	$^4A_1$	xy only (α)
$^4A_2$	$^4B_1$	xy and z ($\alpha + \pi$)
^4E	$^4A_1$	xy only (α)
	$^4B_1$	xy and z ($\alpha + \pi$)
$^4T_1$	$^4A_2$	xy only (α)
	^4E	xy and z ($\alpha + \pi$)
$^4T_2$	$^4B_2$	xy only (α)
	^4E	xy and z ($\alpha + \pi$)

TABLE XI

LINEAR POLARISATIONS OF THE $^4\Gamma \leftarrow {}^6A_1$ TRANSITIONS IN TETRAGONAL SYMMETRY

In this tetragonal scheme, the spin orbit splittings of each $^4\Gamma$ state would be added as a small perturbation. Each $^4A_1$, $^4A_2$, $^4B_1$, and $^4B_2$ state gives rise to two Kramers doublets E' + E", while ^4E gives four, 2E' + 2E". Note also that the $^4A_1 \leftarrow {}^6A_1$ transition is allowed. All the above transitions are allowed in xy-polarisation and will have MCD associated with them, but the signs and magnitudes would require considerable effort to calculate.

If the above scheme were to apply, we should expect to observe large splittings of each of the tetrahedral quartet states into its polarised tetragonal components, but the spectra do not conform to this description. Instead, component separations are roughly 1 - 3 times those predicted by Vala [60] from a complete $3d^5$ spin orbit calculation, which implies that the spin orbit and tetragonal field splittings are of comparable magnitudes. In this case, the only appropriate procedure is to diagonalise the matrix of the two interactions, which is beyond the scope of the present work. However, taking a simplified view, quantitative predictions can be made. We can regard the allowed $^6T_2 \longleftarrow {}^6A_1$ transition to be as follows:

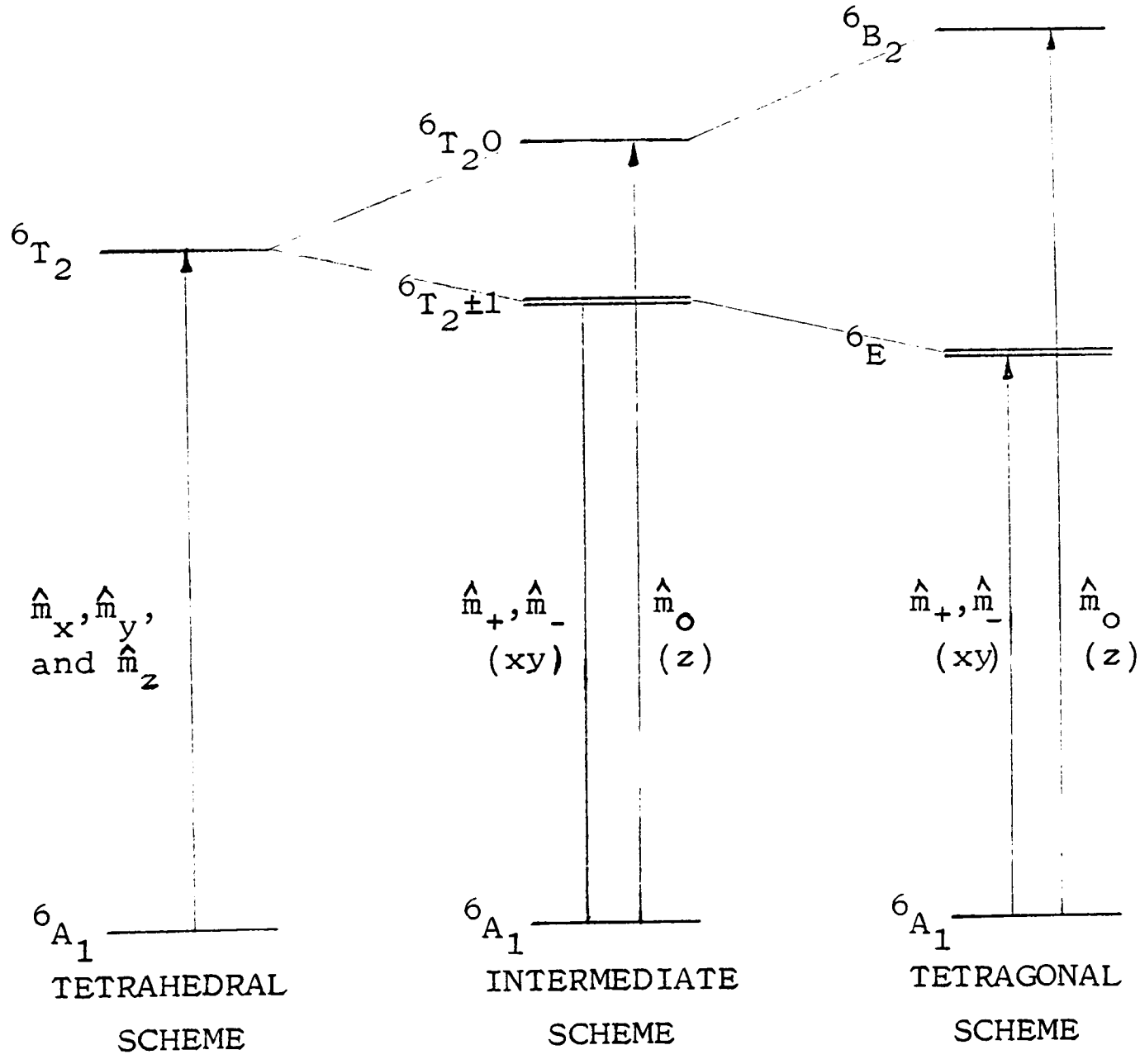

Dealing first with the circular polarisations in an axial magnetic field, the allowed transitions will be:

$$^6T_2{+}1,m_s \longleftarrow {}^6A_1,m_s \quad \text{via } \hat{m}_+ \text{ , LCP ;}$$

and $$^6T_2{-}1,m_s \longleftarrow {}^6A_1,m_s \quad \text{via } \hat{m}_- \text{ , RCP .}$$

The dominant contribution will be from the -5/2 component of the ground state, with a 78.3% population at 4.2K in a 4.75T field. Next most important will be -3/2 with 17.0%, followed by -1/2 with 3.7%. Therefore the MCD of a quartet will be largely determined by the extent to which it mixes via the spin orbit interaction with the -5/2 components of $^6T_2{+}1$ and $^6T_2{-}1$, with smaller contributions from -3/2 and -1/2. The intensity will depend on λ^2, EQUATION (3.13), and hence on $\langle {}^6T_2 | \hat{\mathcal{H}}_{soc} | {}^4\Gamma \rangle^2$. These matrix elements are given in TABLE XII, and were calculated previously by means of EQUATION (3.14). Linear polarisation arises in a similar manner, as mixing with ^6T_2O gives rise to z-intensity, while mixing with $^6T_2{\pm}1$ gives xy:

$$^6T_2O,m_s \longleftarrow {}^6A_1,m_s \quad \text{via } \hat{m}_z \text{ ;}$$

and $$^6T_2{\pm}1,m_s \longleftarrow {}^6A_1,m_s \quad \text{via } \hat{m}_x \text{ and } \hat{m}_y \text{ .}$$

The dipole strength D is given by:

$$D = \frac{1}{d_a} \sum_{j \leftarrow a} |\langle a|\hat{\underset{\sim}{m}}|j\rangle|^2 \qquad \text{EQUATION (2.27)}$$

$$= \frac{1}{6} \sum_{j \leftarrow a} |\langle j|\hat{m}_+|a\rangle|^2 + |\langle j|\hat{m}_-|a\rangle|^2 + |\langle j|\hat{m}_o|a\rangle|^2$$

Writing:

$$D_{xy} = \frac{1}{4} \sum_{j \leftarrow a} |\langle j|\hat{m}_+|a\rangle|^2 + |\langle j|\hat{m}_-|a\rangle|^2$$

and $$D_z = \frac{1}{2} \sum_{j \leftarrow a} |\langle j|\hat{m}_o|a\rangle|^2 \qquad \text{EQUATION (6.1),}$$

we have: $D = \frac{2}{3} D_{xy} + \frac{1}{3} D_z$ EQUATION (6.2),

which can be used in either the tetrahedral or the tetragonal scheme.

Quartet states of the same symmetry type will show the same behaviour, discussed in detail below.

(a) $^4A_1$

As there are no spin orbit coupling matrix elements between $^6T_2$ and $^6A_1$, it can have no intensity derived from first order mixing, and will therefore be weak. It can gain electric dipole intensity through second order interactions with other quartet states, e.g. the nearby $^4E(G)$, or by spin orbit mixing with $^6T_1$ charge transfer states can gain magnetic dipole intensity, as $^6T_1 \longleftarrow {}^6A_1$ is a fully allowed magnetic dipole transition. (Note that in the tetragonal scheme, the $^4A_1 \longleftarrow {}^6A_1$ transition becomes allowed in xy-polarisation.)

(b) $^4A_2$

The MCD of this state will be predominantly +ve because the only connecting element with $^6T_2 \pm 1$ $m_s = -5/2$ is to $^6T_2 + 1$, the element being $1/\sqrt{18}$, see TABLE XII (b). The combined effect of the tetragonal distortion and spin orbit coupling will always be to split the state into two Kramers doublets, cf the ground state of Cs_3CoBr_5 [70], which have the following properties:

E'	$m_s = \pm 3/2$	$D_{xy} = 11/360$	$D_z = 8/360$	$D = 1/36$	$\Delta d = +0.0433$
E''	$m_s = \pm 1/2$	$D_{xy} = 9/360$	$D_z = 12/360$	$D = 1/36$	$\Delta d = +0.0061$
$^4A_2$	overall	$D_{xy} = 1/18$	$D_z = 1/18$	$D = 1/18$	$\Delta d = +0.0494$

(c) ^4E

Within ^4E, there is no first order spin orbit coupling [3], and only small second order interactions with other quartet states will be present [60]. Therefore it is probable that the chief perturbation will be the tetragonal field, and a simple pattern of behaviour is to be expected. The state splits into two components, $^4E\theta$ and $^4E\epsilon$, correlating with $^4A_1$ and $^4B_1$ respectively in D_{2d} symmetry. A further small splitting of each of these into a pair of Kramers doublets may be seen.

Their optical properties are calculated to be as follows:

	E'	$m_s=\pm1/2$	$D_{xy}=9/480$	D_z = zero	D = 9/720	$\Delta d=-0.0046$
$^4E\theta$	E''	$m_s=\pm3/2$	$D_{xy}=11/480$	D_z = zero	D = 11/720	$\Delta d=-0.0324$
	$^4E\theta$	overall	$D_{xy}=1/24$	D_z = zero	D = 1/36	$\Delta d=-0.0370$
	E'	$m_s=\pm3/2$	$D_{xy}=11/1440$	$D_z=32/1440$	D = 9/720	$\Delta d=+0.0108$
$^4E\epsilon$	E''	$m_s=\pm1/2$	$D_{xy}=9/1440$	$D_z=48/1440$	D = 11/720	$\Delta d=+0.0015$
	$^4E\epsilon$	overall	$D_{xy}=1/72$	$D_z=4/72$	D = 1/36	$\Delta d=+0.0123$

(d) $^4T_1$ and (e) $^4T_2$

In the absence of spin orbit splittings, both states are expected to show the same behaviour in linear and circular polarisation:

^4T O	D_{xy} = 1/36	D_z = zero	D = 1/54	Δd = -0.0247 for $^4T_1$, +0.0247 for $^4T_2$.
$^4T\pm1$	D_{xy} = 1/36	D_z = 2/36	D = 2/54	Δd = zero
Sum	D_{xy} = 1/18	D_z = 1/18	D = 1/18	Δd = -0.0247 for $^4T_1$, +0.0247 for $^4T_2$.

The +1 and -1 components of ^4T have equal and opposite Δd values (0.00266) so that the sum is zero. Therefore the largest MCD signal is to be associated with the ^4T 0 component. If there are appreciable spin orbit interactions, this description of the states will no longer hold true, and a more complex behaviour will result. It is then not possible to give a generalised treatment of the two states.

(b) $\Gamma = A_2$

$\hat{H}_{soc}$	$^4A_2$ a_2			
	$+3/2$	$+1/2$	$-1/2$	$-3/2$
$-5/2$				
$+3/2$				
$+1/2$	$\frac{+1}{6\sqrt{5}}$			
$-1/2$		$\frac{+1}{2\sqrt{15}}$		
$-3/2$			$\frac{+1}{\sqrt{30}}$	
$-5/2$				$\frac{+1}{\sqrt{18}}$
$+5/2$				
$+3/2$	$\frac{-1}{3\sqrt{5}}$			
$+1/2$		$\frac{-1}{\sqrt{30}}$		
$-1/2$			$\frac{-1}{\sqrt{30}}$	
$-3/2$				$\frac{-1}{3\sqrt{5}}$
$-5/2$				
$+5/2$	$\frac{+1}{\sqrt{18}}$			
$+3/2$		$\frac{+1}{\sqrt{30}}$		
$+1/2$			$\frac{+1}{2\sqrt{15}}$	
$-1/2$				$\frac{+1}{6\sqrt{5}}$
$-3/2$				
$-5/2$				

$^6T_2$ $+1$ | $^6T_2$ 0 | $^6T_2$ -1

(c) $\Gamma = E$

$\hat{H}_{soc}$	^4E θ				^4E ϵ			
	$+3/2$	$+1/2$	$-1/2$	$-3/2$	$+3/2$	$+1/2$	$-1/2$	$-3/2$
$+5/2$	$\frac{+1}{2\sqrt{6}}$							
$+3/2$		$\frac{+1}{2\sqrt{10}}$						
$+1/2$			$\frac{+1}{4\sqrt{5}}$		$\frac{-1}{12\sqrt{5}}$			
$-1/2$				$\frac{+1}{4\sqrt{15}}$		$\frac{-1}{4\sqrt{15}}$		
$-3/2$							$\frac{-1}{2\sqrt{30}}$	
$-5/2$								$\frac{-1}{6\sqrt{2}}$
$+5/2$								
$+3/2$					$\frac{-1}{3\sqrt{5}}$			
$+1/2$						$\frac{-1}{\sqrt{30}}$		
$-1/2$							$\frac{-1}{\sqrt{30}}$	
$-3/2$								$\frac{-1}{3\sqrt{5}}$
$-5/2$								
$+5/2$					$\frac{-1}{6\sqrt{2}}$			
$+3/2$						$\frac{-1}{2\sqrt{30}}$		
$+1/2$	$\frac{+1}{4\sqrt{15}}$						$\frac{-1}{4\sqrt{15}}$	
$-1/2$		$\frac{+1}{4\sqrt{5}}$						$\frac{-1}{12\sqrt{5}}$
$-3/2$			$\frac{+1}{2\sqrt{10}}$					
$-5/2$				$\frac{+1}{2\sqrt{6}}$				

$^6T_2$ $+1$ | $^6T_2$ 0 | $^6T_2$ -1

TABLE XII .

SPIN ORBIT COUPLING BETWEEN $^6T_2$ AND $^4\Gamma$ IN UNITS OF $\langle T_2 \| \sum su \| \Gamma \rangle$.

(a) $\Gamma = A_1$, all elements zero .

(b) $\Gamma = A_2$.

(c) $\Gamma = E$.

(d) $\Gamma = T_1$, see overleaf .

(e) $\Gamma = T_2$, see overleaf .

$\hat{\mathcal{H}}_{SOC}$		$^4T_1$ +1				$^4T_1$ 0				$^4T_1$ −1			
		+3/2	+1/2	−1/2	−3/2	+3/2	+1/2	−1/2	−3/2	+3/2	+1/2	−1/2	−3/2
$^6T_2$ +1	+5/2					$\frac{+1}{6}$							
	+3/2						$\frac{+1}{2\sqrt{15}}$			$\frac{-1}{3\sqrt{10}}$			
	+1/2							$\frac{+1}{2\sqrt{30}}$			$\frac{-1}{2\sqrt{15}}$		
	−1/2								$\frac{+1}{6\sqrt{10}}$			$\frac{-1}{2\sqrt{15}}$	
	−3/2												$\frac{-1}{3\sqrt{10}}$
	−5/2												
$^6T_2$ 0	+5/2									$\frac{-1}{6}$			
	+3/2										$\frac{-1}{2\sqrt{15}}$		
	+1/2	$\frac{+1}{6\sqrt{10}}$										$\frac{-1}{2\sqrt{30}}$	
	−1/2		$\frac{+1}{2\sqrt{30}}$										$\frac{-1}{6\sqrt{10}}$
	−3/2			$\frac{+1}{2\sqrt{15}}$									
	−5/2				$\frac{+1}{6}$								
$^6T_2$ −1	+5/2												
	+3/2	$\frac{+1}{3\sqrt{10}}$											
	+1/2		$\frac{+1}{2\sqrt{15}}$			$\frac{-1}{6\sqrt{10}}$							
	−1/2			$\frac{+1}{2\sqrt{15}}$			$\frac{-1}{2\sqrt{30}}$						
	−3/2				$\frac{+1}{3\sqrt{10}}$			$\frac{-1}{2\sqrt{15}}$					
	−5/2								$\frac{-1}{6}$				

(d) $\Gamma = T_1$

TABLE XII continued .

$\hat{\mathcal{H}}$ soc		$^4T_2+1$				$^4T_2\,0$				$^4T_2-1$			
		$+3/2$	$+1/2$	$-1/2$	$-3/2$	$+3/2$	$+1/2$	$-1/2$	$-3/2$	$+3/2$	$+1/2$	$-1/2$	$-3/2$
	$+5/2$												
	$+3/2$	$\frac{-1}{3\sqrt{10}}$											
$^6T_2+1$	$+1/2$		$\frac{-1}{2\sqrt{15}}$			$\frac{-1}{6\sqrt{10}}$							
	$-1/2$			$\frac{-1}{2\sqrt{15}}$			$\frac{-1}{2\sqrt{30}}$						
	$-3/2$				$\frac{-1}{3\sqrt{10}}$			$\frac{-1}{2\sqrt{15}}$					
	$-5/2$								$\frac{-1}{6}$				
	$+5/2$	$\frac{+1}{6}$											
	$+3/2$		$\frac{+1}{2\sqrt{15}}$										
$^6T_2\,0$	$+1/2$			$\frac{+1}{2\sqrt{30}}$						$\frac{-1}{6\sqrt{10}}$			
	$-1/2$				$\frac{+1}{6\sqrt{10}}$						$\frac{-1}{2\sqrt{30}}$		
	$-3/2$											$\frac{-1}{2\sqrt{15}}$	
	$-5/2$												$\frac{-1}{6}$
	$+5/2$					$\frac{+1}{6}$							
	$+3/2$						$\frac{+1}{2\sqrt{15}}$			$\frac{+1}{3\sqrt{10}}$			
$^6T_2-1$	$+1/2$							$\frac{+1}{2\sqrt{30}}$			$\frac{+1}{2\sqrt{15}}$		
	$-1/2$								$\frac{+1}{6\sqrt{10}}$			$\frac{+1}{2\sqrt{15}}$	
	$-3/2$												$\frac{+1}{3\sqrt{10}}$
	$-5/2$												

(e) $\Gamma = T_2$

TABLE XII continued .

6.4 REGION I, $^4T_1(G)$

This band lies between 5100 and 4600A, and is among the broadest of the quartets of Cs_3MnCl_5 - see FIGURES 7 and 8. In the Strong Field formalism, $^4T_1(G)$ correlates with an $e^3t_2^2$ electron configuration whereas the ground state arises from $e^2t_2^3$. As a general rule, transitions between states of different electronic configuration are broad, so the large width of $^4T_1(G)$ can be readily explained.

The three low temperature spectra shown in FIGURE 12 are composed of overlapping broad lines without any discernable vibrational structure. The energies of the features which can be distinguished are given below:

$\alpha = \sigma$ (xy)	MCD	π (z)
		20,300 cm^{-1} (shoulder)
		20,620 cm^{-1}
20,700 cm^{-1}		
		20,840 cm^{-1} (shoulder)
21,140 cm^{-1}		
		21,190 cm^{-1} (shoulder)
	21,230 cm^{-1}	
21,410 cm^{-1} (shoulder)	21,410 cm^{-1}	

TABLE XIII

FEATURES IN THE SPECTRA OF $^4T_1(G)$ AT 4.2K

The linear polarisation is strong, indicating that the state is heavily perturbed by the tetragonal distortion, and it is not appropriate to attempt to make origin assignments based on the tetrahedral model. In spite of the perturbation, the

observed and calculated values of $\Delta d/D$ agree quite closely - see TABLE VI.

The appearance of $^4T_1(G)$ is well explained using the tetragonal model outlined in 6.3 above. At low energy is found ^4E, correlating with $^4T_1 \pm 1$, which is more intense in z- than in xy-polarisation but has no MCD. Most probably, ^4E gives rise to all the features of the π-spectrum, and also to the 20700 cm^{-1} peak in σ. To higher energy lies $^4A_2$, correlating with $^4T_1$ 0, allowed xy-only and giving rise to the 21140 and 21410 cm^{-1} σ peaks. All the MCD is associated with $^4A_2$, and is negative as predicted; it follows the axial absorption shape quite closely. Qualitatively, this description of $^4T_1(G)$ is a good one, but in quantitative terms it is less satisfying. For example, the z:xy intensity ratio for ^4E is predicted to be 2:1, but is observed to be much larger; indeed, the ratio for the whole band is over 3:1 while it should be only 1:1. Again, in xy-polarisation ^4E and $^4A_2$ should be of equal intensity, but $^4A_2$ is observed to be more intense by a factor of about 2. These discrepancies arise because we have treated the situation as having perturbed tetrahedral symmetry rather than working in D_{2d} from the outset. Although $^4T_1$ 0 correlates with $^4A_2$ and $^4T_1 \pm 1$ correlates with ^4E, the transition intensities will not be exactly the same. In the first case, transition intensities to the 0, ± 1 components of $^4T_1$ can be given in terms of $\langle {}^6T_2 \| \sum su \| {}^4T_1 \rangle^2$, but those to $^4A_2$ and ^4E will be in terms of two different reduced matrix elements, $\langle {}^6T_2 \| \sum su \| {}^4A_2 \rangle^2$ and $\langle {}^6T_2 \| \sum su \| {}^4E \rangle^2$. Also, the wavefunctions used in the two situations will be different.

Vala's studies of $(R_4N)_2MnCl_4$ crystals show that the $^4T_1(G)$ band is broad; unfortunately, no linear polarisation data is available for comparative purposes. The MCD of $(Et_4N)_2MnCl_4$ is negative in this region, and few features can be distinguished [63]. In $(Me_4N)_2MnBr_4$, the luminescence was shown to be due to $^4T_1(G) \longrightarrow {}^6A_1(S)$ emission [60], and presumably Cs_3MnCl_5 behaves in the same way. This could explain the colour as seen with the naked eye: pale yellow under ordinary conditions, but acquiring a greenish tinge in strong sunlight. Emission from $^4T_1(G)$ should occur at around 5100Å, which is in the green part of the visible spectrum at a wavelength where the eye is quite sensitive as a photodetector.

FIGURE 12.

SPECTRA OF REGION I, $^4T_I(G)$.

6.5 REGION II, $^4T_2(G)$

Here, the absorption lines are reasonably narrow, and vibrational structure is seen. The low temperature spectra are shown in FIGURES 13 and 14, and can be assigned in terms of four electronic origins as follows:

$\alpha = \sigma(xy)$			MCD			π (z)		
ENERGY cm^{-1}	ASSIGNMENT	VIBRL.MODE	ENERGY cm^{-1}	ASSIGNMENT	VIBRL.MODE	ENERGY cm^{-1}	ASSIGNMENT	VIBRL.MODE
21872	A	-	21875	A	-	21872	A	-
						21891	B	-
21901	C	-						
						21949	B+58	ν_{L4}
						21982	B+91	$\nu_4(b_{2g})$
21993	C+92	$\nu_4(b_{2g})$	22006	C+105	$\nu_4(b_{2g})$			
22041	C+140	$\nu_4(e_g)$	22060	C+159	$\nu_4(e_g)$			
						22046	B+155	$\nu_2(b_{1g})$
22095	C+194	$2\nu_4(b_{2g})$	22106	C+205	$2\nu_4(b_{2g})$			
						22163	B+272	$\nu_1(a_{1g})$
22173	D	-	22169	D	-			
						22232	B+ν_1+69	ν_{L4}
22237	D+64	ν_{L4}	22235	D+66	ν_{L4}			
22267	D+94	$\nu_4(b_{2g})$	22276	D+107	$\nu_4(b_{2g})$			
						22272	B+ν_1+109	$\nu_4(b_{2g})$
22316	D+143	$\nu_4(e_g)$	22321	D+152	$\nu_4(e_g)$			
						22326	B+ν_1+163	$\nu_2(b_{1g})$
22371	D+198	$2\nu_4(b_{2g})$	22388	D+219	$2\nu_4(b_{2g})$			
						22437	B+546	$2\nu_1(a_{1g})$
22447	D+274	$\nu_1(a_{1g})$	22447	D+278	$\nu_1(a_{1g})$			
						22502	B+2ν_1+65	ν_{L4}
22507	D+ν_1+60	ν_{L4}	22516	D+ν_1+69	ν_{L4}			
						22548	B+2ν_1+111	$\nu_4(b_{2g})$
22553	D+ν_1+106	$\nu_4(b_{2g})$	22559	D+ν_1+112	$\nu_4(b_{2g})$			
						22559	B+2ν_1+162	$\nu_2(b_{1g})$
						22712	B+821	$3\nu_1(a_{1g})$
22722	D+551	$2\nu_1(a_{1g})$	22725	D+558	$2\nu_1(a_{1g})$			
22789	D+2ν_1+67	ν_{L4}						

TABLE XIV

FEATURES IN THE SPECTRA OF $^4T_2(G)$ AT 4.2K

In axial absorption, the energy difference between origins C and D is 272 cm^{-1} which is very close to the ν_1 frequency. However, if D is assigned as C + ν_1, it becomes very difficult to give a description of the MCD and the linear polarisation without making additional assumptions.

Origin A appears as a shoulder at about 21872 cm^{-1} in both α- and π-spectra, and has a -ve MCD signal at 21875 cm^{-1} associated with it. The intense origin B gives rise to the whole of the π-spectrum barring A, but appears to have no MCD. Sidebands of B due to ν_{L4}, ν_4 (b_{2g} component), and $\nu_2(b_{2g})$ are present, superimposed on a 3-phonon progression in ν_1. The strong line B+ν_1 is very close in energy to origin D, but as the pattern and relative intensities of the sidebands built on B+ν_1 are the same as those built on B itself, it is concluded that D makes no significant contribution to the π-spectrum. For similar reasons of sideband structure, we believe that B makes no significant contribution to the α-spectrum. Origin C appears at 21901 cm^{-1} in α only, and is less intense than B or D. It couples strongly with the ν_4 mode so that two quanta of the b_{2g} component are seen, and one of the e_g. Further sidebands of C are lost under the stronger features due to D. In MCD, C gives rise to some weak +ve signals which are in part cancelled out by -ve contributions from A. Origin D is present in α only and dominates that spectrum below 4510Å. Its intensity is probably augmented by C+ν_1 lying at almost the same energy. In contrast with the other origins, D has a large MCD signal, of positive sign. D couples to both components of ν_4 and to ν_{L4}, and the pattern has two ν_1 repeats.

The tetrahedral model of $^4T_2$ predicts that of the four spin orbit components, only three contribute to the intensity (TABLE V). All the MCD should be +ve, and there should be no linear polarisation. Although these features are not seen in the spectra of $^4T_2(G)$, the predicted $\Delta d/D$ value agrees well with that observed (TABLE VI). The observed pattern is in fact similar to $^4T_1(G)$, but with a smaller amount of tetragonal splitting: origins A,B, and C are spin orbit components of ^4E, correlating with $^4T_2 \pm 1$ as outlined in 6.3, while at higher energy D contains the spin orbit components of $^4B_2$ (correlating with $^4T_2$ 0). In agreement with the model, ^4E is more intense in z- than xy-polarisation, and has no nett MCD although small signals of opposite sign are present. On the other hand, $^4B_2$ is only xy-allowed, and has a large positive MCD. The separation between ^4E and $^4B_2$, caused by the tetragonal field, is about 285 cm^{-1}, and this is to be compared with the spin orbit splittings apparent within ^4E itself of about 30 cm^{-1}. The E-B_2 separation in $^4T_2(G)$ is appreciably less than the E-A_2 separation of $^4T_1(G)$, so that the quantitative results of the tetragonal perturbation model of 6.3 should give better agreement in the former than in the latter. This is found to be true. For $^4T_2(G)$, the overall xy:z intensity ratio is close to the predicted 1:1 value (TABLE VI). The z:xy ratio of ^4E should be 2:1, very close to the observed B:C extinction ratio of 1.77, and its MCD shows evidence of the presence of cancelling +ve and -ve contributions, especially around 4560Å. $^4B_2$ gives rise to all the strong MCD as predicted and has no significant z-intensity. In xy, it appears to be of comparable intensity to ^4E, although this is hard to

assess accurately because of the accidental near-degeneracy of D and C+ν_1, and the overlap of the bands.

The $^4T_2(G)$ band observed by Vala in $(Me_4N)_2MnCl_4$ resembles the Cs_3MnCl_5 α-spectrum, with its intensity maximum near the centre, but has less resolved vibrational structure. In the corresponding bromide, the band is more structured but otherwise similar [60]. Unfortunately, no linear polarisation data is available for comparison. The MCD of $(Et_4N)_2MnCl_4$ is all positive, and shows clear vibrational structure built on two origins about 60 cm^{-1} apart. The higher energy origin near 22130 cm^{-1} is about ten times more intense in MCD, and could be the $^4B_2$ component. The MCD of the bromide appears to resemble that of Cs_3MnCl_5 quite closely, but overlaps with $^4T_1(G)$ to lower energy [63]. Under the conditions used, 6.6K and 0.7T, only +ve MCD would be expected from the C/D values for $^4T_2$ (TABLE V). No sign changes were observed on lowering the temperature to 1.7K.

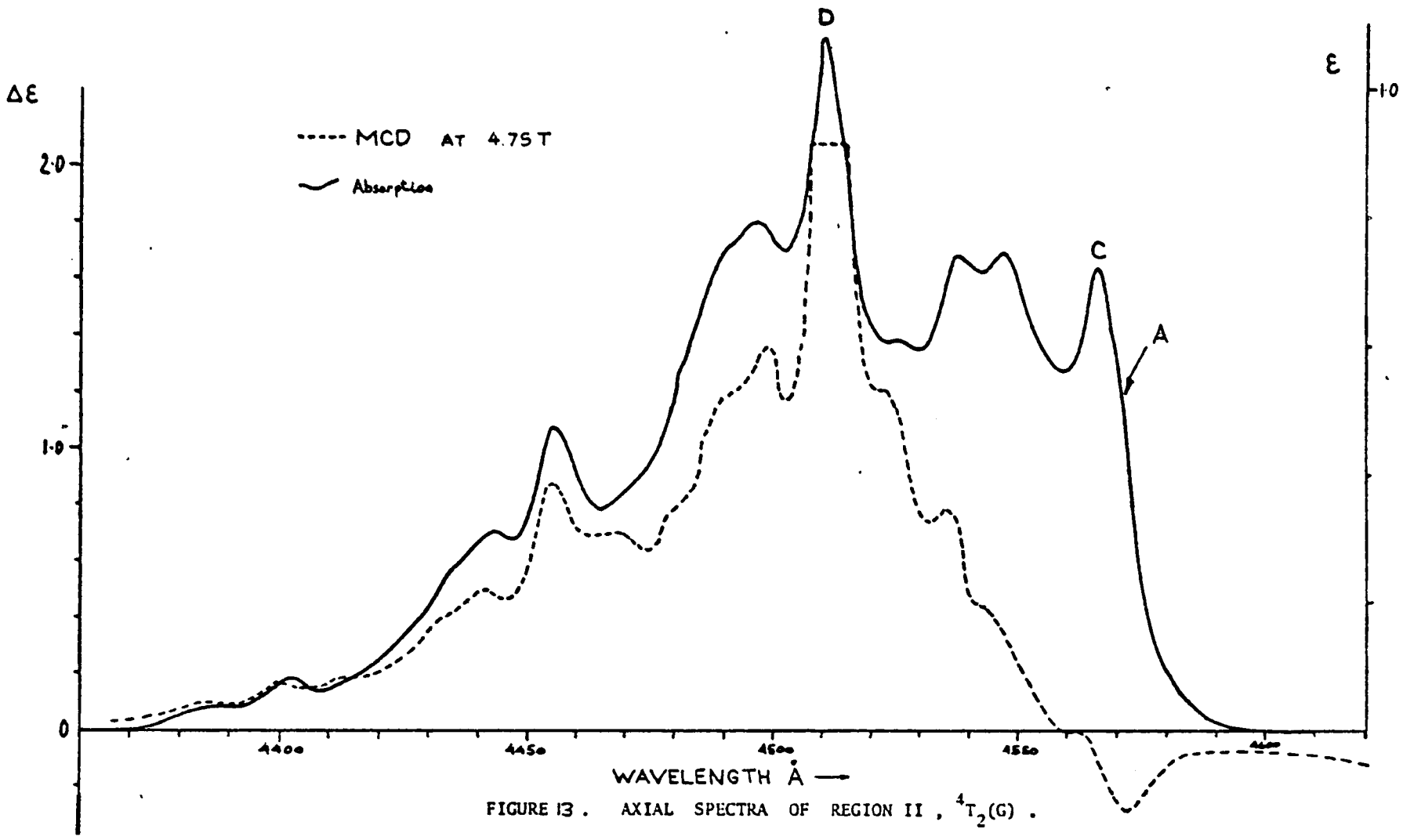

FIGURE 13. AXIAL SPECTRA OF REGION II, $^4T_2(G)$.

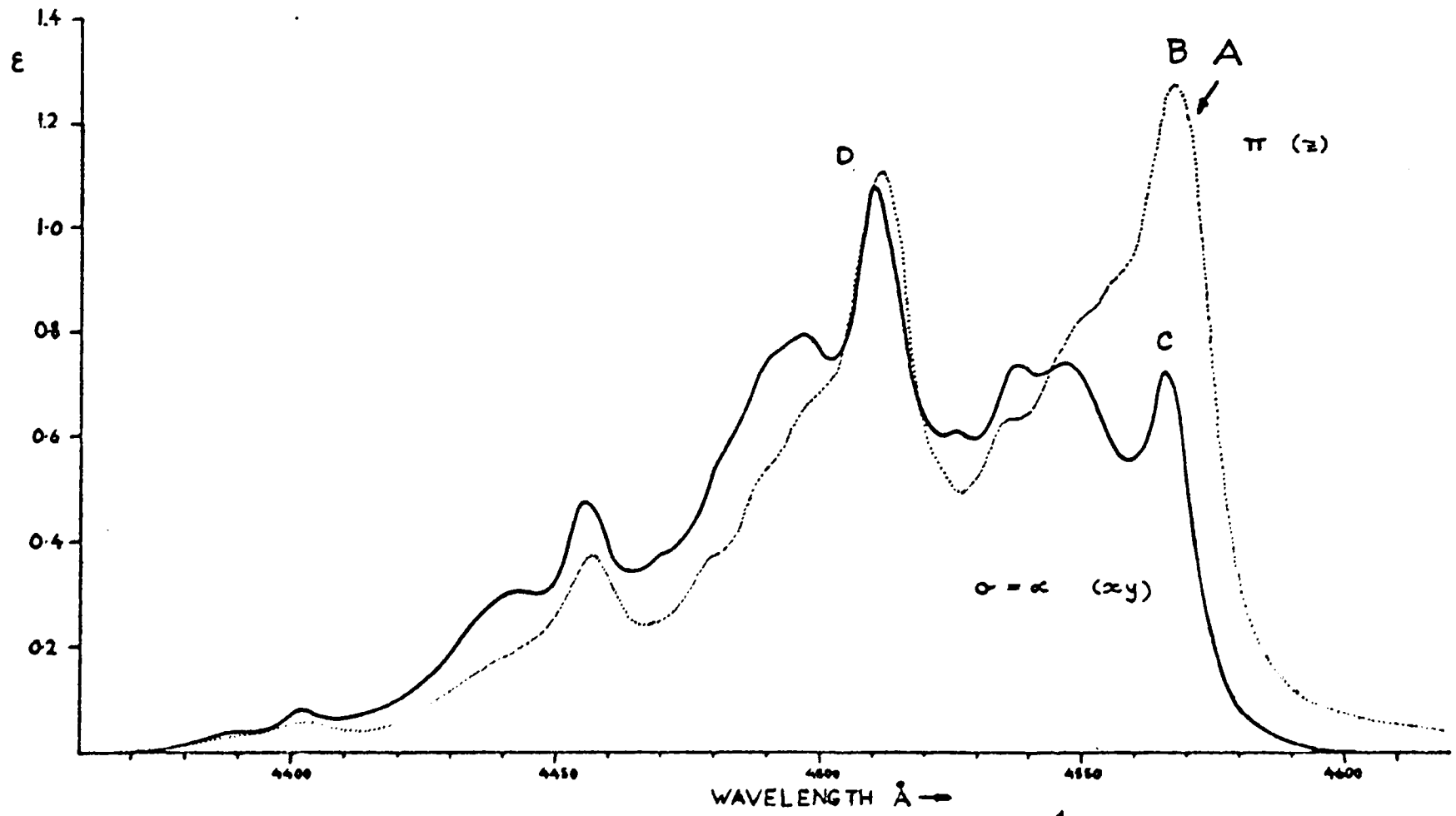

FIGURE 14. POLARISED SPECTRA OF REGION II, $^4T_2(G)$.

6.6 REGION III, $^4A_1$ and $^4E(G)$

The spectra of many Mn(II) compounds show a good deal of fine structure associated with sharp line transitions to $^4A_1$ and ^4E excited states derived from the free ion ^4G. The two states are degenerate to a first approximation. In octahedral coordination, the transitions are vibronically assisted, and the pure electronic 0 - 0 origins are very weak and difficult to identify as they are magnetic dipole transitions. In cases where they have been positively identified, e.g. for Mn^{2+} doped into $KMgF_3$ and $KZnF_3$ [50], the two are of comparable intensities. In tetrahedral coordination, only ^4E is expected to have appreciable intensity as there is no spin orbit mixing between $^4A_1$ and $^6T_2$ in T_d*. However, $^4A_1$ may acquire some small intensity through second order mixing with U' from $^4E(G)$, and is able to gain magnetic dipole intensity through spin orbit mixing with $^6T_1$. In tetragonal symmetry, $^4A_1$ may be allowed in xy-polarisation.

The low temperature spectra are shown in FIGURES 15 and 16. Two electronic origins, designated P and Q, are seen, with respectively positive and negative MCD. Both origins show a small splitting into two equal intensity components, peak separations 2.6 cm^{-1} in P and about 4.2 cm^{-1} in Q. These origin lines are shown in detail in FIGURES 17 and 18. Assignment of the other lines in the band was made on the basis of the following observation. The MCD spectrum has only three strongly positive features, P with two quanta of the ν_1 vibration. All the rest is negative, and can be assigned as Q with

vibrational sidebands. (Note that the resolution here was only 1Å, about 6 cm^{-1}, so that less structural detail is seen in the MCD spectrum.) The π-spectrum is dominated by P, which couples only weakly with lattice and chromophore vibrations apart from ν_1. The full assignment is given below:

$\alpha(xy)$			MCD			$^1\pi(z)$		
ENERGY cm^{-1}	ASSIGN-MENT	VIBRL. MODE	ENERGY cm^{-1}	ASSIGN-MENT	VIBRL. MODE	ENERGY cm^{-1}	ASSIGN-MENT	VIBRL. MODE
22903.2 22905.8	P	-	22901 (-) 22912 (+)	P	-	22903.2 22905.8	P	-
22920.5 22924.2	P+17.9	ν_{L1}				22921.6 22925.2	P+18.9	ν_{L1}
						22932.1 22934.7	P+28.9	ν_{L2}
22939.0 22942.6	Q	-	22938 (+) 22952 (-)	Q	-	22938.4 22942.6	Q	-
22951.0 22956.8	P+49.4	ν_{L3}				22951.6 22955.8	P+49.2	ν_{L3}
22960.0 22963.2	P+57.1	ν_{L4}				22960.5 22963.7	P+57.6	ν_{L4}
22970.0 22974.8	Q+31.6	ν_{L2}	22982 (-)	Q+30	ν_{L2}	22969.0 22973.2	Q+30.6	ν_{L2}
22981.1 22986.4						22980.6		
22995.4	Q+54.6	ν_{L3}				22999.1	Q+58.6	ν_{L3}
23003.3	Q+62.5	ν_{L4}	23012 (-)	Q+60	ν_{L4}	23008.6	Q+68.1	ν_{L4}
23028.8 23034.6	Q+90.9	$\nu_4(b_{2g})$	23041 (-)	Q+89	$\nu_4(b_{2g})$	23028.3 23032.5 23036.0	Q+91.8	$\nu_4(b_{2g})$
23055.3	Q+114.5	$2\nu_{L4}$				23053.7 23056.3	Q+114.5	$2\nu_{L4}$
23063.3	Q+122.5	$\nu_2(a_{1g})$	23063 (-)	Q+111	$2\nu_{L4}+\nu_2$			
23081.4 23089.4	Q+144.6	$\nu_2(b_{1g})$	23092 (-)	Q+140	$\nu_2(b_{1g})$			
						23097.4		
23111.8	Q+171.0	$3\nu_{L4}$	23114 (-)	Q+162	$3\nu_{L4}$			
23134.8 23145.5			23142 (-)			23137.4		

TABLE XV .

LINES IN THE LOW TEMPERATURE SPECTRA OF REGION III , AE(G) .

(The table continues overleaf)

α (xy)			MCD			π (z)		
ENERGY cm^{-1}	ASSIGN-MENT	VIBRL. MODE	ENERGY cm^{-1}	ASSIGN-MENT	VIBRL. MODE	ENERGY cm^{-1}	ASSIGN-MENT	VIBRL. MODE
23179.3 23182.0 23184.1 23186.8	P+278.6	$\nu_1(a_{1g})$	23191 (+)	P+279	$\nu_1(a_{1g})$	23180.3 23182.5 23184.1 23186.8	P+278.9	$\nu_1(a_{1g})$
23196.5 23198.6 23202.4	P+ν_1+20.6	ν_{L1}				23197.0 23199.6	P+ν_1+15.0	ν_{L1}
23214.8 23217.5 23219.6 23220.7 23223.4	Q+278.4	$\nu_1(a_{1g})$	23229 (-)	Q+277	$\nu_1(a_{1g})$	23219.1	Q+278.6	$\nu_1(a_{1g})$
23233.1	P+ν_1+50.0	ν_{L3}				23231.5 23235.3	P+ν_1+50.0	ν_{L3}
23247.8	Q+ν_1+28.5	ν_{L2}	23251 (-)	Q+ν_1+22	ν_{L1} or ν_{L2}	23245.0	P+ν_1+61.6	ν_{L4}
23265.0	Q+ν_1+45.8	ν_{L3}						
23280.7	Q+ν_1+61.5	ν_{L4}	23297 (-)	Q+ν_1+68	ν_{L4}	23285.6	Q+ν_1+66.5	ν_{L4}
23311.1	Q+ν_1+91.9	$\nu_4(b_{2g})$	23323 (-)	Q+ν_1+94	$\nu_4(b_{2g})$	23309.0	Q+ν_1+89.9	$\nu_4(b_{2g})$
23332.9	Q+ν_1+113.7	$2\nu_{L4}$	23344 (-)	Q+ν_1+115	$2\nu_{L4}$	23332.3	Q+ν_1+113.2	$2\nu_{L4}$
23341.0	Q+ν_1+121.8	$\nu_2(a_{1g})$						
23364.5	Q+ν_1+145.3	$\nu_2(b_{1g})$						
23387.4	Q+ν_1+168.2	-						
23411.5	Q+ν_1+192.3	-						
23423.0	Q+ν_1+203.8	-						
23450.0 23453.8 23457.1 23461.0 23465.9 23465.9	P+553.1	$2\nu_1(a_{1g})$	23459 (+)	P+547	$2\nu_1(a_{1g})$	23448.9 23452.7 23456.6 23461.0 23464.8 23467.6	P+553.0	$2\nu_1(a_{1g})$
23471.4 23475.8	P+2ν_1+16.0	ν_{L1}				23470.3 23473.1	P+2ν_1+13.1	ν_{L1}
23485.8 23489.6 23493.5 23497.9 23502.9 23508.9	Q+555.4	$2\nu_1(a_{1g})$	23497 (-)	Q+545	$2\nu_1(a_{1g})$	23488.0 23490.7	Q+548.3	$2\nu_1(a_{1g})$
23519.5	Q+2ν_1+23.1	ν_{L1}	23519 (-)	Q+2ν_1+22	ν_{L1}			
23556.0	Q+2ν_1+59.6	ν_{L4}	23556 (-)	Q+2ν_1+69	ν_{L4}			
23587.7	Q+2ν_1+91.3	$\nu_4(b_{2g})$	23587 (-)	Q+2ν_1+90	$\nu_4(b_{2g})$			
23608.3	Q+2ν_1+111.9	$2\nu_{L4}$	23604 (-)	Q+2ν_1+107	$2\nu_{L4}$			

TABLE XV .

LINES IN THE LOW TEMPERATURE SPECTRA OF REGION III, AE(G).

(Continued from page 117)

The full σ-spectrum is not listed above as it resembles the axial but with differing P and Q intensities - see FIGURE 18 for origin details. Many of the lines in the table are entered under a single assignment. Often, they occur in pairs: a single vibration built onto the two components of P or Q. A clear example of this is seen in FIGURE 17, where the two small features in the absorption spectrum between P and Q - at 22920.5 and 22924.4 cm^{-1} - are assigned as P + 17.9 cm^{-1}, ν_{L1}. This pairing appears to be characteristic when a lattice mode is involved. More remarkable is the situation where a higher energy chromophore vibration is involved, especially ν_1, when 4, 5, or even 6 discrete lines can be seen. We have attributed this phenomenon to the presence of the two chlorine isotopes of masses 35 and 37 [101]. Taking the abundance ratio to be 3:1 in favour of the lighter isotope, and assuming a random distribution among the $MnCl_4^{2\ominus}$ units, five species with the following relative abundances are found:

$Mn(^{35}Cl)_4$	$Mn(^{35}Cl)_3(^{37}Cl)$	$Mn(^{35}Cl)_2(^{37}Cl)_2$	$Mn(^{35}Cl)(^{37}Cl)_3$	$Mn(^{37}Cl)_4$
32	42	20	4	0.3

In reference [101], we showed the effect when a single sharp origin line was involved, the 3947.5A line of $^4T_2(D)$ - not $^4E(D)$ as printed. In the ν_1 sideband, four peaks could clearly be seen with an average separation of 2.1 cm^{-1}. This is in good agreement with the simplest model: the Mn atom remains stationary, tetrahedral symmetry is retained, and the vibrational frequency varies as the square root of the reduced mass.

Assuming that the Raman value for ν_1, 277 cm^{-1}, corresponds to the most abundant of the five species above, the average splitting is calculated to be 1.91 cm^{-1}. In the $2\nu_1$ sideband, the splitting should double; only three lines were observed, due to the high abundance species, and the average separation was 4.5 cm^{-1}, again in good agreement with the theory.

The same simple model provides an explanation of the appearance of the ν_1 sidebands of P and Q, where the additional factor of the splittings of the two origins must be considered. Assuming that the five ν_1 frequencies are $2cm^{-1}$ apart, and that P and Q are split by $2cm^{-1}$ and $4cm^{-1}$ respectively, then one finds:

BAND	NUMBER OF LINES	SEPARATION	INTENSITY RATIOS
P $+\nu_1$	6	2 cm^{-1}	32:74:62:24:4.3:0.3
P + $2\nu_1$	10	2 cm^{-1}	32:32:42:42:20:20:4:4:0.3:0.3
Q + ν_1	7	2 cm^{-1}	32:42:52:46:20:4:0.3
Q + $2\nu_1$	6	4 cm^{-1}	32:74:62:24:4.3:0.3

The predicted pattern of lines is shown superimposed on the observed bands in FIGURE 19, where there is reasonable agreement between calculated and observed relative intensities, and a good fit between the pattern of lines and the observed sideband shape. It seems likely that the vibrational isotope effect gives rise to the observed structuring of other sidebands seen in this region.

Of all the lines shown in FIGURES 15 and 16, only a handful remain unassigned:

weak features at 22980.6 cm^{-1}(π), and 22981.1 and 22986.4 cm^{-1} (α); a broad weak line at 23097.4 cm^{-1} (π); weak lines at 23134.8 and 23145.5 cm^{-1} (α), with associated -ve MCD at 23142 cm^{-1}, and a broad weak line at 23137.4 cm^{-1} (π). If one assumes that P and Q contain the components of ^4E, then this last set of features could be assigned as $^4A_1$. The energy fits the crystal field calculations of CHAPTER 5, which placed $^4A_1$ about 150 cm^{-1} above ^4E, whereas this assignment gives a gap of about 220 cm^{-1}. Assuming that $^4A_1$ borrows intensity from U' of ^4E, it would be predicted to be associated with a -ve MCD signal, and to be weak.

A good account has now been given of the fine structure seen in REGION III apart from the assignment of the origins P and Q. The linear polarisations are strong and clear cut, and indicate that it is the tetragonal perturbation which is dominant over spin orbit coupling. The observed behaviour fits exactly with that predicted in 6.3: origin P is $^4B_1$ (correlating with $^4E\epsilon$), more intense in z- than xy-polarisation and with +ve MCD, while Q is $^4A_1$ (correlating with $^4E\theta$), allowed only in xy and with -ve MCD. The doublet nature of P and Q is then attributable to the small second order spin orbit coupling interaction with other quartet states, giving in each case E' + E'' components. From FIGURE 17, it is clear that for both P and Q, the strong MCD is associated with the upper component of each doublet, so that they can be definitely identified as follows:

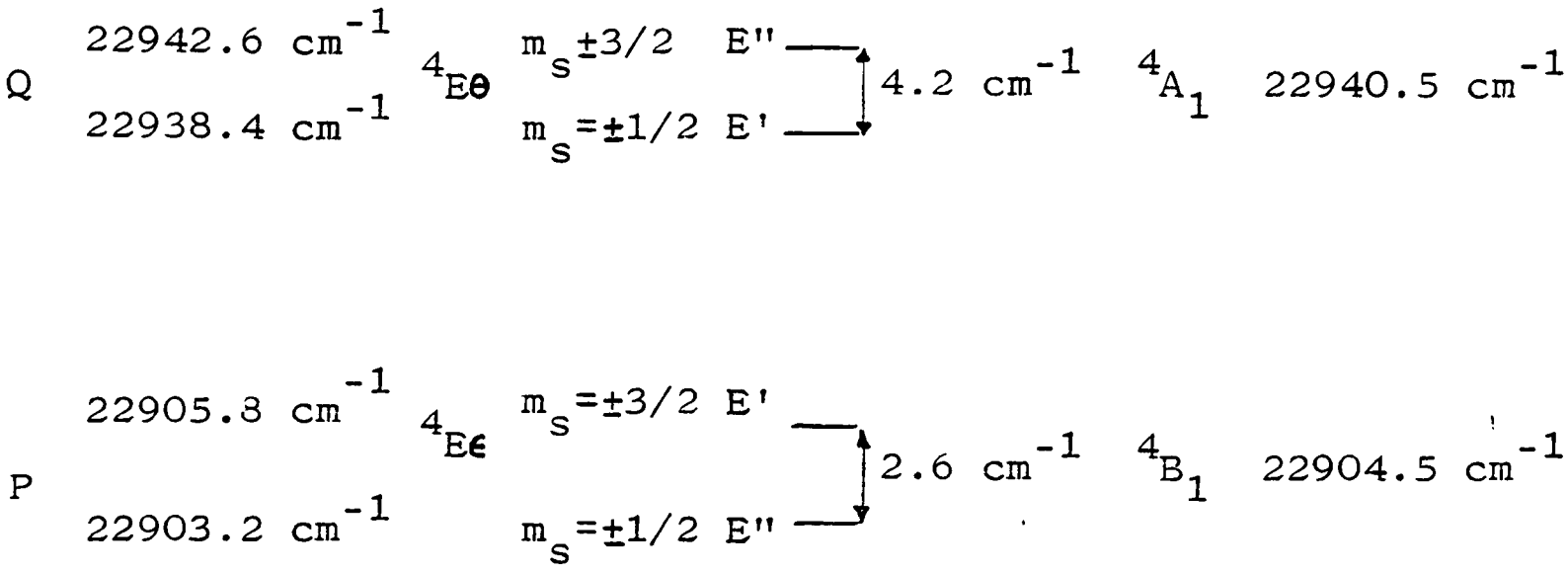

Quantitatively, the tetragonal perturbation model fits the observed origin intensities quite well, as the accompanying figures show. Band areas are in arbitrary units:

	D_{xy}	D_z	Δd	$\int_{\alpha} \varepsilon d\nu$	$\int_{\pi} \varepsilon d\nu$	$\int \Delta\varepsilon d\nu$	
^4E	3/72	-	-0.0370	28.2	2.1	-18.2	Q
^4E	1/72	4/72	+0.0123	12.5	18.7	+6.1	P
	Predicted by the tetra-gonal perturbation model			Observed from the spectra			

The experimental area for P in π-polarisation is low relative to the value predicted from α. It is, however, the hardest to measure accurately because the lines are narrow and of high absorbance, so that stray light becomes a problem. Also the spin orbit interaction which splits P and Q into doublets will cause mixing of the wavefunctions, whereas the calculated values refer to a pure ^4E state. By this means, Q gains a small z-intensity.

In $(Me_4N)_2MnCl_4$, Vala used high resolution to examine the $^4E(G)$ origins and found a situation similar to Cs_3MnCl_5 [60]. His lines "a" and "b", split by 5.3 cm^{-1}, are sharp and correspond to P, while the broad line "d" 53 cm^{-1} higher in energy corresponds to Q. The separation between P and Q

is 36 cm^{-1}, and differs from that of "a/b" and "d" because the two crystal lattices impose differing degrees of tetragonal distortion upon the $MnCl_4^{2\ominus}$ ion. On the other hand, the spin orbit coupling interaction should be almost the same in both cases, so that the "a-b" separation is similar to the 2.6 cm^{-1} splitting of P. This evidence provides indirect support for the assignment given above; unfortunately, no linear polarisation data is available for comparison. The MCD of $(Et_4N)_2MnCl_4$ is all negative in this region, but the conditions used were not the same as for Cs_3MnCl_5 [63], and MCD spectra are very sensitive to changes in the field: temperature ratio where C-terms are involved.

The sharp $^4E(G)$ origin lines of Cs_3MnCl_5 provide ideal conditions for further studies of this interesting and complex region. Accordingly, the temperature dependence of the MCD was recorded at high resolution, giving the results shown in FIGURE 20. Using the method described in APPENDIX III, high resolution axial Zeeman spectra were recorded for fields varying between zero and 4.75T. These results can be seen in FIGURES 21 (Q) and 22 (P). Both sets of drawings come from tracings of single beam spectra and have non-linear intensity scales, but are based on the same arbitrary starting point: 100% transmission of light at 4369Å. All these results can be interpreted in detail on the basis of the assignment given above. We shall treat P in full as the experimental data is clearer owing to the narrower lines, while similar arguments can be used for Q.

(i) MCD Temperature Dependence

If the g-values of both the excited and ground are taken to be equal to the spin-only value 2, and the zero field splitting of P is 2.6 cm^{-1} with $\pm 3/2$ above $\pm 1/2$, then at 5.0T the following MCD will be predicted:

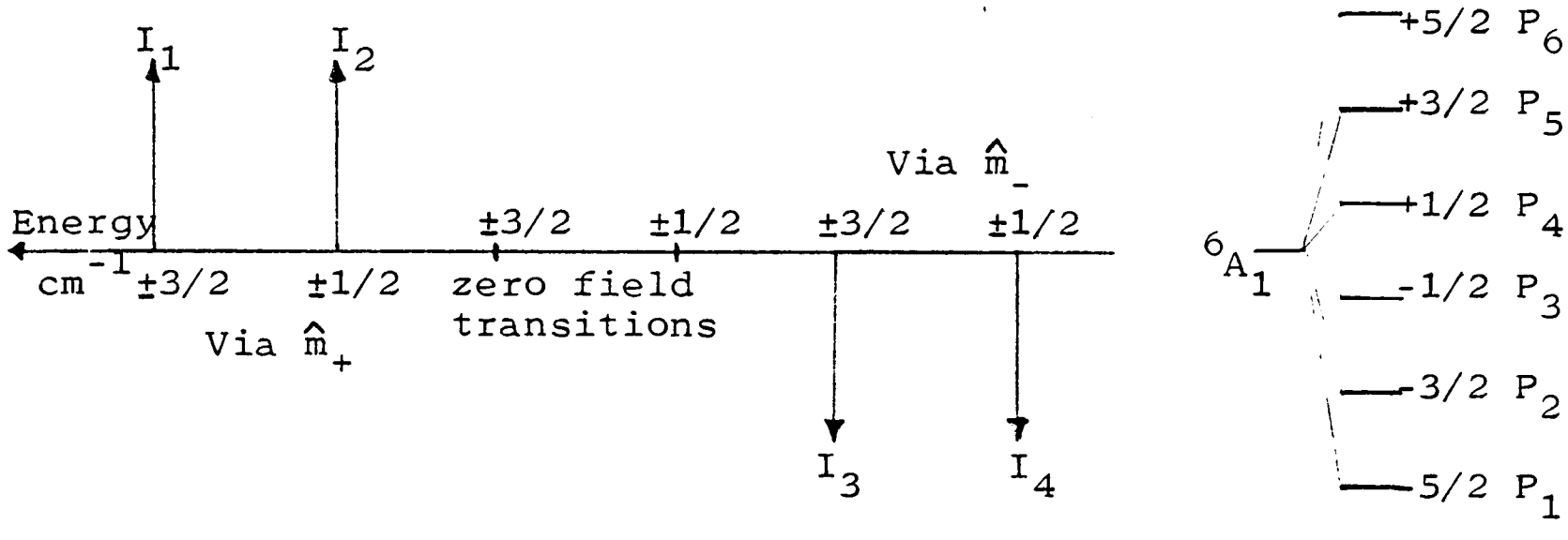

The total spread of the components is 12.0 cm^{-1}, and they are symmetrically arranged about the zero field positions. The 2.6 cm^{-1} splittings are retained. Each of the four transitions contains two contributions to its intensity I. In the upper pair with +ve MCD, the transitions originate in the four lowest Zeeman components of $^6A_1$, and have the relative intensities:

$$I_1 = 1/72\ P_1 + 1/720\ P_4, \quad I_2 = 1/20\ P_2 + 1/240\ P_3$$

The lower pair of transitions originate in the four highest components of $^6A_1$, and have relative intensities:

$$I_3 = 1/720\ P_3 + 1/72\ P_6, \quad I_4 = 1/240\ P_4 + 1/120\ P_5.$$

The factor P_i is the population of the Zeeman component of $^6A_1$.

Comparison with FIGURE 20 shows that four transitions are observed, and that the separations and circular polarisations are correctly predicted. By calculating the population factors P_i, the relative intensities I can also be predicted, and these agree with the observed pattern of lines very well.

Band P	Calculated Relative Intensities			
Temperature	I_1	I_2	I_3	I_4
4K	+1131	+138	-4	-3
8K	+801	+250	-27	-36
12K	+628	+272	-58	-74
20K	+474	+266	-109	-122
45K	+346	+241	-178	-170

For Q, a similar pattern will emerge, but with the MCD signs exchanged, and slightly different splittings and intensities.

(ii) Axial Zeeman Effect

We shall not attempt to give a description of the field dependence of the spectra shown in FIGURES 21 and 22 as there are many lines present which are not fully resolved either for P or Q. Also, with contributions from six ground state components, the pattern is complex, and changes in energy as well as population occur each time the field is altered. However, at the maximum field of 4.75T, the appearance can be understood by reference to the MCD recorded at 5.0T and 4.0K as shown in FIGURE 23. Taking P first, the transitions close to 4365Å (+ve MCD) are via $\hat{m}_+$ to $\pm 3/2$ and $\pm 1/2$, while the weaker lines at 4366.5 and 4367.0Å are via $\hat{m}_-$ to $\pm 3/2$ and $\pm 1/2$ (-ve MCD).

Between these two pairs of lines are found the lines marked X and Y in FIGURE 23. They appear to be sharper than the other features, and lie at the same energies as the zero field lines. From their positions and relative intensities, we infer that X and Y arise in $|^6A_1 - 1/2\rangle$ and $|^6A_1 - 3/2\rangle$ respectively and are transitions having $\Delta m_s = 0$. These do not arise via the magnetic dipole mechanism, but could possibly occur as a result

of the spin orbit mixing between $^6A_1$ and $^4T_1$ excited states. Lines X and Y do not appear to have any MCD.

To higher energy another pair of lines are found (4363.2 and 4363.8Å) associated with weak -ve MCD signals. They arise as follows. Consider the states $|^4E\theta\text{-}3/2\rangle$ and $|^4E\epsilon\text{+}1/2\rangle$, both of which can be written in terms of tetrahedral basis functions $|E''\alpha\rangle$ and $|U''\nu\rangle$. The transition $|^4E\theta\text{-}3/2\rangle \longleftarrow |^6A_1a_1\text{-}5/2\rangle$ is allowed via $\hat{m}_-$, and is intense owing to a large population of that ground state component at high field and low temperature, plus a large matrix element (TABLE XII). As a result of second order spin orbit interactions, both $^4E\theta$ and $^4E\epsilon$ suffer small zero field splittings. The correct wavefunctions are those which diagonalise the combined tetragonal field and spin orbit perturbation matrix, and will no longer be of "pure" θ or ϵ character, e.g. $|^4E\epsilon\text{+}1/2\rangle$ will contain a small amount c_1 of $|^4E\theta\text{-}3/2\rangle$.

Owing to this "impurity" in the wavefunction, the forbidden transition $|^4E\epsilon\text{+}1/2\rangle \longleftarrow |^6A_1a_1\text{-}5/2\rangle$ will be allowed via $\hat{m}_-$, with intensity proportional to c_1^2, and will lie $9.3cm^{-1}$ above the allowed $|^4E\epsilon\text{-}1/2\rangle \longleftarrow |^6A_1a_1\text{-}3/2\rangle$ transition. Similarly, $9.3cm^{-1}$ above the allowed $|^4E\epsilon\text{-}3/2\rangle \longleftarrow |^6A_1a_1\text{-}5/2\rangle$ transition will lie a small signal from the forbidden $|^4E\epsilon\text{+}3/2\rangle \longleftarrow |^6A_1a_1\text{-}3/2\rangle$ transition. In principle, the appearance of Q can be described in the same way, but the lines are less well resolved, making the pattern harder to identify with certainty.

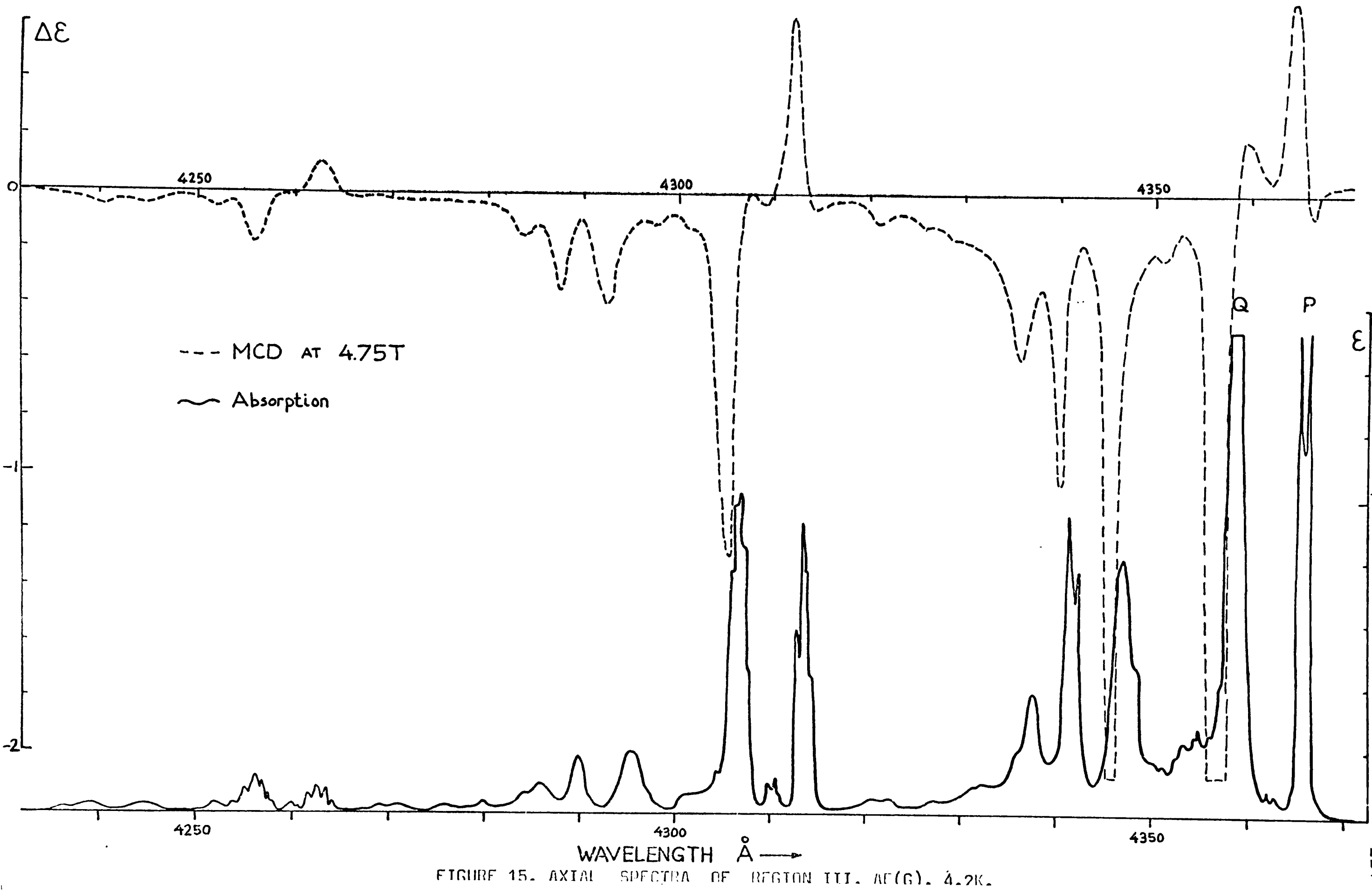

FIGURE 15. AXIAL SPECTRA OF REGION III, AE(G), 4.2K.

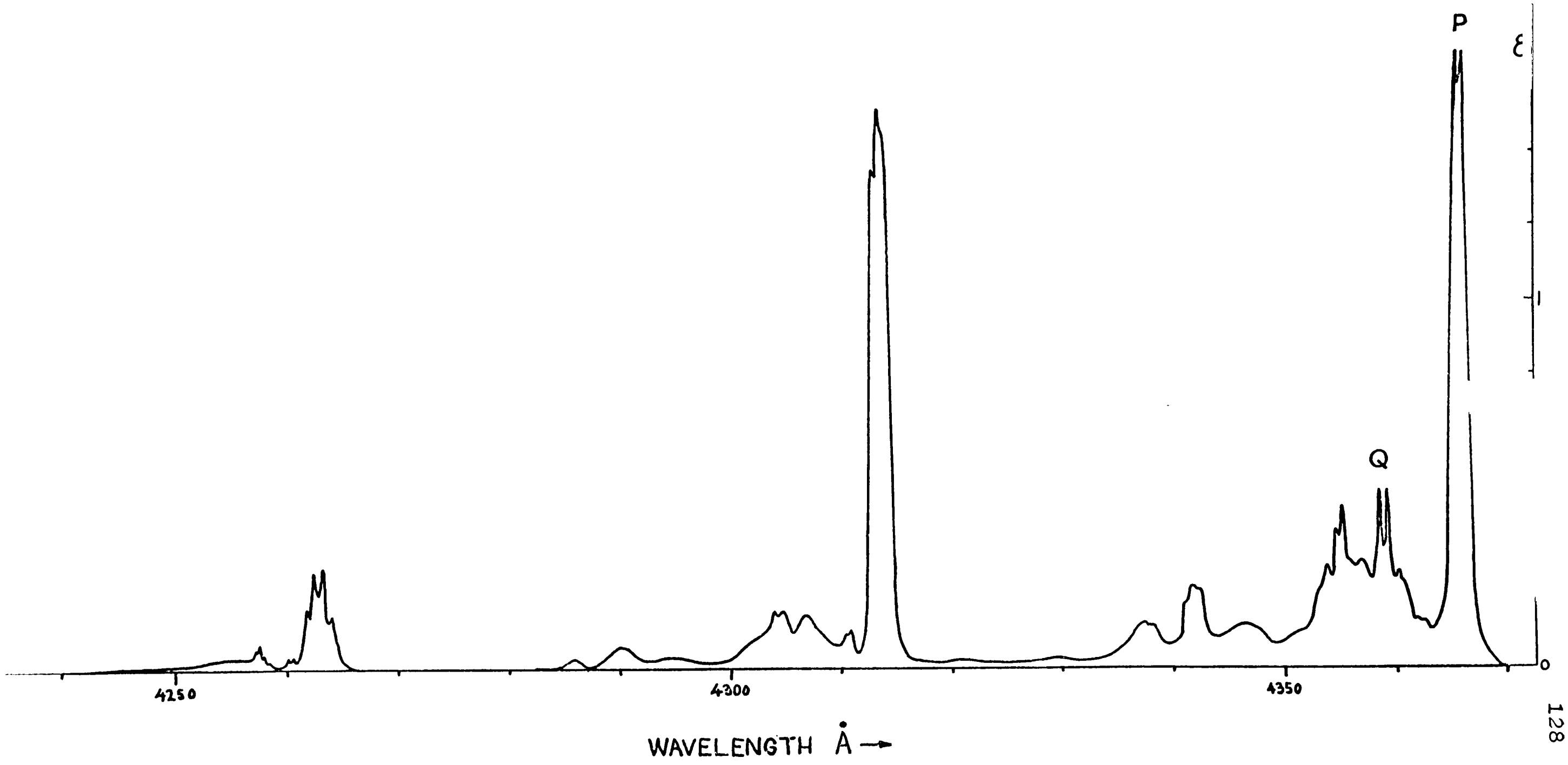

FIGURE 16. π - SPECTRUM OF REGION III, AE(G), 4.2K.

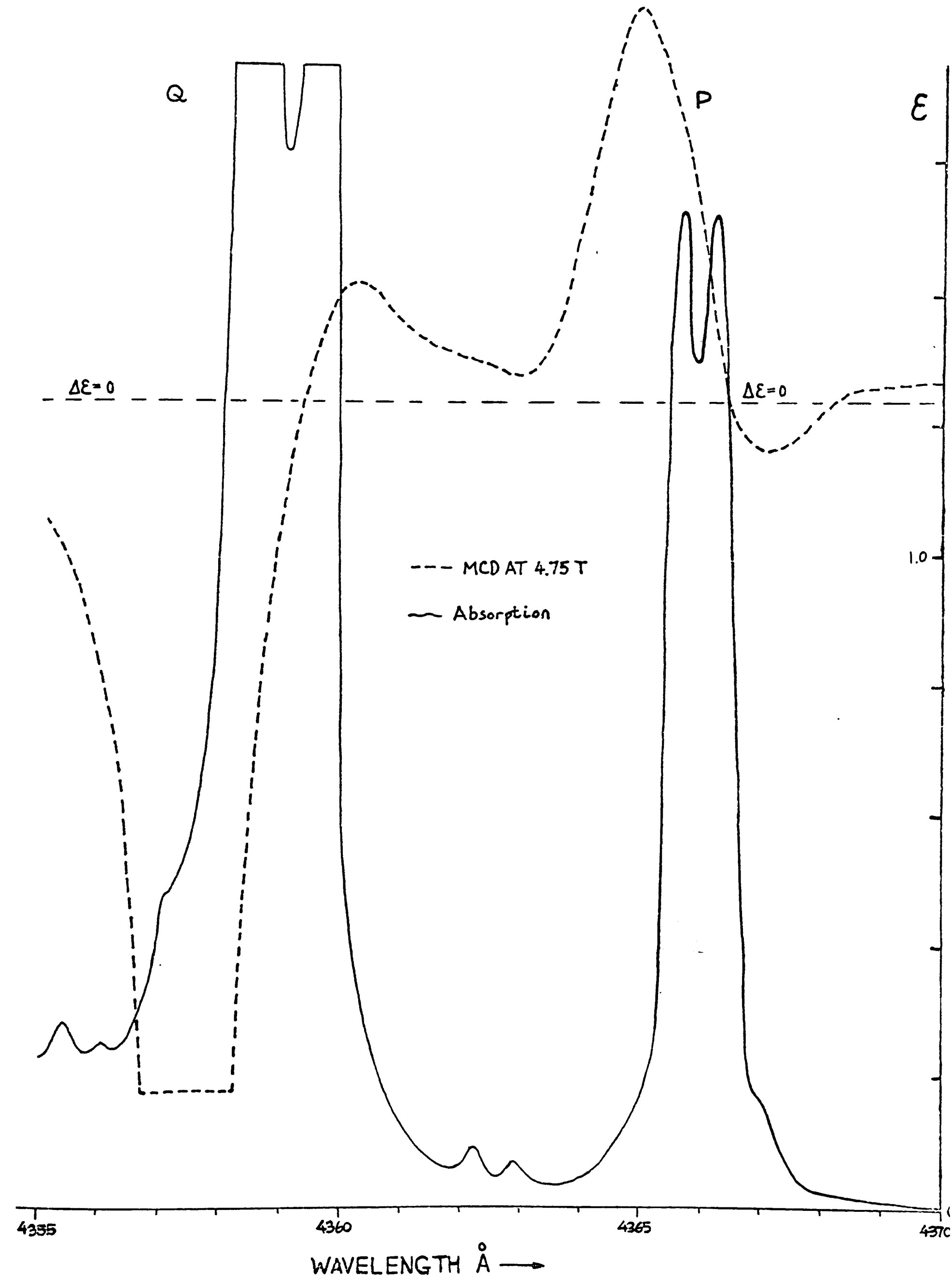

FIGURE 17. REGION III ORIGINS, AXIAL.

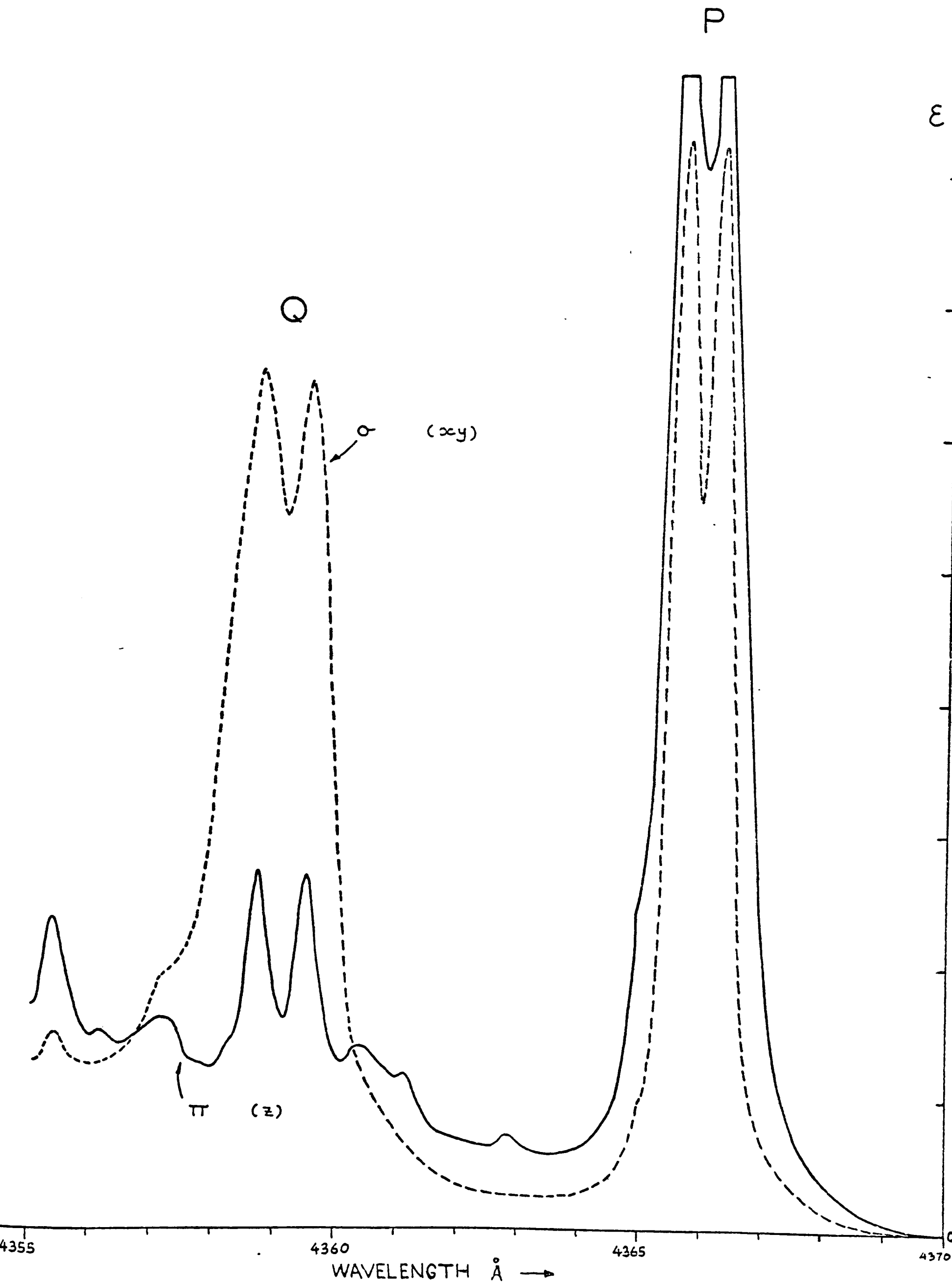

FIGURE 18. REGION III ORIGINS, POLARISED.

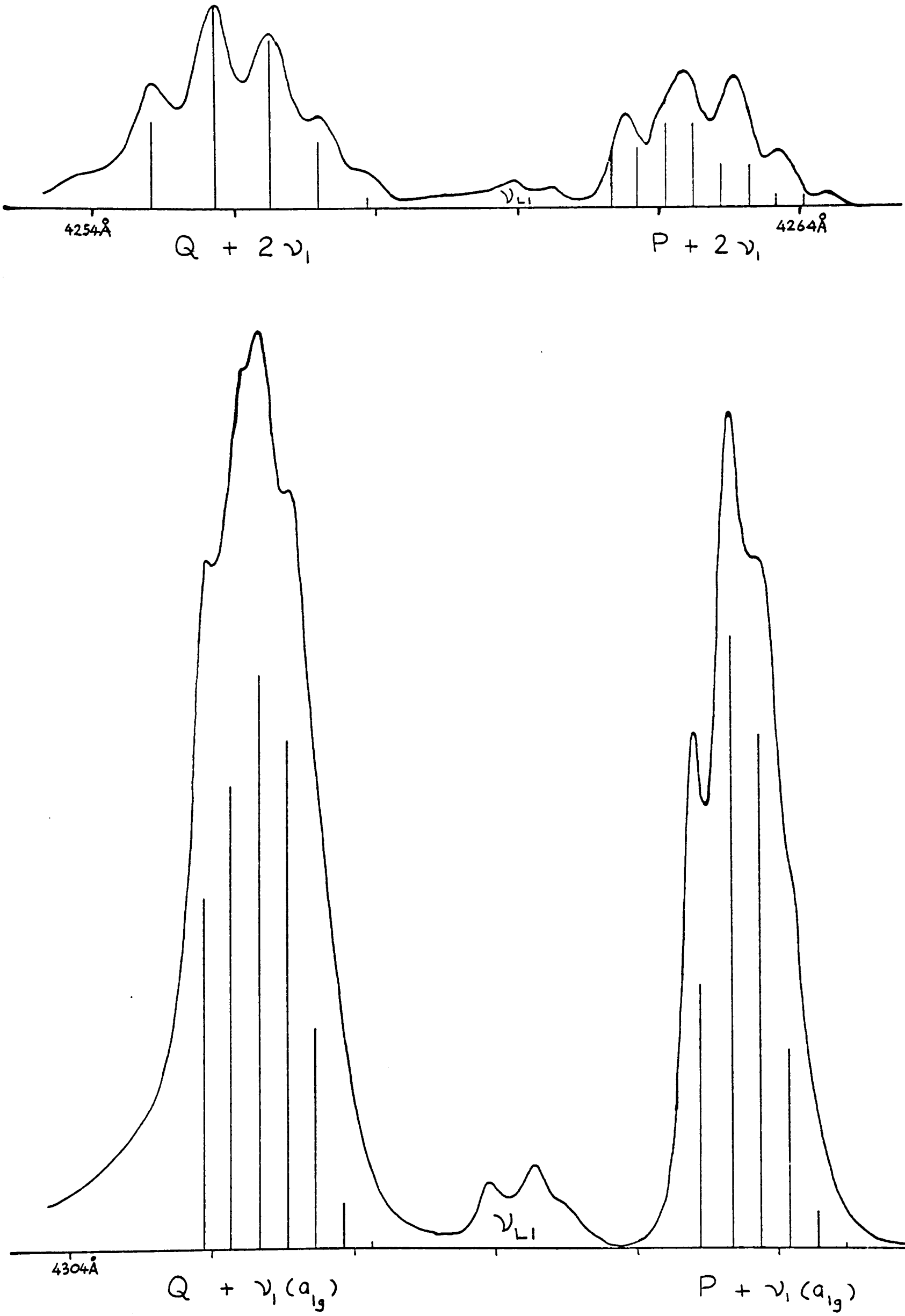

FIGURE 19 .

ν_1 SIDEBANDS OF ORIGINS P AND Q OF REGION III , AXIAL , 4.2K .

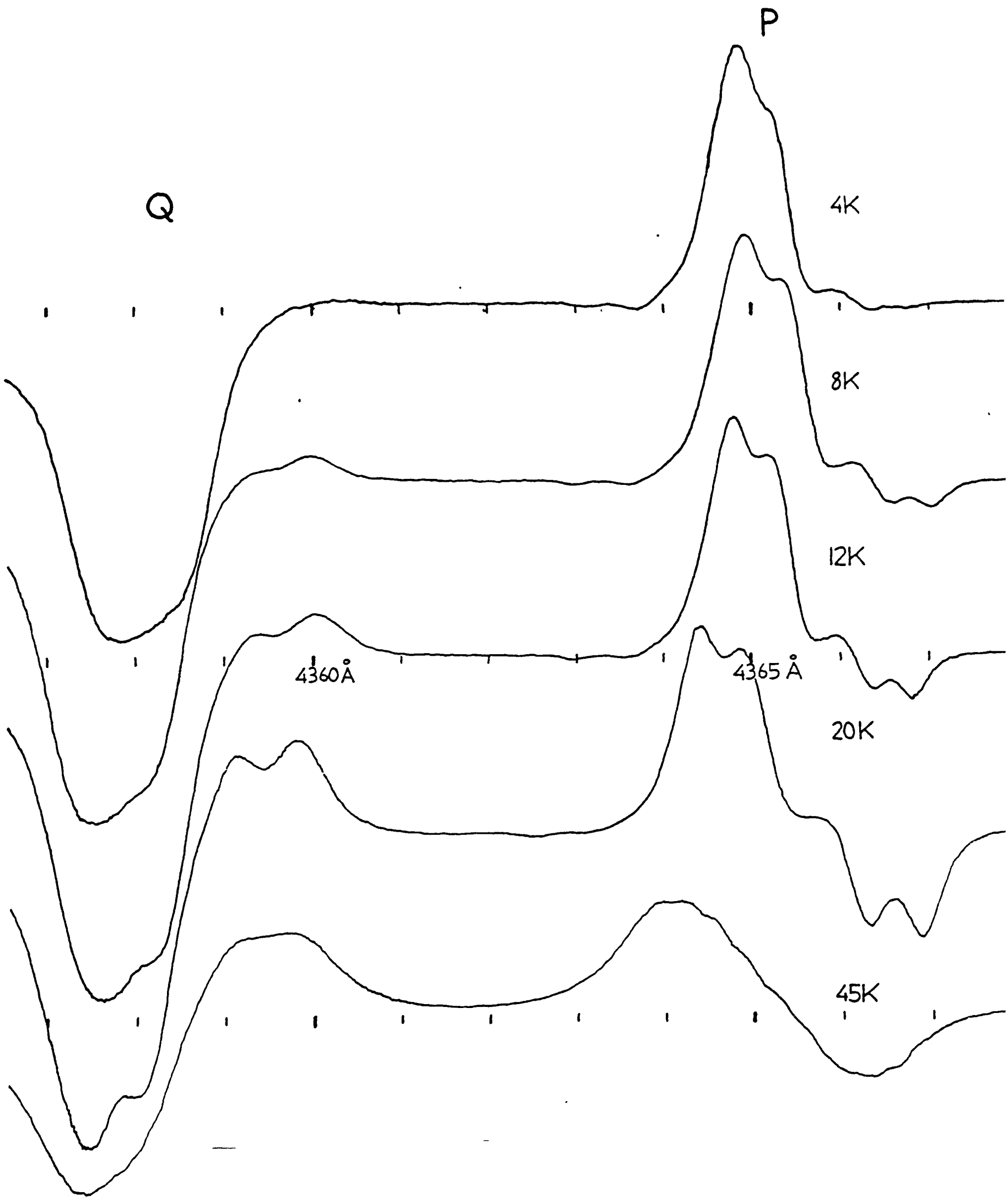

FIGURE 20 .

TEMPERATURE DEPENDENCE OF THE MCD OF ORIGINS P ($^4B_1$) AND Q ($^4A_1$) OF REGION III RECORDED AT 5.0T .

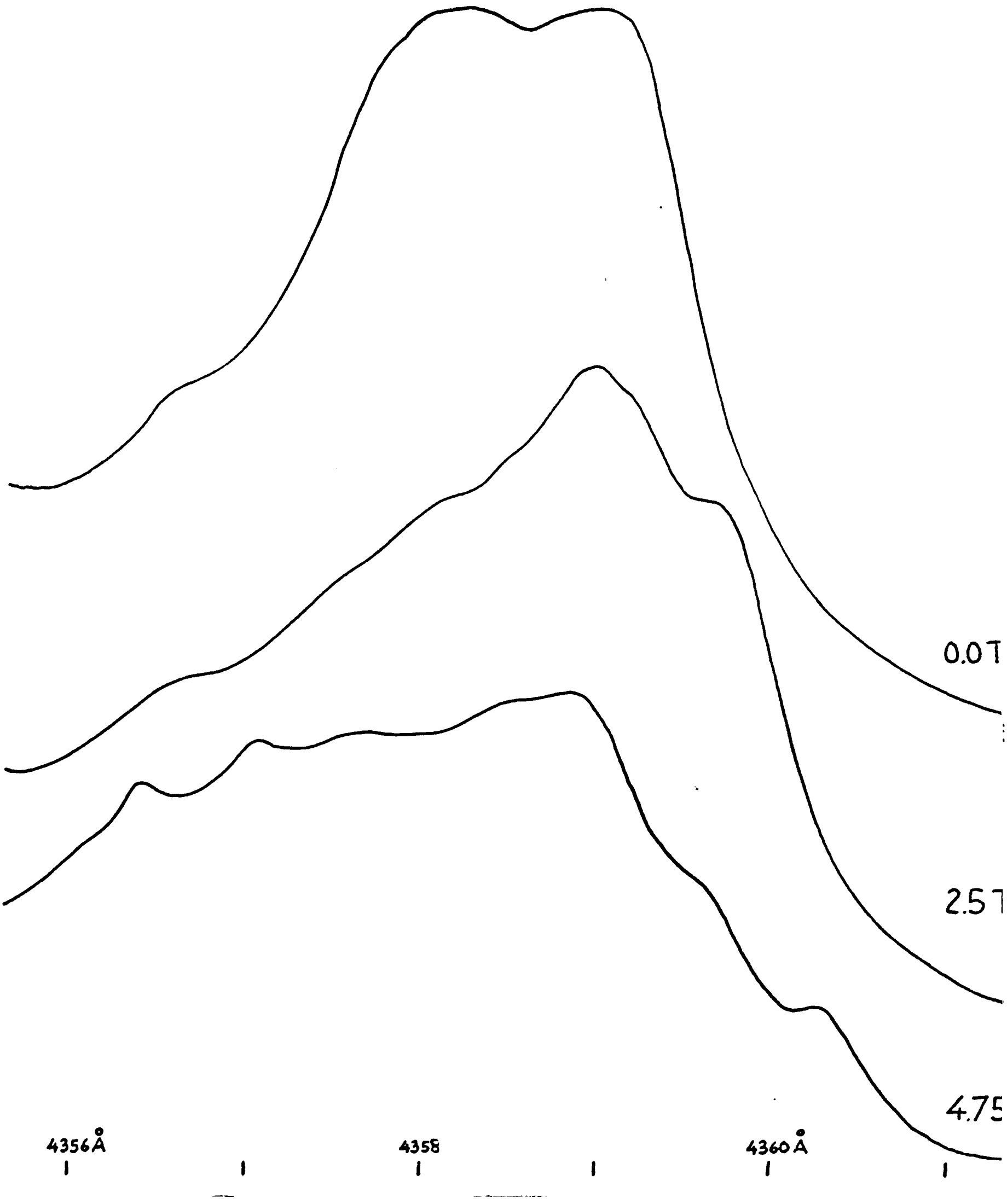

FIGURE 21 .

AXIAL ZEEMAN SPECTRA OF ORIGIN Q ,
$^4A_1$, OF REGION III AT 4.2K .

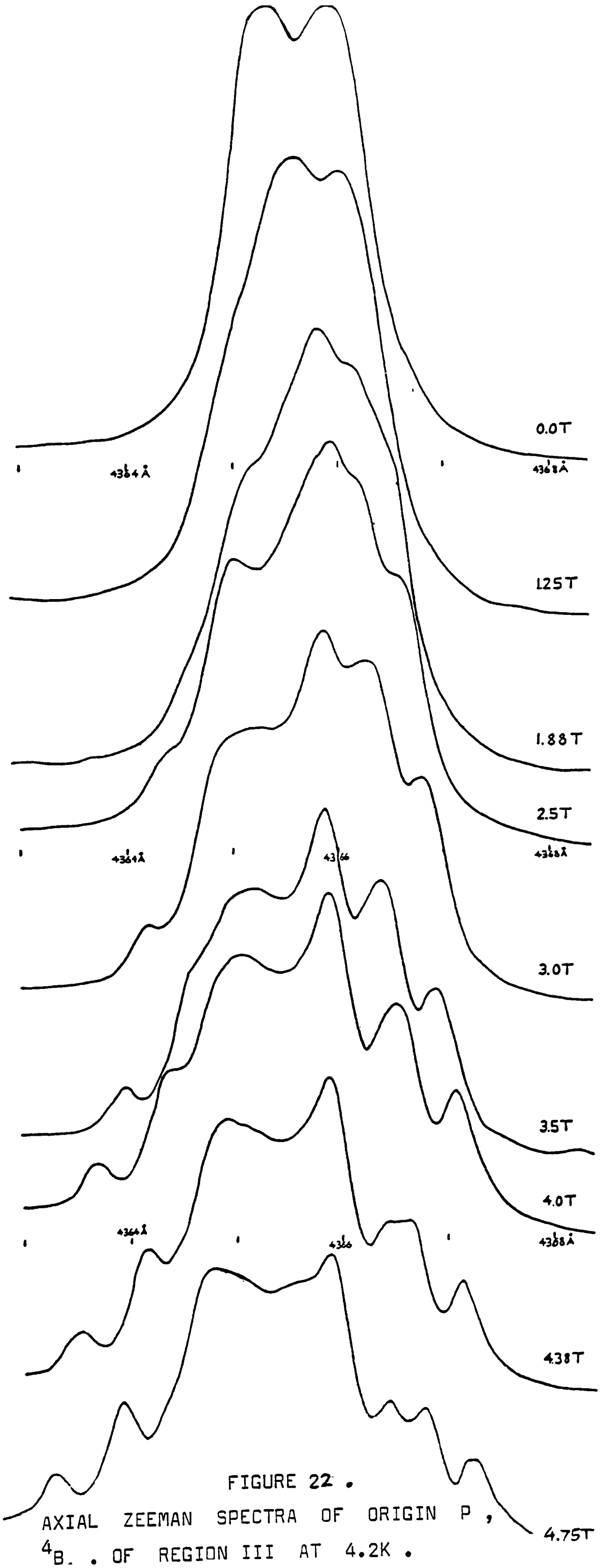

FIGURE 22 .

AXIAL ZEEMAN SPECTRA OF ORIGIN P , $^4B_{.}$. OF REGION III AT 4.2K .

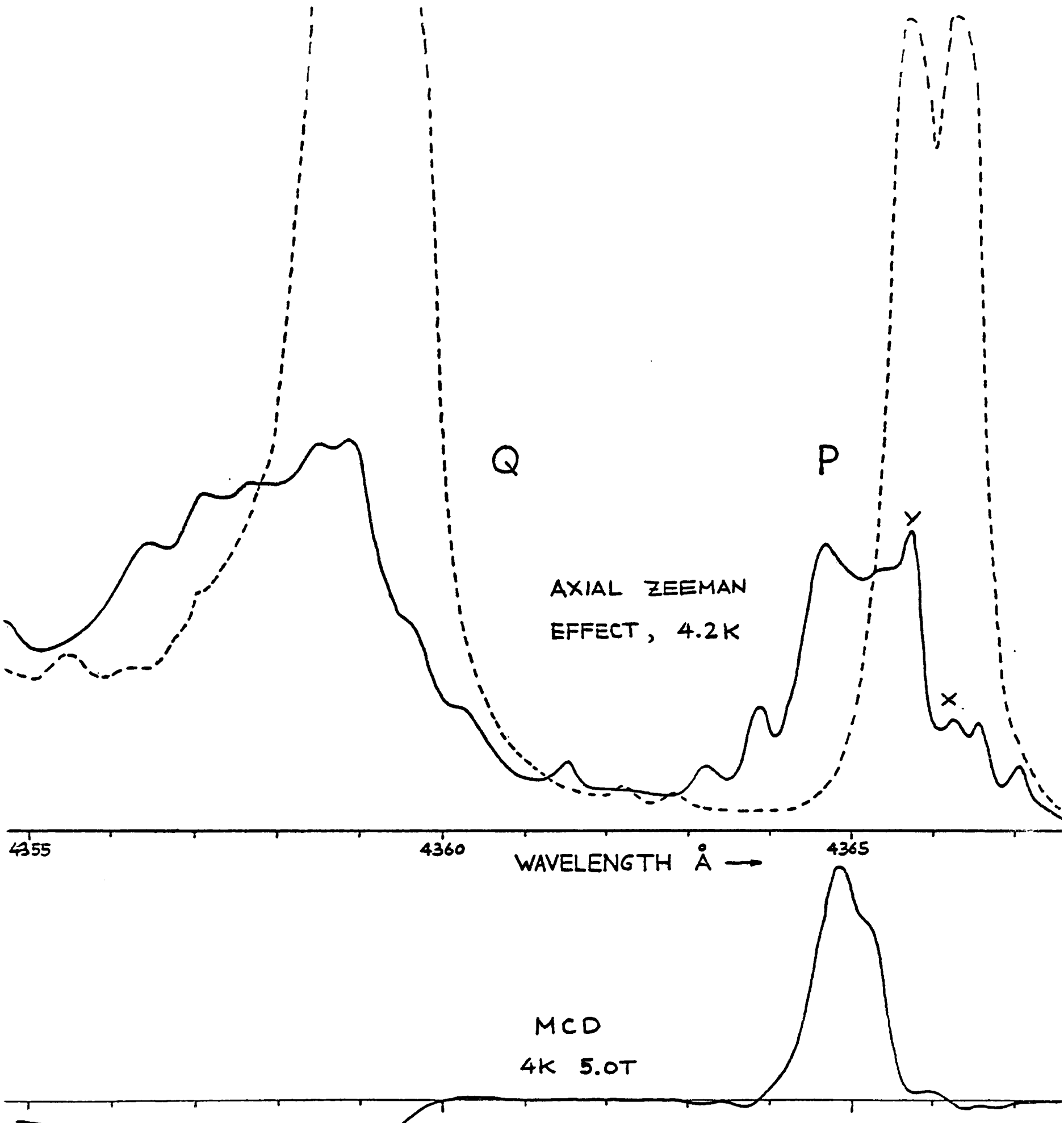

FIGURE 23.

COMPARISON OF AXIAL ZEEMAN AND MCD SPECTRA OF REGION III ORIGIN LINES.

TOP : 4.75T Zeeman (——) and zero field (– – –), single beam.

BOTTOM : MCD at 5.0T.

6.7 REGION IV GENERAL

The part of the spectrum between 3950Å and 3480Å designated as REGION IV contains three overlapping band systems. They are, in order of increasing energy:

(i) $^4T_2(D)$ from 3950Å to about 3750Å;

(ii) $^4E(D)$ from about 3780Å to about 3630Å;

(iii) $^4T_1(P)$ from about 3700Å to 3480Å,

and are each discussed in detail below. Their spectra are shown in FIGURES 24 and 25.

All three excited states correlate with the $e^2t_2^3$ electronic configuration, the same as the ground state, and this may explain the presence of sharp features in the absorption spectra of $^4T_2(D)$ and $^4E(D)$. In all cases, the α- and σ-spectra are identical so that there are no magnetic dipole contributions. The positions of the band maxima are reasonably close to those predicted in the crystal field calculations of CHAPTER 5, and the band assignments are not in doubt. The observed $\Delta d/D$ ratios agree well with the theoretical values except for $^4E(D)$, which overlaps with the two more intense bands on either side.

A general comparison can be made with the bands observed by Vala. In $(Me_4N)_2MnCl_4$, bands of similar shape and relative intensity were found, but lacking sharp line structure. In the corresponding bromide, $^4T_2(D)$ was weak and featureless, $^4E(D)$ strong and structured, while $^4T_1(P)$ was strong and showed considerable structure [60]. In $(Et_4N)_2MnCl_4$, the weak $^4T_2(D)$ band showed few features and was separated from the others; it had +ve MCD, but again lacked fine structure. The $^4E(D)$

band was weak and had -ve MCD, while the strong $^4T_1(P)$ band showed some structure and again had -ve MCD. In the bromide, overlapping bands are present with some structure visible, with $^4T_2(D)$ again the weakest. All three bands gave -ve MCD signals, as did the overlapping bands of the iodide [63].

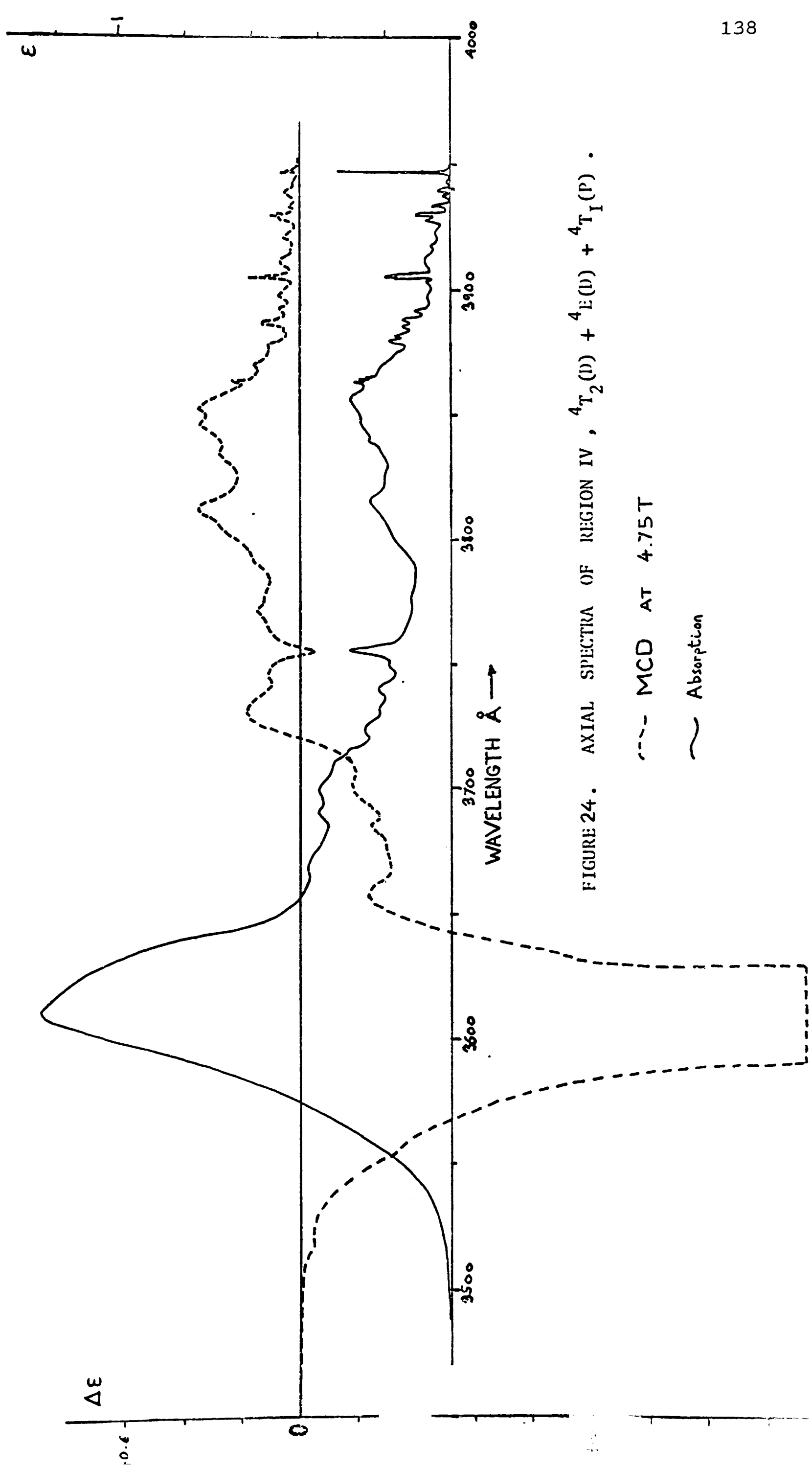
ε
4000
3900
3800
3700
3600
3500
WAVELENGTH Å →
Δε
0
AXIAL SPECTRA OF REGION IV , $^4T_2(D) + {}^4E(D) + {}^4T_1(P)$.
---- MCD AT 4.75T
~ Absorption

FIGURE 24.

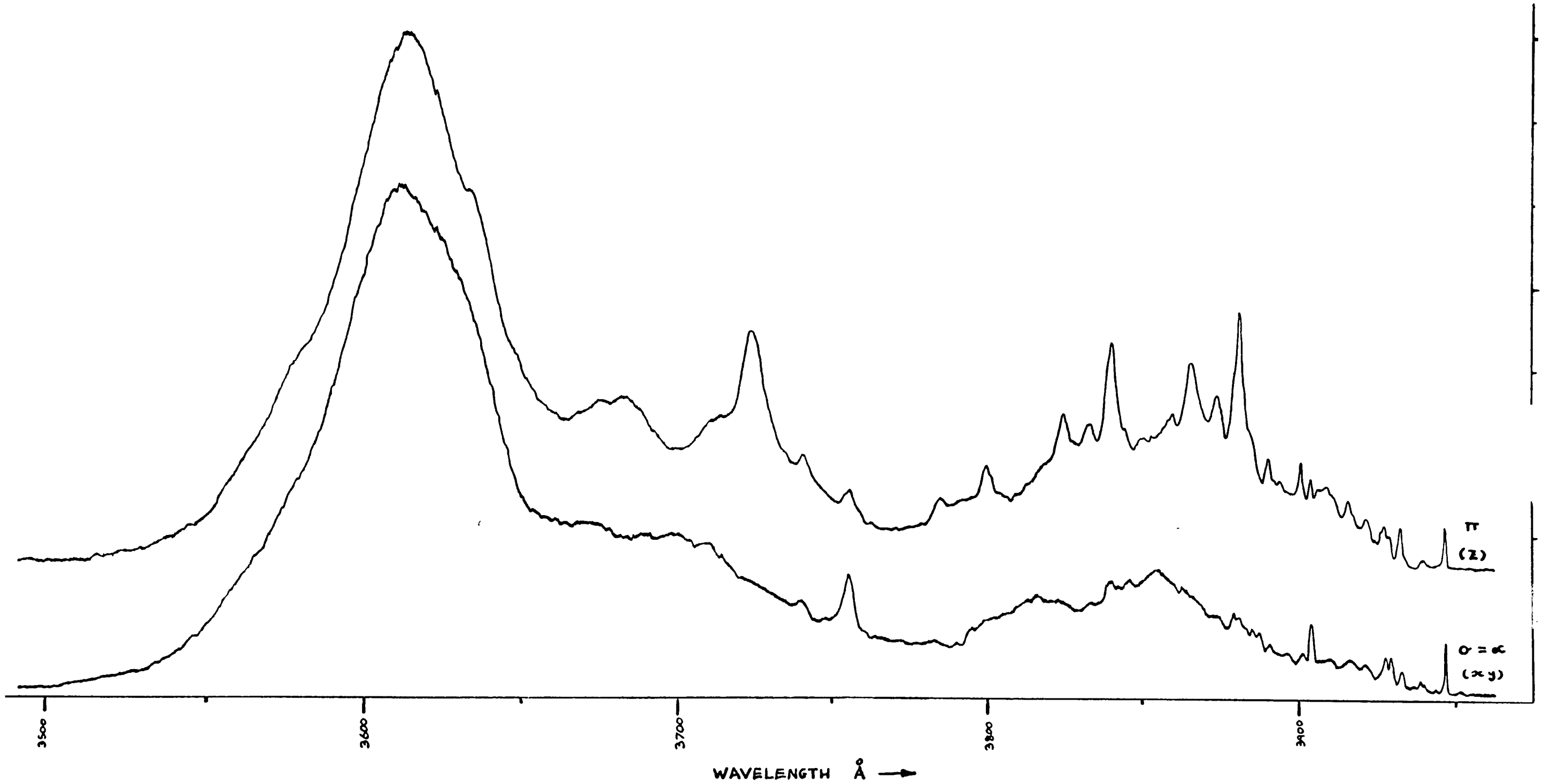

FIGURE 25. POLARISED SPECTRA OF REGION IV .

6.8 $^4T_2(D)$

The spectra of this band are shown in FIGURES 26 (axial) and 27 (polarised), in which the three electronic origins are indicated as A, B, and C. The very high axial intensity of A arises from the fact that the origin is extremely sharp, the half-width being instrument limited, and the drawing was made from a very slow wavelength scan. In MCD, the resolution was much lower, while the polarised spectra were taken from a more rapid scan. The other origins (B and C) are broader, and do not suffer such gross instrumental distortion. The $^4T_2(D)$ band is unique among the $^4\Gamma$ absorptions of Cs_3MnCl_5 in having sharp lines superimposed upon a broad band of absorption. However, a very similar shape occurs in the $^4T_2(D)$ band of $CsMnCl_3.2H_2O$ in the weak polarisation [102].

In the axial spectra, origin lines A and B both give rise to numerous vibrational sidebands which are quite sharp, while the weaker C origin produces only a few broad humps in the region below $A + 2\nu_1$. Because of the extreme sharpness of A, and the high resolution available, structuring of the ν_1 and $2\nu_1$ sidebands is clearly visible, and has been assigned to the presence of the two chlorine isotopes [101] as discussed previously. Features in the MCD built on the +ve origins A and B follow the absorption, while C appears to be associated with a dip at 25767 cm^{-1} and may have -ve MCD. This could explain the shape of the MCD beyond this point, where weak features based on A, B, and C overlap. Assignments here must be regarded as tentative. The broad absorption band rises to a peak at 25929.6 cm^{-1} (D), has a shoulder to lower energy ($\sim$25420 cm^{-1}, beneath the sharp lines), and an apparent ν_1 repeat at

26196.5 cm^{-1}, beyond which there is a steady decline in intensity up to the region where overlap with $^4E(D)$ occurs. The MCD signal peaks at 25962 cm^{-1}, with the ν_1 repeat at 26238 cm^{-1}, but the low energy shoulder is absent. Apart from this, the shape is similar to the absorption but with the peaks and troughs accentuated, perhaps indicating overlap of MCD signals of opposite signs in this area. The MCD peaks occur at higher energies than the corresponding axial absorption features, the difference of about 30 cm^{-1} being much larger than either the ground state splitting in the magnetic field or the energy difference observed for the sharp line origins. Possibly the MCD peak does not correspond to D, or else there is a large magnetic field splitting of the excited state. At about 26550 cm^{-1} there is a point of inflexion in the MCD signal, indicating overlap with the sharp -ve origin A of $^4E(D)$.

The polarised spectra of FIGURE 27 exhibit similar features to the axial absorption. The α- and σ-spectra are identical, and the π-spectrum also has sharp lines superimposed on a rising broad absorption band. Origins A and B are both weaker than in α, while C is very much more intense. Thus a very similar pattern of lines is seen in the σ- and π-spectra up to about 25740 cm^{-1}, beyond which point the π-spectrum is dominated by C, with vibrational sidebands in a characteristic pattern repeating with frequency ν_1. The peak D of the broad absorption is lost under this pattern, but the low energy shoulder is clearly more intense in π-polarisation. This, together with the intensity of the C-features, accounts for the observed

difference in the oscillator strengths of α- and π-spectra, the ratio being 1:1.57. The energies and detailed assignments of the features in the spectra of $^4T_2(D)$ are tabulated below.

$\alpha = \sigma(xy)$			MCD			$\pi(z)$		
ENERGY cm^{-1}	ASSIGN-MENT	VIBRL. MODE	ENERGY cm^{-1}	ASSIGN-MENT	VIBRL. MODE	ENERGY cm^{-1}	ASSIGN-MENT	VIBRL. MODE
25332.5	A	-	25338	A	-	25332.5	A	-
25348.5	A+16.0	ν_{L1}	25356	A+18	ν_{L1}			
25359.5	A+27.0	ν_{L2}	25368	A+30	ν_{L2}	25356.9	A+24.4	ν_{L2}
25374.9 25378.8						25376.1		
25384.9	A+52.4	ν_{L3}	25388	A+50	ν_{L3}	25385.1	A+52.6	ν_{L3}
25396.8	A+64.3	ν_{L4}	25404	A+66	ν_{L4}	25396.7	A+64.2	ν_{L4}
25413.3						25414.1		
25420.4	A+87.5	$\nu_4(b_{2g})$	25430	A+92	$\nu_4(b_{2g})$	25420.7	A+87.8	$\nu_4(b_{2g})$
25444.0	B	-	25454	B	-	25444.5	B	
25455.0	A+122.5	$\nu_2(a_{1g})$	25465	A+127	$\nu_2(a_{1g})$	25455.6	A+123.1	$\nu_2(a_{1g})$
25462.1	A+129.6	$\nu_4(e_g)$			$\nu_4(e_g)$	25462.8	A+130.3	$\nu_4(e_g)$
						25492.5	B+48.0	ν_{L3}
25502.7	B+58.7	ν_{L4}	25509	B+55	ν_{L3}, ν_{L4}			
25528.4	B+84.4	$\nu_4(b_{2g})$	25543	B+89	$\nu_4(b_{2g})$	25529.0	B+84.5	$\nu_4(b_{2g})$
25554.5	B+110.5	$\nu_2(a_{1g})$	25566	B+112	$\nu_2(a_{1g})$	25560.3	B+115.8	$\nu_2(a_{1g})$
25564.7	B+120.7	$\nu_4(e_g)$	25579	B+125	$\nu_4(e_g)$,			
25573.5	B+129.5	$\nu_2(b_{1g})$			$\nu_2(b_{1g})$	25576.0	B+131.5	$\nu_4(e_g)$
						25587.8	B+143.3	$\nu_2(b_{1g})$
25602.9 25605.0 25606.9 25609.2	A+273.5	$\nu_1(a_{1g})$	25617	A+279	$\nu_1(a_{1g})$	25602.9 25606.1 25607.5 25610.1	A+274.2	$\nu_1(a_{1g})$
25622.0 25633.1	A+295.1	$\nu_3(b_{2g}+e_g)$				25628.9	A+296.4	$\nu_3(b_{2g}+e_g)$
			25648	A+ν_1+31	ν_{L2}			

TABLE XVI .

FEATURES IN THE SPECTRA BETWEEN 3950Å AND 3780Å, $^4T_2(D)$, AT 4.2K .

(The table continues overleaf)

$\alpha = \sigma$ (xy)			MCD			TT (z)		
ENERGY	ASSIGN-MENT	VIBRL. MODE	ENERGY	ASSIGN-MENT	VIBRL. MODE	ENERGY	ASSIGN-MENT	VIBRL. MODE
25651.6								
25660.2	$A+\nu_1+54.2$	ν_{L3}	25665	$A+\nu_1+48$	ν_{L3}			
25671.6	$A+\nu_1+65.6$	ν_{L4}				25672.0	$A+\nu_1+65.3$	ν_{L4}
25696.4	$A+\nu_1+90.4$	$\nu_4(b_{2g})$	25705	$A+\nu_1+88$	$\nu_4(b_{2g})$	25696.4	$A+\nu_1+89.7$	$\nu_4(b_{2g})$
25718.8	B+274.8	$\nu_1(a_{1g})$	25730	B+276	$\nu_1(a_{1g})$			
25732.7	$A+\nu_1+126,7$	$\nu_2(a_{1g})$	25741	$A+\nu_1+124$	$\nu_2(a_{1g})$	25733.4	$A+\nu_1+126.7$	$\nu_2(a_{1g})$
25748.0	$A+\nu_1+132.0$	$\nu_4(e_g)$	25757	$A+\nu_1+140$	$\nu_4(e_g)$	25749.2	$A+\nu_1+132.5$	$\nu_4(e_g)$
25759.9	C	-	25767	C	-	25759.3	C	-
25771.9	$A+\nu_1+155.9$	$\nu_2(b_{2g})$	25792			25771.2	C+11.9	ν_{L1}
25803.8	C+44.9	ν_{L3}				25803.8	C+44.5	ν_{L3}
						25809.1	C+49.8	ν_{L4}
25841.8								
						25856.5	C+97.2	$\nu_4(b_{2g})$
25861.8								
						25866.5	C+107.2	$\nu_2(a_{1g})$
25875.4 25879.4 25884.3	A+547.2	$2\nu_1(a_{1g})$	25896	A+558	$2\nu_1(a_{1g})$			
						25901.0	C+141.7	$\nu_4(b_{2g})$
25929.6	D	-						
						25940.3		
			25962	D	-			
25967.3	$A+2\nu_1+87.6$	$\nu_4(b_{2g})$				25967.3	$A+2\nu_1+87.6$	$\nu_4(b_{2g})$
25993.6	$A+2\nu_1+113.9$	$\nu_2(a_{1g})$						
			26003	D+41	ν_{L3}			
						26014.6	$A+2\nu_1+134.9$	$\nu_4(e_g)$
						26035.6	C+276.3	$\nu_1(a_{1g})$
26042.3	D+112.7	$\nu_2(a_{1g})$						
						26083.8	$C+\nu_1+48.2$	ν_{L3}
			26086	D+124	$\nu_2(a_{1g})$			
						26140.7	$C+\nu_1+105.1$	$\nu_2(a_{1g})$
26148.6	A+816.1	$3\nu_1(a_{1g})$						
						26186.2	$C+\nu_1+150.6$	$\nu_2(b_{1g})$
26196.5	D+265.9	$\nu_1(a_{1g})$						
26216.5								
			26238	D+276	$\nu_1(a_{1g})$			
			26285	$D+\nu_1+37$	ν_{L3}			
						26313.0	C+553.7	$2\nu_1(a_{1g})$
			26372	$D+\nu_1+134$	$\nu_2(a_{1g})$			
						26418.0	$C+2\nu_1+105.0$	$\nu_2(a_{1g})$
			26486	D+524	$2\nu_1(a_{1g})$			

TABLE XVI .

FEATURES IN THE SPECTRA BETWEEN 3950Å AND 3780Å, $^4T_2(D)$, AT 4.2K .

(Continued from page 142)

The natures of the electronic origins remain to be discussed. Vala's calculations [60] predict large splittings of the cubic spin orbit components of $^4T_2(D)$ as follows:

E" (+326 cm^{-1}) U' (+204 cm^{-1}) E' (+66 cm^{-1}) U' (zero).

In partial agreement with this, the three sharp origins A, B, and C are found to be spread over 427 cm^{-1}, with A and B close together, while the broad feature D is almost 600 cm^{-1} above A in energy. However, it is difficult to fit the observed MCD signals into this pattern. Again it appears that the tetragonal field component is the dominant perturbing influence, separating the state into $^4B_2$ (correlating with $^4T_2$ 0) and ^4E (correlating with $^4T_2 \pm 1$) which we identify as follows. The broad peak D seen in the α-spectrum and associated with the strong +ve MCD signal is assigned to $^4B_2$, predicted to be xy-allowed only and to have large +ve MCD by the tetragonal perturbation model of 6.3. To lower energy, origins A, B, and C, seen in both α- and π-spectra and with small MCD signals are assigned as three of the four possible spin orbit components of ^4E. Their properties arise from the combined effects of spin orbit coupling and the tetragonal field component. This assignment provides a good explanation of the MCD spectrum, and is compatible with the observed linear polarisations. Thus the lower energy part of the band, ^4E, is more intense in z- than xy-polarisation, the predicted ratio being 2:1, while the higher energy part of the π-spectrum is dominated by features built onto origin C of ^4E, masking the possible presence of any features assignable to D, $^4B_2$.

Further experimental data is available on the sharp origin A, 4.2K axial Zeeman spectra recorded at various fields up to 4.75T, and the temperature dependence of the MCD at a field of

5.0T, shown in FIGURES 28 and 29 respectively. In the Zeeman spectra, both first- and second-order effects must be present in order to give rise to the non-linear line shifts with increasing field strength, assuming that the Rigid Shift model can be applied in this case. Origin A must be a Kramers doublet to give rise to so few Zeeman components. Comparing the Zeeman trace for 4.2K, 4.75T with the MCD at 5.4K, 5.0T, we see very similar separations of the two lines, 4.2 and 4.5 cm^{-1} respectively. (Note that the MCD wavelength scale is more compressed.) Both transitions are via $\hat{m}_+$ as the MCD is +ve. As the temperature is raised, the MCD signal becomes progressively smaller, and the shape changes from that characteristic of a C-term into that of an A-term. Again, the small number of components visible indicates that A is a Kramers doublet. These observations agree with the assignment of A as one of the four possible spin orbit components of ^4E (2E' + 2E''), each of which is expected to be a Kramers doublet.

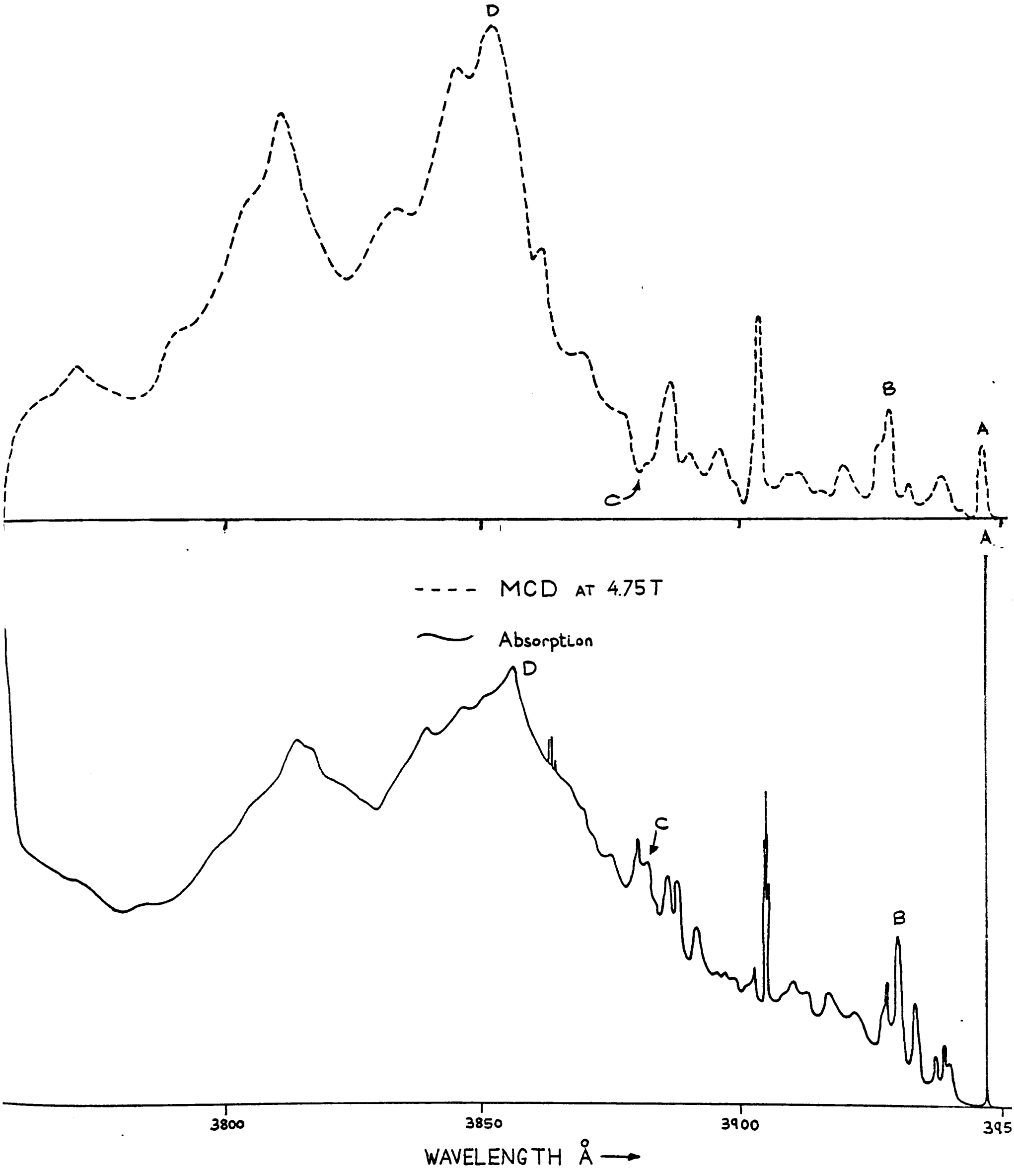

FIGURE 26 .

AXIAL SPECTRA OF $^4T_2(D)$ ON APPROXIMATELY EQUAL MOLAR EXTINCTION SCALES .

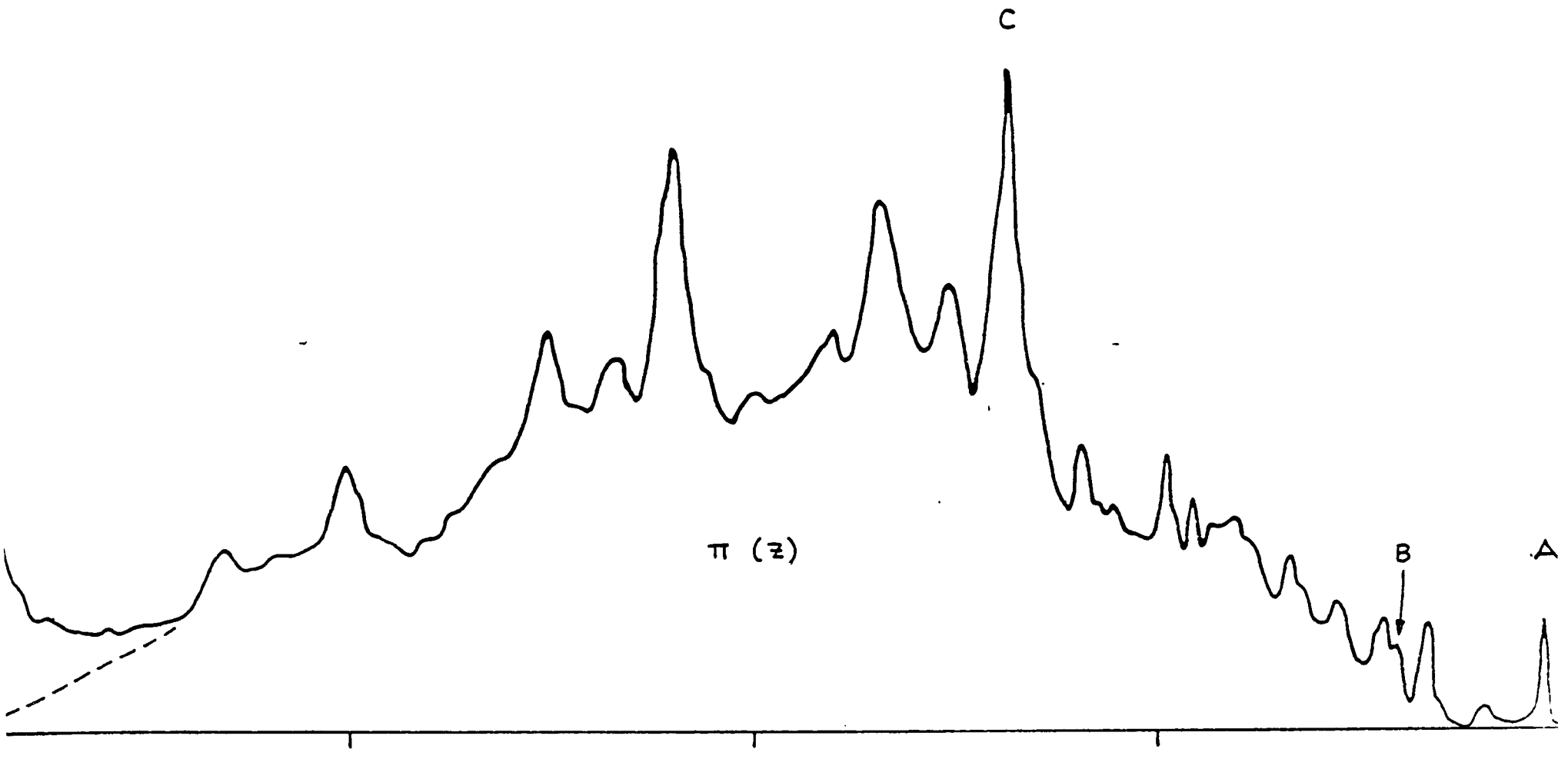

FIGURE 27.

POLARISED SPECTRA OF $^4T_2(D)$ ON EQUAL MOLAR EXTINCTION SCALES.

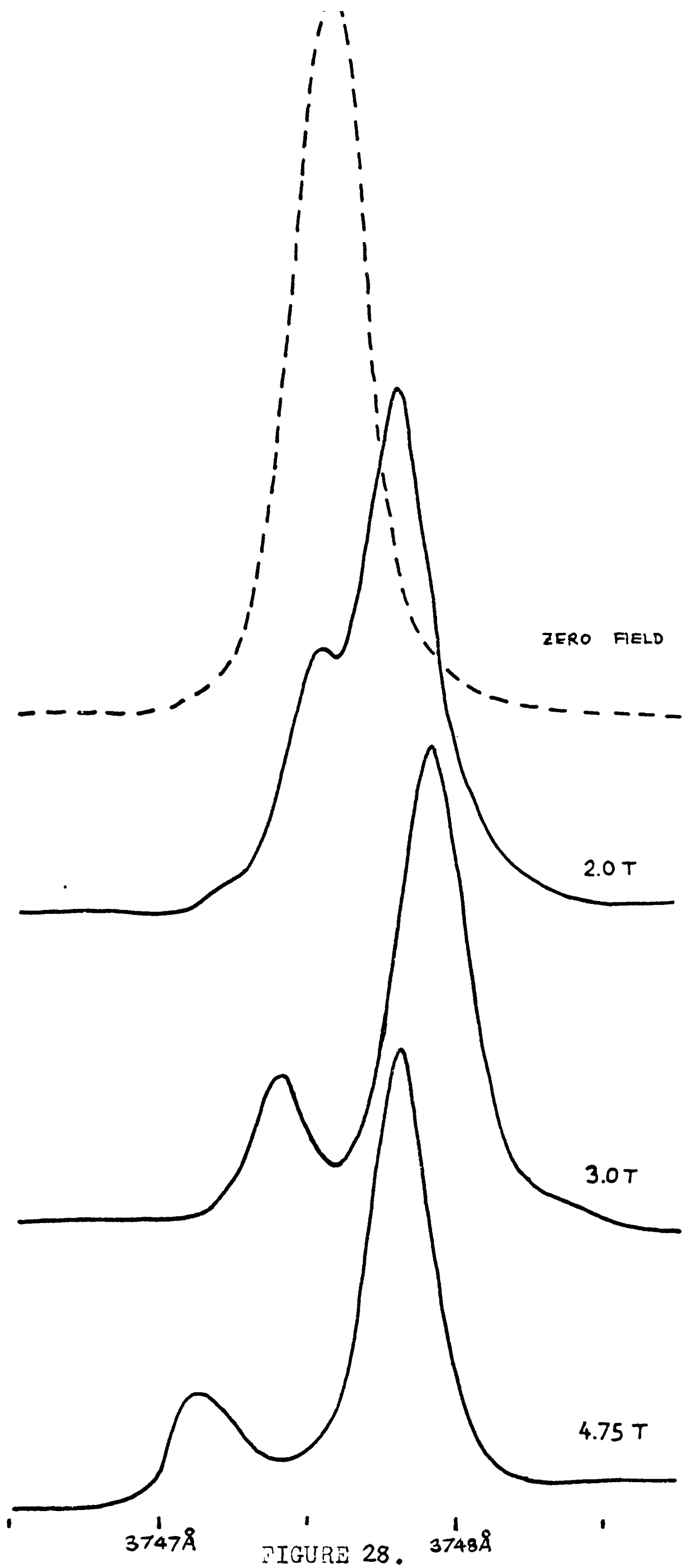

FIGURE 28.

AXIAL ZEEMAN SPECTRA OF ORIGIN "A" OF $^4T_2(D)$ AT 4.2K .

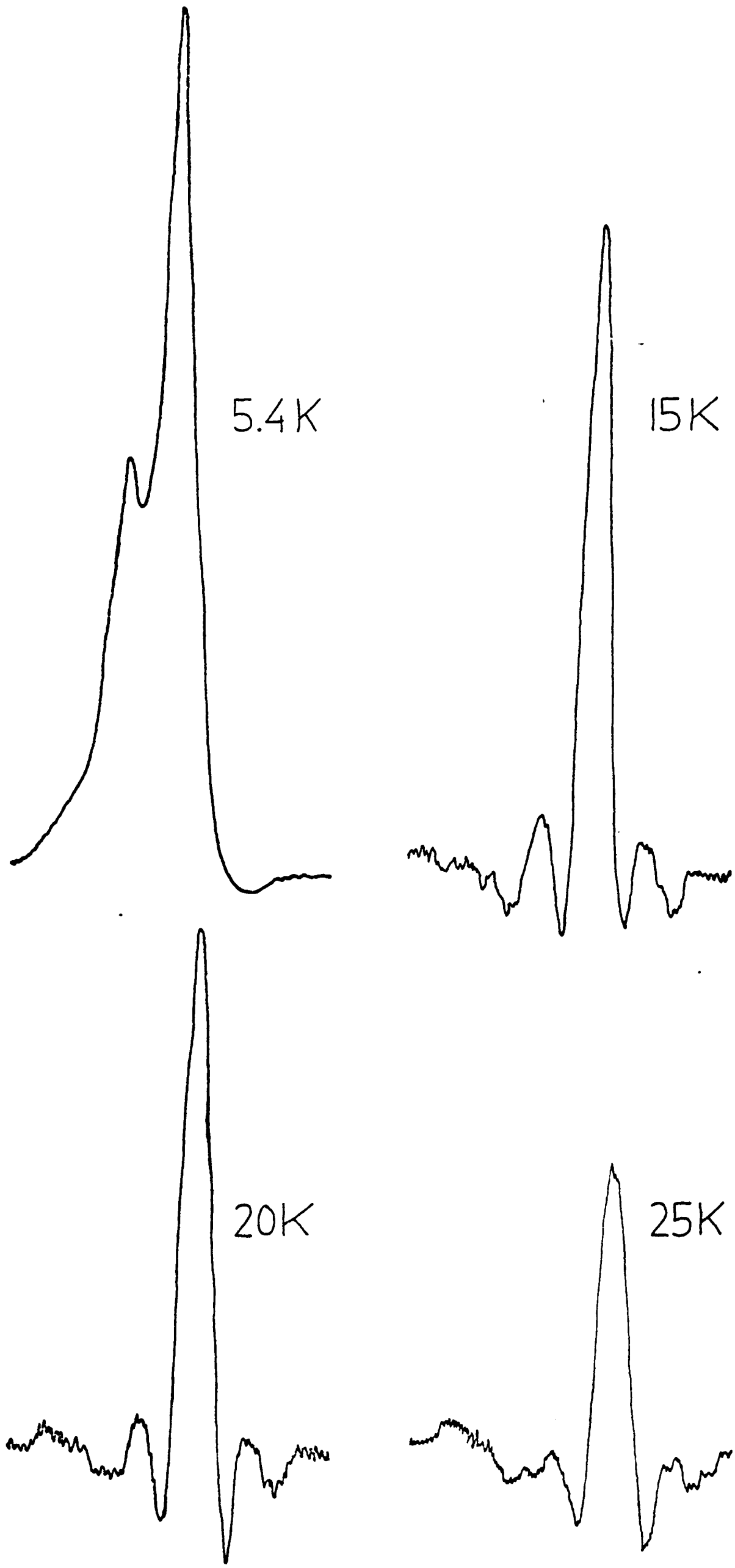

FIGURE 29.

TEMPERATURE DEPENDENCE OF THE MCD OF ORIGIN "A" OF $^4T_2(D)$ AT 5.0T.

6.9 $^4E(D)$

FIGURE 30 shows in detail the spectra of this band, and the prominent absorption features are tabulated below. Energies are quoted to the nearest wavenumber as the lines are relatively broad.

$\alpha = \sigma$ (xy)			π (z)		
ENERGY cm^{-1}	ASSIGNMENT	VIBRATIONAL MODE	ENERGY cm^{-1}	ASSIGNMENT	
26624	A	-	26624	A	-
26674	A + 50	ν_{L3}			
26738	A + 114	$\nu_2(a_{1g})$	26731	A + 107	$\nu_2(a_{1g})$
26846	B	-	26851	B	-
26903	A + 279	$\nu_1(a_{1g})$			
			26921	B + 70	ν_{L4}
			26932	B + 81	$\nu_4(b_{2g})$
26947	A + ν_1 + 44	ν_{L3}			
27034			27031		
27110			27115		
			27159		
			27211		
27241					
			27263		

TABLE XVII

FEATURES IN THE POLARISED SPECTRA BETWEEN 3780 AND 3670Å, $^4E(D)$, AT 4.2K.

The MCD overlaps with the stronger bands on either side and does not follow the axial absorption shape. Origin A at about 26632 cm^{-1} is the only line which clearly correlates with the

α-spectrum; it is a sharp -ve line superimposed on a broad +ve signal of the blue tail of $^4T_2(D)$. Between A and B, the +ve MCD signal increases in strength, then falls quite rapidly and becomes a broad -ve feature, finally overlapping into the strongly negative $^4T_1(P)$ signal. In absorption, neither A nor B couples strongly with vibrational modes, and the bulk of the intensity of $^4E(D)$ is associated with broad bands whose approximate maxima are 27030 cm^{-1} (α), and 26900 and 27200 cm^{-1} (π).

Vala's calculations [60] indicate that in cubic symmetry the spin orbit components of $^4E(D)$ should be well separated from each other as follows:

E' (+105cm^{-1}) U' (+48cm^{-1}) E'' (zero).

A very tentative assignment would be to equate E'' with A and U' with B, both predicted to have -ve MCD (see TABLE V). The other origin E' is expected to have +ve MCD and could perhaps be identified as the small upturn in the MCD signal near 3685Å, about 27516cm^{-1}, which appears to correlate with a small peak in the π-spectrum at 27159cm^{-1}. This pattern fits that calculated by Vala, but with the energy separations increased by a factor of about 5. This does not, however, account for the broad band or the linear polarisations.

Comparing with the tetragonal model (6.3) and $^4E(G)$, origin A of $^4E(D)$ has similar properties to Q, $^4A_1$, being stronger in xy- than z-polarisation and having -ve MCD. Origin B of $^4E(D)$ resembles P, $^4B_1$, stronger z than xy and with +ve MCD. Neither of the above accounts of $^4E(D)$ is fully satisfactory, however, and the true nature of the state must be left open to doubt.

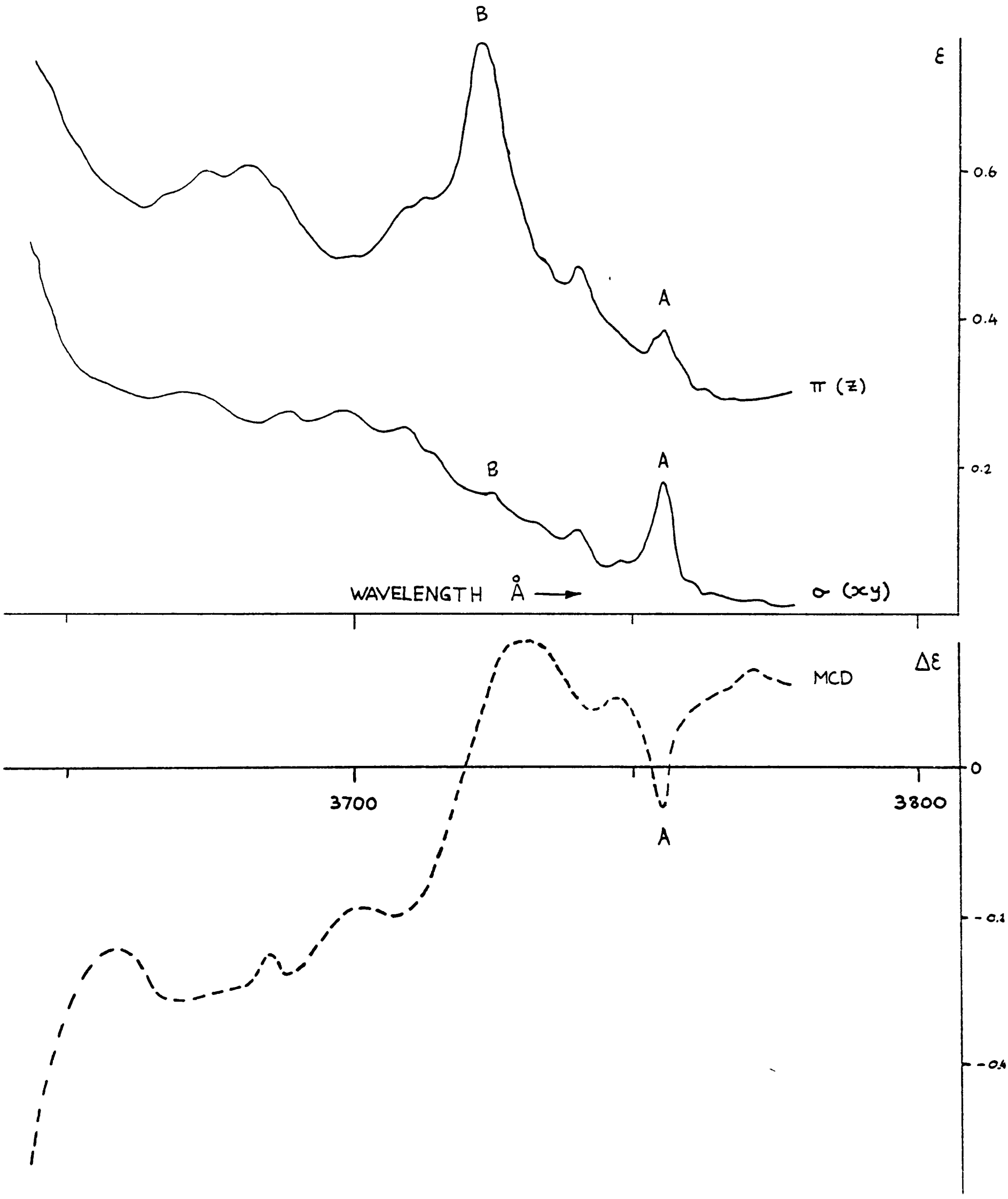

FIGURE 30.

LOW TEMPERATURE SPECTRA OF $^4E(D)$ ON EQUAL MOLAR EXTINCTION SCALES.

6.10 $^4T_1(P)$

The final band contained in REGION IV is the most intense of all the quartets, but has few features. Those which can be distinguished are tabulated below, all energies being approximate:

$\alpha = \sigma$ (xy)	MCD	π (z)
	27500 cm^{-1} (shoulder)	
27530 cm^{-1} (shoulder)		27550 cm^{-1} (shoulder)
27700 cm^{-1}	27690 cm^{-1}	27690 cm^{-1}
		27930 cm^{-1} (shoulder)
		28090 cm^{-1} (shoulder)
	28160 cm^{-1} (shoulder)	
	28420 cm^{-1} (shoulder)	
	28620 cm^{-1} (shoulder)	

TABLE XVIII

FEATURES IN THE LOW TEMPERATURE SPECTRA OF $^4T_1(P)$

Vala [60] calculated that the spin orbit components should lie close together, and they are likely to be found between 27500 and 27700 cm^{-1}. Only negative MCD is observed, the signal being very large. Given the lack of polarisation or structure of the band, no assignment can be attempted and no statements made about the relative importance of spin orbit interactions and the tetragonal perturbation.

6.11 REGION V

As previously described, no bands were found in the absorption spectra of Cs_3MnCl_5 between 3480 and 2650Å, nor was there any evidence of an MCD signal in this area, even when scanned with the electronic gain increased one hundred times above the normal level.

6.12 REGION VI GENERAL

The part of the spectrum between 2950 and 2650Å contains three band systems whose low temperature spectra are shown in FIGURES 31 and 32. Owing to the reduced efficiency of the xenon arc lamps and grating monochromators employed in the spectrometers, it was necessary to use larger slit widths to compensate for the reduced energy at these short wavelengths. Hence the resolution was poorer: about 1Å in absorption compared with 0.15Å elsewhere, and 4Å for MCD as against 1Å elsewhere. In order of increasing energy, the bands are:

(i) $^4T_1(F)$ from 2950Å to 2795Å;

(ii) $^4A_2(F)$ from 2795Å to about 2745Å;

(iii) $^4T_2(F)$ from about 2775Å to 2650Å,

and are each discussed in detail below.

The assignment of these bands has been dealt with in CHAPTER 5. $^4T_1(F)$ is just separated from the others, whose origins lie close together, so that $^4A_2(F)$ and $^4T_2(F)$ are treated together. A magnetic dipole contribution to the intensity of $^4T_2(F)$ is evident as the α- and σ-intensities are not identical.

General comparison can be made with the bands observed by Vala. In $(Me_4N)_2MnCl_4$, scattering of light produced rather

indistinct bands at high energy, while in the bromide three overlapping bands were observed [60]. The one at lowest energy was broad and relatively weak, and should probably be assigned as $^4T_1(F)$. The two higher energy bands were both structured, one with sharper, more intense lines than the other. No data on the ^4F bands of $(Et_4N)_2MnCl_4$ was available, but the bromide and iodide clearly showed three bands assigned in order of increasing energy as $^4T_1$ (-ve MCD), $^4A_2$ (+ve MCD), and $^4T_2$ (+ve MCD). In both compounds, $^4T_1$ was the weakest of the three bands in absorption.

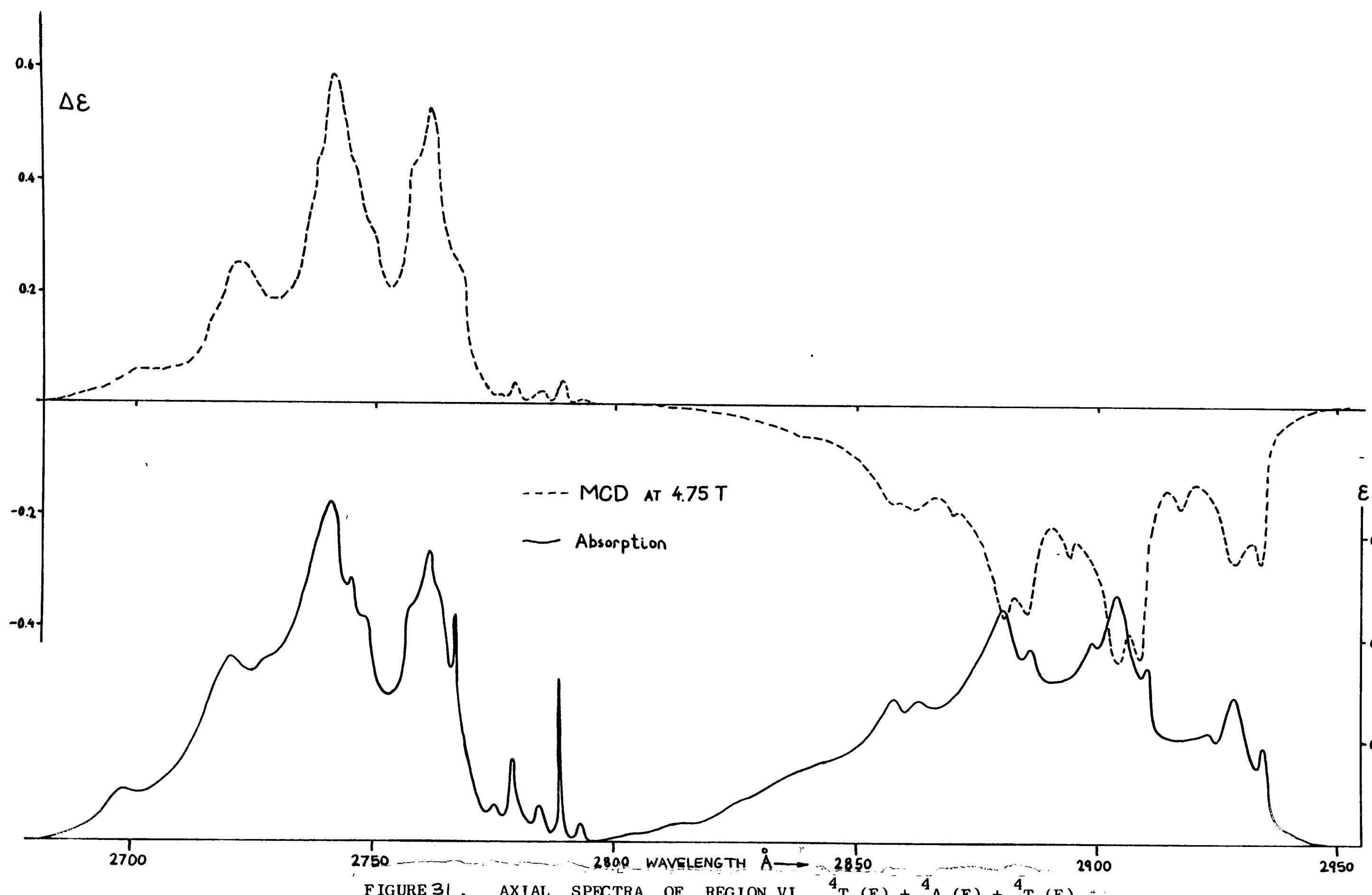

FIGURE 31. AXIAL SPECTRA OF REGION VI, $^4T_1(F) + {}^4A_2(F) + {}^4T_1(F)$.

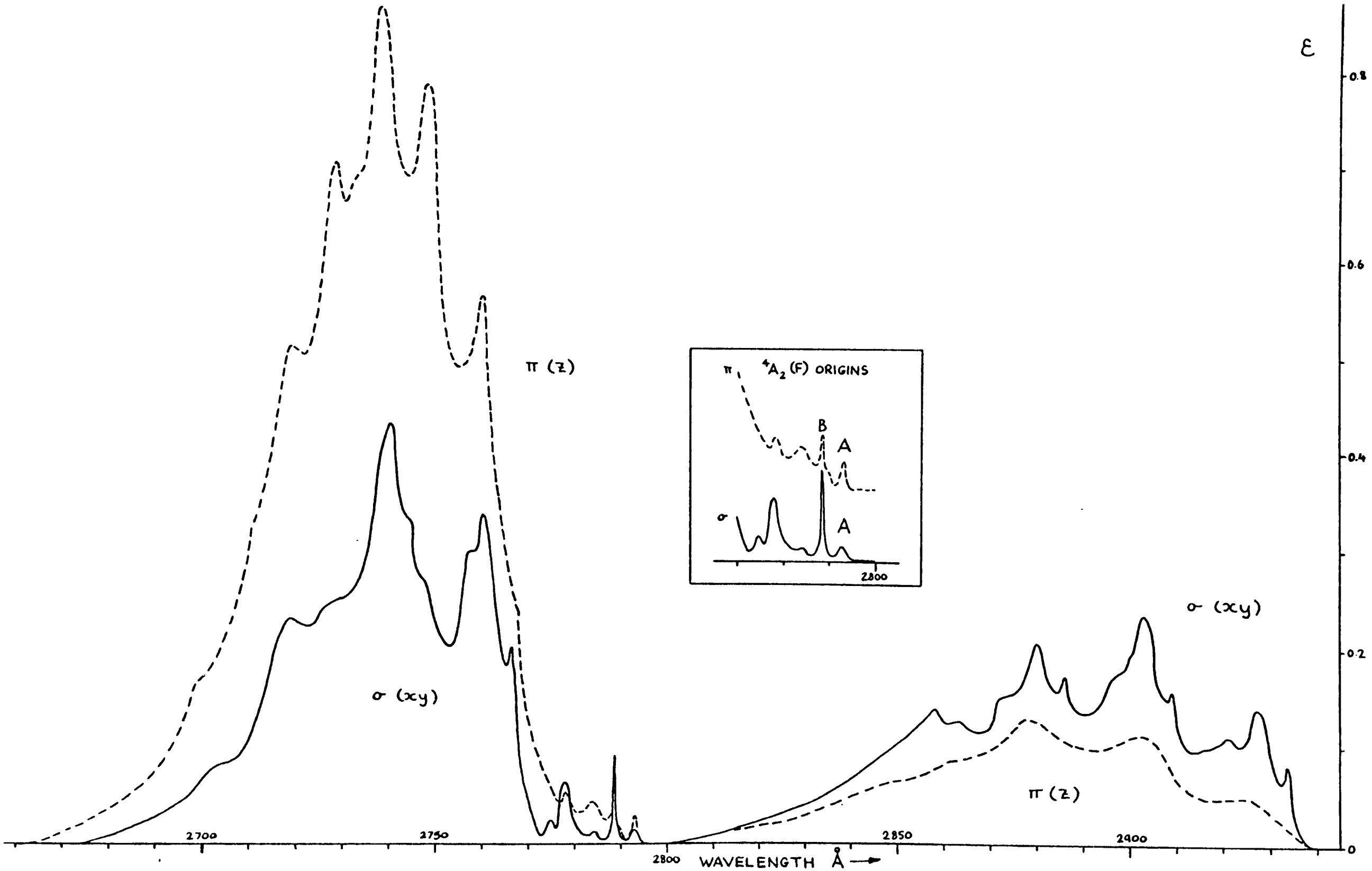

FIGURE 32. POLARISED SPECTRA OF REGION VI , 4.2K .

6.13 $\underline{^4T_1(F)}$

FIGURE 33 shows the spectra of this band recorded at 4.2K. The α- and σ-spectra are identical, and are built upon two electronic origins A and B. These couple strongly only with ν_1, five quanta of this vibration being visible, the longest progression in any of the quartets. B also couples weakly with one of the lattice modes, ν_{L4}. The MCD signal is large and entirely negative, and follows the axial absorption in shape, but with the addition of D which we assign as an electronic origin. The weaker π-spectrum shows no sharp features, but again has a long ν_1 progression built on a single broad origin C. In all cases, the details become less distinct after the third ν_1 repeat. The approximate positions of the lines are given below:

$\alpha = \sigma$ (xy)			MCD			π (z)		
ENERGY cm^{-1}	ASSIGN-MENT	VIBRL. MODE	ENERGY cm^{-1}	ASSIGN-MENT	VIBRL. MODE	ENERGY cm^{-1}	ASSIGN-MENT	VIBRL. MODE
34080	A	-	34085	A	-			
34147	B	-	34147	B	-			
						34168	C	-
34211	B+64	ν_{L4}						
			34279	D	-			
34358	A+278	$\nu_1(a_{1g})$	34377	A+292	$\nu_1(a_{1g})$			
34435	B+288	$\nu_1(a_{1g})$	34432	B+285	$\nu_1(a_{1g})$			
						34459	C+291	$\nu_1(a_{1g})$
34495	B+ν_1+60	ν_{L4}						
			34548	D+269	$\nu_1(a_{1g})$			
34647	A+567	$2\nu_1(a_{1g})$	34656	A+571	$2\nu_1(a_{1g})$			
34716	B+569	$2\nu_1(a_{1g})$	34720	B+573	$2\nu_1(a_{1g})$			
						34746	C+578	$2\nu_1(a_{1g})$
34780	B+2ν_1+64	ν_{L4}						
			34831	D+552	$2\nu_1(a_{1g})$			
34928	A+848	$3\nu_1(a_{1g})$	34947	A+862	$3\nu_1(a_{1g})$			
34990	B+843	$3\nu_1(a_{1g})$	35002	B+852	$3\nu_1(a_{1g})$			
						35039	C+871	$3\nu_1(a_{1g})$
			35119	D+840	$3\nu_1(a_{1g})$			
35224	A+1144	$4\nu_1(a_{1g})$	35227	A+1142	$4\nu_1(a_{1g})$			
35286	B+1139	$4\nu_1(a_{1g})$	35296	B+1149	$4\nu_1(a_{1g})$			
						35335	C+1168	$4\nu_1(a_{1g})$
35474	A+1394	$5\nu_1(a_{1g})$	35457	A+1372	$5\nu_1(a_{1g})$			
35537	B+1390	$5\nu_1(a_{1g})$	35524	B+1377	$5\nu_1(a_{1g})$			
						35587	C+1419	$5\nu_1(a_{1g})$

TABLE XIX.

FEATURES IN THE LOW TEMPERATURE SPECTRA OF $^4T_1(F)$.

Vala's spin orbit calculations give the components of $^4T_1(F)$ the following relative energies:

U' (+173 cm^{-1}) E" (+153 cm^{-1}) U' (+13 cm^{-1}) E' (zero)

which are quite close in magnitude to the observed origin spearations. A and D clearly have larger MCD than absorption intensity, and according to the cubic model these would be E" and U'3/2, see TABLE V. Origin B would then correspond to E' with a smaller $\Delta d/D$ value, while C could be U'5/2 which has effectively no MCD intensity. This ordering does not agree with Vala's predictions nor does it account for the observed linear polarisation behaviour. For a possible account of this, we refer to the tetragonal perturbation model outlined in 6.3 Origins A and B are seen only in xy-polarisation and have large MCD, and are assigned as the E' and E" components of $^4A_2$ (correlating with $^4T_1$ O). As A is the more intense in MCD, it is assigned as E' with $m_s = \pm 3/2$, while B is E" with $m_s = \pm 1/2$. The broad origin C seen alone in the π-spectrum is assigned to ^4E (correlating with $^4T_1 \pm 1$). There could be a contribution to the xy-intensity from C as demanded by the model, but this would lie under the sharper features due to A and B. The assignment of D remains uncertain. As a sharp feature with strong MCD, it shows a resemblance to A and B, but $^4A_2$ can only give rise to two origins in D_{2d}*. Possibly D is a sideband of A made apparent only through the increased intensity of A in MCD relative to B, but the spacing of about 194 cm^{-1} does not fit in well with any of the known vibrational frequencies except $2\nu_4(b_{2g})$. However, the "missing" $A + \nu_4(b_{2g})$ line could be obscured by B, and the ν_1 repeats of D follow the same intensity pattern as those of A. Alternatively, D could be one of the components of ^4E made prominent

in MCD by the presence of a small +ve signal close to it on the low energy side. This would explain why D does not correlate with any definite feature in the α- or π-spectra. Whatever the explanation may be, it is clear that the tetragonal distortion is dominant over spin orbit coupling in perturbing $^4T_1(F)$, yet the $\Delta d/D$ value remains close to the theoretical prediction, see TABLE VI.

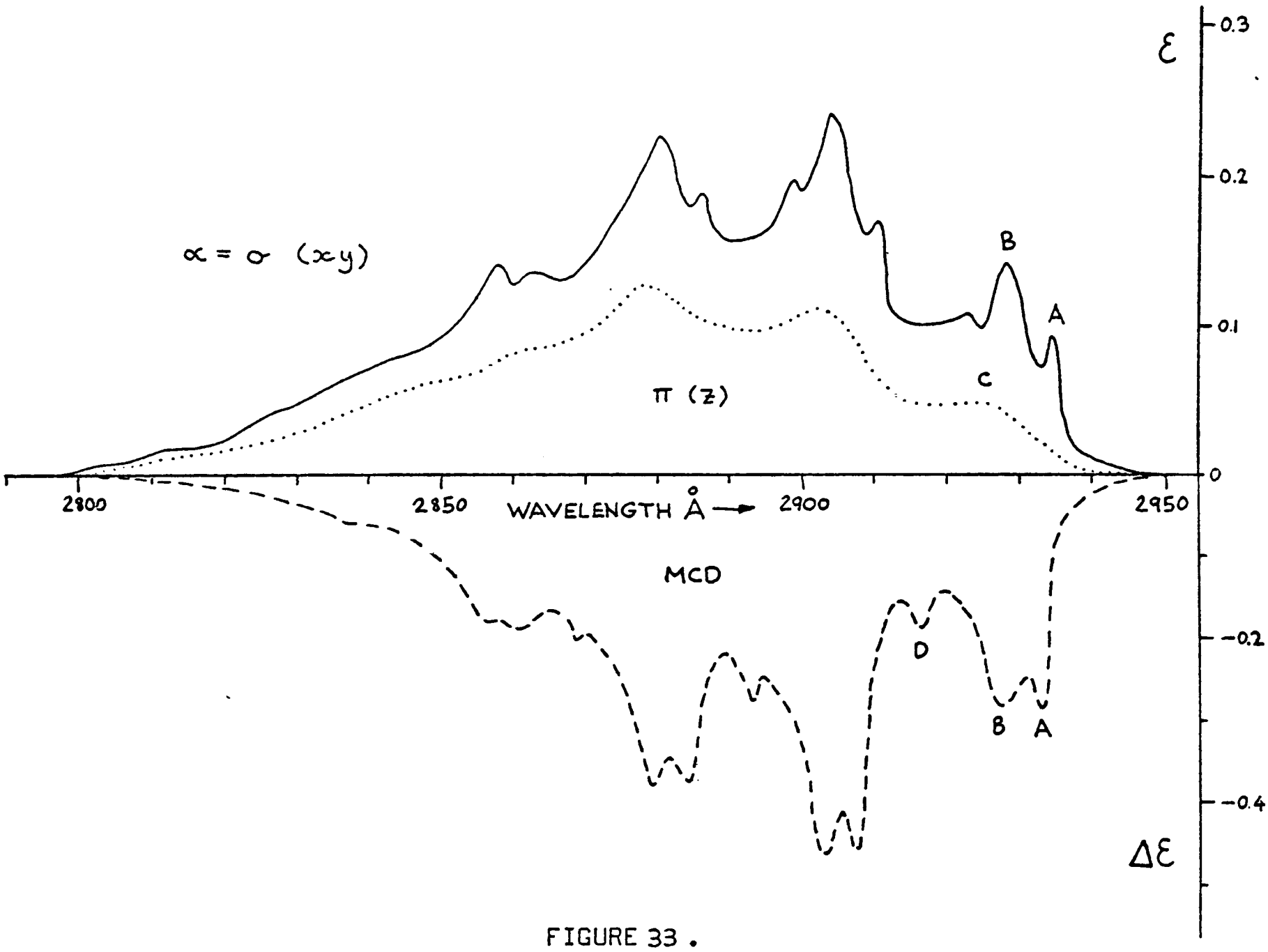

FIGURE 33 .

LOW TEMPERATURE SPECTRA OF REGION VI , $^4T_1(F)$.

6.14 $^4A_2(F)$ AND $^4T_2(F)$

Between 2795 and 2650Å in the spectra of Cs_3MnCl_5 are found two overlapping band systems as shown in FIGURE 34. These are assigned as being built upon a total of four electronic origins, A and B from $^4A_2$, and C and D from $^4T_2$. Each band is of a very different character. The lines of $^4A_2$ are of very low oscillator strength, but are quite sharp and show coupling of the electronic origins with lattice vibrations as well as chromophore ion modes. In contrast, C and D of $^4T_2$ are intense and broad, and show strong coupling only with ν_1. Smaller features seen on the $^4T_2$ band can be assigned as sidebands of origin B of $^4A_2$, as shown below:

(xy)			MCD			(z)		
ENERGY cm^{-1}	ASSIGNMENT	VIBRL. MODE	ENERGY cm^{-1}	ASSIGNMENT	VIBRL. MODE	ENERGY cm^{-1}	ASSIGNMENT	VIBRL. MODE
35803	A	-	35813	A	-	35804	A	-
35861	B	-	35877	B	-	35863	B	-
35916	B+55	ν_{L3}, ν_{L4}	35932	B+55	ν_{L3}, ν_{L4}	35920	B+57	ν_{L3}, ν_{L4}
35956	B+95	$\nu_4(b_{2g})$						
35991	B+130	$\nu_4(e_g)$	35997	B+120	$\nu_4(e_g)$	35997	B+134	$\nu_4(e_g)$
36036								
			36053			36049		
36140	B+281	$\nu_1(a_{1g})$	36135	B+258	$\nu_1(a_{1g})$	36140	B+277	$\nu_1(a_{1g})$
36193	B+ν_1+53	ν_{L3}, ν_{L4}						
36219	C	-	36212	C	-	36232	C	-
36267	B+ν_1+127	$\nu_4(e_g)$	36234	B+ν_1+99	$\nu_4(e_g)$			
36390	D	-	36370	D	-	36390	D	-
36423	B+562	$2\nu_1(a_{1g})$						
36490	C+271	$\nu_1(a_{1g})$	36476	C+264	$\nu_1(a_{1g})$	36516	C+284	$\nu_1(a_{1g})$
36550	B+2ν_1+127	$\nu_4(e_g)$						
36663	D+273	$\nu_1(a_{1g})$				36653	D+263	$\nu_1(a_{1g})$
36768	C+548	$2\nu_1(a_{1g})$	36753	C+541	$2\nu_1(a_{1g})$	36785	C+553	$2\nu_1(a_{1g})$
						36941	D+551	$2\nu_1(a_{1g})$
37058	C+839	$3\nu_1(a_{1g})$	37036	C+824	$3\nu_1(a_{1g})$	37092	C+860	$3\nu_1(a_{1g})$

TABLE XX .

FEATURES IN THE SPECTRA BETWEEN 2795Å AND 2650Å OF REGION VI , $^4A_2(F)$ + $^4T_2(F)$, AT 4.2K .

Origins A and B are assigned as the components E'' and E' respectively which arise in D_{2d}^{*} from $^4A_2$. This is based on the intensities of the linear polarisations and the MCD. The tetragonal perturbation model of 6.3 predicts that E' will be more intense in xy- than z-polarisation (theoretical ratio 11:9) and have large +ve MCD, while E'' will be more intense in z- than xy-polarisation (theoretical ratio 12:8) and will have a +ve MCD about 7 times smaller than that of E'. These predictions are in good agreement with the observed σ, π, and MCD spectra shown in FIGURE 34. The reason for the large intensity of B in the α-spectrum is that the wavelength scan was slower and so gives a true indication of the intensity of the line, whose half width is instrument limited. The σ- and π-spectra were taken from more rapid scans. Thus it is not possible to determine if the α- and σ-spectra show any important differences in origin intensity attributable to the presence of magnetic dipole transitions. The sidebands however seem to be of very similar intensities. The agreement between observed and calculated $\Delta d/D$ values is not very good, but there are large uncertainties in the measured band areas owing to difficulty of measurement and possible overlap with the more intense $^4T_2$.

According to Vala's calculations [60], the spin orbit components of $^4T_2(F)$ are separated as follows:

U' (+149 cm^{-1}) E' (+143 cm^{-1}) U' (+84 cm^{-1}) E'' (zero).

In the tetrahedral model, E'' has no first order intensity either in absorption or MCD, so that three origins should be observed. As two are calculated to be only 6 cm^{-1} apart, or 0.5Å at this wavelength, then the presence of only two origins C and D

supports this prediction. However, the separation is over three times the calculated value. From the axial and MCD intensities, C is tentatively assigned as U'3/2, leaving D as E' + U'5/2. The model is not able to explain the observed strong linear polarisation of origins C and D. It is possible that the weak features at 36036 cm^{-1} (α) and 36049 cm^{-1} (π), which were not assigned as part of $^4A_2$, could be due to E". Their low intensities must then arise as a result of second order spin orbit interactions. The behaviour of $^4T_2(F)$ can not readily be explained by means of the tetragonal perturbation model, which predicts separation into $^4B_2$ (xy-only) and ^4E (allowed xy and z). As origins C and D are both more intense in π than α, they should be components of ^4E and should only have small +ve MCD, whereas in fact they give rise to large signals. Further, the α- and σ- spectra are not identical, for although the same lines are present in each, the σ-intensities are larger by a factor of about 1.3, and we must conclude that magnetic dipole transitions are present. In spite of this, there is good agreement between the observed and calculated $\Delta d/D$ values.

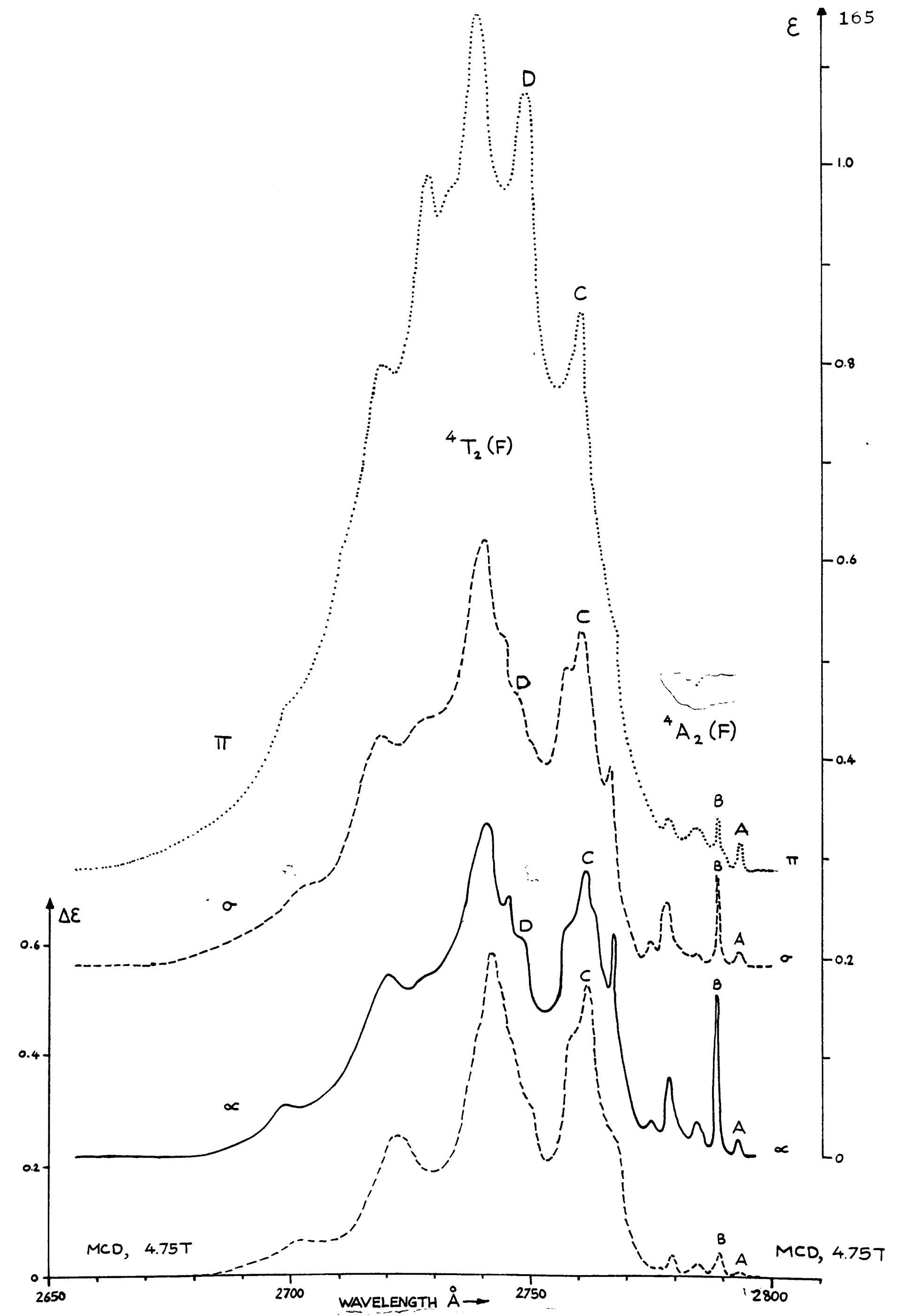

FIGURE 34.

SPECTRA OF $^4T_2(F)$ AND $^4A_2(F)$ AT 4.2K .

A P P E N D I X I

CHARACTER, MULTIPLICATION, AND CORRELATION TABLES FOR T_d AND T_d^*.

These tabulations are from references [1,3, and 4], where their derivation and use are explained.

(i) CHARACTER TABLES FOR T_d AND T_d^*.

T_d	1	$8C_3$	$3C_2$	$6S_4$	$6\sigma_d$		
A_1	1	1	1	1	1		$(x^2+y^2+z^2)$
A_2	1	1	1	-1	-1		$(2z^2-x^2-y^2,\ x^2-y^2)$
E	2	-1	2	0	0		
T_1	3	0	-1	1	-1	(R_x, R_y, R_z)	
T_2	3	0	-1	-1	1	(x, y, z)	(xy, yz, zx)

T_d^*	1	R	$8C_3$	$8C_3R$	$6C_2$	$6S_4$	$6S_4R$	$12\sigma_d$
E'	2	-2	1	-1	0	$\sqrt{2}$	$-\sqrt{2}$	0
E''	2	-2	1	-1	0	$-\sqrt{2}$	$\sqrt{2}$	0
U'	4	-4	-1	1	0	0	0	0

(ii) MULTIPLICATION TABLE FOR T_d AND T_d^*.

$T_d+T_d^*$	A_1	A_2	E	T_1	T_2	E'	E''	U'
A_1	A_1							
A_2	A_2	A_1						
E	E	E	A_1+A_2+E					
T_1	T_1	T_2	T_1+T_2	$A_1+E+T_1+T_2$				
T_2	T_2	T_1	T_1+T_2	$A_2+E+T_1+T_2$	$A_1+E+T_1+T_2$			
E'	E'	E''	U'	E'+U'	E''+U'	A_1+T_1		
E''	E''	E'	U'	E''+U'	E'+U'	A_2+T_2	A_1+T_1	
U'	U'	U'	E'+E''+U'	E'+E''+2U'	E'+E''+2U'	E+T_1+T_2	E+T_1+T_2	A_1+A_2+E +2T_1+2T_2

(iii) CORRELATION OF THE REPRESENTATIONS OF T_d, T_d^* AND D_{2d}, D_{2d}^*

T_d		D_{2d}	T_d^*		D_{2d}^*
A_1	⟶	A_1	E'	⟶	E'
A_2	⟶	B_1	E''	⟶	E''
E	⟶	$A_1 + B_1$	U'	⟶	$E' + E''$
T_1	⟶	$A_2 + E$			
T_2	⟶	$B_2 + E$			

In a simplistic way, one can imagine that the existence of an S_4-axis in tetrahedral symmetry permits up to fourfold degeneracy, while the C_2-axis in the lower symmetry allows only twofold degeneracy.

A P P E N D I X II

PREPARATION AND PROPERTIES OF Cs_3MnCl_5

II.1 PREPARATION OF SINGLE CRYSTALS

The CsCl-$MnCl_2$ phase diagram is given in the compilation of Levin et al [103]. This shows that Cs_3MnCl_5 exists as a distinct compound, melting point 511°C [104]. The preparation was carried out by the Bridgman-Stockbarger method using the apparatus of the Crystal Growing Unit, in the Clarendon Laboratory, Oxford. The best results were obtained as follows:

"AnalaR" grade CsCl and $MnCl_2$ were purified by sublimation under vacuum, and were weighed out in the stoichiometric proportions. This was done in a dry box as both materials are strongly hygroscopic. They were mixed and again sublimed under vacuum into a silica tube in which a small quantity of pure benzene had been pyrolysed. The coating of carbon deposited on the walls of the tube prevented the contents from adhering to the walls during cooling. The tube was sealed under vacuum, and the ampule so formed was placed in the crystal growing apparatus. It was slowly heated up to 520°C in the furnace, causing the contents to form a homogeneous melt of Cs_3MnCl_5. The ampule was then lowered over a period of three days through a very carefully controlled temperature gradient into a region at 500°C. During this period, crystallisation took place along with a certain amount of zone refining. Cooling then proceeded more rapidly to room temperature. Over the range 500° to 20°C, the crystal contracted by about 20%, and broke up into large lumps, each a single crystal.

II.2 PROPERTIES OF Cs_3MnCl_5.

Anhydrous $MnCl_2$ is extremely air sensitive, but crystalline pieces of $CsMnCl_5$ were found to be stable in air if kept dry. On removal from the ampule, the crystals were kept in a dry box. They displayed no obvious morphology, and the optical axis was located by use of x-rays. This work was performed in the Chemical Crystallography Department, Oxford with the kind assistance of Dr. D.J. Watkin. A large piece of crystal was mounted in soft wax on a goniometer head, a thin edge was brought into the x-ray beam, and a precession photograph was taken. A long exposure time, 4-5 hours, was found to be necessary because of the opacity of the crystal to x-rays. During this time, the surface of the crystal acquired a white film, but the bulk remained clear. By examination of the photographs and reorientation of the crystal, the fourfold symmetry axis was located. Faces were polished perpendicular to this axis for axial absorption and MCD measurements. A second crystal was examined in the same way, and faces polished parallel to the fourfold axis for polarised absorption. Thus the optical properties of Cs_3MnCl_5 were determined, using crystals 1.5 to 2.5 mm thick.

To the naked eye, Cs_3MnCl_5 crystals have a pale yellow colour under natural light. They are stable in dry air and can be handled quite casually provided that the natural surface of the crystal is intact. After repeated handling, polishing, and cooling to low temperatures, deterioration was more rapid. However, it was possible to use the same section of polished crystal for several experiments by exercising due care in handling and storage, and repolishing the surfaces immediately prior to each experiment.

The crystal structure of Cs_3MnCl_5 is illustrated in FIGURE 35. The crystal belongs to the tetragonal class, space group D_{4h}^{18}, with four formula units in the unit cell, whose dimensions [2] are:

$$a = b = 9.214\text{Å}, \quad c = 14.908\text{Å}.$$

Based on the above parameters, the density is calculated as 3.313 gm/cm^3, and the $MnCl_4^{2\ominus}$ chromophore concentration is 5.25M. This factor was used in all calculations for the conversion of observed (differential) optical density to extinction units.

Magnetic and thermodynamic measurements down to very low temperatures [71] showed that Cs_3MnCl_5 becomes antiferromagnetic at 0.6K, with a very small degree of short range ordering persisting up to about 0.8K. Above these temperatures, the crystal is magnetically dilute, and the magnetic susceptibility follows the Curie-Weiss law accurately. All the magnetic data was in accord with S = 5/2 and a g-value very close to 2 for the ground state [33].

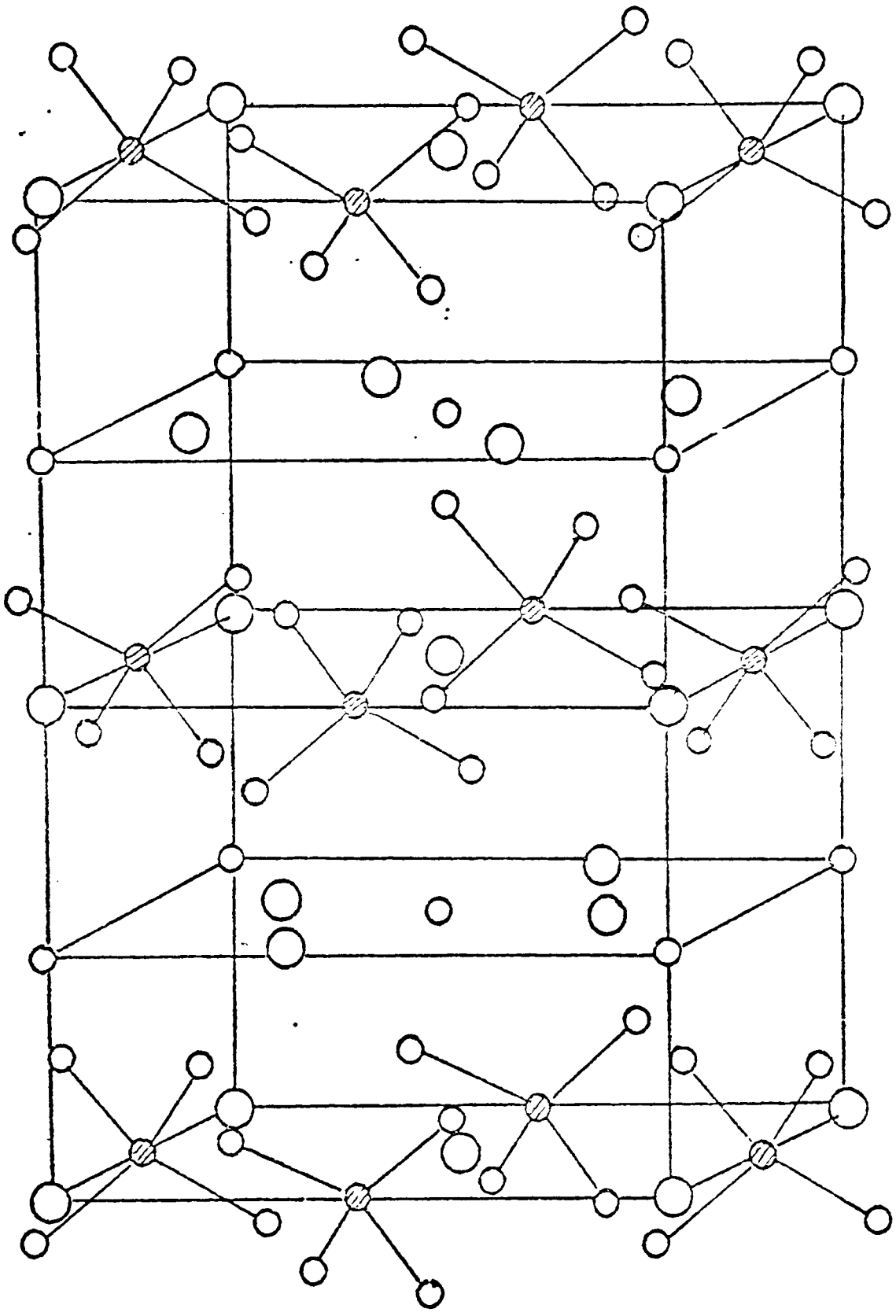

FIGURE 35 .

UNIT CELL OF Cs_3MnCl_5 [2] .

Dimensions of isomorphous ccmpounds :

○ Cs
○ Cl
⊘ Mn

	a = b (Å)	c (Å)
Cs_3MnCl_5	9.2	14.9
Cs_3CoCl_5	8.7	14.0
Cs_3CoBr_5	9.6	15.2
Cs_3ZnCl_5	9.2	14.9

A P P E N D I X III

MEASUREMENT OF MCD SPECTRA

III.1 GENERAL DESCRIPTION

The MCD spectra of Cs_3MnCl_5 were recorded on an instrument whose optical and electronic design and performance have been reported in detail [80]. It combines "simultaneous" measurement of circular dichroism and absorption spectra at high resolution. A schematic diagram of the optical arrangement is shown in FIGURE 36. Briefly. light from a water cooled 500 watt xenon arc lamp passes through a Hilger and Watts D331 double monochromator, is filtered, collimated, and linearly polarised. Right and left circularly polarised light alternating at 50 kHz is then produced using a quartz accousto-optic modulator. The beam then passes through the sample housing to the detector, a photomultiplier. Part of the light beam bypasses the sample to provide a reference signal for the absorption channel. The photomultiplier output signal is then processed by the electronic circuits outlined in FIGURE 36, and the absorbance and circular dichroism signals are plotted out on a dual channel chart recorder.

III.2 CRYOSTAT

The crystals were mounted in an Oxford Instruments cryostat which has superconducting coils wound round the bore. Magnetic fields up to 4.75 Tesla may be generated, co-axial with the light beam passing down the bore. Samples suitably mounted on a copper plate can be maintained at a steady temperature in the range 4.2 - 77K with the help of a "Harwell" automatic

temperature controller. The sample plate is screwed onto a copper block provided with heating wires and a thermocouple for temperature measurement. The block is insulated from the liquid helium well by a vacuum space. By introducing a small quantity of helium gas, about 10^{-3} torr, the crystal is cooled to 4.2K. This transfer gas is then pumped off to minimise the rate at which the liquid helium boils off; the crystal remains at 4.2K.

III.3 ABSORPTION CHANNEL

In spite of the desirability of having absorption and MCD spectra measured simultaneously, the absorption channel was not used in this study. There were several reasons for this: the baseline was not flat, and was badly affected by lamp lines; the signal:noise ratio was poor owing to the low light levels and short sampling time (1/30th second); it offered poor resolution compared with the McPherson RS10 (see APPENDIX IV); and the absorption signal often interfered with the more important MCD on the chart recorder. In addition to these practical considerations, the absorption spectrum so measured would be subject to serious deviations from the Beer-Lambert law. Woldbye and Baggar [105] showed that the simple form:

$$OD = \log_{10}(I_o/I) = \varepsilon cd$$

does not apply to a non-isotropic medium. The actual dependence was shown to be:

$$OD = \varepsilon cd - \log_{10}\left\{\cosh(\ln 10\,\Delta\varepsilon cd/2)\right\},$$

where $\varepsilon = (\varepsilon_L + \varepsilon_R)/2$

and $\Delta\varepsilon = (\varepsilon_L - \varepsilon_R)$.

To a first approximation,

$$\text{True OD} = \text{Apparent OD} - 0.288\ (\Delta\text{OD})^2.$$

The correction becomes important at large values of OD; if OD 1, then ΔOD = 0.6 gives a noticeable distortion. Also, the effect will vary with wavelength, and will be dependent on the temperature and the field strength. For many of the bands of Cs_3MnCl_5 crystals, differential optical densities over 2 were encountered.

III.4 MCD CHANNEL

The circular dischroism signal is electronically recovered and processed from the 50kHz coherent component of the alternating output of the PMT. It is a sine wave whose amplitude is directly related to the size of the CD, and its phase relative to the reference signal from the modulator determines the sign. The instrument is calibrated by use of a reference material, (+) $[Co(en)_3]\,Cl_3$ in aqueous solution. The first absorption band in the visible region around 4900Å is known to have $\Delta OD_{max}/OD_{max} = 0.0202$, the absolute sign being positive [73]. Thus a solution of known ΔOD can easily be prepared, and used to calibrate the MCD scale and to check the linearity of the variable gain amplifier and automatic gain control loop. The system was found to function well.

In order to determine the calibration factor, we use the description of circular dichroism given in 2.2, and follow the treatment of Velluz et al [106]. The Beer-Lambert law can be stated in the form:

$$I = I_o e^{-4\pi\chi d/\lambda}.$$

A circularly dichroic material possesses two distinct indices of extinction χ_L and χ_R referring to LCP and RCP light respectively. In an electro-optic modulator, linearly polarised light is subject to a lag:

$$\delta = \delta_o \sin wt$$

where w is the modulation frequency.

The emergent flux ϕ_o may be considered as being composed of left and right circularly polarised parts, ϕ_L and ϕ_R respectively:

$$\phi_L = \frac{\phi_o}{2}(1 + \sin\delta) = \frac{\phi_o}{2}[1 + \sin(\delta_o \sin wt)]$$

$$_R = \frac{\phi_o}{2}(1 - \sin\delta) = \frac{\phi_o}{2}[1 - \sin(\delta_o \sin wt)]$$

The total flux $\phi_L + \phi_R$ is constant at all times.

After passage through a dichroic material, we have:

$$\phi'_L = \phi_L \; e^{-4\pi\chi_L d/\lambda} \qquad \phi'_R = \phi_R \; e^{-4\pi\chi_R d/\lambda}$$

Photomultiplier output voltage is the product of sensitivity $S(\lambda)$ and flux ϕ. The total output will be composed of two parts, one static, V_c, and the other V_{mod} varying at the modulation frequency:

$$V_c = \frac{S\phi_o}{2}\left[e^{-4\pi\chi_L d/\lambda} + e^{-4\pi\chi_R d/\lambda}\right]$$

$$V_{mod} = \frac{S\phi_o}{2}\left[e^{-4\pi\chi_L d/\lambda} - e^{-4\pi\chi_R d/\lambda}\right]\sin(\delta_o \sin wt)$$

The observed output from the phase sensitive detector (PSD) corresponds to the modulated part of the photomultiplier output, and is given by:

$$V_{PSD} = \frac{GS\phi_o}{2}\left[e^{-4\pi\chi_L d/\lambda} - e^{-4\pi\chi_R d/\lambda}\right] \times \frac{1}{\pi}\int_0^{\pi} \sin(\delta_o \sin wt)\, dwt.$$

$\mathcal{G}$ is the electronic amplification (gain) applied to the alternating component of the PMT output. The ratio of the alternating and static signals is:

$$\frac{V_{PSD}}{V_c} = \mathcal{G}\left\{\frac{e^{-4\pi\chi_L d/\lambda} - e^{-4\pi\chi_R d/\lambda}}{e^{-4\pi\chi_L d/\lambda} + e^{-4\pi\chi_R d/\lambda}}\right\} \times \frac{1}{\pi}\int_0^{\pi} \sin(\delta_0 \sin wt)\, dwt$$

$$= \mathcal{G} \tanh\left[2\pi(\chi_R - \chi_L)d/\lambda\right] \times \frac{1}{\pi}\int_0^{\pi} \sin(\delta_0 \sin wt)\, dwt$$

The integral factor can be taken as constant as the instrument is always set up so as to maximise the PSD output voltage for the standard test material, (+) $[Co(en)_3]Cl_3$ solution. Then we have:

$$\frac{V_{PSD}}{V_c} = -\mathcal{G}\, k' \tanh\left[2\pi(\chi_L - \chi_R)d/\lambda\right]$$

$$= \mathcal{G}\, k'' \tanh\left[2\pi\Delta\chi\, d/\lambda\right].$$

This is related to the differential optical density ΔOD since:

$$e^{-4\pi\Delta\chi d/\lambda} = 10^{-\Delta OD}$$

i.e. $4\pi\Delta\chi\, d/\lambda = \Delta OD \ln 10$

$$\frac{V_{PSD}}{V_c} = \mathcal{G}\, k'' \tanh\left[\Delta OD \frac{\ln 10}{2}\right].$$

The hyperbolic tangent can be expanded as a power series:

$$\tanh x = x - \frac{x^3}{6} + \ldots.$$

and to a first approximation we have:

$$\frac{V_{PSD}}{V_c} = \mathcal{G}\, k\, \Delta OD \quad \text{where } k = k'' \frac{\ln 10}{2}.$$

This expression will be valid only for small values of ΔOD as only the first term of the power series has been considered. For $\Delta OD \sim 0.3$ optical density units, the error is about 1%, rising rapidly as ΔOD increases.

In FIGURE 36, the electronic diagram shows that it is the output of the phase sensitive detector V_{PSD} which is displayed on the chart recorder as the MCD signal. Rearranging the above equations, we have:

$$\Delta OD = \frac{2}{\ln 10} \tanh^{-1} \left\{ \frac{\ln 10 \; V_{PSD}}{2 G k V_c} \right\},$$

while for small values of OD we can use the simpler form:

$$\Delta OD = \frac{V_{PSD}}{G k V_c}$$

The calibration factor k was determined by use of $(+)[Co(en)_3]Cl_3$ as follows. A solution was made up to have an absorbance just below unity at 4800Å, the exact value being found by measurement on a Cary 14 double beam spectrophotometer. Such a solution gives rise to a small positive circular dichroism signal around 4900Å related to the absorbance value by the factor +0.0202 [73]. Knowing the electronic gain G and the set control level V_c, the observed peak deflection of the chart recorder can be determined in differential optical density units, yielding the calibration factor k. As the ΔOD value is small, no error arises from the use of the approximate formula.

In the measurement of the MCD spectra of crystals at low temperatures and high magnetic fields, ΔOD values are often quite large, and the error arising from use of the approximate relationship becomes more serious. This is illustrated in FIGURE 37, where the true value of ΔOD is always larger than the apparent value displayed on the chart recorder. The most obvious effect is that intense bands appear to be flat topped when the spectrum is scanned. If spectra are also recorded digitally, e.g. on punched tape, for computer processing and

plotting, it is a relatively easy matter to incorporate the inverse hyperbolic tangent correction into the data-handling program. This was done for some spectra of $(Et_4N)_2ZnI_4$ crystals doped with Co^{2+} [107], and a typical result is shown in FIGURE 38. (The two bands shown are the E'' and U' components of the $^2T_2(D) \longleftarrow {}^4A_2(F)$ transition measured at 4.2K in a magnetic field of 4.75T parallel to the fourfold axis of the tetragonal crystal.) Spectra which were not digitised were corrected by replotting by hand point by point taking into account the gain and control level settings. This latter method was used for Cs_3MnCl_5. In either case, the inverse hyperbolic tangent function $\tanh^{-1}x$ becomes very sensitive to small changes in x as x approaches unity - see FIGURE 37 - and peaks showing very large circular dichroism are truncated at or below a ΔOD value of 2.4, corresponding to x = 0.984, or an apparent ΔOD value of 1.14.

The limit of resolution with the D331 monochromator was about 1Å, and this becomes a severe restriction when very sharp line spectra are being studied. In order to overcome this, modifications were made to the McPherson RS10 spectrometer by Dr. E.R. Krausz, allowing MCD spectra to be recorded at a resolution of about 0.15Å. Also, a Thor Instruments cryostat generating fields up to 5 Teslas became available. It was with this system that the MCD spectra shown in FIGURES 20 and 29 were recorded.

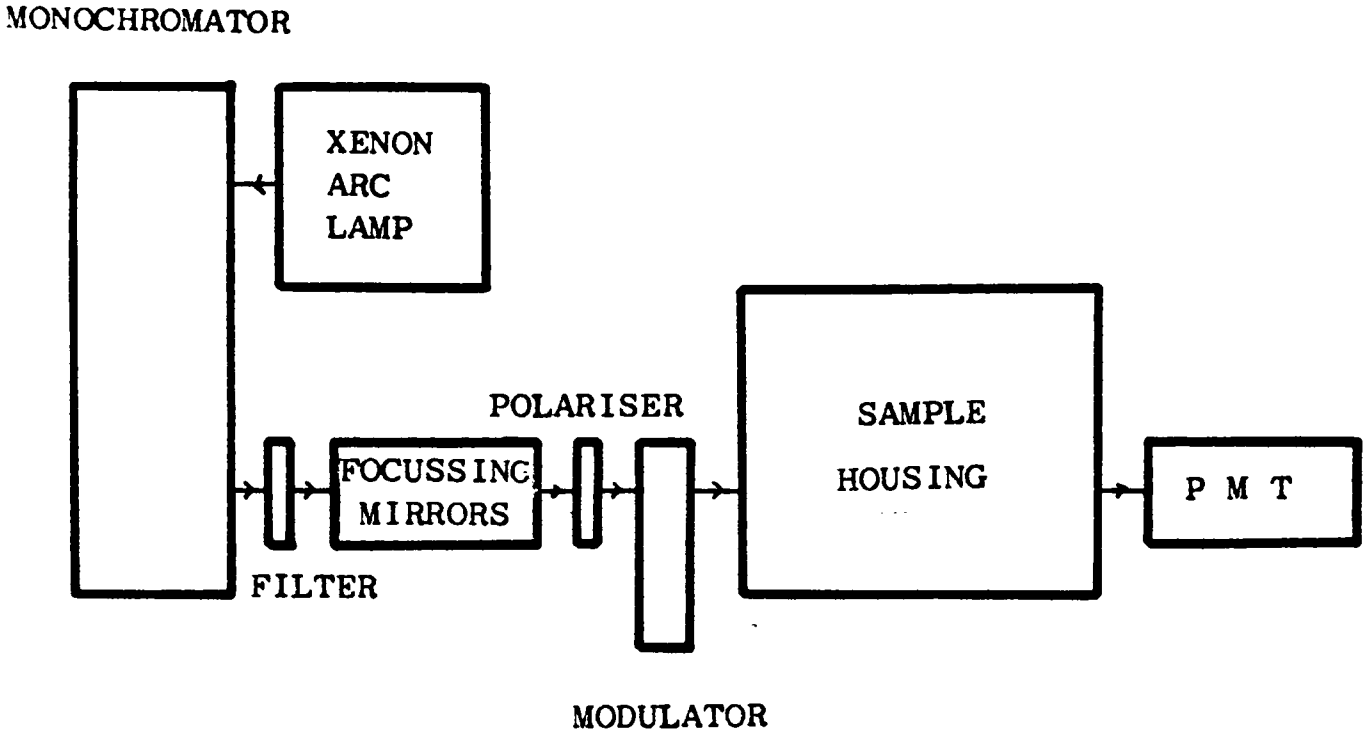

FIGURE 36.

AN OUTLINE OF THE M C D MACHINE
TOP : OPTICS BOTTOM : ELECTRONICS

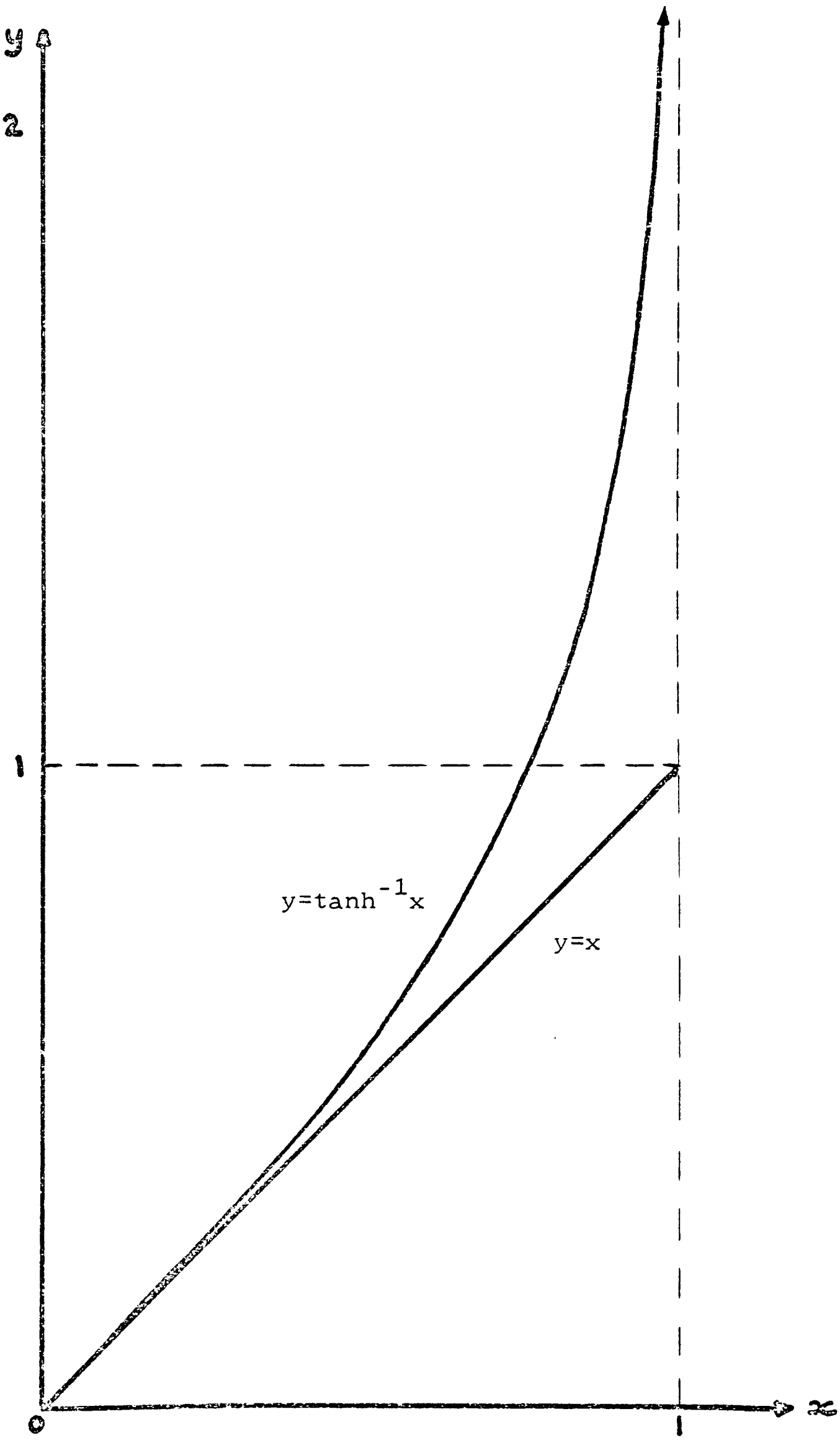

FIGURE 37.

COMPARISON OF REAL AND APPARENT ΔOD .

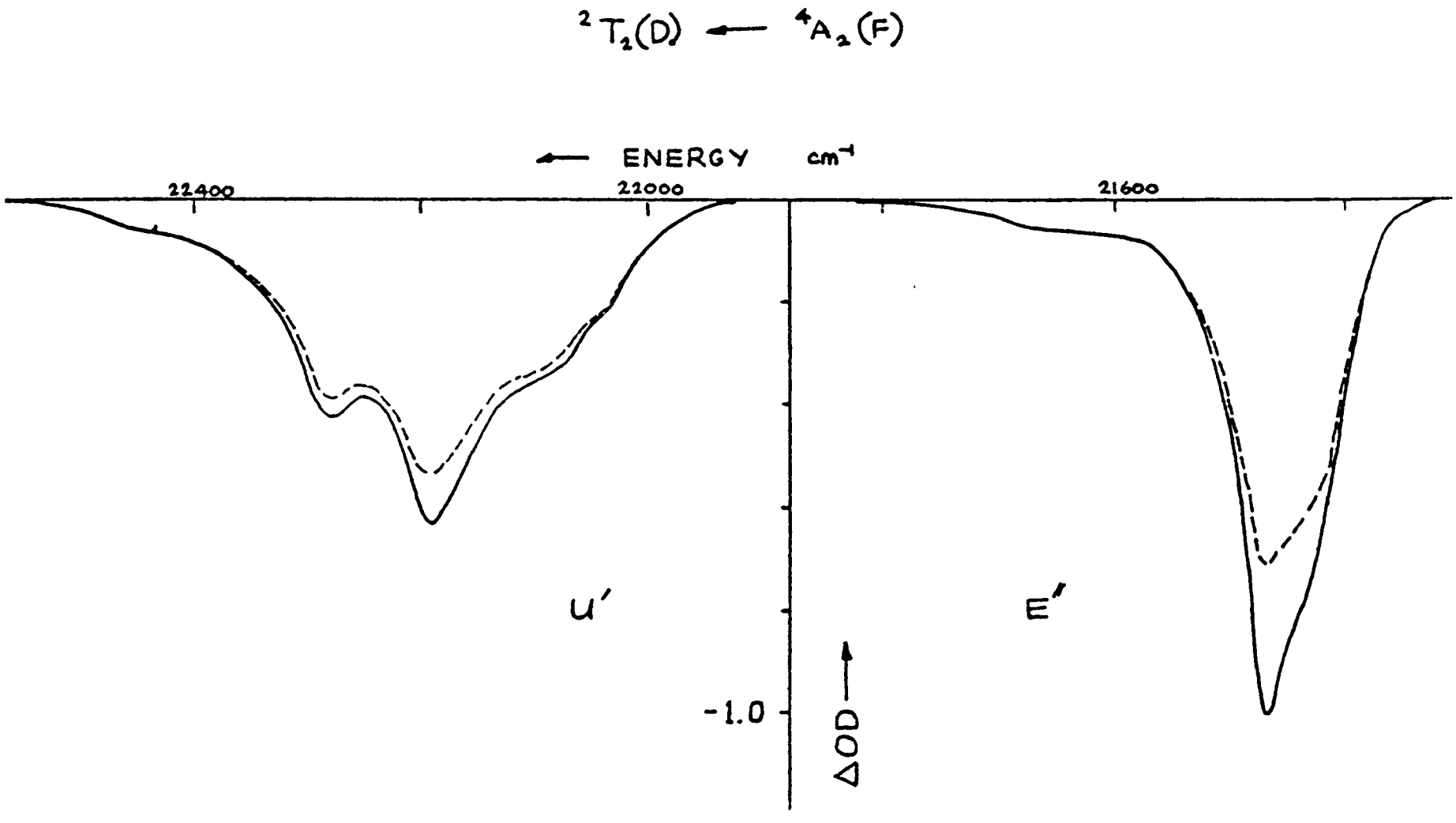

FIGURE 38.

AN EXAMPLE OF THE EFFECT OF THE INVERSE HYPERBOLIC TANGENT CORRECTION APPLIED TO AN MCD SPECTRUM .

Axial crystal of $(Et_4N)_2ZnI_4$ doped with Co^{2+} measured at 4.75T , 4.2K .

SPECTRUM AS RECORDED — — — —

CORRECTED BY COMPUTER ————

A P P E N D I X IV

MEASUREMENT OF ABSORPTION AND ZEEMAN SPECTRA

IV.1 ABSORPTION SPECTRA

All the absorption spectra reported in this study were measured on a McPherson RS10 spectrophotometer equipped with an Oxford Instruments continuous flow cryostat. When used with liquid helium as the cryogenic fluid, it was possible to record crystal spectra over the temperature range 3-80K with good stability. Some preliminary studies were also made on a Cary 14, but this did not give adequate resolution of the bands as its limit is 1Å over the spectral range 1950 to 25000Å. Also, it has an automatic slit control mechanism and a limited range of scanning speeds, and is less adaptable than the newer McPherson RS10. This latter instrument has a narrower operating range, 2300 to 12000Å, but offers better resolution with more control than the Cary 14.

A brief description of the McPherson RS10 spectrophotometer will now be given. It is a relatively new instrument, manufactured by the GCA Corporation of Massachusetts, USA. The light source is a 100 watt high pressure xenon arc, which provides a fairly uniform radiation intensity across the visible region with a few broad weak emission lines around 4200Å. Near 8000Å there are several very strong emission lines, and these can produce spurious peaks on spectra recorded in the double beam mode. In this region, a tungsten filament lamp provides a more uniform

emission of radiation, so the lamp housing was modified to accommodate a 60 watt tungsten bulb alongside the xenon arc. Light from either source was focussed on the entrance slit of the monochromator by means of an adjustable concave mirror. The monochromator is a 1-meter Czerny-Turner, fitted with a prism predisperser on the entrance slit. The grating is blazed for maximum efficiency at 5000Å, and has 1200 lines per millimeter. With slits set at their narrowest, 5μm, this gives a theoretical resolution of 0.1Å across the visible region. In practice, 0.15Å would be a more typical estimate of the resolution achieved with crystals. The monochromator entrance and exit slits are manually adjusted in experiments to give the best results in terms of resolution or noise level: wider slits give more light, hence lower noise in the spectra, but also provide lower resolution. The noise level is also a function of the EHT voltage applied to the photomultiplier tube (PMT), and this is set manually in the range 1000 to 1300 volts for crystal spectra. For work into the infra red region, 7000Å and below, a special PMT is used. It has extended red response with a cooled S-1 photocathode to eliminate thermal noise, and is mounted in a special insulated housing cooled with dry ice/methanol to -60°C. The effective range of this PMT is 3000 - 12000Å, and it may also be used on the MCD machine.

When the McPherson RS10 is used in the normal fashion to obtain absorption spectra, a "double beam attachment" is fitted to the exit slit of the monochromator. This has first an adjustable polarising prism, followed by a beam-splitter (a double-sided vibrating mirror driven electrically at 70Hz), and two separate compartments for sample and reference. Light passing through these compartments is directed with mirrors to a single

photomultiplier. The output of the PMT goes through fixed gain amplifiers to a logarithmic ratiometer, so that absorbances can be recorded directly in optical density units on the built-in Hewlett Packard chart recorder. Alternatively, the PMT output current for either channel, reference or sample, can be amplified and measured on an ammeter, or fed to the chart recorder for single beam measurements. Using this facility, the crystal mounted in the cryostat-can be moved around inside the sample compartment to the position at which it transmits the maximum amount of light. The light level in the reference channel is then adjusted to the same value using suitable attenuators, variable sized holes and neutral density filters. These preliminary settings are made at a wavelength at which the sample crystal, cooled if necessary, does not absorb light. The instrument can then be used in the double beam mode, and an appropriate optical density range is selected on the ratiometer (0.1, 1, 2, or 3 OD full scale deflection). On the highest range, intense peaks are sometimes seen to be flat topped. This can be caused by stray light in the sample compartment, or by insufficient light in the reference channel. Thus great care must be exercised when mounting crystals in the cryostat to ensure that no pin-hole light leaks are present at the edges of the mounting plate. Also, using the exit slit shutter, the PMT dark current can be measured and offset to zero as this is effectively a contributor to stray light and will cause error in the measurement of large optical densities.

Single beam experiments may be performed by setting the vibrating mirror to the sample position, and measuring the PMT output on the chart recorder as the wavelength is scanned. It

is necessary to record a baseline separately for extended scans, although over a few Ångstroms it may be considered to be flat. Again, the dark current should be offset to zero, and the "no light" level marked on the recorder trace at the beginning and end of each scan. This allows the linear transmission measurements to be converted to optical densities, the other point of reference being the "no sample" baseline.

IV.2 ZEEMAN MEASUREMENTS

In these experiments, a magnetic field is applied across the crystal on which optical measurements are being made. The arrangement adopted for measurements on Cs_3MnCl_5 was as follows. The crystal was mounted in the large cryostat normally used on the MCD machine, so that fields up to 4.75Tesla could be generated by means of the superconducting coils. As this cryostat was much too big to fit inside the sample compartment of either the Cary 14 or McPherson RS10 double beam spectrophotometers, a single beam arrangement was adopted on the McPherson. The double beam attachment was removed from the exit slit assembly, and the MCD cryostat, supported on a Dexion frame, was "mated" to it using a simple optical bench. This consisted of an adjustable lens and a polariser for use with non-axial crystals. The bench was made light tight with aluminium covers, and a blackout cloth was wrapped around the outside. As a further precaution, experiments were performed under subdued lighting. The photomultiplier was removed from the double beam attachment and mounted in a 50-cm. long brass tube normally used on the MCD machine. An adaptor plate was made to allow this tube to be attached directly onto the MCD cryostat. The intention of this arrangement was to reduce the effect of the very large magnetic

field on the electrons in the PMT, which had a mu-metal screen placed around it. Its output was measured in the single beam mode.

With the apparatus set up and the crystal mounted in the cryostat, basic optical alignment was done by eye. As an axial crystal of Cs_3MnCl_5 was being examined, the polariser was not needed, but the lens on the optical bench was adjusted to give maximum transmission of light through the crystal. The cryostat was then cooled using liquid nitrogen, a process requiring several hours. The inner reservoir was then blown dry with nitrogen gas, and filled with liquid helium, and the sample cooled to 4.2K. It was found that when the magnetic field was brought up to 4.75T, there was a considerable loss of PMT output owing to inadequate shielding from the field. The gain was increased by raising the applied EHT to restore the signal to give a constant light level at the starting point of the wavelength scan. In subsequent scans at lower magnetic fields, the EHT setting was reduced so as to maintain the same initial light level. By means of this procedure we were able to produce Zeeman spectra of some of the very sharp origin lines seen in Cs_3MnCl_5 at 4.2K in such a way that successive traces made at different fields were directly comparable.

A P P E N D I X V

C-TERM FOR A $^1S \leftarrow {}^1P$ TRANSITION

We shall first establish the splitting pattern for ^1P in a magnetic field H_z. The Hamiltonian operator is:

$$\hat{\mathcal{H}} = -\hat{\underset{\sim}{\mu}} \cdot \underset{\sim}{H}$$

$$= -\hat{\mu}_z H_z$$

$$E = \langle a|\hat{\mathcal{H}}|a\rangle$$

$$= -\langle a|\hat{\mu}_z|a\rangle H_z$$

$$= \beta\langle a|\hat{L}_z + 2\hat{S}_z|a\rangle H_z$$

For ^1P, $L = 1$, $S = 0$, $M_L = +1$, 0, or -1.

$M_L = +1$: $E = \beta\langle +1|\hat{L}_z|+1\rangle H_z$

$= \beta\ +1\langle +1|+1\rangle H_z$

$= +\beta H_z$

$M_L = 0$: $E = \beta\langle 0|\hat{L}_z|0\rangle H_z$

$= 0$

$M_L = -1$: $E = \beta\langle -1|\hat{L}_z|-1\rangle H_z$

$= -\beta H_z$

This gives the splitting pattern below, with the circularly polarised transitions:

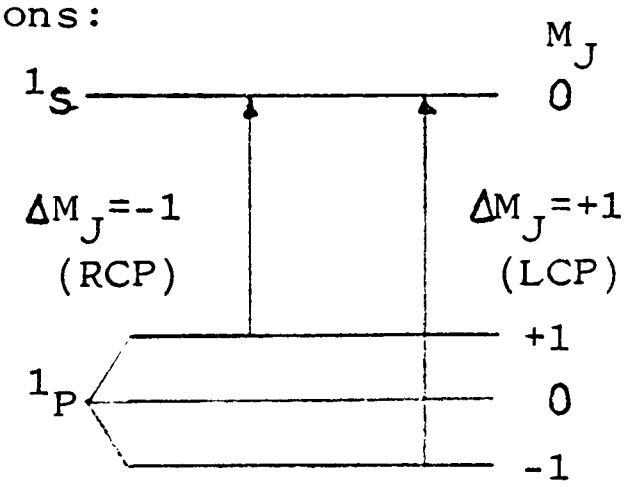

The polarisation properties are as shown for transitions via the electric dipole moment operator because of the angular momentum properties of RCP and LCP light. These arise as a result of the defining equations, and give a "right-handed" photon $J = 1$, $M_J = -1$, while a "left-handed" photon has $J = 1$, $M_J = +1$. The rule of conservation of momentum applies to M_J.

The C-term is given by:

$$C = \frac{3}{d_a} \sum_{j \leftarrow a} \langle a|\hat{\mu}_z|a\rangle \, \mathrm{Im}\left\{\langle a|\hat{m}_x|j\rangle\langle j|\hat{m}_y|a\rangle\right\} \qquad \text{EQUATION (2.23)}$$

$$= \frac{3}{2d_a} \sum_{j \leftarrow a} \langle a|\hat{\mu}_z|a\rangle \left\{|\langle j|\hat{m}_-|a\rangle|^2 - |\langle j|\hat{m}_+|a\rangle|^2\right\} \qquad \text{EQUATION (3.9)}$$

Since the excited state wavefunction $|j\rangle$ has $M_J = 0$, the matrix elements $\langle j|\hat{m}_\pm|a\rangle$ will be zero unless the operator acting on a component of $|a\rangle$ gives $|0\rangle$. Out of the six possibilities, we find

$\langle 0|\hat{m}_+|-1\rangle = 1$ and $\langle 0|\hat{m}_-|+1\rangle = 1$.

Thus the LCP transition, $\Delta M_J = +1$, correlates with the matrix element $\langle j|\hat{m}_+|a\rangle$; the RCP transition, $\Delta M_J = -1$, correlates with the matrix element $\langle j|\hat{m}_-|a\rangle$.

$$C = \frac{1}{2}\left[+\beta(0\text{-}1) + -\beta(1\text{-}0)\right]$$

from $^1P_{-1}$ from $^1P_{+1}$

$$= -\beta$$

$\Delta\varepsilon$ is related to $-CH_z$, and will be positive - see EQUATION (2.24). Examination of the above diagram confirms this, as the two transitions have equal intrinsic probabilities but the LCP transition is the more intense as it comes from the most heavily populated component of the ground state, and $\Delta\varepsilon = \varepsilon_L - \varepsilon_R$. This clearly demonstrates how a negative C-term corresponds to a positive MCD signal.

EQUATION (3.9) can be recast into an alternative form by use of the Hermitian conjugate nature of lowering operators [76]:

$$\langle j|\hat{m}_{\pm}|a\rangle = -\langle a|\hat{m}_{\mp}|j\rangle .$$

Substituting into (3.9), we find:

$$C = \frac{3}{2d_a} \sum_{j \leftarrow a} \langle a|\hat{\mu}_z|a\rangle \left\{ |\langle a|\hat{m}_+|j\rangle|^2 - \langle a|\hat{m}_-|j\rangle|^2 \right\} .$$

Again for the $^1S \leftarrow {}^1P$ transition, we have the non-zero matrix elements:

$\langle +1|\hat{m}_+|0\rangle = 1$ and $\langle -1|\hat{m}_-|0\rangle = 1$, and:

$$C = \frac{1}{2}\left[+\beta(0-1) \; + \; -\beta(1-0) \right]$$

$$\text{from } {}^1P_1 \qquad \text{from } {}^1P_{+1}$$

$$= -\beta.$$

The two formulae for C are thus shown to be equivalent.

The energy of ^1P_o is independent of the magnetic field and acts as a reference point, E = 0. The optical transition $^1S \leftarrow {}^1P_o$ by the electric dipole mechanism is allowed only in z-polarisation.

A P P E N D I X VI

ELECTROSTATIC ENERGY MATRICES FOR $3d^5$ IONS IN A CUBIC ENVIRONMENT

These matrices are taken from the work of Stout [39] and are in the Weak Field representation. Energies are relative to the $^6A_1(S)$ ground state. Trees correction terms have been added as these have been shown to improve the fit to the observed energy levels for the $FeCl_4^{\ominus}$ ion [108].

$^4A_1(G) = 10B+5C+20\alpha - \epsilon(10B+5C)$.

$^4A_2(F) = 22B+7C+12\alpha+2\beta - \epsilon(38B+11C)$.

^4E

^4D	^4G
$17B+5C+6\alpha - \frac{\epsilon}{7}(124B+34C)$	$\frac{2\epsilon\sqrt{3}}{7}(17B+5C)$
	$10B+5C+20\alpha - \frac{\epsilon}{7}(58B+29C)$

$^4T_1$

^4F	^4P	^4G
$22B+7C+12\alpha+2\beta - \epsilon(7.4B+2.9C)$	$-\epsilon(3.8B+1.8C)$	$-2\sqrt{5}\,Dq - \epsilon\sqrt{5}(1.8B-0.9C)$
	$7B+7C+2\alpha+2\beta - \epsilon(5.6B+5.6C)$	$-4\sqrt{5}\,Dq - 2\epsilon\sqrt{5}(1.8B-0.9C)$
		$10B+5C+20\alpha - \epsilon(9B+4.5C)$

$^4T_2$

^4F	^4G	^4D
$22B+7C+12\alpha+2\beta - \epsilon(21B+6.5C)$	$-10Dq\sqrt{3/7} - 5\epsilon\sqrt{3/7}(1.8B-0.9C)$	$-20Dq\sqrt{1/7} - 10\epsilon\sqrt{1/7}(1.8B-0.9C)$
	$10B+5C+20\alpha - \frac{\epsilon}{14}(86B+43C)$	$-\frac{\epsilon}{7}\sqrt{3}(17B+5C)$
		$17B+5C+6\alpha - \frac{\epsilon}{7}(76B+24C)$

B and C are the Racah Parameters, and Dq is the Crystal Field Splitting parameter. As the matrices are written above, they represent octahedral coordination [39]. For the tetrahedron, Dq is of opposite sign (EQUATION 1.8), so that negative values of Dq are used to fit the energy levels of Cs_3MnCl_5. ϵ is the Koide and Pryce covalency parameter for octahedral coordination given by [37]:

$$\epsilon = 1 - \frac{N_e^2}{N_t^2} ,$$

where N_e and N_t are the normalisation factors of the e- and t_2-orbitals respectively. In tetrahedral coordination:

$$\epsilon_T = 1 - \frac{N_t^2}{N_e^2}$$

$$= 1 - 1/(1-\epsilon)$$

$$= -\epsilon \text{ to a first approximation.}$$

This explains why negative values of ϵ are used to describe the effect of covalency upon the energy levels of the tetrahedral $MnCl_4^{2\ominus}$ ion.

In the Weak Field representation, the Trees and seniority correction terms appear only in the diagonal energies, and can easily be added to Stout's original matrices. The Trees correction for a d^n configuration is given by [109]:

$$\alpha[L(L+1)-6n] + \beta Q.$$

L is the orbital angular momentum of the state, while the factor "-6n" is common to all the multiplets of $3d^5$ and does not contribute to the differences in energy between them. Q is the total seniority operator [3]. Multiplets of d^n have a seniority number v, and:

$$Q(n,v) = 1/4(n-v)(4l+4-n-v).$$

For $3d^5$, n=5 and l=2,and

^6S, ^4G, and ^4D have v=5, giving Q=0;

^4P and ^4F have v=3, giving Q=2.

In the free ion, $\alpha = 65cm^{-1}$ and $\beta = -131cm^{-1}$ [21]. For the calculations on Cs_3MnCl_5 given in CHAPTER 5, the values of Vala [60] were used in order to simplify the comparison of results, that is, $\alpha = 76cm^{-1}$, $\beta = 0$.

R E F E R E N C E S

[1] F.A. Cotton, "Chemical Applications of Group Theory", Wiley-Interscience (1963 and 1971).

[2] D.J.W. Ijdo, Thesis, University of Leiden (1960).

[3] J.S. Griffith, "The Theory of Transition Metal Ions", Cambridge University Press (1961).

[4] E.B. Wilson, J.C. Decius, and P.C. Cross, "Molecular Vibrations", McGraw-Hill (1955).

[5] J. Gielessen, Annalen der Physik 22, 537 (1935).

[6] A.D. Buckingham and P.J. Stephens, Ann. Rev. Phys. Chem. 17, 399 (1966).

[7] D.R. Woodwark, Part II Thesis, University of Oxford (1974); R.G. Denning, T.R. Snellgrove, and D.R. Woodwark, Mol. Phys 30, 1819 (1975).

[8] J.E. Ferguson, Progress in Inorganic Chemistry 12, 159 (1970).

[9] B.N. Figgis, "Introduction to Ligand Fields", Wiley-Interscience (1962).

[10] L.E. Orgel, "An Introduction to Transition Metal Chemistry", Methuen (1960 and 1966).

[11] T.M. Dunn, D.S. McClure, and R.G. Pearson, "Some Aspects of Crystal Field Theory", Harper and Row (1965).

[12] C.A. Coulson, "Valence", Oxford University Press (1952 and 1961).

[13] G. Joos, Annalen der Physik 81, 1076 (1926) and 85, 641 (1928).

[14] H.A. Bethe, Annalen der Physik 3, 133 (1929).

[15] C.W. Nielson and G.F. Koster, "Spectroscopic Coefficients for the p^n, d^n, and f^n Configurations", M.I.T. Press(1963).

[16] G.Racah, Phys. Rev. 62 438 (1942).

[17] Y.Tanabe and S.Sugano, J.Phys. Soc. Japan, 9, 86 and 9, 753 (1954).

[18] L.E.Orgel, JCP 23,11819 (1955).

[19] R.E.Trees, Phys. Rev. 83, 756 (1951); 84, 1059 (1951); and 85, 382 (1952).

[20] G. Racah, Phys. Rev. 85, 381 (1952).

[21] O. Garçia- Riquelme, Optica Pura Aplicanda 1, 53 (1968).

[22] D. Curie, C. Barthou, and B. Canny, JCP 61, 3048 (1974).

[23] See, for example, J.H. Van Vleck, JCP 3, 803 and 807 (1935); 7, 61 and 72 (1939).

[24] D.P. Craig and E.A. Magnusson, Disc. Far. Soc. 26, 116 (1958).

[25] K. Rajnak and B.G. Wybourne, JCP 41, 565 (1964).

[26] M.E. Gerloch and R.C. Slade, "Ligand Field Parameters", Cambridge University Press (1973).

[27] J.H. Van Vleck and W.G. Penney, Phil. Mag. 17, 961 (1934).

[28] H. Wanatabe, Prog. Theoret. Phys. (Kyoto) 18, 405 (1957).

[29] J. Baker, B. Bleaney, and W. Hayes, Proc. Roy. Soc. A247, 141 (1958).

[30] T.P.P. Hall, W. Hayes, and F.I.B. Williams, Proc. Phys. Soc. London 78, 883 (1961).

[31] W. Low, Phys. Rev. 105, 792 (1957).

[32] G.D. Watkins, Phys. Rev. 110, 986 (1958).

[33] J.C.M. Henning and P.F. Bongers, J. Phys. Chem. Solids 27, 745 (1966).

[34] B.N. Figgis,M.E.Gerloch , and R. Mason, Acta Cryst. 17, 506 (1964).

[35] N.S. Hush and R.J.M. Hobbs, Progress in Inorganic Chemistry 10, 326-344 (1968).

[36] L.E. Orgel, JCP 23, 1004, 1819, and 1824 (1955).

[37] S. Koide and M.H.L. Pryce, Phil. Mag. 3, 607 (1958).

[38] R. Englman, Mol. Phys. 4, 183 (1961).

[39] J.W. Stout, JCP 31, 709 (1958).

[40] D.M. Finlayson, I.S. Robertson, T. Smith and R.W.H. Stevenson, Proc. Phys. Soc. London 76, 335 (1960).

[41] R. Pappalardo, JCP 31, 1050 (1959) and 33, 613 (1960).

[42] J.W. Stout, JCP 33, 303 (1960).

[43] I. Tsujikawa, J.Phys. Soc. Japan 13, (1958); I. Tsujikawa and E. Kanda, ibid. 18, 1382 (1963).

[44] I. Tsujikawa and L. Couture, Comptes Rendus 250, 2013 (1960).

[45] I. Tsujikawa, J. Phys. Soc. Japan 18, 1391 (1963).

[46] D.S. McClure, JCP 39, 2850 (1963).

[47] J. Ferguson, H.J. Guggenheim, and Y. Tanabe, J. Phys. Soc. Japan 21, 692 (1966).

[48] J. Ferguson, Austral. J. Chem. 21, 201 (1968).

[49] R. Stevenson, Phys. Rev. 152, 531 (1966).

[50] J. Ferguson, E.R. Krausz, and H.J. Guggenheim, Mol. Phys. 27, 577 (1974).

[51] F.A. Cotton, D.M.L. Goodgame, and M. Goodgame, J. Am. Chem. Soc. 84, 167 (1962).

[52] A.I. Ryskin, G.I. Khilko, B.I. Maksakov, and K.K. Dubenskii, Optics and Spectroscopy 16, 149 (1964).

[53] D.W. Langer and S. Ibuki, Phys. Rev. 138A, 809 (1965).

[54] D.W. Langer and H.J. Richter, Phys. Rev. 146, 554 (1966).

[55] E.M. Wray and J.W. Allen, J. Phys. (C) 4, 512 (1971).

[56] K. Motizuku and I. Harada, Solid State Commun. 8, 951 (1971).

[57] R. Parrot and C. Blanchard, Phys. Rev. 6B, 3992 (1972).

[58] K.E. Lawson, JCP 47, 3627 (1967).

[59] C. Stoneman, Ph.D. Thesis, University of London (1968).

[60] M.T. Vala, C.J. Ballhausen, R. Dingle, and S.L. Holt, Mol. Phys. 23, 217 (1972).

[61] A.J. McCaffery, P.J. Stephens, and P.N. Schatz, Inorg. Chem. 6, 1614 (1967).

[62] H. Kato, JCP 58, 1964 (1973).

[63] M.T. Vala, J.C. Rivoual, and J. Badoz, Mol. Phys. 30, 1325 (1975). (This paper gives a theoretical treatment of the MCD and MLD, while the spectra are to be published later in Molecular Physics.)

[64] N.N. Greenwood, "Spectroscopic Properties of Inorganic and Organometallic Compounds", Specialist Periodical Reports of the Chemical Society, London (1968-1972).

[65] P. Day, "Electronic Structure and Magnetism of Inorganic Compounds", Specialist Periodical Reports of the Chemical Society, London (1970 onwards).

[66] L.L. Lohr, JCP 45, 3611 (1966).

[67] L.L. Lohr and D.S. McClure, JCP 49, 3516 (1968).

[68] L.L. Lohr, JCP 55, 27 (1971).

[69] E.A. Cooke, D. Phil. Thesis, Oxford (1970).

[70] P.N. Quested, R.J. Tacon, P. Day, and R.G. Denning, Mol. Phys. 27, 1553 (1974).

[71] H.W.J. Blötte and W.J. Huiskamp, Physica 53, 445 (1971).

[72] P. Day and B.D. Bird, Chem. Commun. 741 (1967;
B.D. Bird, Part II Thesis, Oxford (1967).

[73] S.F. Mason, Quart. Review 17, 10 (1963).

[74] P.N. Schatz and A.J. McCaffery, Quart. Review 23, 552 (1969).

[75] A. Moscowitz, Adv. Chem. Phys. 4, 67 (1962).

[76] P.W. Atkins, "Molecular Quantum Mechanics", Oxford University Press (1970).

[77] P.J. Stephens, JCP 52, 3489 (1970).

[78] C.H. Henry, S.E. Schnatterly, and C.P. Slichter, Phys. Rev. 137A, 583 (1965).

[79] P.N. Quested and R.J. Tacon, unpublished work.

[80] J.C. Collingwood, P. Day, R.G. Denning, P.N. Quested, and T.R. Snellgrove, J. Phys. (E) 7, 991 (1974).

[81] P.G. Russell, D.S. McClure, and J.W. Stout, Phys. Rev. Letters 16, 176 (1966).

[82] J.S. Griffith, "The Irreducible Tensor Method for Molecular Symmetry Groups", Prentice-Hall (1962).

[83] B.D. Bird, D. Phil. Thesis, Oxford (1969).

[84] B.D. Bird and P. Day, JCP 49, 392 (1968).

[85] J.C. Rivoual, Ph.D. Thesis, Paris (1971).

[86] W. Low and G. Rosengarten, J. Mol. Spectroscopy 12, 319 (1964).

[87] M. Rotenberg, R. Bivins, N. Metropolis, and J.K. Wooten, "The 3-j and 6-j Symbols", The Technology Press, M.I.T. (1959).

[88] R.L. Greene, D.D. Sell, W.M. Yen, A.L. Schawlow, and R.M. White, Phys. Rev. Letters 15, 656 (1965).

[89] E.V. Sayre, K. Sancier, and S. Freed, JCP 23, 2060 (1955).

[90] P.N. Quested, R.J. Tacon, R.G. Denning, and P. Day, unpublished results.

[91] D.S. McClure, "Electronic Spectra of Molecules and Ions in Crystals", Academic Press (1964).

[92] L.J. Heidt, G.F. Koster, and A.M. Johnson, J. Am. Chem. Soc. 80, 6471 (1958).

[93] D. Oehlkrug and A. Wölpl, Ber. Bunsenges physik. Chem. 76, 680 (1972).

[94] M.T. Vala, personal communication (July 1975).

[95] See, for example, R. McWeeny, "Symmetry, an Introduction to Group Theory and its Applications", MacMillan (1963).

[96] J.S. Avery, C.D. Burbridge, and D.M.L. Goodgame, Spectrochim. Acta A24, 1721 (1968).

[97] S. Thomas, personal communication (September 1974); Ph.D. Thesis, Victoria University of Manchester.

[98] D.J. Drury, personal communication (November 1974).

[99] T.R. Gilson, personal communication to E.A. Cooke in [69].

[100] J.T.R. Dunsmuir and A.P. Lane, J. Chem. Soc. (A), 404 (1971).

[101] R.J. Tacon, P. Day, and R.G. Denning, JCP 61, 751 (1974).

[102] P. Day and L. Dubicki, J. Chem. Soc. Faraday Trans. II, 69, 363 (1973).

[103] E.M. Levin, C.R. Robbins, M.K. Reser, and H.F. McMurdie, "Phase Diagrams for Ceramists", American Ceramic Society, Columbus, Ohio (1964, Supplement 1969).

[104] B.F. Markov and R.V. Chernov, Ukr. Khim. Zh. 24, 139 (1958).

[105] F. Woldbye and S. Baggar, Acta Chem. Scand. 20, 1145 (1966).

[106] L. Velluz, M. Legrand, and M. Grosjean, "Optical Circular Dichroism", Academic Press (1965).

[107] R.G. Denning, P.N. Quested, and R.J. Tacon, unpublished results.

[108] M.T. Vala and P.J. McCarthy, Spectrochim. Acta 26A, 2183 (1970).

[109] R. Stevenson, "The Multiplet Structure of Atoms and Molecules", W.B. Saunders (1965).